Probing low–mass X–ray binaries with X–ray timing

Probing low–mass X–ray binaries with X–ray timing

Onderzoek naar lage massa röntgendubbelsterren met röntgen tijd–variaties

Academisch Proefschrift

ter verkrijging van de graad van doctor
aan de Universiteit van Amsterdam,
op gezag van de Rector Magnificus prof. dr J.J.M. Franse,
ten overstaan van een door het college voor promoties ingestelde commissie,
in het openbaar te verdedigen in de Aula der Universiteit op

vrijdag 19 oktober 2001, te 10:00 uur

door

Peter Gustaaf Jonker

geboren te Amersfoort

PROMOTIECOMMISSIE

PROMOTOR	prof. dr Michiel van der Klis
OVERIGE LEDEN	prof. dr Ed van den Heuvel
	prof. dr F.L. Linde
	dr Mariano Méndez
	prof. dr Henk Spruit
	prof. dr Frank Verbunt
	prof. dr Rens Waters

Sterrenkundig Instituut “Anton Pannekoek”
Faculteit der Natuurwetenschappen
Universiteit van Amsterdam

Cover illustration by Leander and Peter Jonker after M.C. Escher

Contents

Chapter 1

Introduction

1.1 Low–mass X–ray binaries

The studies presented in this thesis concern low–mass X–ray binaries (LMXBs). LMXBs are binary systems in which a low–mass companion star ($\lesssim 1\,M_{\odot}$) transfers matter to a compact object, either a neutron star or a black hole. The compact object is formed in a supernova explosion (although a neutron star might also be formed by accretion induced collapse of a white dwarf, Whelan & Iben 1973). The companion star loses mass to the compact object either via a stellar wind or via Roche lobe overflow. The presented work focuses on Roche lobe overflow systems with a neutron star compact object. The transferred matter nearly always forms an accretion disk where matter spirals in along (nearly) circular orbits. Such a disk is formed since particle orbits which are initially elliptical will precess due to the presence of the companion star, causing them to intersect. Particle collisions convert orbital energy into heat, circularizing the orbit as a circular orbit has the least energy for a given angular momentum. After the accretion disk has formed transferred matter joins the disk flow after impacting on the accretion disk rim.

The matter accretes onto the neutron star when nearly all of the angular momentum is transported away, e.g. to the outer parts of the disk by internal viscous torques (Shakura & Sunyaev 1973). There, it can for instance be fed back to the binary system by tidal torques. The remaining angular momentum will add to that of the neutron star, spinning it up. Neutron stars with a strong magnetic field ($\sim 10^{11-12}$ G) can be spun–up to millisecond periods by a combination of accretion and magnetic field decay (Bhattacharya 1995). Recently, it has become clear that in analogy with active galactic nuclei a jet–like outflow is present in most LMXBs (Mirabel & Rodríguez 1998).

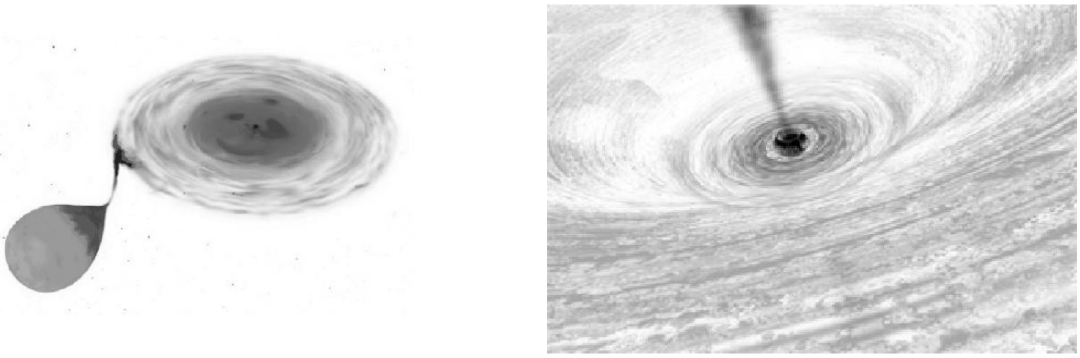

Figure 1.1: An artist's impression of an LMXB (left image) and of the center of the accretion disk around a neutron star (right panel;credit NASA). The system in the left image is rotating clockwise.

1.2 Why study low–mass X–ray binaries?

There are several reasons to study neutron star LMXBs. Probably the most important one is that the neutron stars in LMXBs provide a laboratory to test the behavior of matter under physical conditions that are unattainable on earth. The description of the relations between the pressure, temperature, and density of matter comprised by the neutron star (the equation of state; EoS) and the description of motion of matter close to the neutron star (where the Newtonian description of physics is no longer valid) are the ultimate goals of studies of LMXBs. Stellar structure theory predicts the neutron star mass–radius relation and provides a firm upper limit on the mass of a neutron star for each EoS. Neutron star mass and radius measurements are therefore important in distinguishing between the various theoretical models (see the discussion by van Paradijs & McClintock 1995). Although Einstein's theory of General Relativity is widely accepted, its predictions have not yet been tested in the strong field regime. Direct detection of a strong field effect such as the existence of a marginally stable inner circular orbit would provide an excellent test of the theory. Another key prediction relevant for the study of accretion onto a neutron star is the dragging of inertial frames causing the accretion disk to precess if the orbits of motion of matter in the disk are inclined with respect to the equatorial plane of the spinning neutron star. This effect, although not restricted to the strong field regime was first described by Thirring & Lense (1918) and is commonly referred to as Lense–Thirring precession. While

Lense–Thirring precession near neutron stars has frequencies of several tens of Hz, near the earth such an effect will only be $\sim 1 \times 10^{-15}$ Hz.

Rapidly rotating neutron stars may emit gravitational radiation; the neutron stars in LMXBs may in fact be the strongest persistent sources of gravitational radiation in the sky (Bildsten 1998). This gravitational radiation of LMXBs might be detectable with instruments such as LIGO(2), providing an important test of predictions of General Relativity. Knowledge of the spin period of the neutron star derived from X–ray timing studies facilitates the searches for this gravitational radiation.

The neutron stars in LMXBs can acquire a short rotational period during the mass transfer phase. After the accretion stops the spin period may manifest itself in the form of millisecond pulsations at radio wavelengths, making LMXBs the predecessors of millisecond radio pulsars (Alpar et al. 1982; Radhakrishnan & Srinivasan 1982). The discovery of Wijnands & van der Klis (1998) of the first millisecond accreting X–ray pulsar provided strong support for this evolutionary scenario. However, to date no other accretion powered X–ray pulsars have been found. In fact X–ray pulsations have only been found in 6 LMXBs (see Chapter 11).

1.3 Observing low–mass X–ray binaries

To date more than 150 LMXBs have been found in our galaxy and in the Small and Large Magelanic Clouds (see the catalogue of van Paradijs 1995 and its update by Liu et al. 2001). The number of detected LMXBs outside our Galaxy is growing rapidly due to their detection in other galaxies using the Chandra satellite, although the definite classification of these sources awaits further observations (see Fabbiano 1995 for an overview of the X–ray sources in other galaxies detected primarily with the Einstein and Rosat satellites). LMXBs can in principle be observed at all wavelengths although most of the accretion energy is emitted in X–rays.

Optical and ultraviolet

In the optical and ultraviolet measurements are often hampered by the strong extinction, especially towards the galactic center where many of the LMXBs are located. An overview of the optical and ultraviolet properties of the galactic LMXBs has been given by van Paradijs & McClintock (1995). The optical flux generated in the accretion disk due to reprocessing of the impinging X–rays dominates over the optical flux generated internally in the accretion disk. In some LMXBs a periodic modulation of the optical flux is seen. This modulation is often caused by the changing aspect of the heated side of the companion star. Absorption lines in the spectrum are formed in the companion star, allowing for the study of its motion around the center of mass. Together with knowledge of the motion of the neutron star (e.g. from Doppler shifts of X–ray pulses) this leads to mass estimates for both binary components given the inclination.

Radio and infrared

The ratio of flux emitted by the disk to that emitted by the companion is nearly always larger in the optical than in the infrared (e.g. for K–dwarf or giant companions), furthermore, the extinction is less at infrared than at optical wavelengths, increasing the detectability of LMXBs. Recently, evidence has been presented that besides the thermal emission from the star and accretion disk, synchrotron emission from highly relativistic electrons contributes to the emission at infrared wavelengths (Fender et al. 1997; Brocksopp et al. 2001). This synchrotron emission is also responsible for the radio emission of the LMXBs. Several LMXBs show highly relativistic jet–like outflows (Mirabel & Rodríguez 1994; Fender & Hendry 2000). The mechanical energy in the jet may in fact be a substantial fraction of the accretion luminosity.

X–rays: spectra

The research presented in this thesis primarily makes use of data obtained with the *Rossi X–ray Timing Explorer* satellite (throughout the thesis referred to as RXTE satellite; Bradt et al. 1993, see Chapter 2). The X–rays are thought to arise from close to the neutron star. In case of neutron star LMXBs a thermal component is produced by release of gravitational potential energy near the surface. The energy is released in an equatorial boundary layer (Popham & Sunyaev 2001; Sibgatullin & Sunyaev 2000) or, if the neutron star magnetic field is dynamically important, on the poles of the neutron star (Miller et al. 1998). Steady hydrogen burning on the surface of the neutron star also contributes to the X–ray flux, although this is only a small fraction of the total since the accretion efficiency is $\gtrsim$20 times that of fusion. A disk blackbody from the inner parts of an optically thick accretion disk contributes to the LMXB soft X–ray spectrum. A hard ($>$20 keV) power law contribution is detected in the spectra preferentially (but not exclusively) during

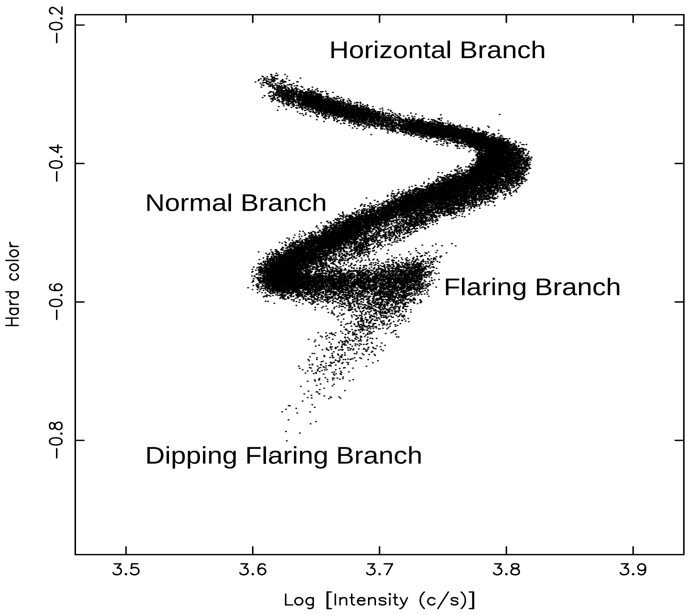

Figure 1.2: Hardness–intensity diagram for the Z source GX 5–1.

phases of relatively low 2–10 keV X–ray fluxes. This component could arise from inverse–Compton scattering of soft seed photons by relativistic electrons (Shapiro et al. 1976; Sunyaev & Titarchuk 1980; see Poutanen 1998 for a review). The hot electrons causing the infrared/radio emission may be the same as those producing (some of) the hard X–rays observed of LMXBs (Markoff et al. 2001).

X–ray spectral changes can be studied by fitting spectral models to the data, however, given the relatively low spectral resolution of the RXTE satellite and the subtle spectral changes, most of the spectral information presented and used in this thesis comes from color–color or hardness–intensity diagrams (CDs and HIDs, respectively). Count rate ratios in different energy bands are plotted vs. each other. Using this technique provides insight in the differences and similarities between the various types of LMXBs and in the source spectral changes with time (but see Chapter 7 for a cautioning note). Hasinger & van der Klis (1989) divided the neutron star LMXBs into two categories named Z and atoll sources after the patterns they trace out in a CD or HID with time (see Figures 1.2, 1.3, and Chapter 2). The Z branches are called from top to bottom, Horizontal Branch, Normal Branch, and Flaring Branch. In three of the six Z sources an extra branch trailing the Flaring Branch called ’Dipping Flaring Branch’ is also observed (Kuulkers et al. 1994).

The nomenclature for the atoll sources is just as colorful; one distinguishes

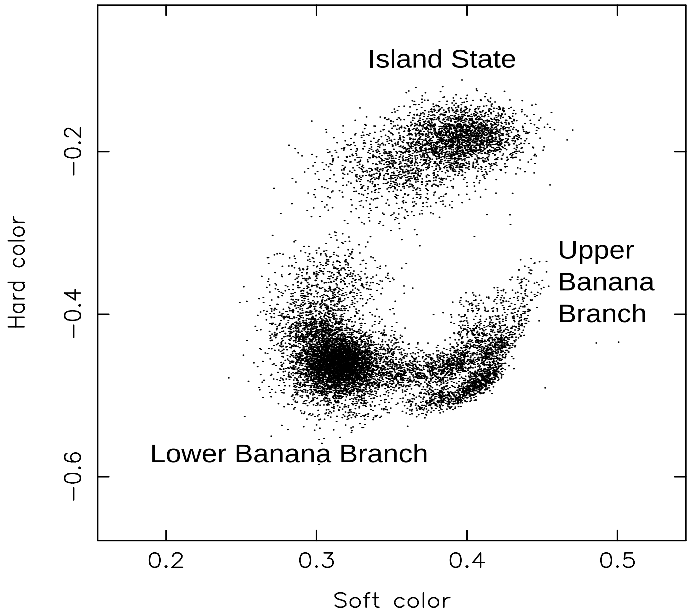

Figure 1.3: Color–color diagram for the atoll source 4U 1608–52.

the Island state and the Banana branch. The latter is sub–divided into a lower and an upper Banana (see Figure 1.3). The typical timescale for the source to move from one part of the diagram to another is hours to days for the Banana branch, although a source can stay in the Island state for weeks. The Z sources are among the brightest persistent X–ray sources in the sky. The less luminous but more numerous atoll sources are thought to accrete at lower rates (0.01–0.5 $L_{\rm Edd}$).

Besides the X–ray spectrum, variations in the X–ray flux in a certain energy range as a function of time are studied. This is called timing analysis; it is the main tool I employed and the results thereof constitute the major part of this thesis.

1.4 X–ray timing of low–mass X–ray binaries

1.4.1 Variability types

X–ray variability involves a wide range of timescales, varying from as long as several years to milliseconds. In addition to timescale variability is characterized by its coherence. It can be highly coherent (periodic), moderately coherent (quasi–periodic), or incoherent (white or red noise) like. Processes are called quasi–

periodic as the centroid frequency divided by the full–width at half maximum is more than 2. In LMXBs variability processes of all these types have been detected. A brief overview of the timescales and the probable causes of observed variability is given below. The processes are discussed in order of decreasing variability timescale. After this phenomenological overview the implications of the findings presented in the subsequent chapters of this thesis will be addressed.

Variations in X–ray flux can be associated with changes in the mass transfer rate onto the neutron star, some of which are caused by accretion disk instabilities. Accretion disk instabilities leading to periods of alternatingly very low and high mass accretion rate are a likely explanation for the transient systems, which are characterized by episodic periods of outbursts in X–rays, optical, and radio. The recurrence timescale of transient outburst events, attributed to the periods of a high mass accretion rate is typically of the order of years.

Eclipses and dips

Variability taking place on timescales of less than an hour to more than a day with a periodic nature can be identified with the orbital motion of the compact object around the binary center of mass. Variability due to the orbital period manifests itself especially in systems viewed under a high inclination; the most obvious types of orbital modulation are X–ray eclipses and/or X–ray dips (Figure 1.4, see Chapters 3, 4 and, 11). X–ray dips are thought to be caused by a periodic obscuration of the central source by a structure formed in an interaction between the accretion stream emerging from the companion and the accretion disk (White & Swank 1982; White et al. 1995).

Type I X–ray bursts

Further variability is associated with thermo–nuclear runaway reactions taking place on the surface of a neutron star, the so–called type I X–ray bursts (see Figure 1.4, Chapters 3, 4, and 9). These type I bursts are a distinctive sign of the presence of a neutron star in the LMXB, since black holes have no solid surface. Stable burning of hydrogen via the CNO cycle takes place on the surface of a neutron star if the local mass accretion rate is high (for solar abundances $\sim \dot{M} > 2 \times 10^{-10} M_{\odot} yr^{-1}$). For lower mass accretion rates the burning is thermally unstable and thermo–nuclear runaways occur occasionally (see Lewin et al. 1995; Bildsten 2000). Some of these bursts, called radius expansion bursts, are thought to provide a standard candle since their peak luminosities are close to

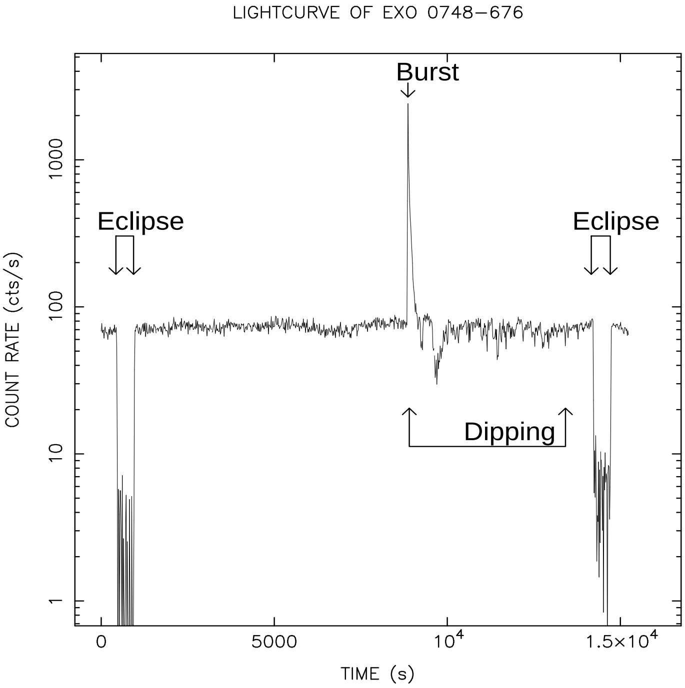

Figure 1.4: Lightcurve of the eclipsing and dipping LMXB EXO 0748–676. Besides the dip and the eclipses also a type I X–ray burst is present.

the Eddington luminosity. This means that the distance to the source can be estimated (van Paradijs 1978). Using observations obtained with the RXTE satellite, Strohmayer et al. (1996) discovered slightly drifting oscillations with a timescale of milliseconds during some of these type I bursts. The period of these oscillations probably approximately reflects the spin period of the neutron star. In this scenario they arise due to the changing aspect of a transient slightly drifting hot spot in the surface layers of the neutron star (Strohmayer et al. 1996).

Pulsations

Only six LMXBs show X–ray pulsations. These provide a *direct* measurement of the spin of the neutron star (see Chapter 11). From the spin–up rate and the luminosity of the source the magnetic field can be estimated (Ghosh & Lamb 1979; Psaltis & Chakrabarty 1999). In four of the LMXB pulsars, pulse arrival time measurements have allowed for a measurement of the orbital velocity of the neutron star.

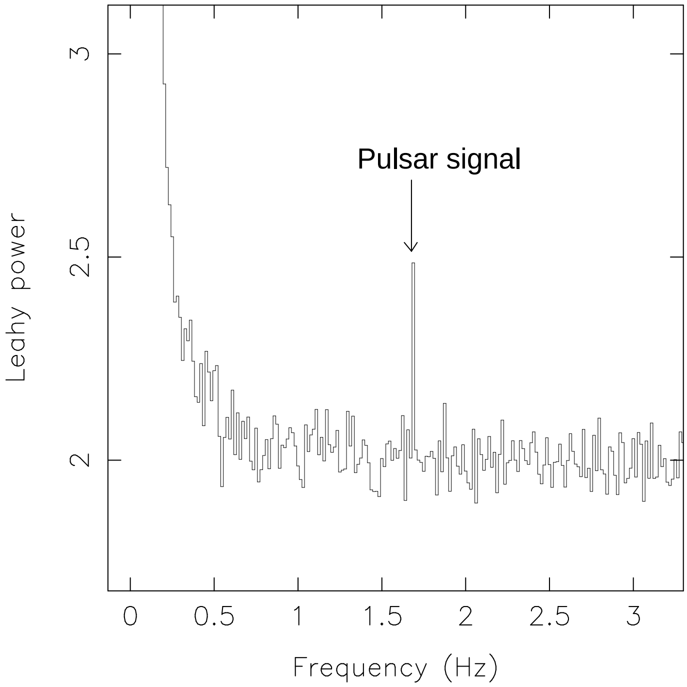

Figure 1.5: Detail of the power spectrum of the source 2A 1822–371 showing the weak signal caused by the X–ray pulsations.

Some of the variability can be directly observed in the lightcurve or is detected using a folding technique. For the detection of weak (quasi–) periodic oscillations (QPOs) an analysis in the frequency domain has proven to be very successful (van der Klis 1989; see Chapter 2; Figure 1.5). QPOs provide a direct diagnostic of accretion flows in a region of a strong gravitational field and they are ubiquitous in all bright persistent and transient LMXBs. QPO phenomena of neutron star LMXBs relevant for the subsequent chapters are discussed below.

1.4.2 Quasi–periodic oscillations

Overview of the phenomenology

Since the early days of X–ray astronomy, variability and intrinsic noise in the X–ray intensity variations of the brightest LMXBs has been studied (e.g. in Sco X–1, Lewin et al. 1968). The work on QPOs was boosted by the discovery in 1985 of a 20–36 Hz QPO in the Z source GX 5–1 by van der Klis et al. (1985) (called the

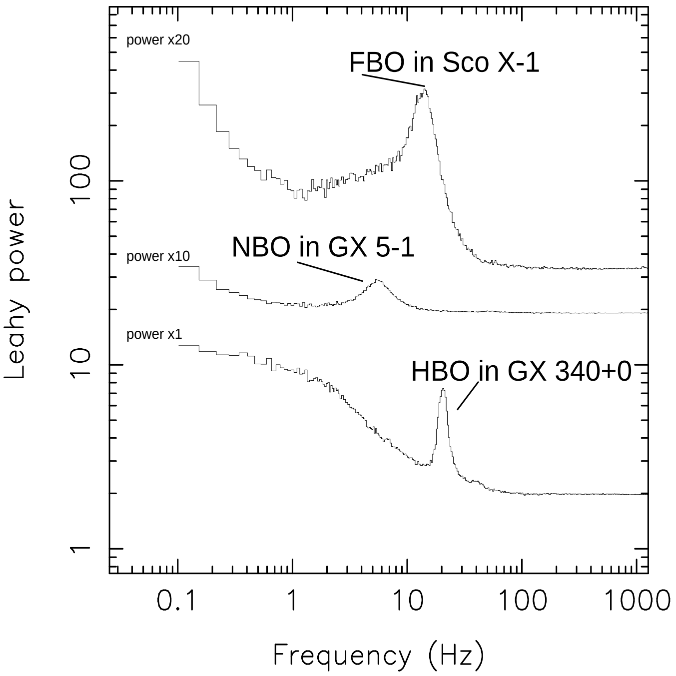

Figure 1.6: Power density spectra of the Z sources GX 340+0, GX 5–1, and Sco X–1. For clarity the power spectra of GX 5–1 and Sco X–1 were shifted upwards. The power spectrum of GX 340+0 shows the HBO and its weak second harmonic, that of GX 5–1 the NBO, and that of Sco X–1 the FBO.

Horizontal Branch Oscillation, HBO, after the branch of the Z on which they were found; Figure 1.6). It turned out that the frequency of the HBO increased as the source moved towards the Normal Branch. On the Normal Branch a QPO with a frequency of 5–6 Hz was found (the NBO, Figure 1.6; Priedhorsky et al. 1986). In Sco X–1 and GX 17+2 the frequency of this QPO changes to 16–20 Hz on the Flaring Branch (the FBO, Figure 1.6).

Two QPOs with frequencies of nearly 1000 Hz, the kHz QPOs, were discovered with data obtained by the RXTE satellite (see Figure 1.7; van der Klis et al. 1996; Strohmayer et al. 1996). These QPOs provided the first direct evidence of variations on the dynamical timescale close to the neutron star surface; predicted general relativistic effects such as the existence of an innermost stable circular orbit and the previously mentioned Lense–Thirring precession might be detected. Subsequent observations led to the discovery of kHz QPO peaks other than the kHz QPO pair only after combining nearly five years of observations: the

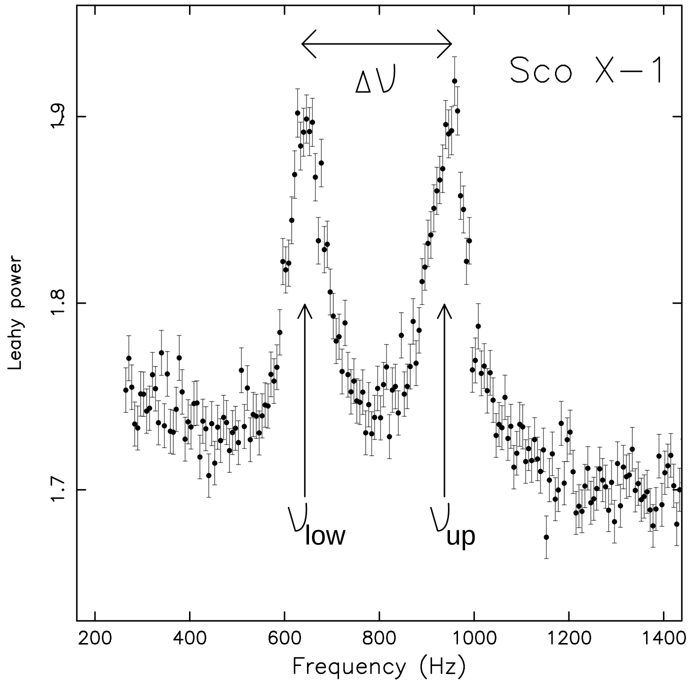

Figure 1.7: Power density spectrum normalized after Leahy et al. (1983) showing a close–up of the lower and upper kHz QPO peak (ν_{low} and ν_{up}, respectively).

sidebands to the lower kHz QPO (see Chapters 10, and 1.5). Besides the high frequency QPOs, new QPOs with frequencies less than 100 Hz were found. One of the newly discovered phenomena is the ∼1 Hz 'dipper' QPO (Chapter 3, Homan et al. 1999, and Chapter 4). In atoll sources QPOs with similar frequencies as the Z source HBO were found (Homan et al. 1998; Ford & van der Klis 1998; referred to as low–frequency QPOs). In Z sources it was found that the HBO frequency is not the fundamental frequency; a sub–harmonic (Chapters 1.5, 6, and 7, Homan et al. 2001) and a QPO at 1.5 times the HBO frequency were found (Chapter 7).

Except on a few occasions, all the QPO properties such as frequency, full–width at half–maximum (FWHM), and strength change with time. The QPO properties correlate well with X–ray flux (on timescales of hours) and X–ray colors. This led to the idea that most of the variations in QPO properties are related to changes in mass accretion rate.

1.4.3 Models

The nature of many of the quasi–periodic oscillations is not yet fully understood, although over the years a large variety of models have been proposed (references for some of these are provided here; Alpar & Shaham 1985; Lamb et al. 1985; Fortner et al. 1989; Klein et al. 1996; Titarchuk et al. 1998; Stella & Vietri 1998; Perez et al. 1997; Miller et al. 1998; Stella & Vietri 1999; Psaltis & Norman 2001). An important issue dividing the models is whether in neutron star LMXBs forces exerted by a magnetic field prevail over the strong gravitational forces at radii where the X–rays and the variations therein are generated.

The two leading classes of models providing an explanation for the HBO in Z sources or the low–frequency QPOs in atoll sources, and for the kHz QPOs are discussed below.

Beat frequency models

In the magnetospheric beat–frequency model the modulations at the HBO frequency arise due to a beat between inhomogeneities orbiting at the Keplerian frequency and the magnetosphere rotating at the frequency of the neutron star (Alpar & Shaham 1985; Lamb et al. 1985). Matter is channelled from the disk to the neutron star poles via the magnetic field lines. Most of the energy is released near the neutron star poles in the form of X–rays. The mass flow and therefore the emerging X–ray flux is modulated at the beat period.

The later discovery of the kHz QPOs pair led to the re–use of this basic beat frequency idea (Strohmayer et al. 1996). The sonic point beat frequency model is the most elaborate of such models (Miller et al. 1998). In the framework of their model the upper peak of the two kHz QPO peaks reflects (Keplerian) motion near the inner edge of the disk (see Figure 1.8). A sharp inner edge of the disk is formed at the radius where the radial velocity of the accreting gas changes from sub–sonic to super–sonic, the sonic point radius. The frequency of the lower kHz QPO is determined by the beat period between the prograde rotating disk and a pulsar beam emerging from the magnetic poles of the neutron star. Due to radiation drag of the pulsar beam on inhomogeneities orbiting near the inner edge of the disk the mass flow towards the neutron star is enhanced once each beat period. The pulsar beam itself is not detected since it is attenuated by scattering and light deflection (Miller 2000). In case the beat frequency model is to explain both the HBO and the two kHz QPOs, the accretion flow should partially penetrate the magnetosphere to close to the neutron star (Miller et al. 1998). The presence of the slightly drifting

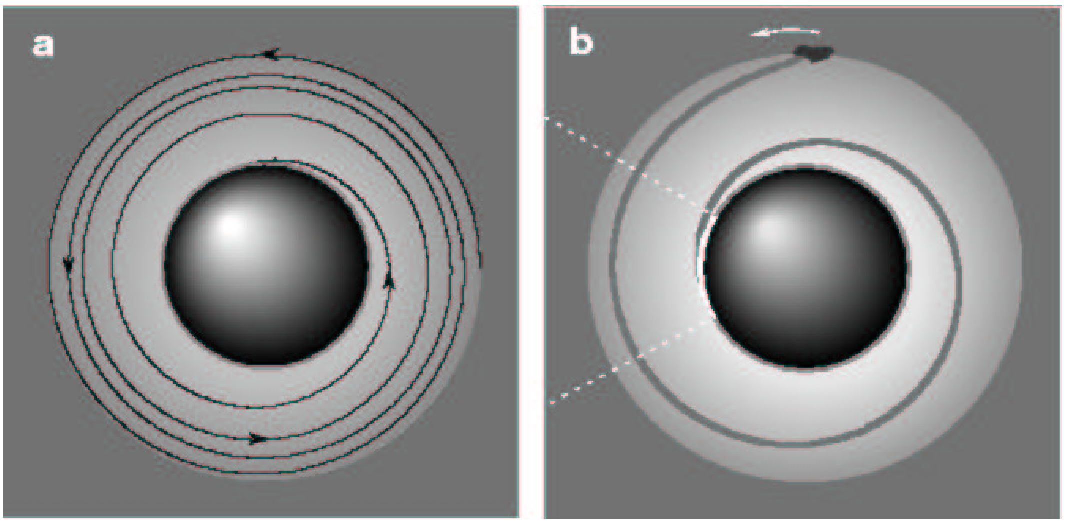

Figure 1.8: Schematic view of the generation of the upper kHz QPO in the sonic point beat frequency model. Due to angular momentum losses caused by radiation drag matter spirals towards the neutron star surface and generates the X–rays on impact (grey ring around the neutron star a: left panel). Inhomogeneities forming near the transition radius will give rise to an enhanced mass flow. A bright footpoint will form near the surface of the neutron star orbiting at the Keplerian frequency of the sonic radius (b: right panel). The black spiral in the left panel indicates the streamline of matter falling towards the neutron star, whereas the thick grey spiral in the right panel indicates the pattern traced out by particles subsequently released from the inhomogeneity at the inner edge. Figure from Miller et al. (1998).

oscillations during some of the type I X–ray bursts at frequencies nearly equal to the kHz QPO peak separation frequency is a strong argument favoring a beat frequency model.

As a function of changes in the mass accretion rate the sonic point radius and the radius of the magnetosphere change. Figure 1.9 provides a schematic overview of the radii and their changes as the mass accretion rate changes such that the HBO frequency changes from ∼10–50 Hz (dashed and drawn circles, respectively). Similarly the frequency of the upper kHz QPO changes from ∼500–1000 Hz. According to general relativity there is a radius within which no stable circular Keplerian orbits exist (the ISCO). The frequency associated with the ISCO (∼1570 Hz for a 1.4 $M_\odot$ neutron star) provides an upper limit to the frequency of the upper kHz QPO both in the sonic point beat frequency model as well as in the rivalling relativistic precession model, which is discussed next.

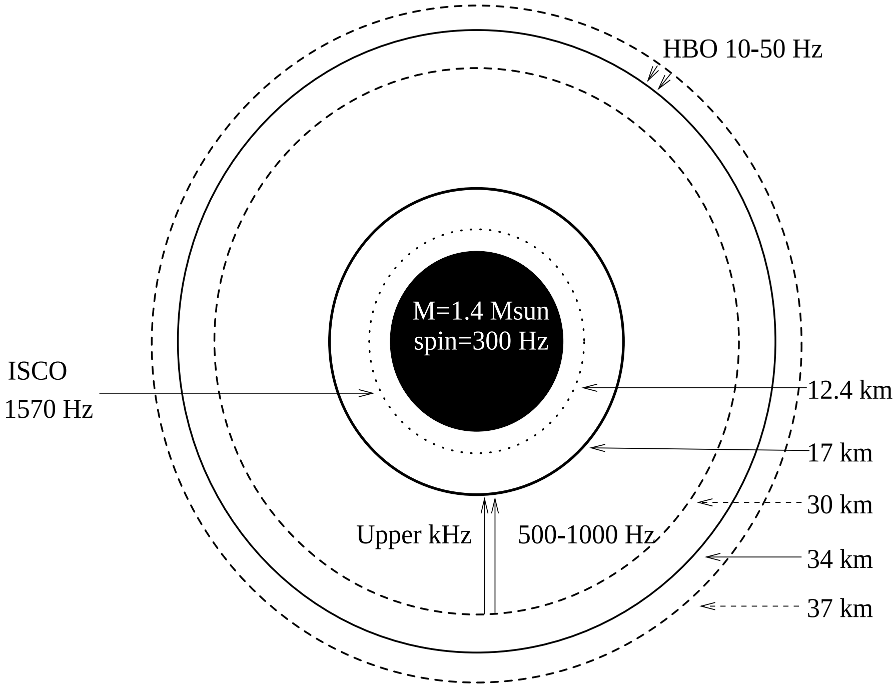

Figure 1.9: Schematic view of the radii at which, according to the (magnetic and sonic point) beat frequency models, modulations of the mass flow towards the neutron star occur. ISCO stands for inner–most stable circular orbit. The frequency of the HBO (a beat frequency) increases from ∼10 Hz to ∼50 Hz in Z sources under influence of changes in the mass accretion rate (dashed and drawn circles, respectively). Similarly, the Keplerian frequency of the upper kHz QPO increases from ∼500 Hz to ∼1000 Hz. All numbers in the plot are approximate and for a 1.4 $M_\odot$ neutron star spinning at 300 Hz.

The relativistic precession model

In the relativistic precession model the fundamental frequencies of three QPOs (the HBO in Z sources or the low–frequency QPO in the atoll sources, and the two kHz QPOs) are a direct measure for the three (relativistic) frequencies of geodesic motion of a test particle in orbit around a compact object; the azimutal, the vertical, and the radial frequencies of motion. The HBO or the low–frequency QPO reflects the prograde nodal precession frequency of an orbit with a plane inclined with respect to the equational plane of the neutron star (the difference between the azimutal and the vertical frequency of motion; the Lense–Thirring precession; Stella & Vietri 1998). For various neutron star EoS, Morsink & Stella

(1999) showed that the frequency of the low–frequency QPOs in atoll sources is consistent with twice the Lense–Thirring precession frequency. That of the HBO in Z sources is approximately four times the Lense–Thirring precession frequency. A two–fold symmetry, naturally present as the orbit crosses the equatorial plane twice, could cause a doubling of the observed frequency. The situation is definitely more complex since viscous torques on the accretion disk tend to drive and keep the inner parts of the accretion disk in the equatorial plane (the Bardeen–Petterson effect, after Bardeen & Petterson 1975; see also Marković & Lamb 1998 and Shirakawa & Lai 2001 for the inclusion of magnetic and radiation torques). The spin frequency of the neutron star, which enters the calculations describing the Lense–Thirring precession frequency and the (retrograde) classical precession due to the quadrupole moment of the neutron star, is determined from the burst oscillations present during some of the type I X–ray bursts. The upper kHz QPO is the frequency of motion in the azimutal direction, and the lower kHz QPO frequency is the frequency associated with the difference between the frequency of motion in the radial and azimutal direction (the periastron precession frequency; Stella & Vietri 1999). If this model is validated the kHz QPOs in LMXBs provide an accurate test for strong field general relativity.

The relativistic precession model predicts relations between the three frequencies which agree qualitatively with the observed trends, both in neutron stars and black hole candidates (Psaltis et al. 1999; Stella et al. 1999). However, the eccentricity of the test particle orbits which is needed in order to describe the data, is so large that the particle orbits would intersect and circularize within a few revolutions (Marković & Lamb 2001). Psaltis & Norman (2001) present a model, the so–called transition layer model, in which the QPO frequencies, similar to the relativistic precession model, are largely set by the properties of the metric without the need for elliptical orbits. They show that when a broad frequency spectrum of pertubations is imposed on the accretion disk inside a (postulated) transition radius, the emergent frequency spectrum of the modulations shows strong resonances close to the Lense–Thirring precession frequency, the periastron precession frequency, and the Keplerian frequency.

1.5 This thesis

The work presented in this thesis is the result of a careful and critical examination of data produced by the RXTE satellite. Most of this data were obtained by us to study specific aspects of the inner accretion flows around neutron star LMXBs, but we also made use of the RXTE public archive. Directed searches led to the discovery of signals such as the sidebands to the lower kHz QPO (Chapter 10) and the pulsations in 2A 1822–371 (Chapter 11).

In Chapter 3, and 4 we describe the discovery of a new type of QPO; the 1 Hz ’dipper’ QPO. The 1 Hz QPO properties are remarkable and quite distinct from properties of previously known QPOs; the strength of the QPO is nearly independent of photon energy and does not change during a 10–50–fold increase in X–ray flux during a type I X–ray burst. Most likely the variations are caused by a structure in or on the accretion disk quasi–periodically covering and uncovering the central X–ray source. In 4U 1746–37 (Chapter 4) we found that the accretion disk structure or the central source shape changed when the source state changed from island state to banana branch.

A major part of the work described in this thesis consists of work on two Z sources; GX 340+0 and GX 5–1 (Chapters 5, 6, 7, and 8). The most important finding of the timing studies of these two sources is that the HBO is most likely not the fundamental frequency. In both sources a peak at half the frequency of the HBO, a sub–HBO, was found. Prior to this detection the HBO frequency in Z sources was hard to reconcile with the Lense–Thirring precession frequency, as proposed by Stella & Vietri (1998). However, the frequency of the sub–HBO is a factor $\sim$2 higher than the prediced Lense–Thirring precession frequency, similarly to the low–frequency QPOs in atoll sources. This gap can be bridged by exploiting the presence of a two–fold symmetry in the accretion flow.

With our study of GX 5–1 we showed that the ‘two–oscillator’ model (Osherovich & Titarchuk 1999) proposed as an explanation for the kHz QPOs and the HBO can, in its current form, not explain the data (Chapter 7). Our finding of a set of four harmonically related QPO peaks, whose coherences alternate between $\sim$1 for the odd harmonics and $\sim$5 for the even harmonics seem to favor disk models such as the relativistic precession model over the magnetic beat frequency model for the HBO. Such a harmonic structure of alternatingly less– and more coherent QPO peaks has also been found in the black hole candidate XTE J1550–564, and may be explained by the different timescales involved in changes in the two–fold symmetry (see Chapter 7). We identified the infrared counterpart to GX 5–1 by comparing the magnitude of stars near the radio error–circle in the narrow–band Brγ filter with that in the broad–band K filter (Chapter 8). The proposed counterpart is brighter in the narrow–band Brγ filter compared to the other stars indicating the presence of a Brγ emission line, such as commonly found in accretion disk sources.

The findings presented in Chapter 9 show that the amplitude of the upper kHz QPO observed in each source is anti–correlated both with the X–ray luminosity changes within a source and with the X–ray luminosity differences between sources. This is an important element for QPO formation models to explain. Distances to the sources were in many cases derived using the peak luminosities of type I X–ray bursts.

The presence of QPO peaks in the kHz range additional to the two discribed above (Section 1.4.2) was predicted in nearly all the kHz QPO models. However, directed searches were unsuccessful (Méndez & van der Klis 2000). Why this was the case became clear as the sidebands to the lower kHz QPO we discovered in three atoll sources turned out to be at frequencies different from those predicted by the models (Chapter 10). Magnetospheric modulation of the lower kHz QPO as well as a beat phenomenon taking place inside the marginally stable orbit are conceivable explanations for these sidebands (Miller private communication; Chapter 10). The initial explanation suggested by several theoretical groups for the new phenomenon was Lense–Thirring precession. However, several theoreticians changed their mind since the frequency separation between the lower kHz QPO and the sideband seems uncomfortably large. In retrospect, Psaltis (2001) realised that the sideband peaks are at a frequency predicted by his transition layer model. Extensive work on the frequency variations of these sidebands can in principle distinguish between the explanations now proposed for them; however, as these oscillations are weak this will take some time to accomplish.

The discovery of an X–ray pulsar in the accretion disk corona source 2A 1822–371 is the sixth accreting X–ray pulsar in a LMXB (Chapter 11). If the orbital motion of the relatively bright companion star to this neutron star can be determined from its spectrum, the known high inclination ($\gtrsim 80^\circ$) of this partially eclipsing system will provide an accurate (better than 10%) neutron star mass determination. Preliminary analysis of data obtained with the 6.5 m Magellan telescope indicates that the neutron star mass may be less than 1 $M_\odot$.

Bibliography

Alpar, M. A., Cheng, A. F., Ruderman, M. A., & Shaham, J. 1982, Nature, 300, 728
Alpar, M. A. & Shaham, J. 1985, Nature, 316, 239
Bardeen, J. M. & Petterson, J. A. 1975, ApJ, 195, L65
Bhattacharya, D. 1995, Millisecond pulsars, eds Lewin, van Paradijs, van den Heuvel (ISBN 052141684, Cambridge Univ. Press, 1995.)
Bildsten, L. 1998, ApJ, 501, L89
Bildsten, L. 2000, in Rossi2000: Astrophysics with the Rossi X-ray Timing Explorer. March 22-24, 2000 at NASA's Goddard Space Flight Center, Greenbelt, MD USA, p.E65, E65–+, see also astro–ph 0001135
Bradt, H. V., Rothschild, R. E., & Swank, J. H. 1993, A&AS, 97, 355
Brocksopp, C., Jonker, P. G., Fender, R. P., et al. 2001, MNRAS, 323, 517
Fabbiano, G. 1995, Normal galaxies and their X-ray binary populations, eds Lewin, van Paradijs, van den Heuvel (ISBN 052141684, Cambridge Univ. Press, 1995.)
Fender, R. P. & Hendry, M. A. 2000, MNRAS, 317, 1
Fender, R. P., Pooley, G. G., Brocksopp, C., & Newell, S. J. 1997, MNRAS, 290, L65
Ford, E. C. & van der Klis, M. 1998, ApJ, 506, L39
Fortner, B., Lamb, F. K., & Miller, G. S. 1989, Nature, 342, 775
Ghosh, P. & Lamb, F. K. 1979, ApJ, 234, 296
Homan, J., Jonker, P. G., Wijnands, R., van der Klis, M., & van Paradijs, J. 1999, ApJ, 516, L91
Homan, J., van der Klis, M., Jonker, P. G., et al. 2001, ApJ
Homan, J., van der Klis, M., Wijnands, R., Vaughan, B., & Kuulkers, E. 1998, ApJ, 499, L41
Klein, R. I., Arons, J., Jernigan, G., & Hsu, J. J. . 1996, ApJ, 457, L85
Kuulkers, E., van der Klis, M., Oosterbroek, T., et al. 1994, A&A, 289, 795
Lamb, F. K., Shibazaki, N., Alpar, M. A., & Shaham, J. 1985, Nature, 317, 681
Leahy, D. A., Darbro, W., Elsner, R. F., et al. 1983, ApJ, 266, 160
Lewin, W. H. G., Clark, G. W., & Smith, W. B. 1968, ApJ, 152, L55
Lewin, W. H. G., van Paradijs, J., & Taam, R. E. 1995, X-ray Bursts , eds Lewin, van Paradijs, van den Heuvel (ISBN 052141684, Cambridge Univ. Press, 1995.)
Liu, Q. Z., van Paradijs, J., & van den Heuvel, E. P. J. 2001, A&A, 368, 1021
Markoff, S., Falke, H., & Fender, R. 2001, å
Marković , D. & Lamb, F. K. 1998, ApJ, 507, 316
—. 2001, MNRAS
Méndez, M. & van der Klis, M. 2000, MNRAS, 318, 938
Miller, M. C. 2000, ApJ, 537, 342
Miller, M. C., Lamb, F. K., & Psaltis, D. 1998, ApJ, 508, 791
Mirabel, I. F. & Rodríguez, L. F. 1994, Nature, 371, 46+
—. 1998, Nature, 392, 673
Morsink, S. M. & Stella, L. 1999, ApJ, 513, 827
Osherovich, V. & Titarchuk, L. 1999, ApJ, 522, L113
Perez, C. A., Silbergleit, A. S., Wagoner, R. V., & Lehr, D. E. 1997, ApJ, 476, 589+
Popham, R. & Sunyaev, R. 2001, ApJ, 547, 355
Poutanen, J. 1998, in Theory of Black Hole Accretion Disks, 100+
Priedhorsky, W., Hasinger, G., Lewin, W. H. G., et al. 1986, ApJ, 306, L91

Psaltis, D. 2001, Advances in Space Research, submitted, talk presented at the 33rd COSPAR Scientific Assembly, Warsaw, Poland, 16-23 July 2000, astro-ph/0012251

Psaltis, D., Belloni, T., & van der Klis, M. 1999, ApJ, 520, 262

Psaltis, D. & Chakrabarty, D. 1999, ApJ, 521, 332

Psaltis, D. & Norman, C. 2001, ApJ, submitted

Radhakrishnan, V. & Srinivasan, G. 1982, Curr. Sci, 51, 1096

Shakura, N. I. & Sunyaev, R. A. 1973, A&A, 24, 337

Shapiro, S. L., Lightman, A. P., & Eardley, D. M. 1976, ApJ, 204, 187

Shirakawa, A. & Lai, D. 2001, ApJ

Sibgatullin, N. R. & Sunyaev, R. A. 2000, Astronomy Letters, 26, 772

Stella, L. & Vietri, M. 1998, ApJ, 492, L59

—. 1999, Phys. Rev. Lett

Stella, L., Vietri, M., & Morsink, S. M. 1999, ApJ, 524, L63

Strohmayer, T. E., Zhang, W., Swank, J. H., et al. 1996, ApJ, 469, L9

Sunyaev, R. A. & Titarchuk, L. G. 1980, A&A, 86, 121

Thirring, H. & Lense, J. 1918, Phys. Z, 19, 156

Titarchuk, L., Lapidus, I., & Muslimov, A. 1998, ApJ, 499, 315+

van der Klis, M. 1989, in Proceedings of the NATO Advanced Study Institute on Timing Neutron Stars, held in Çeşme, İzmir, Turkey, April 4–15, 1988. Editors, H. Ögelman and E.P.J. van den Heuvel; Publisher, Kluwer Academic, Dordrecht, The Netherlands, Boston, Massachusetts, p. 27

van der Klis, M., Jansen, F., van Paradijs, J., et al. 1985, Nature, 316, 225

van der Klis, M., Swank, J. H., Zhang, W., et al. 1996, ApJ, 469, 1

van Paradijs, J. 1978, Nature, 274, 650

—. 1995 (X-ray Binaries, eds. W.H.G. Lewin, J. van Paradijs, and E.P.J. van den Heuvel (Cambridge: Cambridge Univ. Press), p. 58), 536+

van Paradijs, J. & McClintock, J. E. 1995, Optical and Ultraviolet Observations of X-ray Binaries (X-ray Binaries, eds. W.H.G. Lewin, J. van Paradijs, and E.P.J. van den Heuvel (Cambridge: Cambridge Univ. Press), p. 58), 58+

Whelan, J. & Iben, I. J. 1973, ApJ, 186, 1007

White, N., Nagase, F., & Parmar, A. N. 1995, The properties of X-ray binaries (Cambridge Astrophysics Series, Cambridge, MA: Cambridge Univ. Press, —c1995, edited by Lewin, Walter H.G.; Van Paradijs, Jan; Van den Heuvel, Edward P.J.), p. 1

White, N. E. & Swank, J. H. 1982, ApJ, 253, L61

Wijnands, R. & van der Klis, M. 1998, Nature, 394, 344

Chapter 2

Data acquisition and analysis

2.1 Data acquisition

Data obtained with the *Rossi X–ray Timing Explorer* satellite (RXTE, Bradt et al. 1993) are used in all the work described in this thesis except that of Chapter 8. A major advantage of RXTE over previous X–ray timing instruments is the large sustainable throughput. There are three instruments on board the *RXTE* satellite: the proportional counter array (PCA; Jahoda et al. 1996), the all–sky monitor (ASM; Levine et al. 1996), and the high energy X–ray timing experiment (HEXTE; Rothschild et al. 1998). The complete manual can be found in Bradt et al. (1993) or in the Technical Appendix available for download at:
ftp://legacy.gsfc.nasa.gov/xte/nra/appendix_f/

The satellite orbits the earth at an altitude of $\sim$600 km in an inclined orbit (inclination $\sim 23°$). Therefore, it passes through the South Atlantic Anomaly (SAA) in 6 of the 14–15 daily orbits. During such a passage, lasting typically 10–20 minutes, the instruments are put in a safe mode to protect them against the high particle flux. Furthermore, unless sources are located near one of the poles of the orbit they will be occulted for typically 30 minutes by the earth once each 100 minute orbit. By efficient scheduling of the various targets the satellite operation staff often manages to overlap the earth occultations with the passage of the SAA.

2.1.1 ASM

The ASM operates in the 1.5–12 keV energy range and scans the sky while the satellite orientation is stationary. Typically, a source is observed 5–10 times a day. Such an observation, a dwell, is a $\sim$90 s integration, with a time resolution of 1/8 s and limited energy resolution (3 energy bands). The ASM consists of 3 Scanning Shadow Camera's; a proportional counter with positional sensitivity is placed below a collimator. The proportional counters (each with an effective area of $\sim$30 cm^2) view the sky through a coded mask. The ASM provides unequally sampled data for known sources above the ASM one–day average sensitivity cut–off of $\sim$10 mCrab. Long term source variations, such as transient events and source state changes (e.g. Figure 2.1) can be studied with the ASM. Pointed observations with the PCA instrument are often triggered by source variations observed with the ASM; e.g. the observations of the source 4U 1608–52 used in Chapter 10 were triggered by the ASM (see the ASM light curve of this source in Figure 2.1). This triggering usually involves the quicklook ASM data provided by the RXTE team. This data is obtained for $\sim$150 sources, among which that of known transients and made available through the world wide web. In case of sudden changes in the ASM count rate indicating a source state change, pointed PCA observations can start several hours after the trigger.

The HEXTE instrument is sensitive to X–rays in the energy range from 15–250 keV with a time resolution down to 7μs. In this thesis no data obtained with this instrument are used.

2.1.2 The proportional counter array

The PCA consists of five coaligned detectors, called proportional counter units (PCUs). The PCUs operate independently, e.g. each detector can be switched off or on separately. Although the PCUs are identical they differ in the details of their energy calibration and background. The PCUs comprise a collimator (1° FWHM) and two gas–filled chambers mounted on top of each other. The first chamber is filled with propane and filters out background electrons. The second chamber is filled with a Xenon/Methane gas and comprises the main X–ray detection part. This chamber contains 4 layers of anode grids separated by cathode wires. Per grid 20 anodes are present. The upper 3 layers are used for X–ray detection. The X–rays impacting a Xenon atom trigger a cascade of electrons onto the high voltage anodes. The higher the photon energy, the more electrons are released, and thus the higher the electron pulse–amplitude. The anodes in the grid of the last layer

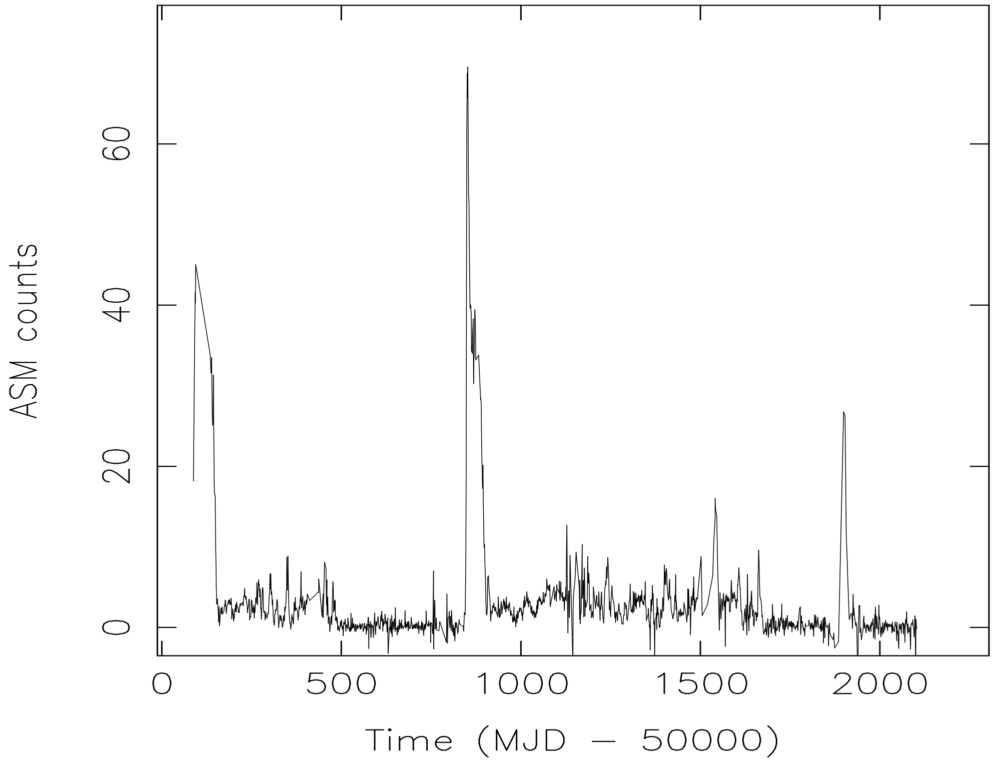

Figure 2.1: The ASM light curve of the transient LMXB 4U 1608–52. Pointed PCA observations, such as those used in Chapter 10 have been triggered by ASM observations. Note that the first outburst of 4U 1608–52 at day ∼0–100 was not fully sampled by the ASM.

(together with the anodes closest to the detector walls) serve as a discriminator for charged particles entering through the detector walls. Each PCU has an effective area of ∼1200 cm^2 at 10 keV, adding up to ∼6000 cm^2. The effective energy range is 2–60 keV, since the detector efficiency decreases rapidly above 60 keV.

Each ASM and PCA event is time–tagged by an on–board computer, called the Experiment Data System (EDS), to an accuracy of $\sim 1\mu$s. This EDS has 8 Event Analysers (EAs): 6 for the PCA data stream and 2 for that of the ASM. The EAs work in parallel; each EA 'sees' the whole data stream. The EAs bin the individual events in time and energy according to criteria set by the guest observer and the RXTE operation staff. Two EAs have preset modes:

- the Standard 1 data mode provides data in the 2–60 keV band with a 0.125 s time resolution and no energy resolution

- the Standard 2 data mode provides data in the same 2–60 keV band with a time resolution of 16 s and high spectral resolution (the pulse amplitude is recorded in 129 channels covering the 2–60 keV energy range).

The modes of the remaining four EAs dedicated to the PCA could be set by the guest observer. For example one of the EAs could be set such that it processes only events if their energy is between 2–9.7 keV. Another EA can be set to process only those events with energy between 9.7–60 keV. Combined, these two EAs cover the total energy range of RXTE. The EA ‘event’, ‘binned’, and ‘single bit’ modes are used most often. In an *event* mode all or part of the data is transported to the ground station on an event–to–event basis, e.g. the photon arrival time is recorded for each photon. In a *binned* mode the exact photon arrival time is lost. The events are binned with respect to time, photon energy, and detector number. The Standard 1 and 2 mode are examples of binned mode data. Data of the *single–bit* mode consists of a string of zeros and ones. A ‘0’ will be written at each time–bin boundary, while a ‘1’ denotes the occurrence of a detector event. The time spacing of the writing of the ‘0’s’ (the boundary events which set the time resolution) and the energy range for a detector event can be set. This mode can provide a high time resolution at a low telemetry rate when the photon rate is of the same order as the time bin rate.

2.2 Analysis

2.2.1 Power spectra

Most of the work on time variability in this thesis is based on Fourier analysis of the data, although other methods and tools, such as phase dispersion minimization (Stellingwerf 1978), acceleration searches (Anderson et al. 1990), Lomb–Scarcle searches (Lomb 1976; Scargle 1982), and the Partial Coherence Recovery Technique (Jouteux 2001) were also explored. Fourier analysis is well suited for the detection and study of (quasi–) periodic and noise phenomena (see van der Klis 1989 for a review on Fourier Techniques in X–ray timing). Because RXTE high time resolution data are either equidistantly sampled (or can easily be rebinned in equidistant bins in case of event mode data) a Fast Fourier Transformation (FFT) algorithm can be used. FFTs are best implemented if the number of points to be transformed is a power of 2 (e.g. Press et al. 1992). For several reasons transforms of typically 16 s segments of the data are calculated, although longer transforms provide a higher frequency resolution (the frequency resolution is $1/T$, where T

is the length of the transform). In practice source variations and/or data gaps limit the length of a transform. If the source varies on a timescale similar to the length of the transform, the power spectral properties would change during a transform, which is something one would like to avoid. The RXTE data stretches are continuous for ~3000 seconds only, limiting the transform to a maximum length of 2048 s. Power spectra can be calculated using photons of all energies between 2–60 keV or subsets of that if high time–resolution data is provided in different energy ranges by the EAs.

The power density spectra are averaged and normalized. The convention is to either use the normalization introduced by Leahy et al. (1983) or that described in van der Klis (1995) (rms normalization). In the Leahy normalization powers due to Poissonian counting noise have an average value of 2. In the rms normalization the integrated power in the frequency range of interest, P_{int}, is directly related to the variance in the X–ray intensity ($P_{int} = [\sigma/\langle I \rangle]^2$, where σ is the standard deviation, i.e., the square root of the variance in the chosen frequency range and $\langle I \rangle$ is the average source count rate). So, the fractional rms amplitude, $\sigma/\langle I \rangle$, the measure of QPO or noise strength, is simply the square root of the integrated power in the rms normalization. Because the quantity $\sigma/\langle I \rangle$ is dimensionless (it is a fractional amplitude of the variability, usually expressed in %), the dimension of the power density estimates in an rms normalized power spectrum is reciprocal frequency, i.e., [t]. The unit of power is commonly expressed as ([rms/mean]^2/Hz), where rms/mean stands for $\sigma/\langle I \rangle$. The signal–to–noise ratio, n, of a power spectral component in a power spectrum depends on the fractional rms amplitude of the QPO or noise feature (rms), the FWHM, the source and background count rates (S, B, respectively), and the observing time (T_{obs}) in the following manner; $n = \frac{1}{2}\frac{S^2}{B+S} rms^2 (\frac{T_{obs}}{FWHM})^{1/2}$ (van der Klis 1998).

Averaging multiple power spectra or averaging adjacent bins (degrading the frequency resolution) reduces the uncertainty of the powers; averaging N power spectra or N bins will reduce the standard deviation of the errors by a factor $\sqrt{N}$. An improvement in the detection level for weak *periodic* signals will only be obtained if the frequency of such a component changes less than the frequency resolution of the power spectra over the time–period spanned by the averaged power spectra. Otherwise the component will be broadened and smeared. Properties of *quasi–periodic* signals such as the FWHM will also be affected if the frequency of the component varies. Therefore, only power spectra where the power spectral components are the same within the errors should be averaged.

From the EXOSAT era it is known that the properties of the power spectra

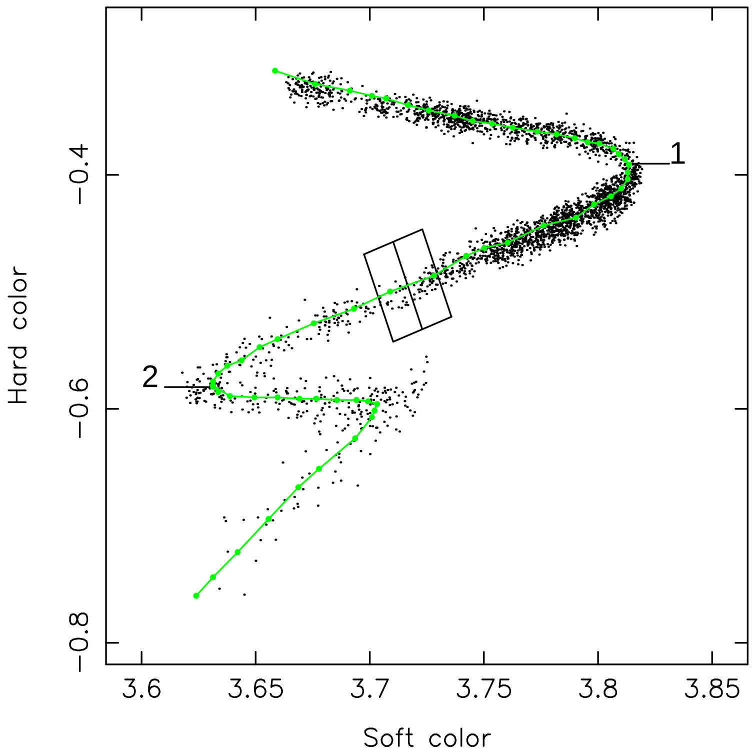

Figure 2.2: Hardness–intensity diagram of the Z source GX 5–1. The spline is plotted in grey. To scale the curve length along the spline, the top vertex is assigned the value '1' and the middle vertex the value '2'. As an example of manual selection two boxes are indicated.

depend strongly on the position of the source along the pattern traced in an X–ray color–color or hardness–intensity diagram (CD or HID, respectively; Hasinger & van der Klis 1989). CDs and HIDs are produced using the Standard 2 data. What is called soft color in this thesis is defined as (the logarithm of) the count rate ratio of the 3.5–6.4 to the 2–3.5 keV energy band. Hard color is defined as (the logarithm of) the count rate ratio of the 9.7–16 to the 6.4–9.7 keV energy band. The intensity is the total count rate in the 2–16 keV energy band (unless otherwise stated; see also the discussion in Chapter 7).

As explained above, due to spectral and intensity variations sources trace out branches or patterns in CDs and HIDs. There are various ways to characterize the source position along such a pattern. One can manually divide the traced pattern into segments (such as the boxes in Figure 2.2), or define curve length along the curve by drawing a spline through manually selected points in the curve (Hasinger et al. 1990; Hertz et al. 1992; Dieters & van der Klis 2000; see the spline in Figure 2.2). Provided that besides the Standard 2 data, simultaneous high–time resolution data is available, each point in a CD or HID corresponds to a specific power spectrum. Power spectra falling in a curve length range of interest can now be averaged.

With RXTE it has become possible to select the power spectra on the frequency of a strong power spectral feature (such as in the case of the HBO in GX 340+0; see Chapter 6). The accuracy with which the centroid frequency of a QPO peak is determined can be estimated as $\delta_\nu = 2FWHM^{3/2}/Irms^2T_{obs}^{1/2}$, where I is the count rate, *rms* the QPO fractional rms amplitude and T_{obs} the integration time. The frequency of a strong QPO peak is determined in, for instance, each 64 s transform; on that timescale the source power density properties vary little in most cases. Only power spectra with frequencies in a narrow range are averaged. Alternatively, the peaks of the strong QPO are aligned by applying a frequency shift to the power spectra (see the *top right panel* in Figure 2.3). Only after the power spectra have been shifted they are averaged (using this method sidebands to the lower kHz QPO were found, see Chapter 10). This method has been pioneered by Méndez et al. (1998). Power spectral components varying in frequency in the same way as the strong QPO peak will be aligned. A disadvantage of this averaging method is that in the average power spectrum only the frequency differences between components are meaningful.

A similar technique can be applied in a search for X–ray pulsars. The frequency of a binary pulsar is smeared by Doppler shifts due to the binary orbital motion. For systems with a known orbital period and ephemeris one can correct for a pulsar velocity by stretching the power spectra. The factor by which a power spectra has to be stretched is determined by the velocity of the pulsar ($factor = 1 - \frac{v_{pulsar}}{c}$). Since the pulsar velocity depends on the usually unknown masses of the two binary components and on the system inclination, a range of velocities has to be scanned. By taking the length of the FFT such that the change in frequency during a transform is less than the frequency resolution one can collect all the pulsation power in one frequency bin. To our knowledge this method was first applied in this thesis. In the course of such work on 2A 1822–371, a pulsar was found in this system (Chapter 11).

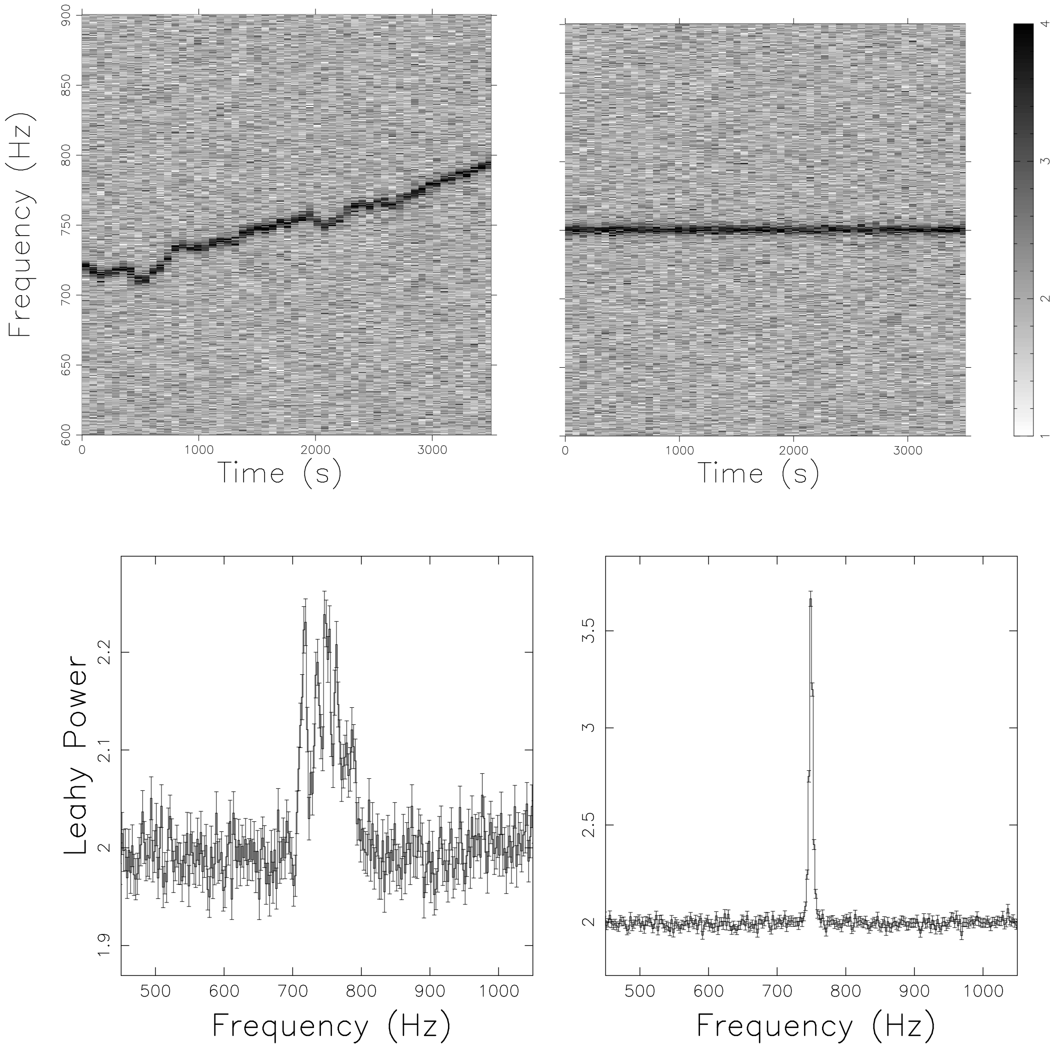

Figure 2.3: (Top panel:) Compilation of two dynamical power spectra of the source 4U 1608–52. Power spectra consecutive in time are stacked next to each other; the grey scale indicates the Leahy power. The lower kHz QPO frequency clearly changes as a function of time (top left panel). Averaging the power spectra without correcting for the frequency changes leads to a loss of signal–to–noise. (lower left panel). Correcting for the frequency change by shifting each power spectrum such that the measured peak frequencies are aligned (top right panel) before averaging results in an increase in signal–to–noise (lower right panel).

Table 2.1: Functions and their expressions used in the fits

Function	Expression
Lorentzian[a]	$P(\nu) \propto \frac{1}{(\nu^2-\nu_0^2)+HWHM^2}$
Power law	$P(\nu) \propto \nu^{-\alpha}$
Cut–off power law[b]	$P(\nu) \propto \nu^{-\alpha} exp^{-\nu/\nu_{cut}}$
Broken power law[c]	$P(\nu) \propto \nu^{-\alpha}\ (\nu < \nu_{break})$ $\nu^{-\beta}\ (\nu > \nu_{break})$

[a] ν_0 is the centroid frequency, $HWHM$ is the half–width at half the maximum
[b] ν_{cut} is the cut–off frequency
[c] ν_{break} is the break frequency

2.2.2 Fitting the power spectra

The averaged power spectra are fit by a composite fit–function. The fit–function is composed of a varying number of Lorentzians, an exponentially cut–off power laws, and/or a power law. Sometimes a broken power law is used instead of a cut–off power law (see for the functional shapes Table 2.1). The composite function is compared with the data using a χ^2 minimization technique. The actual minimization is performed using a grid–search method (Bevington & Robinson 1992). Errors on the fit–parameters are determined using $\Delta\chi^2 = 1.0$, corresponding to 1-σ (single parameter) errors (Press et al. 1992). In cases where power spectral components were not significantly detected, upper limits of 95% confidence were determined using $\Delta\chi^2 = 2.71$.

Bibliography

Anderson, S. B., Gorham, P. W., Kulkarni, S. R., Prince, T. A., & Wolszczan, A. 1990, Nature, 346, 42
Bevington, P. R. & Robinson, D. K. 1992, Data reduction and error analysis for the physical sciences (New York: McGraw-Hill, —c1992, 2nd ed.)
Bradt, H. V., Rothschild, R. E., & Swank, J. H. 1993, A&AS, 97, 355
Dieters, S. W. & van der Klis, M. 2000, MNRAS, 311, 201
Hasinger, G. & van der Klis, M. 1989, A&A, 225, 79
Hasinger, G., van der Klis, M., Ebisawa, K., Dotani, T., & Mitsuda, K. 1990, A&A, 235, 131
Hertz, P., Vaughan, B., Wood, K. S., et al. 1992, ApJ, 396, 201
Jahoda, K., Swank, J. H., Giles, A. B., et al. 1996, Proc. SPIE, 2808, 59
Jouteux, J. e. 2001, Phys. Rev. Lett
Leahy, D. A., Darbro, W., Elsner, R. F., et al. 1983, ApJ, 266, 160
Levine, A. M., Bradt, H., Cui, W., et al. 1996, ApJ, 469, L33
Lomb, N. R. 1976, Ap&SS, 39, 447
Méndez, M., van der Klis, M., van Paradijs, J., et al. 1998, ApJ, 494, L65
Press, W. H., Teukolsky, S. A., Vetterling, W. T., & Flannery, B. P. 1992, Numerical recipes in FORTRAN. The art of scientific computing (Cambridge: Univ. Press, —c1992, 2nd ed.)
Rothschild, R. E., Blanco, P. R., Gruber, D. E., et al. 1998, ApJ, 496, 538
Scargle, J. D. 1982, ApJ, 263, 835
Stellingwerf, R. F. 1978, ApJ, 224, 953
van der Klis, M. 1989, in Proceedings of the NATO Advanced Study Institute on Timing Neutron Stars, held in Çeşme, İzmir, Turkey, April 4–15, 1988. Editors, H. Ögelman and E.P.J. van den Heuvel; Publisher, Kluwer Academic, Dordrecht, The Netherlands, Boston, Massachusetts, p. 27
van der Klis, M. 1995, in X-ray binaries (Cambridge Astrophysics Series, Cambridge, MA: Cambridge Univ. Press, —c1995, edited by Lewin, Walter H.G.; Van Paradijs, Jan; Van den Heuvel, Edward P.J.), p. 252
van der Klis, M. 1998, in NATO ASIC Proc. 515: The Many Faces of Neutron Stars., 337

Chapter 3

A persistent $\sim$1 Hz quasi-periodic oscillation in the dipping low-mass X-ray binary 4U 1323–62

Peter G. Jonker, Michiel van der Klis, & Rudy Wijnands

Astrophysical Journal Letters, 1999, **511**, L41

Abstract

We have discovered a $\sim$1 Hz quasi-periodic oscillation (QPO) in the persistent-emission, the dips, and the type I X-ray bursts of the low-mass X-ray binary 4U 1323–62. The rms amplitude of the QPO is approximately 9%, only weakly depending on photon energy. The amplitude is consistent with being constant throughout the persistent-emission, the dips and the bursts in all but one observation, where it is much weaker during one dip. These properties suggest that we have observed a new type of QPO, which is caused by quasi-periodic obscuration of the central X-ray source by a structure in the accretion disk. This can only occur when the binary inclination is high, consistent with the fact that 4U 1323–62 is a dipping source. The quasi-periodic obscuration could take place by partial covering of an extended central X-ray source by a near-opaque medium, or by covering of a point source by a medium of suitable characteristics to produce the relatively energy-independent oscillations.

3.1 Introduction

The low-mass X-ray binary (LMXB) 4U 1323–62 shows both type I X-ray bursts and periodic dips. The bursts and dips were discovered with the EXOSAT satellite (van der Klis et al. 1984, 1985a,b). The periodic dips in the light curves of dipping LMXBs are thought to be caused by periodic obscuration of the central source by a structure formed in an interplay between the gas stream from the companion and the accretion disk (White & Swank 1982; White et al. 1995); the period of the dips is the orbital period.

In 4U 1323–62, the dip period is 2.93 hours and the dips last ~50 minutes (van der Klis et al. 1985a,b; Parmar et al. 1989). From the burst properties and peak fluxes, and from the absence of eclipses the distance of the source is inferred to be 10–20 kpc, and the inclination $\leq 80^\circ$. The energy spectrum fits an absorbed power law with energy spectral index $\alpha = 0.53 \pm 0.07$, and $N_H = (4.0 \pm 0.3)$x10^{22} atoms cm^{-2}.

In non-dipping LMXBs, numerous QPO phenomena have been reported, at frequencies of several Hertz to $>$ 1200 Hz (van der Klis 1995, 1998 for reviews). So far observations of any $<$ 100 Hz QPO phenomena in dipping LMXBs have been lacking (kHz QPOs were recently reported in 4U 1916–05 by Barret et al. (1997). In this Letter we report the discovery of ~1 Hz QPOs in the dipper 4U 1323–62. The frequency as well as the amplitude of the QPO is approximately constant thoughout the bursts, dips, and persistent-emission. This is the first QPO reported to persist both through type I X-ray bursts and the persistent-emission, and the first $<$ 100 Hz frequency QPO in a dipper.

3.2 Observations and analysis

4U 1323–62 was observed five times with the proportional counter array (PCA; Jahoda et al. 1996) on board the RXTE (Rossi X-ray Timing Explorer; Bradt et al. 1993) satellite on 1997 April 25, 26, and 27 (see Table 3.1). The total amount of good data was 80 ksec. During each observation one or two bursts and one or two dips were observed, resulting in a total of seven type I X-ray bursts and eight dips (some of which were only partially observed). Two bursts in observation 3 showed a secondary burst ~500 s after the primary one. These last approximately 30 s, rise quikly up to count rates of 370 c/s (2–60 keV; this is ~21% of the primary burst peak count rate) and 650 c/s (~37%) and decrease slowly. A burst in observation 2 took place during a dip. The dips lasted ~60 minutes, slightly longer

Table 3.1: Log of the observations. The average persistent-emission count rate of each observation is given in column 5.

Number	Observation	Date	Time (UTC)	Persistent emission 2–60 keV (c/s/5PCU)
1	20066-02-01-00	25 April 1997	22:03–03:56	106
2	20066-02-01-03	26 April 1997	05:06–09:41	104
3	20066-02-01-01	26 April 1997	22:02–03:55	95
4	20066-02-01-04	27 April 1997	05:08–09:42	102
5	20066-02-01-02	27 April 1997	23:12–03:54	94

than those reported by Parmar et al. (1989). The mean background-subtracted persistent 2–60 keV count rate changed little between observations (see Table 3.1). In observation 4, during 40% of the time only 4 of the 5 PCA detectors were active. All reported count rates are for 5 detectors.

Data were obtained over an energy range of 2–60 keV with 16 s time resolution in 129 energy channels, and simultaneously with a time resolution of 1μs in 255 energy channels.

In Figure 3.1 (top panel), we show part of the light curve of observation 1, showing a dip, a burst, and the persistent-emission. The dip starts ~600 s after the beginning of the observation and lasts untill ~4300 s. We also show the corresponding hardness curve (lower panel); the hardness is defined as the 16 s averaged ratio of the count rate in the 9.7–16 keV energy band to that in the 2–7.9 keV band. During the dips the hardness ratio is higher than in the persistent emission, and at the burst start the hardness ratio decreases.

Using the light and hardness curves, we divided the data into three different categories; the dips, the bursts and the persistent emission. This led to the definition of time intervals during which the source is in one of these three states. When analyzing the data the same time intervals were applied in each energy band. We defined dip ingress by the decrease in count rate and simultaneous increase in hardness evident in Figure 3.1; dip egress is the inverse. In between dip ingress and egress, the count rate and hardness behavior is erratic during ~60 minutes. Sometimes during a dip the persistent-emission count rate and hardness levels are briefly reached. We still considered those data to be part of the dip. The onset of a burst is characterized by a steep rise in the count rate simultaneously with a decrease in the hardness ratio. We determined the burst decay time by fitting an

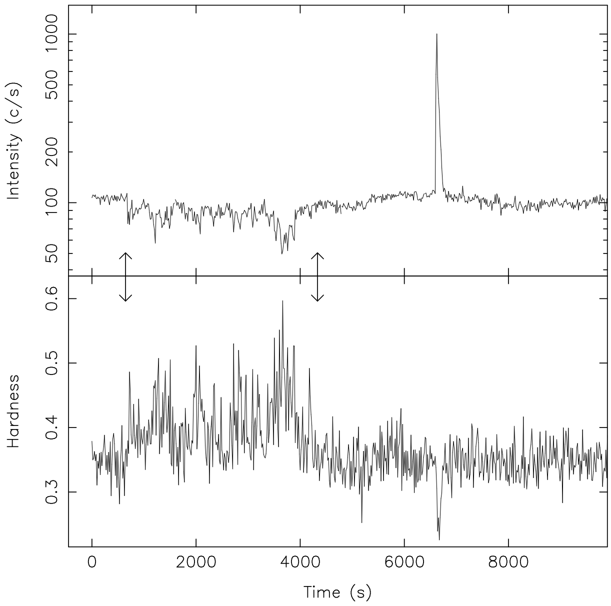

Figure 3.1: Top: The 2–60 keV, 16-s averaged, background–subtracted light curve beginning at the start of the first observation (see Table 3.1) showing a dip and a burst. No dead time corrections have been applied. The statistical uncertainty is typically 5 c/s. Bottom: The 16 s averaged hardness curve (9.7–16 keV/2–7.9 see text) of the same data. Typical errors in the hardness are 0.03. The arrows indicate the start and end of the dip in both the light– and hardness curve.

exponential to the (2–60 keV) decay at a time resolution of 1/8th second. The end of the burst was taken as three times the e-folding time after the onset. One burst decay time was 60 ± 2 s, five were consistent with 82 s and one was 92 ± 3 s. In our power spectral analysis of the bursts concerning the $\sim$1 Hz QPO, we only used the burst decay interval; in our search for $>$ 100 Hz burst oscillations we also used the burst rises.

We calculated power spectra separately for the persistent-emission and for the dips using 64-s segments with a time resolution of 1 ms in the 2–60 keV band, as well as in four energy bands (2–5.0, 5.0–6.4, 6.4–8.6, 8.6–13.0 keV). We applied a similar analysis to the bursts, but using 16-s segments enabling us to obtain 5 power spectra for most of the bursts, and reducing the low frequency component in the power spectra due to the burst profile.

In each energy band all 1/64–512 Hz power spectra corresponding to dips (320 in number), or persistent emission (881) were averaged. The power spectra were fitted with a fit function consisting of a Lorentzian (the QPO), an exponentially cut-off power law, and a constant to represent the Poisson noise. In case of the (1/16–512 Hz) power spectra calculated from the 16-s segments (32) obtained during bursts, an extra Lorentzian centered on ~0 Hz was used in order to account for the power spectral component due to the burst profile. The errors on the fit parameters were determined using $\Delta\chi^2 = 1.0$ (1σ single parameter), and upper limits by using $\Delta\chi^2 = 2.71$, corresponding to a 95% confidence level.

3.3 Results

In the persistent-emission power spectra, we discovered a very significant (31 σ) ~1 Hz QPO (Figure 3.2). Its frequency was 0.87 ± 0.01 Hz in observation 1, 2, and 3, and 0.77 ± 0.01 Hz in observation 4 and 5. This shift of ~0.1 Hz between observations is not correlated to the changes in the persistent count rate level (Table 3.1). The QPO was detected during the persistent emission as well as during the dips and the bursts. It can be directly observed in the light curves of the bursts (see Figure 3.3). During a burst the amplitude of the QPO increases by a factor of ~10 to keep the fractional amplitude approximately constant (see below). The Poisson counting noise prevented us to directly see the QPO in the non-burst parts of the lightcurve.

Except during the dip in observation 4 when the fractional rms amplitude was only 2.2 ± 0.2% and the FWHM only 0.07 ± 0.02 Hz, the frequency, 2–60 keV fractional rms amplitude, and FWHM of the QPO are consistent with being the same for the dips and the persistent-emission in each observation at values of 0.77 or 0.87 Hz, 9%, and 0.25 Hz, respectively. To improve the signal to noise, we averaged the power spectra corresponding to the persistent emission and the dips across all observations in our further analysis. The FWHM and frequency of the QPO in all the persistent-emission and dip data combined is 0.25 ± 0.01 Hz and 0.84 ± 0.02 Hz, respectively; in the individual energy bands we found numbers consistent with this. In determining the fractional rms amplitudes reported below, we fixed FWHM and frequency to these values. The 2–60 keV fractional rms amplitudes in all observations combined have values of 9.1 ± 0.1%, 8.9 ± 0.4%, and 10.9 ± 0.5% for persistent emission, dips, and bursts, respectively. While the persistent-emission and the dip rms amplitudes are identical within the errors, the rms amplitude of the QPO during the bursts is slightly higher. Systematic errors in the rms normalization due to the trend in the count rate in the 16-s data segments caused by the burst profile, and due to the interaction in the fit procedure with the

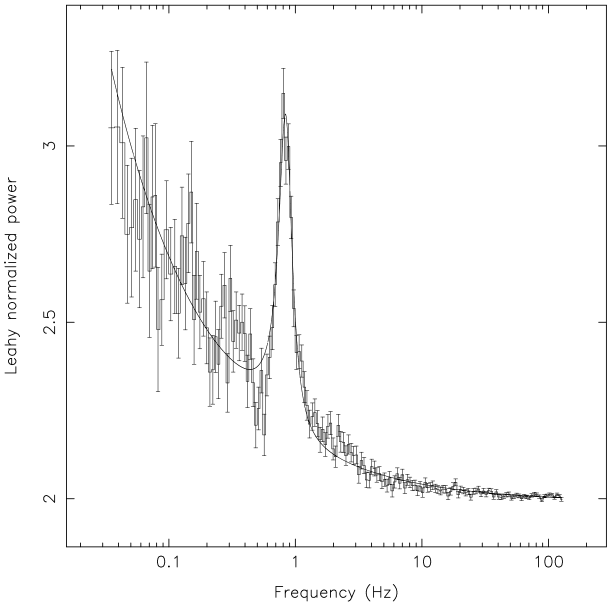

Figure 3.2: Power density spectrum of the full (2–60 keV) energy band of the persistent emission of all the observations combined showing the ∼1 Hz peak. The line drawn through the data points represents the best fit to the data. No dead time corrections have been applied.

extra Lorenzian component can probably account for this small difference. We estimate their influence to be of the order of the discrepancy, since with 64-s burst power spectra, where both of these effects are more prominent, we obtained an rms amplitude of $11.9^{+3.4}_{-0.9}$%.

The rms amplitude of the QPO only weakly depends on energy (Table 3.2); in the persistent-emission it is consistent with a small increase towards higher energies. The fractional rms amplitudes during the dips, and the bursts are consistent with this small increase. No time delay was found in the QPO (0.7–0.9 Hz) between the 2.8–7.5 keV and 7.5–60 keV energy bands, with a 95% confidence upper limit of 14.5 ms for a soft lag (1.8x10^{-2}) times the QPO cycle) and an upper limit of 5.4 ms (6.8x10^{-3} times the QPO cycle) for a hard lag.

We seached for kHz QPOs, but none were found with upper limits of 8–10% for a fixed FWHM of 25 Hz over a frequency range of 100–1000 Hz in all persistent-emission and dip data combined. These upper limits do not exclude the presence of kHz QPOs since many other sources have kHz QPO fractional rms amplitudes below this (van der Klis 1998).

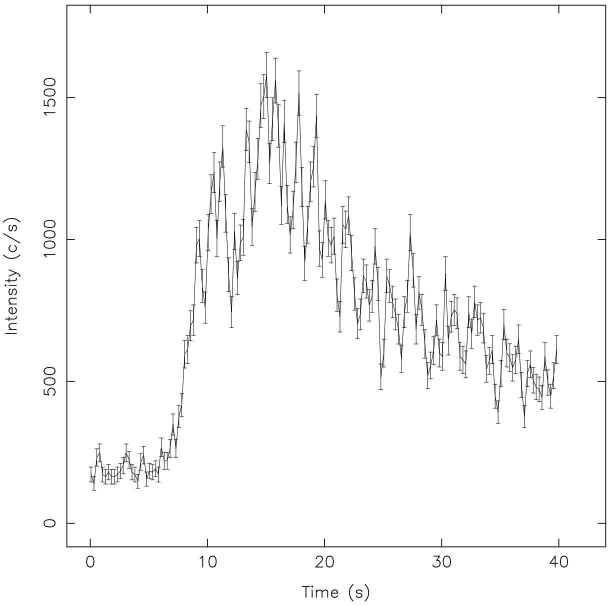

Figure 3.3: Light curve showing the QPO during a burst. Five points correspond to 1.25 s, close to the QPO period.

Table 3.2: Fractional rms amplitudes (in %) of the ~1 Hz QPO. In determining these values the FWHM and frequency were fixed to 0.25 and 0.84 Hz, respectively.

Category	Energy (keV)				
	2–5.0	5.0–6.4	6.4–8.6	8.6–13.0	2–60
Persistent	8.0 ± 0.3	9.9 ± 0.5	9.8 ± 0.4	10.9 ± 0.4	9.1 ± 0.1
Dips	8.1 ± 0.9	9.2 ± 1.1	10.2 ± 0.8	9.7 ± 0.8	8.9 ± 0.4
Bursts	10.3 ± 0.9	10.2 ± 0.9	10.0 ± 1.0	10.6 ± 1.0	10.9 ± 0.5

We set upper limits on any band-limited noise component by adding an exponentially cut-off power law to the fit function. Fixing the power law index to values of 0–1, we derived upper limits of 4.2%–6.4%.

We searched the primary and secondary burst data for high frequency burst oscillations in various ways. In order to increase the sensitivity we averaged the burst rise power spectra of the different bursts using different energy bands (see also Miller 1999). No high frequency burst oscillations were found with upper limits from 0.5-s power spectra varying between 24% at the top and 45% near the end of the burst.

For reference we fitted the persistent-emission energy spectrum of part of observation 2 with a model consisting of an absorbed power law and a gaussian line at 6.5 ± 0.2 keV with a FWHM of $\sim$1 keV. The fit was good, with a χ^2 per degree of freedom of 36/40. The photon index of the power law was 1.75 ± 0.02, and the hydrogen column density is (4.0 ± 0.3)x10^{22} atoms cm^{-2}. This spectrum implies a 2–25 keV flux of 1.5x10^{-10}erg cm^{-2} s^{-1}. Using a distance of 10 kpc this results in a 2–25 keV luminosity of 1.8x10^{36} erg s^{-1}. The spectrum is similar to that previously found by Parmar et al. (1989), although our photon index is somewhat steeper.

3.4 Discussion

We have discovered a QPO with a frequency of approximately 1 Hz. This QPO shows a unique combination of properties;

1) it is observed during the bursts, dips and persistent emission with the same rms amplitude (except during the dip in observation 4);

2) the rms amplitude of the QPO depends only weakly on photon energy;

3) no band-limited noise component was found with upper limits of $\sim$5%.

In all types of LMXBs, QPOs are known to occur with frequencies ranging from 0.01 to 1200 Hz (see van der Klis 1995, 1998 for reviews). Low frequency (0.01–10 Hz) QPOs are known to occur in a number of black hole candidates and atoll sources (see van der Klis 1995 for a review). Unlike the QPO we found in 4U 1323–62, the fractional amplitudes of low frequency QPO in these sources depend strongly on photon energy, and the QPOs are found to be superimposed on a strong band-limited noise component (Wijnands & van der Klis 1999). In the Z sources (the most luminous neutron star LMXBs) low frequency (5–20 Hz) QPOs are also well known (van der Klis 1995), the so called NBOs. However these QPOs occur at or around the Eddington mass accretion rate, which is different from the case in 4U 1323–62. Perhaps our $\sim$1 Hz QPO is related to that reported by Kommers et al. (1998) in the pulsar 4U 1626–67, which they suggest is caused by a structure orbiting the neutron star. However there is no information on the energy dependence of the 0.048 Hz QPO. We conclude that so far the $\sim$1 Hz QPO seems to be in a class of its own.

Models for the $\sim$1 Hz QPO must explain why the rms amplitude of the QPO is constant during bursts, dips and persistent-emission. In models involving a radiation-dominated (inner) disk, we would expect these properties to be different during a burst. Therefore, we consider explanations of the QPO in terms of modulations caused by wave packets of sound waves in the disk (Alpar & Yilmaz 1997) and in terms of fluctuations in the electron scattering optical depth at the critical Eddington mass accretion rates (Fortner et al. 1989) to be unlikely. Furthermore, assuming isotropic emission, the 2–25 keV flux in 4U 1323–62 is too low to produce these fluctuations in the way proposed by Fortner et al. (1989).

Since this QPO is observed in a dipper, we suggest an origin related to the high inclination at which we observe this system. The $\sim$1 Hz QPO cannot be formed by a ripple in the same structure that is also causing the dips, since the fractional rms amplitude of the QPO should then vary with energy in the same way as the dips. This seems not to be the case, since during the persistent emission the spectrum is softer than during the dips, whereas the QPO rms amplitude increases slightly with photon energy. The fact that the QPO properties are the same in and outside the dips also makes this model unlikely. However, quasi-periodic obscuration of the central source by a structure elsewhere in the accretion flow may cause the QPO. If we assume that the QPO is caused by structures orbiting the neutron star with a Keplerian frequency of $\sim$1 Hz, the orbital radius is $\sim$2x10^8 cm for a 1.4 $M_{\odot}$ neutron star. A limited lifetime of the modulating structures, and/or different or shifting radii can cause the modulation of the X-rays to be quasi-periodic instead of periodic. Using the fact that no eclipses have been observed, we derive the height above the plane of the structure causing the $\sim$1 Hz QPO to be $> 5\,10^7$ cm for a lower main sequence companion and a neutron star of 1.4 $M_{\odot}$. This scale-height is difficult to explain in view of the Shakura-Sunyaev thin α disk model. Recently, Pringle (1996) discussed a model where accretion disks in LMXBs are subject to radiation driven instabilities, causing the accretion disks to warp. If these warps are responsible for the X-ray modulations as observed, the radius and structure of the warp may change on viscous time scales, which for typical parameters is on the order of days to weeks (Frank et al. 1992). Scheduled observations of this source will enable us to test this hypothesis.

Neither inverse Compton scattering nor regular Compton scattering can cause the observed X-ray modulation on its own. Both would result in a strong energy dependence of the QPO such as has been observed for kHz QPOs in, e.g., 4U 0614+09 (Méndez et al. 1997), which is inconsistent with what we observe in 4U 1323–62. However, an intermediate-temperature structure, one containing both hot and cold electrons, or one combining Compton scattering with absorption could cause the observed modulations.

A much simpler model is possible in terms of partial covering of an extended source. Quasi-periodic obscuration of part of this central source by an opaque medium, for example an orbiting bump on the disk's surface, can be responsible for modulations with little energy dependence as observed.

Acknowledgments This work was supported in part by the Netherlands Foundation for Research in Astronomy (ASTRON) grant 781-76-017. This research has made use of data obtained through the High Energy Astrophysics Science Archive Research Center Online Service, provided by the NASA/Goddard Space Flight Center. We would like to thank Jeroen Homan for stimulating discussions and the referee for his/her comments and suggestions.

Bibliography

Alpar, M. A. & Yilmaz, A. 1997, New Astronomy, 2, 225
Barret, D., Olive, J. F., Boirin, L., et al. 1997, IAU Circ., 6793, 2+
Bradt, H. V., Rothschild, R. E., & Swank, J. H. 1993, A&AS, 97, 355
Fortner, B., Lamb, F. K., & Miller, G. S. 1989, Nature, 342, 775
Frank, J., King, A., & Raine, D. 1992, Accretion Power in Astrophysics (Accretion Power in Astrophysics, ISBN 0521408636, Cambridge Univ. Press, 1992.)
Jahoda, K., Swank, J. H., Giles, A. B., et al. 1996, Proc. SPIE, 2808, 59
Kommers, J. M., Chakrabarty, D., & Lewin, W. H. G. 1998, ApJ, 497, L33
Méndez, M., van der Klis, M., van Paradijs, J., et al. 1997, ApJ, 485, L37
Miller, M. C. 1999, ApJ, 515, L77
Parmar, A. N., Gottwald, M., van der Klis, M., & van Paradijs, J. 1989, ApJ, 338, 1024
Pringle, J. E. 1996, MNRAS, 281, 357
van der Klis, M. 1995, in X-ray binaries (Cambridge Astrophysics Series, Cambridge, MA: Cambridge Univ. Press, —c1995, edited by Lewin, Walter H.G.; Van Paradijs, Jan; Van den Heuvel, Edward P.J.), p. 252
van der Klis, M. 1998, in NATO ASIC Proc. 515: The Many Faces of Neutron Stars., 337
van der Klis, M., Jansen, F., van Paradijs, J., & Stollmann, G. 1985a, Space Science Reviews, 40, 287
van der Klis, M., Parmar, A., van Paradijs, J., et al. 1985b, IAU Circ., 4044, 1+
van der Klis, M., van Paradijs, J., Jansen, F. A., & Lewin, W. H. G. 1984, IAU Circ., 3961, 1+
White, N., Nagase, F., & Parmar, A. N. 1995, The properties of X-ray binaries (Cambridge Astrophysics Series, Cambridge, MA: Cambridge Univ. Press, —c1995, edited by Lewin, Walter H.G.; Van Paradijs, Jan; Van den Heuvel, Edward P.J.), p. 1
White, N. E. & Swank, J. H. 1982, ApJ, 253, L61
Wijnands, R. & van der Klis, M. 1999, ApJ, 514, 939

Chapter 4

Discovery of a $\sim$1 Hz quasi–periodic oscillation in the low–mass X–ray binary 4U 1746–37

Peter G. Jonker, Michiel van der Klis, Jeroen Homan, Rudy Wijnands, Jan van Paradijs, Mariano Méndez, Erik Kuulkers, & Eric C. Ford

Astrophysical Journal, 2000, **531**, 453

Abstract

We have discovered a $\sim$1 Hz quasi-periodic oscillation (QPO) in the persistent X-ray emission and during type I X-ray bursts of the globular cluster source, dipper and low-mass X-ray binary (LMXB) 4U 1746–37. The QPO properties resemble those of QPOs found recently in the LMXB dippers 4U 1323–62, and EXO 0748–676, which makes 4U 1746–37 the third source known to exhibit this type of QPOs. We present evidence for X-ray spectral changes in this source similar to those observed in LMXBs referred to as atoll sources. We detect two states, a low intensity and spectrally hard state, and a higher intensity and spectrally soft state. This may explain the different spectral characteristics reported for 4U 1746–37 earlier. The high intensity state resembles the banana branch state of atoll sources. The QPOs are only seen in the low intensity state, and are absent when the source is in the banana branch. This strongly suggests that either the accretion disk or an extended central source changes shape between the low intensity state and the banana branch. Twelve bursts were detected, of which 5 took place while the

source was on the banana branch and 7 when the source was in the low intensity state. The bursts occurring on the banana branch had an e-folding time $\sim$3 times longer than those which occurred in the low intensity state. Whereas previously detected dips showed only a decrease in count rate of $\sim$15%, we found a dip in one observation for which the count rate dropped from $\sim$200 counts per second to $\sim$20 counts per second. This dip lasted only $\sim$250 seconds, during which clear spectral hardening occured. This is the first time strong evidence for spectral changes during a dip are reported for this source.

4.1 Introduction

The low–mass X–ray binary (LMXB) 4U 1746–37 shows type I X–ray bursts (Li & Clark 1977) and dips (Parmar et al. 1989b) which recur on the 5.7 hours (Sansom et al. 1993) orbital period. The source is located in the globular cluster NGC 6441. Deutsch et al. (1998) reported the probable detection of the optical counterpart. The dips in dip sources such as 4U 1746–37 are thought to be caused by periodic obscuration of the central source by a structure formed in an interplay between the accretion stream from the companion towards the disk and the disk itself (White & Swank 1982; White et al. 1995; Frank et al. 1987). This structure moves through the line of sight fully or partially obscuring the central source once per binary cycle. Often, the X–ray spectral properties change during the dips. Spectral hardening occurs in 4U 1323–62 (Parmar et al. 1989a), and spectral softening in deep dips seen in 4U 1624–49 (Church & Balucinska-Church 1995). In 4U 1746–37 no energy dependence was found so far (Sansom et al. 1993). The type I X-ray bursts are observed to have peak luminosities around the Eddington luminosity for the estimated distance to the globular cluster (10.7 kpc; Djorgovski 1993). Combined with the fact that the ratio of the X-ray to optical luminosities $L_x/L_{opt} \sim 10^3$, this makes it likely that outside the dips the central source is viewed directly (Parmar et al. 1999).

Recently, in two dipping LMXBs, 4U 1323–62 (Jonker et al. 1999) and EXO 0748–676 (Homan et al. 1999), quasi-periodic oscillations (QPOs) with a typical frequency of 1 Hz were discovered. In EXO 0748–676 these frequencies vary between 0.58–2.44 Hz on timescales ranging from several days to weeks (Homan et al. 1999). Observations with intervals of several days to weeks revealed similar frequency shifts in 4U 1323–62 (Jonker et al. 1999). These QPOs are strong, with fractional rms amplitudes of $\sim$10%, which are the same in the persistent emission, during dips, and during type I X-ray bursts. The rms amplitude of the QPOs does not, or only weakly, depend on the photon energy, unlike that of various other types of QPO observed from LMXBs (van der Klis 1995, 1998). From these properties, and the fact that the ~1 Hz QPOs are observed in high inclination systems, Jonker et al. (1999) suggested that partial obscuration of the central source by a near-opaque or gray medium in or on the disk covering and uncovering the source quasi-periodically at the observed QPO frequency could explain the QPO properties. The most natural location for such a medium would be at the radius where the orbital frequency in the disk is equal to the QPO frequency, which corresponds to a radius of ~ 2 x 10^8cm for a $1.4 M_\odot$ neutron star (Jonker et al. 1999).

On the basis of the timing and spectral properties of LMXBs Hasinger & van der Klis (1989) defined the atoll and the Z sources. The atoll sources show at least two states, named after the associated structures in the X-ray color-color diagram (CD): the island and the banana branch. The timing and spectral properties of the sources in these states are different. In the island state strong band limited noise is present in the power spectra. When the source moves up the banana branch the fractional rms amplitude of this noise component decreases and simultaneously the rms amplitude of a very low frequency power law noise (VLFN) component increases. The Z sources have higher luminosities and trace out a Z track in the CD. The timing properties are correlated with the position along this track (for a complete overview of the timing and spectral properties of the atoll and Z sources, see van der Klis 1995).

In this Letter, we report the discovery of a ~1 Hz QPO in the source 4U 1746–37. We also show that the spectral characteristics and some of the timing properties of this source are reminiscent of those of an atoll source.

4.2 Observations and analysis

We analysed 9 observations of 4U 1746–37 obtained with the proportional counter array (PCA) on board the *RXTE* satellite (Bradt et al. 1993), in 1996 on October 25, 27, 31, and in 1998 on June 5, June 6, August 3, November 7, and November 22. The total amount of good data analysed was ~129 ksec. A log of the observations can be found in Table 4.1. Data were obtained over an energy range of 2–60 keV simultaneously with time resolutions of 0.125 s, 16 s, and 1 μs in 1, 129, and 255 energy bins; the Standard 1, Standard 2, and GoodXenon data modes, respectively.

The average persistent emission count rates varied from 66 counts per second

Table 4.1: Log of the observations. The 5 detector average 2–60 keV persistent emission count rate of each observation is given in column 6.

Number	Observation ID	Date	Start time (UTC)	Amount of good data (ksec.)	Persistent emission (c/s)
1	10112-01-01-00	October 25 1996	00:10:55	$\sim$22	73
2	10112-01-01-01	October 27 1996	03:25:07	$\sim$17	73
3	10112-01-01-02	October 31 1996	08:26:19	$\sim$21	66
4	30701-11-01-00	June 5 1998	00:09:55	$\sim$6	365
5	30701-11-01-01	June 5 1998	14:09:03	$\sim$15	415
6	30701-11-01-02	June 6 1998	07:45:43	$\sim$3	414
7	30701-11-02-00	August 3 1998	03:15:03	$\sim$25	296
8	30701-11-03-01	November 7 1998	08:19:37	$\sim$7	728
9	30701-11-04-00	November 22 1998	11:18:33	$\sim$13	785

(observation 3) to nearly 800 counts per second (observation 9; see Table 4.1). All count rates reported are background subtracted and for five PCA detectors, unless otherwise stated. We observed shallow dips in the lightcurve showing a decrease in count rate of only $\sim$15%, and one deep dip with evidence for spectral hardening (see Figure 4.1, and Section 3). During the last part of observation 9 a solar flare occured; we excluded these data from our analysis.

Since the dips were often difficult to distinguish from the persistent emission (Sansom et al. 1993; Parmar et al. 1999), we divided the data into just two categories; non-burst (which combines persistent emission and dip data) and burst data.

For the selection of the burst data the start of a burst was characterized by the sharp increase in flux and simultaneous decrease in hardness. The burst e-folding time was determined by fitting an exponential to the burst decay in the 2–60 keV lightcurve of the Standard 1 data. The end of the burst was chosen to be three times the e–folding time after the onset (see also Jonker et al. 1999).

Using the Good Xenon data, we calculated power spectra of non-burst data segments of 64 s length and of burst data segments of 16 s length in the energy bands 2–60 keV, 2–6.4 keV, and 6.4–60 keV, with a Nyquist frequency of 512 Hz. We also calculated power spectra of segments of 16 s length with a Nyquist frequency of 2048 Hz in the 2–60 keV band. The power spectra within each energy band were added and averaged for each observation, separately for burst and non-burst data. To search for burst oscillations we also calculated power

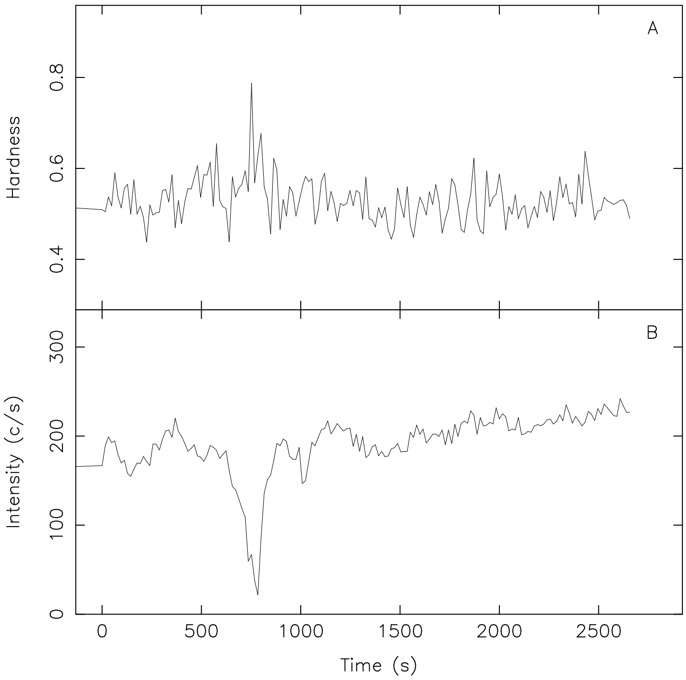

Figure 4.1: A: Hardness curve (ratio between the count rates in the 9.7–16 keV and the 2–9.7 keV bands) of the last part of observation 7 (time zero corresponds to August 3 14:15:03 UTC). B: The simultaneous 2–60 keV, background-subtracted light curve. There is clear spectral hardening during the dip apparent in the lower panel. No dead time corrections were applied (the deadtime fraction was <1.5%). Since the photon-photon deadtime is completely negligible both in and outside the dip, the deadtime does not affect the hardening during the dip.

spectra of a length of 1 s with a Nyquist frequency of 2048 Hz.

We constructed a CD from all non-burst Standard 2 data, using four detectors (0, 1, 2, and 3). The hard color in this diagram is defined as the logarithm of the ratio between the count rates in the 9.7–16.0 keV band and the count rates in the 6.0–9.7 keV band, and the soft color as the logarithm of the ratio between the count rates in the 3.5–6.0 keV band and the count rates in the 2–3.5 keV band

4.3 Results

In the non-burst data of October 25 1996 (observation 1), we discovered a QPO in the 2–60 keV band with a frequency, FWHM, and rms amplitude of 1.04 ± 0.03

Hz, 0.36 ± 0.09 Hz, and 7.7%±0.7% (6σ), respectively (see Figure 4.2). In the observations of October 27 (observation 2) and October 31 (observation 3) 1996, we observed QPOs with similar frequencies, FWHMs and rms amplitudes, albeit at a lower significance level (see Table 4.2).

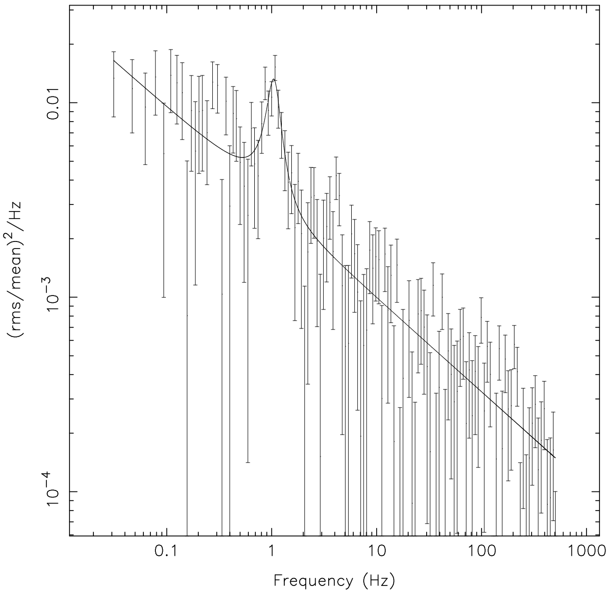

Figure 4.2: Normalized (van der Klis 1989) power spectrum of observation 1. The Poisson noise has been subtracted. The solid line represents the best fit to the data using two components in the fit: a Lorentzian at ∼1 Hz (the QPO), and a power law.

We measured the QPO properties in the 2–6.4 keV and 6.4–60 keV bands. Upper limits on the presence of the QPO were derived fixing the values of the FWHM and frequency obtained in the 2–60 keV energy band, except for observation 2. For this observation we used the values obtained in the 2–6.4 keV band, since the QPO was not detected at a significance higher than 3σ in the 2–60 keV band (see Table 4.2). Only for observation 1 the QPO was detected at a significance higher than 3σ in both the 2–6.4 keV and the 6.4–20 keV energy band. Within the errors the rms amplitude of the QPO in the two energy bands was the same (see Table 4.2).

The QPO was also detected when all 16 s segment power spectra (9 in total) of the decay of the three bursts of observation 1 were combined, at a similar fractional rms amplitude (7.2%±0.8%). The averaged count rate was ∼720 counts per second, i.e., about ten times that in the persistent emission. The frequency

Table 4.2: The fractional rms amplitudes, frequencies and FWHMs of the QPO in the observations where 4U 1746–37 was observed in the low intensity state. If no QPO at a significance level higher than 3σ was detected, the 95% confidence upper limit is given. The FWHM and the frequency were measured in the 2–60 keV band, except for observation 2, where they were measured in the 2–6.4 keV band.

Observation	rms amplitude (2–60 keV)	rms amplitude (2–6.4 keV)	rms amplitude (6.4–20 keV)	ν_{QPO} (Hz)	FWHM (Hz)
1	$7.7\% \pm 0.7\%$	$7.8\% \pm 0.9\%$	$6.7\%^{+2.0}_{-1.1}\%$	1.04 ± 0.03	0.36 ± 0.09
2	$< 7\%$	$6.9\%^{+1.2}_{-0.9}\%$	$<6.8\%$	1.59 ± 0.05	0.4 ± 0.2
3	$7.5\%^{+1.4}_{-1.1}\%$	$<7.4\%$	$<8.7\%$	1.01 ± 0.06	0.25 ± 0.13

increased significantly with respect to the frequency of the QPO in the persistent emission to $1.39^{+0.05}_{-0.10}$ Hz. The FWHM of the QPO was consistent with being the same as in the persistent emission. In the bursts of observations 2 and 3 no significant QPO was detected, with upper limits on the rms amplitude of 7% to 8%.

We fitted a power law to the noise component evident in Figure 4.2. Its rms amplitude integrated over 0.0156–1 Hz varied from 7.1%±0.3% to 5.9%±0.4% and to 9.3%±0.4%, from observation 1–3, while the power law index was consistent with being constant at 0.5 ± 0.3. In the observations 4–9, the noise amplitude was in the range of 1.6%–5.7%. Here, the fractional rms amplitude increased with increasing intensities (see Table 4.1), except for observation 8 were it was only 1.6%. The power law indices ranged from 1.7 ± 0.4 to 2.1 ± 0.4. The rms amplitude of this power law component is slightly higher in the 6.4–20 than in the 2–6.4 keV band. The 6.4–20/2–6.4 keV spectral hardness did not significantly depend on the presence or absence of the QPO.

Combining all non-burst data into a CD, we observed a pattern which resembles the atoll shape (Hasinger & van der Klis 1989), (Figure 4.3). Two distinct parts can be distinguished in the CD, a hard (low intensity, upper part of the diagram) island-like state, and a softer (higher intensity, lower part of the diagram) banana branch. The ~1 Hz oscillations were only found when the source was in the upper (hard) part of the diagram (made up of observations 1–3). Upper limits on the presence of a QPO in the range of 0.5–2.5 Hz of 1%–2% were derived for the banana part of the diagram (made up of observations 4–9).

We observed a total of 12 type I bursts. One burst in the second observation and two bursts in the third observation showed secondary bursts, occurring several

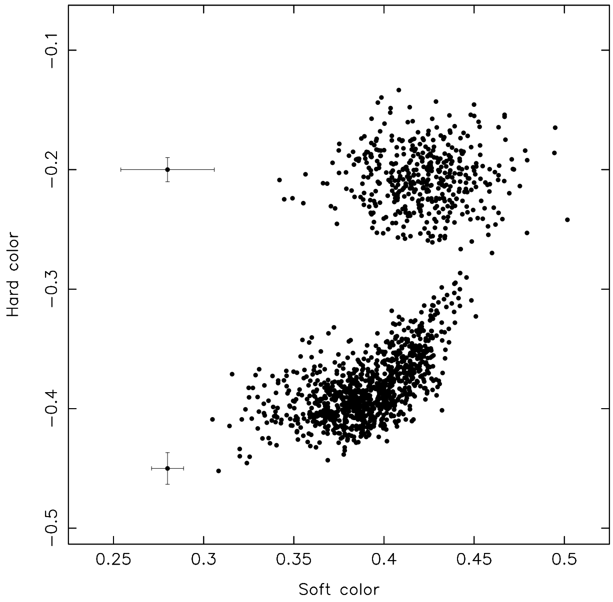

Figure 4.3: Color-color diagram of 4U 1746–37. The hard color is defined as the log of the 9.7–16.0 keV / 6.0–9.7 keV count rate ratio, the soft color as the log of the 3.5–6.0 keV / 2–3.5 keV ratio. No dead–time corrections have been applied (the deadtime fraction was $<$2%). The data are background subtracted and bursts were removed. The data points are 64 s and 128 s averages for the banana branch (lower part) and for the presumed (see text) island state (upper part), respectively. Typical error bars are shown for data in the hard (island) state and for data on the banana branch.

hunderd seconds after the first burst and with a 3–4 times lower peak flux (see Lewin et al. 1995). The burst e–folding times ranged from 7.5 to 11.3 seconds for bursts observed in observations 1–3, and from 7.5 to 14.5 for the secondary bursts. The burst e-folding time of 4 of the 5 bursts observed in observation 8 and 9 ranged from 27.7–30.1 seconds, while one burst in observation 9 which occured $\sim$600 seconds after a burst with a 2.3 higher peak flux had an e–folding time of only 3.0 seconds (the peak flux of this very short burst was similar to that of the bursts in the low intensity state). Upper limits on burst oscillations in the 100–1000 Hz frequency range during the peak and decay of the bursts adding the different bursts of typically $\sim$15% were derived.

One of the dips observed in observation 7 was different from the others; it showed a simultaneous sharp increase in hard color of $\sim$28%, and drop in count rate from $\sim$200 counts per second to $\sim$21 counts per second. The dip was quite short ($\sim$250 s), whereas previous dips were shallow ($\sim$15%), and exhibited no clear spectral hardening (see Figure 4.1). Due to the uncertainties in the orbital ephemeris, we could not relate the exact time of this deep dip to the dips in the other observations.

Upper limits on the presence of kHz QPOs in the frequency range of 100–1000 Hz were derived using a fixed FWHM of 50 Hz. The upper limits were in the range of 3.4%–6.5%.

4.4 Discussion

We discovered a QPO in 4U 1746–37 with a frequency of $\sim$1 Hz, and an rms amplitude of $\sim$7.5%. The QPO was also observed during type I X-ray bursts where the count rate was a factor of 10 higher, with similar fractional rms amplitudes. The QPO in 4U 1746–37 was only observed when the source intensity was low. The frequency of the QPO, the weak energy dependence of its rms amplitude, and the ratio Q between the QPO frequency and its FWHM are similar to the frequencies, the rms amplitude energy dependence, and Q-values (3–4) of the QPOs discovered recently in the persistent emission, dips, and during the type I X-ray bursts in the dippers and LMXBs 4U 1323–62 (Jonker et al. 1999) and in EXO 0748–676 at low intensity (Homan et al. 1999). The similarities in QPO properties and the fact that 4U 1746–37 is a dipper suggest that the $\sim$1 Hz QPO is a general property of high-inclination LMXBs at low intensities, and has a common origin in these systems.

We found for the first time that 4U 1746–37 showed spectral characteristics of an atoll source; the timing properties of observations 4–9 were consistent with banana branch behavior reported for atoll sources (van der Klis 1995). Although no band limited noise was detected, upper limits (1–512 Hz) in the low intensity (hard) state were 20%–28%, whereas they were 2.5%–5.5% when the source was on the apparent banana branch. So, with respect to the band limited noise the timing behavior of the source is consistent with that of an atoll source. Also the fact that on the banana branch the rms amplitude of the power law noise component increased as the source moved up in count rate is consistent with the behavior of the VLFN on the banana branch of an atoll source. However, the high (5.9%–7.1%) rms amplitude and low power law index (0.5) of the power law noise component when the source is at low intensities is not consistent with island-state VLFN. We note that this could be due to effects observable only at high inclinations, similar to those which cause the dips and the $\sim$1 Hz QPO. In EXO 0748–676 strong power law noise (6%–11%) with indices 0.5–0.8 was also present. This noise had no or weak dependence on photon energy, just as the $\sim$1 Hz QPOs (Homan et al. 1999), suggesting a similar origin for both phenomena. In the one observation of EXO 0748–676 where no QPO was found the rms amplitude of the VLFN was lower ($\sim$4%) and the power law index was $\sim$1. The spectral changes we report in 4U 1746–37 related to changes in the position along the atoll, probably reflect the changing spectral characteristics reported before for this source (eg. see Parmar et al. 1999).

Homan et al. (1999) found that the QPO in EXO 0748–676 was present in all observations except one, where the persistent emission count rate was $\sim$2.5 times higher than in the other observations. The fact that the QPO is not detected at higher source count rates (and inferred mass accretion rates) may be due to changes in the accretion geometry with $\dot{M}$. We expect that if we observe 4U 1323–62 at higher $\dot{M}$, the QPO may disappear as well. In 4U 1746–37 the QPO also disappeared when the count rate increased. The rms amplitude dropped by at least a factor of five when the source moved from the low intensity state to the banana branch. This can be accounted for if the size of the central source increased by a factor of 2–3 in radius, decreasing the modulated fraction of the X-rays below our treshold of 1%–2%. If this is the explanation the dip fraction should decrease, making the dips more shallow. Since in 4U 1746–37 the dips were shallow and the source count rates were low, we were not able to check this prediction for this source. Another possibility is that the structure in or on the disk responsible for the $\sim$1 Hz QPO disappeared or decreased in size, or the optical depth of the gray medium changed.

We found that the burst e-folding time is shorter ($\sim$10 s) when the source is in the low intensity state than when the source is on the higher intensity banana branch ($\sim$30 s). This is opposite to what was found by van Paradijs et al. (1988) for several sources. van der Klis et al. (1990) found for 4U 1636–53 that the burst duration was longer (> 20 s) when the source was in the island part of the CD than when the source was in the banana branch (< 10 s). Either the state where we observed the short burst e-folding times is not the product of an island state and high inclination effects as we propose, but a state at a higher mass accretion rate than the banana branch mass accretion rate, or another parameter rather than $\dot{M}$ is also affecting the burst duration.

The frequency of the QPO was 0.35 Hz higher during the type I X-ray bursts than during the persistent emission of observation 1. Similar increases in the QPO frequency during bursts were observed in EXO 0748–676 by Homan et al. (1999).

Acknowledgments This work was supported by the Netherlands Organization for Scientific Research (NWO) under contract number 614-51-002, and by NWO Spinoza grant 08-0 to E.P.J.van den Heuvel. This research has made use of data obtained through the High Energy Astrophysics Science Archive Research Center Online Service, provided by the NASA/Goddard Space Flight Center. MM is a fellow of the Consejo Nacional de Investigaciones Científicas y Técnicas de la República Argentina.

Bibliography

Bradt, H. V., Rothschild, R. E., & Swank, J. H. 1993, A&AS, 97, 355
Church, M. J. & Balucinska-Church, M. 1995, A&A, 300, 441+
Deutsch, E. W., Anderson, S. F., Margon, B., & Downes, R. A. 1998, ApJ, 493, 775+
Djorgovski, S. 1993, in ASP Conf. Ser. 50: Structure and Dynamics of Globular Clusters, 373+
Frank, J., King, A. R., & Lasota, J. . 1987, A&A, 178, 137
Hasinger, G. & van der Klis, M. 1989, A&A, 225, 79
Homan, J., Jonker, P. G., Wijnands, R., van der Klis, M., & van Paradijs, J. 1999, ApJ, 516, L91
Jonker, P. G., van der Klis, M., & Wijnands, R. 1999, ApJ, 511, L41
Lewin, W. H. G., van Paradijs, J., & Taam, R. E. 1995, X-ray Bursts , eds Lewin, van Paradijs, van den Heuvel (ISBN 052141684, Cambridge Univ. Press, 1995.)
Li, F. & Clark, G. 1977, IAU Circ., 3095, 2+
Parmar, A. N., Gottwald, M., van der Klis, M., & van Paradijs, J. 1989a, ApJ, 338, 1024
Parmar, A. N., Oosterbroek, T., Guainazzi, M., et al. 1999, A&A, 351, 225
Parmar, A. N., Stella, L., & Giommi, P. 1989b, A&A, 222, 96
Sansom, A. E., Dotani, T., Asai, K., & Lehto, H. J. 1993, MNRAS, 262, 429
van der Klis, M. 1989, in Proceedings of the NATO Advanced Study Institute on Timing Neutron Stars, held in Çeşme, İzmir, Turkey, April 4–15, 1988. Editors, H. Ögelman and E.P.J. van den Heuvel; Publisher, Kluwer Academic, Dordrecht, The Netherlands, Boston, Massachusetts, p. 27
van der Klis, M. 1995, in X-ray binaries (Cambridge Astrophysics Series, Cambridge, MA: Cambridge Univ. Press, —c1995, edited by Lewin, Walter H.G.; Van Paradijs, Jan; Van den Heuvel, Edward P.J.), p. 252
van der Klis, M. 1998, in NATO ASIC Proc. 515: The Many Faces of Neutron Stars., 337
van der Klis, M., Hasinger, G., Damen, E., et al. 1990, ApJ, 360, L19
van Paradijs, J., Penninx, W., & Lewin, W. H. G. 1988, MNRAS, 233, 437
White, N., Nagase, F., & Parmar, A. N. 1995, The properties of X-ray binaries (Cambridge Astrophysics Series, Cambridge, MA: Cambridge Univ. Press, —c1995, edited by Lewin, Walter H.G.; Van Paradijs, Jan; Van den Heuvel, Edward P.J.), p. 1
White, N. E. & Swank, J. H. 1982, ApJ, 253, L61

Chapter 5

Discovery of kilohertz quasi–periodic oscillations in the Z source GX 340+0

Peter G. Jonker, Rudy Wijnands, Michiel van der Klis, Dimitrios Psaltis, Erik Kuulkers, & Frederick K. Lamb

Astrophysical Journal Letters, 1998, **499**, L191

Abstract

We have discovered two simultaneous kHz quasi–periodic oscillations (QPOs) in the Z source GX 340+0 with the Rossi X–ray Timing Explorer. The X–ray hardness–intensity and color–color diagram each show a full Z–track, with an extra limb branching off the flaring branch of the Z. Both peaks moved to higher frequencies when the mass accretion rate increased. The two peaks moved from 247 ± 6 and 567 ± 39 Hz at the left end of the horizontal branch to 625 ± 18 and 820 ± 19 Hz at its right end. The higher frequency peak's rms amplitude (5–60 keV) and FWHM decreased from $\sim 5\%$ and 383 ± 135 Hz to $\sim 2\%$, and 145 ± 62 Hz, respectively. The rms amplitude and FWHM of the lower peak were consistent with being constant near 2.5 % and 100 Hz. The kHz QPO separation was consistent with being constant at 325 ± 10 Hz. Simultaneous with the kHz QPOs we detected the horizontal branch oscillations (HBO) and its second harmonic, at frequencies between 20 and 50 Hz, and 38 and 69 Hz, respectively. The normal branch oscillations were only detected on the upper and middle normal branch, and became undetectable on the lower normal branch. The HBO frequencies do not fall within the range predicted for Lense–Thirring (LT) precession, unless ei-

ther the ratio of the neutron star moment of inertia to neutron star mass is at least 4, $10^{45} g\,cm^2/M_\odot$, the frequencies of the HBO are in fact the sub-harmonic oscillations, or the observed kHz peak difference is half the spin frequency and not the spin frequency. During a 1.2 day gap between two observations, the Z–track in the hardness-intensity diagram moved to higher count rates by about 3.5%. Comparing data before and after this shift, we find that the HBO properties are determined by position on the Z–track and not directly by count rate or X–ray colors.

5.1 Introduction

GX 340+0 is a bright low–mass X–ray binary and a Z source (Hasinger & van der Klis 1989). The Z–track traced out in the X–ray color–color (CD) and hardness–intensity diagram (HID) is usually built up of three components, the horizontal branch (HB), the normal branch (NB), and the flaring branch (FB). The mass accretion rate ($\dot{M}$) is thought to increase from a few tens of the Eddington mass accretion rate when the source is on the HB, to near–Eddington on the NB, and super–Eddington on the FB. On the HB and the upper part of the NB of GX 340+0, quasi–periodic oscillations (QPOs) with frequencies of 32–50 Hz, the horizontal branch oscillations (HBOs), were detected by Penninx et al. (1991). On the central part of the NB, QPOs with a typical frequency of 5.6 Hz, the normal branch oscillations (NBOs), were detected by van Paradijs et al. (1988).

In four Z sources, Sco X–1 (van der Klis et al. 1996a, 1997), GX 5–1 (van der Klis et al. 1996b), GX 17+2 (Wijnands et al. 1997a), and Cyg X–2 (Wijnands et al. 1998a) two simultaneous kilo Hertz (kHz) QPOs have been observed, with frequencies reflecting flux changes on timescales close to the dynamical timescales near a neutron star. The higher frequency peak (henceforth called upper peak) has been proposed to reflect the Keplerian frequency of blobs of material orbiting around the neutron star, at a preferred radius in the disk, such as the sonic radius (Miller et al. 1998). The lower frequency peak (henceforth called lower peak) is the proposed beat frequency between the frequency of the upper peak and the spin frequency of the neutron star. The kHz QPO frequency is observed to increase with increasing $\dot{M}$. Similar kHz QPOs are also found in atoll sources. The frequencies of the kHz QPOs are between 300 and 1200 Hz. (See van der Klis 1998 for a recent overview).

In this Letter we report the discovery of two simultaneous kHz QPOs in the Z source GX 340+0. A preliminary announcement of these results was already made by Wijnands & van der Klis (1998).

5.2 Observations and analysis

We observed GX 340+0 with the proportional counter array onboard the Rossi X-ray Timing Explorer on 1997 Apr. 17, Sept. 21, 23, 25, and Nov. 1, 2, 3, and 4. The total amount of good data obtained was 138 ksec. During 5% of this time only three or four of the five detectors were active. For our CD and HID we used only the data from the three detectors that were always active. In our power spectral analysis we used all available data. The mean five-detector countrate was 6443 $\mathrm{cts\,s^{-1}}$. The data were obtained using 16s time resolution in 129 photon energy bands (effective energy range 2–60 keV), and simultaneously with 122 μs time resolution in four bands (2–5.0 keV, 5.0–6.4 keV, 6.4–8.6 keV, and 8.6–60 keV) on Apr. 17 or in two bands for the other dates (2–5.0 keV and 5.0–60 keV).

We calculated power density spectra using the 122 μs data divided into 16s segments. To determine the properties of the kHz QPOs we fitted the 95–4096 Hz power spectra with a function that consisted of one or two Lorentzians (the kHz QPOs) and a constant plus a broad sinusoid (the dead-time modified Poisson noise) (Zhang et al. 1995). The Very Large Event window (van der Klis et al. 1997) was set to 55 μs, so that its effect on the Poisson noise is small and could be incorporated in the sinusoid. To determine the properties of the HBO, we fitted the 0.125–126.5 Hz power spectra using a function which consisted of the sum of a constant, one or two Lorentzian peaks, and two exponentially cut-off power-law components. The errors were determined using $\Delta\chi^2 = 1.0$ ($1\,\sigma$ single parameter) and upper limits using $\Delta\chi^2 = 2.71$, corresponding to a 95% confidence level. Upper limits on the kHz QPOs were determined using a fixed FWHM of 150 Hz. When only the lower peak was detected, the upper limit on the upper peak was determined by setting the frequency to the value of the frequency of the lower peak plus the mean frequency difference between the two peaks. Upper limits on the HBO were determined by keeping the FWHM fixed at 10 Hz.

In the HID and CD, the hard color is defined as the logarithm of the 9.7–16.0 keV/6.4–9.7 keV countrate ratio. The soft color is defined as the logarithm of the 3.5–6.4 keV/2–3.5 keV countrate ratio. The intensity is defined as the logarithm of the countrate in the 2–16.0 keV band. The HID and CD are background–corrected but no dead-time correction was carried out. The dead–time correction factor was $\sim 2\%$. In order to measure the position along the Z–track, we use the S_z parametrization (e.g. Wijnands et al. (1997b)) applied to the HID. In this parametrization the HB/NB vertex is fixed at $S_z = 1.0$ and the NB/FB vertex at $S_z = 2.0$. We selected the power spectra according to S_z, and determined the average S_z and standard deviation for each selection.

The track of the Nov. 4 data is shifted towards higher intensity and softer colors with respect to the Z–track in the other data. We therefore determined the HBO properties for the Nov. 4 data ($\sim$18 ksec) separately. To determine the kHz QPO properties we combined the Nov. 4 data with the rest in order to get a higher signal to noise ratio. As the kHz QPOs were only significantly detected in the 5.0–60 keV band and the significance did not increase combining the two bands, we used only the 5.0–60 keV band in our analysis.

5.3 Results

We observed a full Z–track in the HID and CD (Figure 5.1). The Z-shape shows a fourth branch beyond the FB. This extra, trailing branch was seen before in GX 340+0 (Penninx et al. 1991) and GX 5–1 (Kuulkers et al. 1994; Wijnands & van der Klis 1998). Detailed examination of the HB/NB vertex in the HID revealed that the 1997 Nov. 4 data were shifted to higher count rates ($\sim$ 3.5%) and softer colors ($\sim$ 0.5%) than the other data. Due to this shift, which occurred during a 1.2 day gap between two observations, the HB/NB vertex in the HID is broadened. Due to the size of the dots in Figure 5.1 this is not visible. This shift was also seen in EXOSAT data of GX 340+0 (Kuulkers & van der Klis 1996).

We detected kHz QPOs in the 5.0–60 keV band (Figure 5.2). The lower kHz peak was detected at S_z values up to 1.04, the upper peak up to $S_z = 0.95$ (Figure 5.3). The lower peak had a frequency of 247 ± 10 Hz at $S_z = 0.47$ and increased to 625 ± 18 Hz at $S_z = 1.04$, its rms amplitude remained about constant at values near 2%, and its FWHM varied between 30 and 160 Hz with no clear correlation with S_z. The frequency of the upper peak was 567 ± 39 Hz at $S_z = 0.47$ and increased to 820 ± 19 Hz at $S_z = 0.95$, while its rms amplitude decreased from 5.1 ± 0.9% to 2.0 ± 0.4%, and its FWHM from 383 ± 135 Hz to 145 ± 62 Hz. The FWHM ratio did not significantly depend on S_z. When both peaks were detected, the peak separation was consistent with being constant at a value of 325 ± 10 Hz. We did not detect significant kHz QPOs in the 2–5.0 keV bands, with upper limits of 2.8% and 2.3% at $S_z = 0.58$ and 2.7% and 2.8% at $S_z = 0.87$ for the lower and upper peaks, respectively, while in the 5.0–60 keV band the peaks were found with a rms amplitude of 1.5% and 4.4% at $S_z = 0.58$ and 1.6% and 2.8% at $S_z = 0.87$, respectively.

Simultaneously with the kHz QPO, the HBO and its second harmonic were detected. When we used the same S_z selections as in the fitting of the kHz QPOs the HBO sometimes showed double peaks, especially at low S_z. This was caused

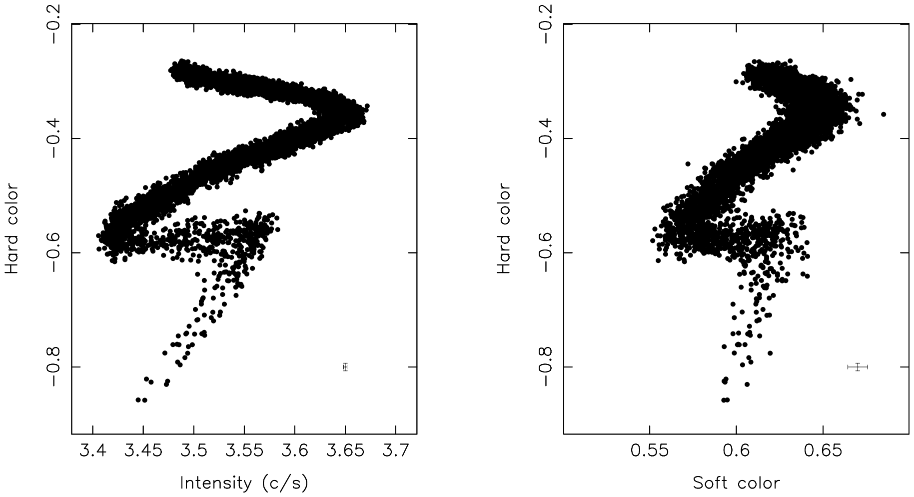

Figure 5.1: Hardness–intensity (left) and color–color diagram (right) of GX 340+0. The hard color is defined as the logarithm of the 9.7–16.0 keV / 6.4–9.7 keV count rate ratio and the soft color as the logarithm of the 3.5–6.4 keV/ 2–3.5 keV countrate ratio. The three–detector countrate is measured in the 2–16.0 keV band. The data was background subtracted but no dead–time correction was applied. The typical error bars are visible in the HID and CD in points in the extra trailing branch.

by the steep dependence of the HBO frequency on S_z and its narrow peak width. Therefore up to $S_z = 0.7$, we used narrower S_z selections in fitting the HBO to prevent the HBO peak from moving too much within the selection. The HBO frequency increased from 19.43 ± 0.03 Hz at $S_z = 0.43$ to 49.92 ± 0.21 Hz at $S_z = 1.05$. Then it remained constant up to $S_z = 1.25$ (Figure 5.3 b). The rms amplitude in the 5.0–60 keV energy band of the HBO decreased smoothly from 9.1 ± 0.1% at the left side of the HB ($S_z = 0.43$) to 1.8 ± 0.2% on the NB ($S_z = 1.25$). For higher S_z selections, no HBO was detected, with upper limits of ~ 2% rms. The FWHM increased from 2.9 ± 0.1 Hz to 15.3 ± 4.2 Hz. We did not find a clear dependence on S_z of the rms amplitude and FWHM of the second harmonic. Due to the presence of a broad noise component around the frequency of the second harmonic it was difficult to determine the properties of either one of the two components.

We found that the HBO frequency vs. S_z relation of the Nov. 4 data was offset with respect to that of the other data (Figure 5.4 left), due to the shift in the vertex of the Nov. 4 data, which along the HB, corresponds to a shift in S_z of ~ 0.05, equal to the offset in the S_z vs. ν_{HBO} plot (Figure 5.4, left). If we correct for the

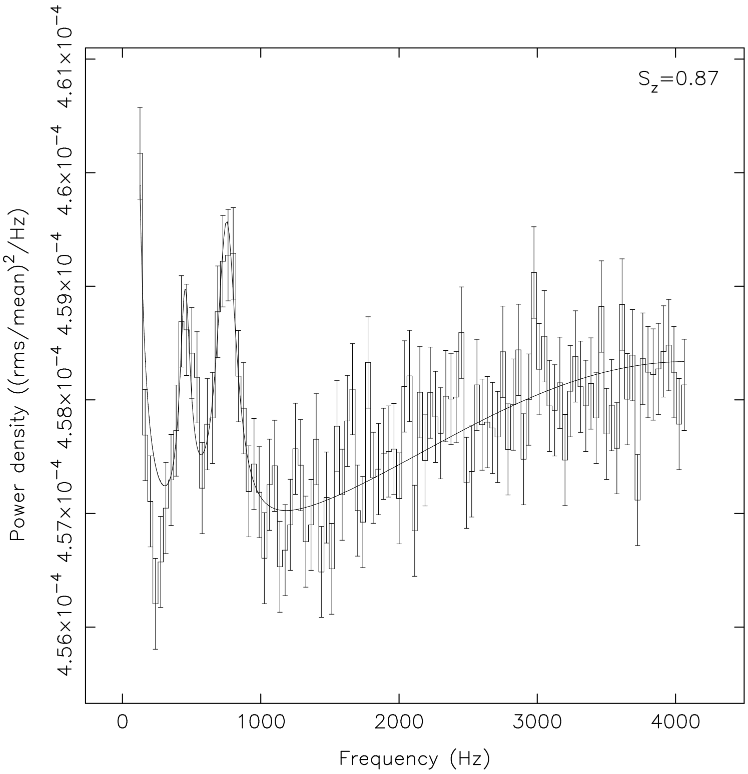

Figure 5.2: Typical power density spectra of GX 340+0; the power is in units of fractional amplitude squared per Hz. The kHz QPOs are at frequencies of 452 and 753 Hz, respectively, at $S_z = 0.87$. The rise in the power density of the left plot towards higher frequencies is caused by instrumental dead–time effects on the Poisson noise.

change in S_z by measuring S_z on Nov. 4 from the HB/NB vertex appropriate for that date, the HBO frequencies, rms amplitude, and FWHM of the Nov. 4 data and the HBO frequencies, rms amplitude, and FWHM of the other data as a function of S_z are the same (Figure 5.4, right). This strengthens previous conclusions (Kuulkers et al. 1994) that S_z, not count rate, is the better measure for $\dot{M}$.

We also detected the NBOs, between $S_z \sim 1.1$ and $S_z \sim 1.8$. These will be more extensively discussed elsewhere.

5.4 Discussion

We have discovered kHz QPOs in the Z source GX 340+0. The frequencies of both the lower and upper peak increased as the source moved along the HB to the HB/NB vertex. The peak separation was consistent with being constant. This is similar to what was found in GX 17+2 (Wijnands et al. 1997a), Cyg X–2 (Wijnands et al. 1998a), and GX 5–1 (van der Klis et al. 1996b; Wijnands et al. 1998b). Only in Sco X–1 (van der Klis et al. 1997) and perhaps in the atoll source 4U 1608–52 (Méndez et al. 1998) the peak separation was found to decrease with increasing $\dot{M}$. If this decrease in Sco X–1 is in some way related to the source approching the Eddington critical luminosity (White & Zhang 1997; Miller et al. 1998), this could mean that if we were able to detect the kHz QPOs in GX 340+0 and the other Z sources (further) up the NB we might also see the peak separation decrease.

The lower peak reaches the so far lowest “kHz” QPO frequency found in any low mass X–ray binary, 247 Hz. The maximum frequency reached by the upper peak, 820 Hz, is also rather low. Using the sonic–point model (Miller et al. 1998) to explain the upper peak kHz QPO frequency, we found lower limits on the mass of the neutron star of $M_{neutr} > 0.6 M_{\odot}$ for a neutron star radius of 4M, and $M_{neutr} > 1.2 M_{\odot}$ for a neutron star radius of 7M. (The implicit assumptions made in calculating these lower limits are: Schwarzschild spacetime metric, non–rotating radiating layer, and photons remove angular momentum from the disk material only in one scattering event.) We note that the frequencies of the kHz QPOs seem to confirm the idea (e.g. Kuulkers et al. 1994) that GX 340+0 is more similar in appearance to GX 5–1 (Wijnands et al. 1998b), than to Sco X–1 (van der Klis et al. 1997), and GX 17+2 (Wijnands et al. 1997a) (frequencies higher than 1000 Hz).

Any straightforward beat–frequency model predicts the upper peak to be narrower than, or as narrow as the lower peak. We find in GX 340+0 that the upper peak is usually broader than the lower peak. In fact, the upper peaks found in GX 340+0 were very broad with $\frac{\delta\nu}{\nu}$ up to 0.67 at $S_z = 0.43$. Therefore, a straightforward beat–frequency interpretation of the two peaks in GX 340+0 is difficult. In GX 340+0, GX 5–1 (Wijnands et al. 1998b), and GX 17+2 (Wijnands et al. 1997a) the upper peak FWHM decreases as a function of S_z. To explain this behavior one could involve scattering in a rapidly variable medium (Méndez et al. 1998). The effect of this scattering should become less as $\dot{M}$ increases.

Although the behavior of the kHz QPOs as a function of inferred $\dot{M}$ in GX 340+0 is similar to that found in other Z sources, the HBO behavior is rather different.

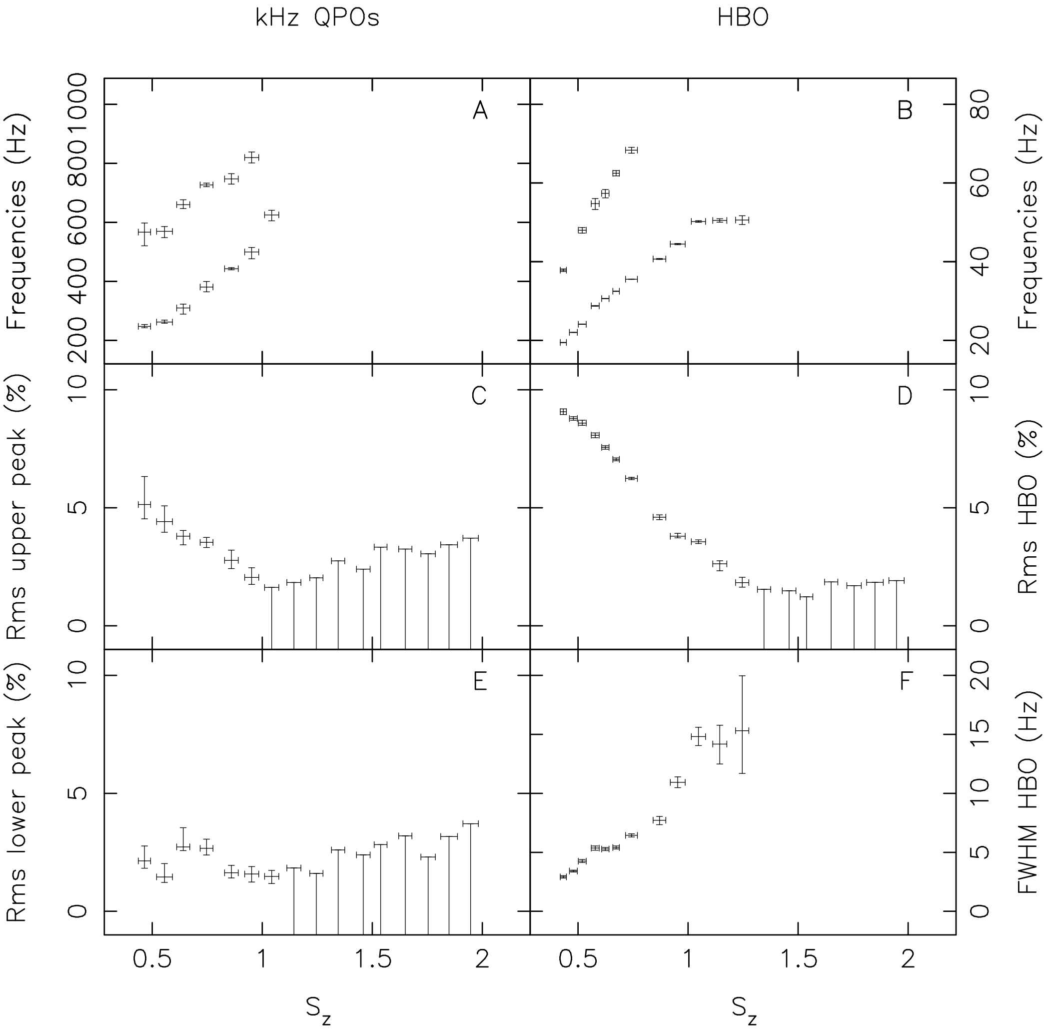

Figure 5.3: (A) Frequencies of the kHz QPOs, (B) frequencies of the HBO and its harmonic, (C) rms amplitude of the upper kHz QPO, (D) rms amplitude of the HBO, (E) rms amplitude of the lower kHz QPO, and (F) FWHM of the HBO, as a function of S_z. The error bars on S_z are standard deviations.

The FWHM of the HBO increased as the rms amplitude decreased, which is unlike what is seen in other Z sources. In Cyg X–2 Wijnands et al. (1997b) found the FWHM to be well–correlated to the rms. In GX 17+2 the FWHM remained about constant while the rms amplitude decreased (Homan private comm.). In previous observations of GX 340+0 (Penninx et al. 1991, Table 2) the behavior is consistent with our findings. In observations of Kuulkers & van der Klis (1996) the FWHM does not show a clear relation as a function of the rms amplitude. Exactly the same behavior (as we reported for GX 340+0) was found in GX 5–1 (Lewin et al. 1992; Wijnands et al. 1998b). This suggests that an extra parameter in addition to $\dot{M}$ determines the timing properties. Another indication of this is that there are differences between the Z sources in the position on the Z–track where the NBO are found. In GX 17+2 (Penninx et al. 1990), and Sco X–1 (van der Klis et al. 1987) the NBO were detected up the FB, e.g. $S_z > 2$. In Cyg X–2 they were detected up to the NB/FB vertex (Wijnands et al. 1997b), while in GX 340+0 and GX 5–1 the NBO were detected up to $S_z = 1.8$.

Recently, it has been proposed that the HBO frequency may reflect the general relativistic Lense–Thirring (LT) precession frequency at the inner edge of a warped accretion disk (Stella & Vietri 1998). If the upper peak is interpreted as a Keplerian frequency in the inner part of the disk, there is a quadratic relation between the LT precession frequency and the upper peak frequency. Applying this theory to our observations and assuming the peak difference to be the neutron star spin frequency, the LT predictions for the HBO frequency are too low by at least a factor of 2. The same discrepancy by a factor of 2 has been reported for the Z source GX 17+2 (Stella & Vietri 1998). There are several ways out, but each

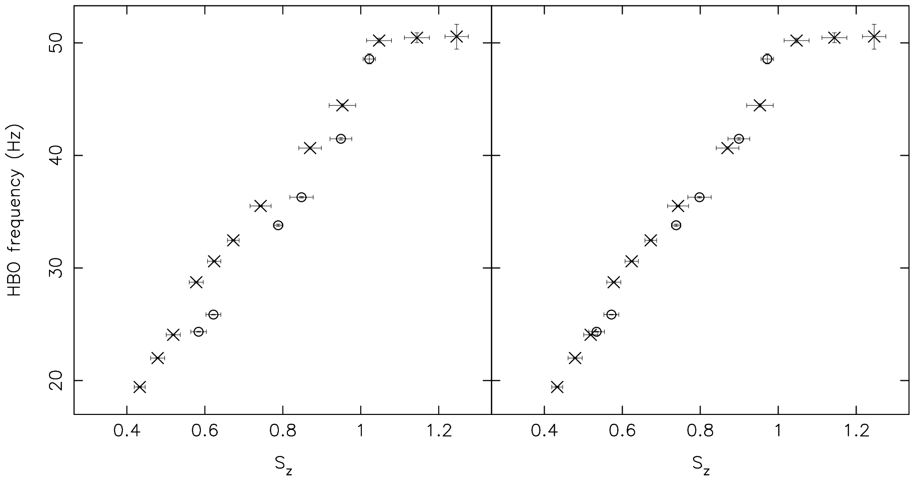

Figure 5.4: Left: The HBO frequencies of the November 4 data (circles) and the other data (X–es). Right: The frequencies of the HBO for the November 4 data corrected for the shift (circles) and the other data (X–es). The error bars in the frequency are smaller than the size of the symbols. (see also Section 3 paragraph 4).

appears to create serious difficulties. I/M (with I the moment of inertia of the neutron star and M its mass) may be a factor of 2 higher than presently thought, however, no sensible equation of state appears to be able to produce such values of I/M. The kHz QPO peak difference may not be equal to the neutron star spin frequency but to half the spin frequency, however, at least in atoll sources this seems to contradict the results obtained from burst QPO (Strohmayer et al. 1996). The HBO may not be the fundamental frequency but the harmonic of the predicted LT frequency, however, in none of the Z sources there is any evidence of excess power at frequencies half the HBO frequencies.

Acknowledgments We would like to thank Jan van Paradijs for commenting on the manuscipt and Cole Miller for the useful discussion on the sonic-point model and the implications of our findings. This work was supported in part by the Netherlands Foundation for Research in Astronomy (ASTRON) grant 781-76-017. D.P. acknowledges support from a Postdoctoral fellowship at the Smithsonian Institute and F.K.L. (NAG 5-2925) from US NASA grants.

Bibliography

Hasinger, G. & van der Klis, M. 1989, A&A, 225, 79

Kuulkers, E. & van der Klis, M. 1996, A&A, 314, 567

Kuulkers, E., van der Klis, M., Oosterbroek, T., et al. 1994, A&A, 289, 795

Lewin, W. H. G., Lubin, L. M., Tan, J., et al. 1992, MNRAS, 256, 545

Méndez, M., van der Klis, M., Wijnands, R., et al. 1998, ApJ, 505, L23

Miller, M. C., Lamb, F. K., & Psaltis, D. 1998, ApJ, 508, 791

Penninx, W., Lewin, W. H. G., Mitsuda, K., et al. 1990, MNRAS, 243, 114

Penninx, W., Lewin, W. H. G., Tan, J., et al. 1991, MNRAS, 249, 113

Stella, L. & Vietri, M. 1998, ApJ, 492, L59

Strohmayer, T. E., Zhang, W., Swank, J. H., et al. 1996, ApJ, 469, L9

van der Klis, M. 1998, in NATO ASIC Proc. 515: The Many Faces of Neutron Stars., 337

van der Klis, M., Stella, L., White, N., Jansen, F., & Parmar, A. N. 1987, ApJ, 316, 411

van der Klis, M., Swank, J. H., Zhang, W., et al. 1996a, ApJ, 469, 1

van der Klis, M., Wijnands, R., Kuulkers, E., et al. 1996b, IAU Circ., 6511, 2+

van der Klis, M., Wijnands, R. A. D., Horne, K., & Chen, W. 1997, ApJ, 481, L97

van Paradijs, J., Hasinger, G., Lewin, W. H. G., et al. 1988, MNRAS, 231, 379

White, N. E. & Zhang, W. 1997, ApJ, 490, L87

Wijnands, R., Homan, J., van der Klis, M., et al. 1998a, ApJ, 493, L87

—. 1997a, ApJ, 490, L157

Wijnands, R., Méndez, M., van der Klis, M., et al. 1998b, ApJ, 504, L35

Wijnands, R. & van der Klis, M. 1998, in Accretion Processes in Astrophysical Systems: Some Like it Hot!, 381+

Wijnands, R. A. D., van der Klis, M., Kuulkers, E., Asai, K., & Hasinger, G. 1997b, A&A, 323, 399

Zhang, W., Jahoda, K., Swank, J. H., Morgan, E. H., & Giles, A. B. 1995, ApJ, 449, 930

Chapter 6

The power spectral properties of the Z source GX 340+0

Peter G. Jonker, Michiel van der Klis, Rudy Wijnands, Jeroen Homan, Jan van Paradijs, Mariano Méndez, Eric C. Ford, Erik Kuulkers, & Frederick K. Lamb

Astrophysical Journal, 2000, **537**, 374

Abstract

We present an analysis of ~390 ksec of data of the Z source GX 340+0 taken during 24 observations with the *Rossi X-ray Timing Explorer* satellite. We report the discovery of a new broad component in the power spectra. The frequency of this component varied between 9 and 14 Hz, and remained close to half that of the horizontal branch quasi–periodic oscillations (HBO). Its rms amplitude was consistent with being constant around ~5%, while its FWHM increased with frequency from 7 to 18 Hz. If this sub–HBO component is the fundamental frequency, then the HBO and its second harmonic are the second and fourth harmonic component, while the third harmonic was not detected. This is similar to what was recently found for the black hole candidate XTE J1550–564. The profiles of both the horizontal– and the normal branch quasi–periodic oscillation peaks were asymmetric when they were strongest. We describe this in terms of a shoulder component at the high frequency side of the quasi–periodic oscillation peak, whose rms amplitudes were approximately constant at ~4% and ~3%, respectively. The peak separation between the twin kHz quasi-periodic oscillations was consistent with being constant at 339±8 Hz but a trend similar to that seen in, e.g. Sco X–1 could not be excluded. We discuss our results within the framework of the various models which have been proposed for the kHz QPOs and low frequency peaks.

6.1 Introduction

GX 340+0 is a bright low–mass X–ray binary (LMXB) and a Z source (Hasinger & van der Klis 1989). The Z–shaped track traced out by Z sources in the X–ray color–color diagram or hardness–intensity diagram (HID) is divided into three branches: the horizontal branch (HB), the normal branch (NB), and the flaring branch (FB). The power spectral properties and the HID of GX 340+0 were previously described by van van Paradijs et al. (1988) and Kuulkers & van der Klis (1996) using data obtained with the EXOSAT satellite, by Penninx et al. (1991) using data obtained with the Ginga satellite, and by Jonker et al. (1998) using data obtained with the *Rossi X-ray Timing Explorer (RXTE)* satellite. An extra branch trailing the FB in the HID has been described by Penninx et al. (1991) and Jonker et al. (1998). When the source is on the HB or on the upper part of the NB, quasi–periodic oscillations (QPOs) occur with frequencies varying from 20–50 Hz: the horizontal branch quasi–periodic oscillations or HBOs (Penninx et al. 1991; Kuulkers & van der Klis 1996; Jonker et al. 1998). Second harmonics of these HBOs were detected by Kuulkers & van der Klis (1996) and Jonker et al. (1998) in the frequency range 73–76 Hz and 38–69 Hz, respectively. In the middle of the NB, van Paradijs et al. (1988) found normal branch oscillations (NBOs) with a frequency of 5.6 Hz. Recently, Jonker et al. (1998) discovered twin kHz QPOs in GX 340+0. These QPOs have now been seen in all six originally identified Z sources (Sco X–1, van der Klis et al. 1996; Cyg X–2, Wijnands et al. 1998a; GX 17+2, Wijnands et al. 1997a; GX 349+2, Zhang et al. 1998; GX 340+0, Jonker et al. 1998; GX 5–1, Wijnands et al. 1998b; see van der Klis 1998, 2000 for reviews), but not in Cir X–1, which combines Z source and atoll source characteristics (Oosterbroek et al. 1995; Shirey et al. 1999; see also Psaltis et al. 1999a).

In the other class of LMXBs, the atoll sources (Hasinger & van der Klis 1989), kHz QPOs are observed as well (see van der Klis 1998, 2000 for reviews). Recently, also HBO–like features have been identified in a number of atoll sources (4U 1728–34, Strohmayer et al. 1996; Ford & van der Klis 1998; Di Salvo et al. 2001; GX13+1, Homan et al. 1998; 4U 1735–44, Wijnands et al. 1998c; 4U 1705–44, Ford et al. 1998a; 4U 1915–05, Boirin et al. 2000; 4U 0614+09, van Straaten et al. 2000; see Psaltis et al. 1999a for a summary). Furthermore, at the highest inferred mass accretion rates, QPOs with frequencies near 6 Hz have been discovered in the atoll sources 4U 1820–30 (Wijnands et al. 1999b), and XTE J1806–246 (Wijnands & van der Klis 1999b; Revnivtsev et al. 1999), which might have a similar origin as the Z source NBOs.

At low mass accretion rates the power spectra of black hole candidates, atoll, and Z sources show similar characteristics (van der Klis 1994a,b). Wijnands & van der Klis (1999a) found that the break frequency of the broken power law which describes the broad-band power spectrum, correlates well with the frequency of peaked noise components (and sometimes narrow QPO peaks) observed in atoll sources (including the millisecond X–ray pulsar SAX J1808.4–3658; Wijnands & van der Klis 1998; Chakrabarty & Morgan 1998), and black hole candidates. The Z sources followed a slightly different correlation. In a similar analysis, Psaltis et al. (1999a) have pointed out correlations between the frequencies of some of these QPOs and other noise components in atoll sources, Z sources, and black hole candidates, which suggests these phenomena may be closely related across these various source types, or at least depend on a third phenomenon in the same manner. Because of these correlations, models describing the kHz QPOs which also predict QPOs or noise components in the low–frequency part of the power spectrum can be tested by investigating this low–frequency part.

In this paper, we study the full power spectral range of the bright LMXB and Z source GX 340+0 in order to further investigate the similarities between the atoll sources and the Z sources, and to help constrain models concerning the formation of the different QPOs. We report on the discovery of two new components in the power spectra of GX 340+0 with frequencies less than 40 Hz when the source is on the left part of the HB. We also discuss the properties of the NBO, and those of the kHz QPOs.

6.2 Observations and analysis

The Z source GX 340+0 was observed 24 times in 1997 and 1998 with the proportional counter array (PCA; Jahoda et al. 1996) on board the *RXTE* satellite (Bradt et al. 1993). A log of the observations is presented in Table 6.1. Part of these data (observations 1, 9–18) was used by Jonker et al. (1998) in the discovery of the kHz QPOs in GX 340+0. The total amount of good data obtained was ~390 ksec. During ~19% of the time only 3 or 4 of the 5 PCA detectors were active.

The data were obtained in various modes, of which the Standard 1 and Standard 2 modes were always active. The Standard 1 mode has a time resolution of 1/8 s in one energy band (2–60 keV). The Standard 2 mode has a time resolution of 16 s and the effective 2–60 keV PCA energy range is covered by 129 energy channels. In addition, high time resolution data (with a resolution of 244 μs or better for the 2–5.0 keV band and with a resolution of 122 μs or better for the

Table 6.1: *Log of the observations.*

Number	Observation ID	Date & Start time (UTC)	Total on source observing time (ksec.)
1	20054-04-01-00	1997-04-17 13:26:21	19.8
2	20059-01-01-00	1997-06-06 06:05:07	34.7
3	20059-01-01-01	1997-06-06 21:39:06	8.1
4	20059-01-01-02	1997-06-07 11:15:05	22.1
5	20059-01-01-03	1997-06-07 23:48:56	21.6
6	20059-01-01-04	1997-06-08 07:51:04	22.9
7	20059-01-01-05	1997-06-09 00:09:03	17.5
8	20059-01-01-06	1997-06-10 01:22:46	22.0
9	20053-05-01-00	1997-09-21 01:04:06	17.5
10	20053-05-01-01	1997-09-23 04:09:30	11.5
11	20053-05-01-02	1997-09-25 01:30:29	8.4
12	20053-05-01-03	1997-09-25 09:37:51	19.3
13	20053-05-02-00	1997-11-01 22:38:58	9.5
14	20053-05-02-01	1997-11-02 03:32:07	9.0
15	20053-05-02-02	1997-11-02 19:42:00	12.7
16	20053-05-02-03	1997-11-03 01:50:07	13.9
17	20053-05-02-04	1997-11-04 01:59:34	11.1
18	20053-05-02-05	1997-11-04 16:18:27	7.2
19	30040-04-01-00	1998-11-13 23:52:00	16.7
20	30040-04-01-01	1998-11-14 13:55:00	17.3
21	30040-04-01-02	1998-11-14 21:03:00	28.1
22	30040-04-01-03	1998-11-15 13:48:00	17.1
23	30040-04-01-04	1998-11-15 20:57:00	17.0
24	30040-04-01-05	1998-11-15 09:53:00	2.6

5.0–60 keV range) were obtained for all observations.

For all observations except observation 1, which had only 4 broad energy bands, and observation 22, for which technical problems with the data occurred, we computed power spectra in five broad energy bands (2–5.0, 5.0–6.4, 6.4–8.6, 8.6–13.0, 13.0–60 keV) with a Nyquist frequency of 256 Hz dividing the data in segments of 16 s length each. We also computed power spectra for all observations using 16 s data segments in one combined broad energy band ranging from 5.0–60 keV with a Nyquist frequency of 4096 Hz.

To characterize the properties of the low-frequency part (1/16–256 Hz) of the power spectrum we experimented with several fit functions (see Section 6.3) but finally settled on a fit function that consisted of the sum of a constant to represent the Poisson noise, one to four Lorentzians describing the QPOs, an exponentially cut–off power law component, $P \propto \nu^{-\alpha} exp(-\nu/\nu_{cut})$ to describe the low frequency noise (LFN), and a power law component to represent the very low frequency noise (VLFN) when the source was on the NB.

To describe the high frequency part (128 to 4096 Hz or 256 to 4096 Hz) of the power spectrum we used a fit function which consisted of the sum of a constant and a broad sinusoid to represent the dead–time modified Poisson noise (Zhang 1995), one or two Lorentzian peaks to represent the kHz QPOs, and sometimes a power law to fit the lowest frequency part ($<$ 150 Hz). The PCA setting concerning the very large event window (Zhang 1995; van der Klis et al. 1997) was set to 55 μs. Therefore, its effect on the Poisson noise was small and it could be incorporated into the broad sinusoid. The errors on the fit parameters were determined using $\Delta\chi^2$=1.0 (1σ single parameter). The 95% confidence upper limits were determined using $\Delta\chi^2$=2.71.

We used the Standard 2 data to compute hardnesses and intensities from the three detectors that were always active. Figure 6.1 shows three HIDs; one (A) for observations 1 and 9–18 combined (data set A), one (B) for observation 2–8 combined (data set B), and one (C) for observation 19–24 combined (data set C). The observations were subdivided in this way because the hard vertex, defined as the HB–NB intersection, is at higher intensities in data set C than in data set A. The hard vertex of data set B falls at an intermediate intensity level.

We assigned a value to each power spectrum according to the position of the source along the Z track using the S_Z parameterization (Dieters & van der Klis 2000; Wijnands et al. 1997b) applied to each HID separately. In this parametrization, the hard vertex (defined as the HB–NB intersection) is assigned the value S_Z = 1.0 and the soft vertex (defined as the NB–FB intersection) is assigned S_Z = 2.0. Thus, the distance between the hard and soft vertex defines the length scale along each branch. Since for HID C we only observed part of the Z track, we used the position of the soft vertex of HID A in HID C. From the fact that the soft vertex of the HID B was consistent with that from HID A, we conclude that the error introduced by this is small.

The shifts in the position of the hard vertex prevented us from selecting the power spectra according to their position in an HID of all data combined. We selected the power spectra according to the S_Z value in each of the three separate Z tracks, since Jonker et al. (1998) showed that for GX 340+0 the frequency

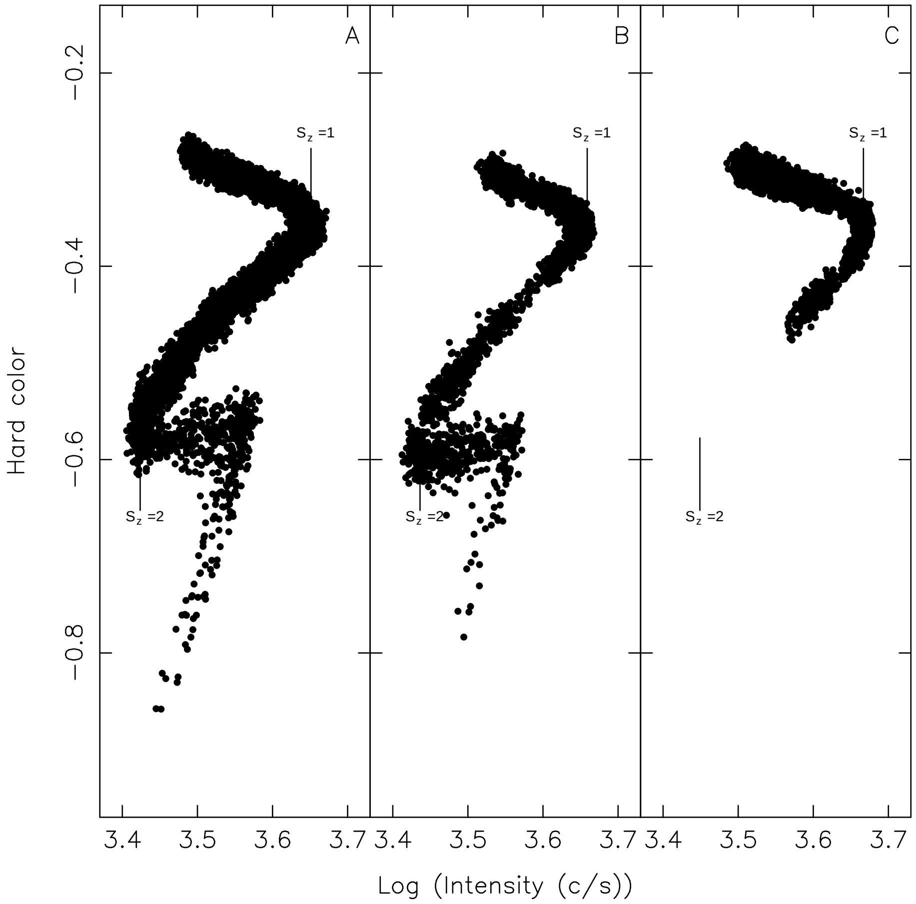

Figure 6.1: Hardness–intensity diagrams for observations 1 and 9–18 (A), 2–8 (B), and 19–24 (C) (see Table 6.1). The hard color is defined as the logarithm of the 9.7–16.0/6.4–9.7 keV count rate ratio. The intensity is defined as the three–detector count rate measured in the 2–16.0 keV band. The data were background subtracted but no dead–time correction was applied. The dead–time correction was less than 1.5%.

of the HBO is better correlated to the position of the source relative to the instantaneous Z track than to its position in terms of coordinates in the HID. The power spectra corresponding to each S_Z interval were averaged. However, employing this method yielded artificially broadened HBO peaks, and sometimes the HBO profile even displayed double peaks. The reason for this is that in a typical S_Z selection interval of 0.05 the dispersion in HBO frequencies well exceeds the statistical one, as shown in Figure 6.2. While the relation between S_Z and HBO

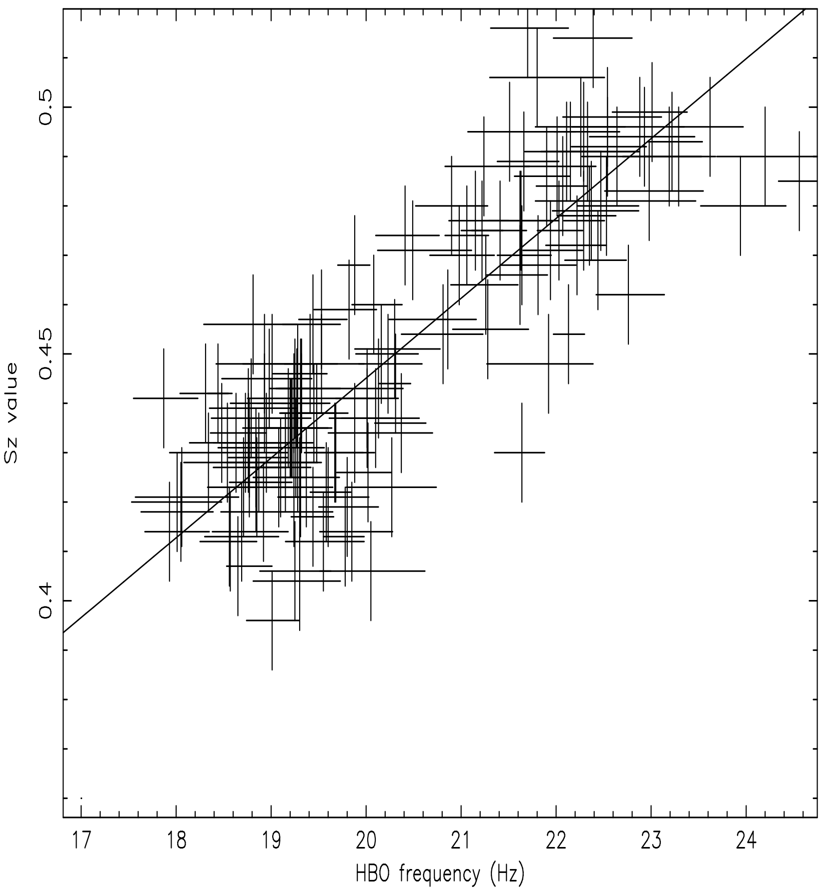

Figure 6.2: The S_z *value of ∼150 individual 16 s length power spectra from observation 1 plotted against their fitted HBO frequency. The line represents the best linear fit. The* χ^2_{red} *is 1.75 for 144 degrees of freedom, the linear-correlation coefficient is 0.83.*

frequency is roughly linear, the spread is large.

For this reason, when the HBO was detectable in the 5.0–60 keV power spectra, we selected those power spectra according to HBO frequency rather than on S_z value. In practice, this was possible for all data on the HB. To determine the energy dependence of the components, the 2–5.0, 5.0–6.4, 6.4–8.6, 8.6–13.0, 13.0–60 keV power spectra were selected according to the frequency of the HBO peak in the 2–60 keV power spectrum, when detectable.

The HBO frequency selection proceeded as follows. For each observation we constructed a dynamical power spectrum using the 5–60 keV or 2–60 keV data

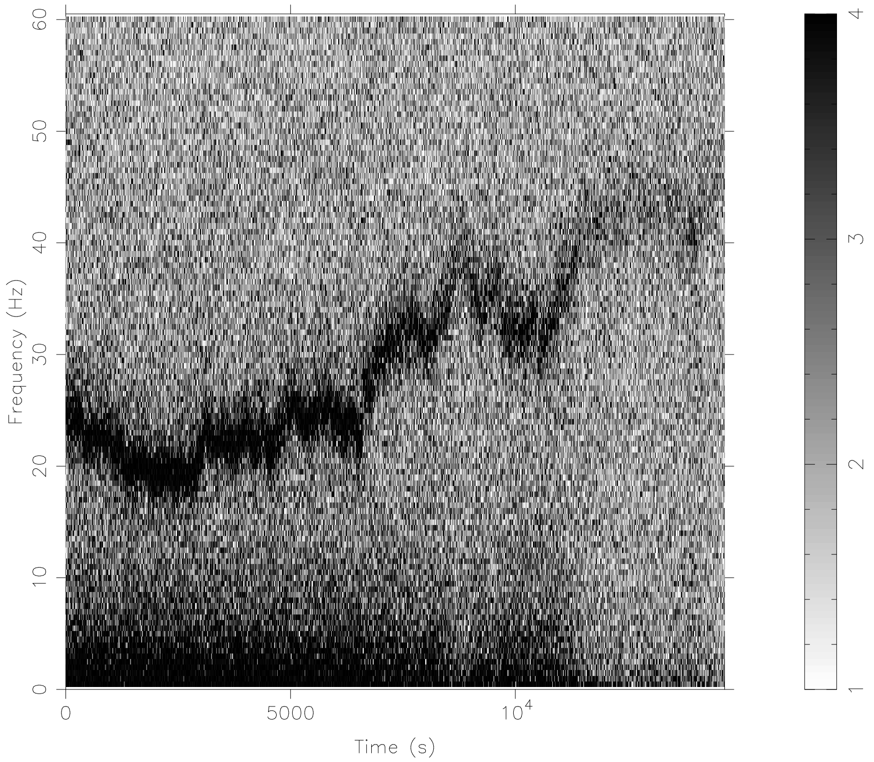

Figure 6.3: The dynamical power spectrum of part of observation 1 showing the 1/16–60 Hz range, with a frequency resolution of 0.5 Hz in the energy band 5–60 keV. The grey scale represents the Leahy normalized power (Leahy et al. 1983). Data gaps have been omitted for clarity. Clearly visible is the HBO at $\sim$ 18 *to* $\sim$ 50 *Hz and the LFN component at low (*$<$ 10 *Hz) frequencies.*

(see above), showing the time evolution of the power spectra (see Figure 6.3). Using this method, we were able to trace the HBO frequency in each observation as a function of time. We determined the maximum power in 0.5 Hz bins over a range of 2 Hz around the manually identified QPO frequency for each power spectrum, and adopted the frequency at which this maximum occurred as the HBO frequency in that power spectrum. This was done for each observation in which the HBO could be detected.

The 18–52 Hz frequency range over which the HBO was detected was divided in 16 selection bins with widths of 2 or 4 Hz, depending on the signal to noise level. For each selection interval the power spectra were averaged, and a mean S_Z value was determined.

The HBO selection criteria were applied to all data along the HB and near the hard vertex. When the source was near the hard vertex, on the NB, or the FB, we selected the power spectra according to the S_z value. An overlap between the two methods occurred for data near the hard vertex; both selection methods yielded the same results for the fit parameters to well within the statistical errors (see Section 6.3). Separately, for each set of observations (A,B, and C) we also determined the kHz QPO properties according to the S_z method.

6.3 Results

Using the fit function described by Jonker et al. (1998) which consisted of two Lorentzians to describe the HBO and the second harmonic of the HBO, and a cut-off power law to describe the LFN noise component, we obtained poor fits. Compared with Jonker et al. (1998) we combined more data, resulting in a higher signal to noise ratio. First we included a peaked noise component (called sub–HBO component) at frequencies below the HBO, since a similar component was found by van der Klis et al. (1997) in Sco X–1. This improved the χ^2_{red} of the fit. Remaining problems were that the frequency of the second harmonic was not equal to twice the HBO frequency (similar problems fitting the power spectra on the HB of Cyg X–2 were reported by Kuulkers et al. 1999), and the frequency of the sub–HBO component varied erratically along the HB. Inspecting the fit showed that both the fit to the high frequency tail of the HBO, and the fit to its second harmonic did not represent the data points very well. Including an additional component in the fit function representing the high frequency tail of the HBO (called shoulder component after Belloni et al. 1997 who used this name) resulted in a better fit to the HBO peak, a centroid frequency of the HBO second harmonic more nearly equal to twice the HBO frequency, and a more consistent behavior of the frequency of the sub–HBO component (which sometimes apparently fitted the shoulder when no shoulder component was present in the fit function).

We also experimented with several other fit function components to describe the average power spectra which were used by other authors to describe the power spectra of other LMXBs. Using a fit function built up out of a broken power law, to fit the LFN component, and several Lorentzians to fit the QPOs after Wijnands & van der Klis (1999a) results in significantly higher χ^2_{red} values than when the fit function described in Section 6.2 was used (χ^2_{red}= 1.66 for 205 degrees of freedom (d.o.f.) versus a χ^2_{red}= 1.28 with 204 d.o.f.). We also fitted the power spectra using the same fit function as described in Section 6.2 but with the frequency of the sub–HBO component fixed at 0 Hz, in order to test whether or not an extra LFN–like component centred around 0 Hz was a good representation of the extra sub–HBO component. Finally, we tested a fit function built up out of two cut–off power laws; one describing the LFN and one either describing the sub–HBO component or the shoulder component, and three Lorentzians, describing the HBO, its second harmonic, and either the sub–HBO or shoulder component when not fitted with the cut–off power law. But in all cases the χ^2_{red} values obtained using these fit functions were significantly higher (for the 24–26 Hz selection range values of 1.52 for 205 d.o.f., 1.62 for 204 d.o.f., and 2.00 for 205 d.o.f. were obtained, respectively).

Settling on the fit function already described in Section 6.2, we applied an F–test (Bevington & Robinson 1992) to the χ^2 of the fits with and without the extra Lorentzian components to test their significance. We derived a significance of more than 8 σ for the sub–HBO component, and a significance of more than 6.5 σ for the shoulder component, in the average selected power spectrum corresponding to HBO frequencies of 24 to 26 Hz. In Figure 6.4 we show the contribution of all the components used to obtain the best fit in this power spectrum.

The properties of all the components used in describing the low–frequency part of the average power spectra along the HB are given in Figure 6.5 as a function of S_z. When the HBO frequency was higher than 32 Hz, the sub-HBO and shoulder component were not significant. We therefore decided to exclude these two components from the fit function in the HBO frequency selections of 32 Hz and higher. When this affected the parameters determined for the remaining components in the fit function, we mention so. Splitting the total counts into different photon energies reduced the signal to noise in each energy band and therefore these effects were more important in the fits performed to determine the energy dependence of the parameters.

6.3.1 The LFN component

The fractional rms amplitude of the LFN decreased as a function of S_z (Fig 6.5 A), with values ranging from 10% to 2.2% (5.0–60 keV). Upper limits on the LFN component were calculated by fixing the power law index at 0.0. The power law index of the LFN component increased from ~ 0 at $S_z \sim 0.5$ to ~ 0.4 around S_z= 0.9; when the source moved on to the NB the index of the power law decreased to values slightly below 0.0 (Fig 6.5 B). The cut-off frequency of the LFN component increased as a function of S_z. For $S_z > 1.0$ the cut–off frequency could not be determined with high accuracy (Fig 6.5 C).

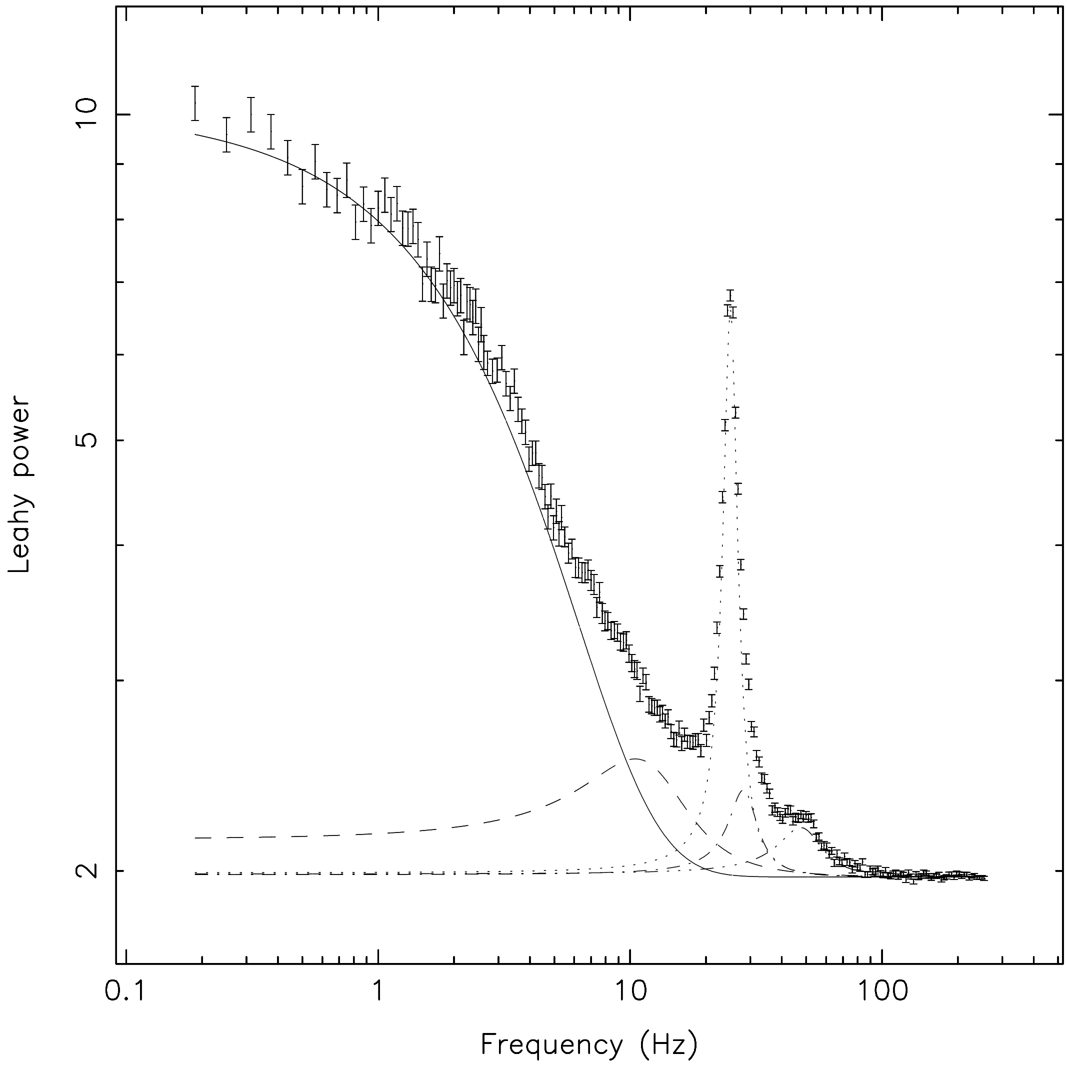

Figure 6.4: Leahy normalized power spectrum showing the different components used to fit the 5.0–60 keV power spectrum. The full line represents the LFN component, and the constant arising in the power spectrum due to the Poisson counting noise; the dashed line represents the sub–HBO component; the dotted line represents the HBO; the dashed–dotted line represents the shoulder component; and the dash–three dots–dash line represents the harmonic of the HBO.

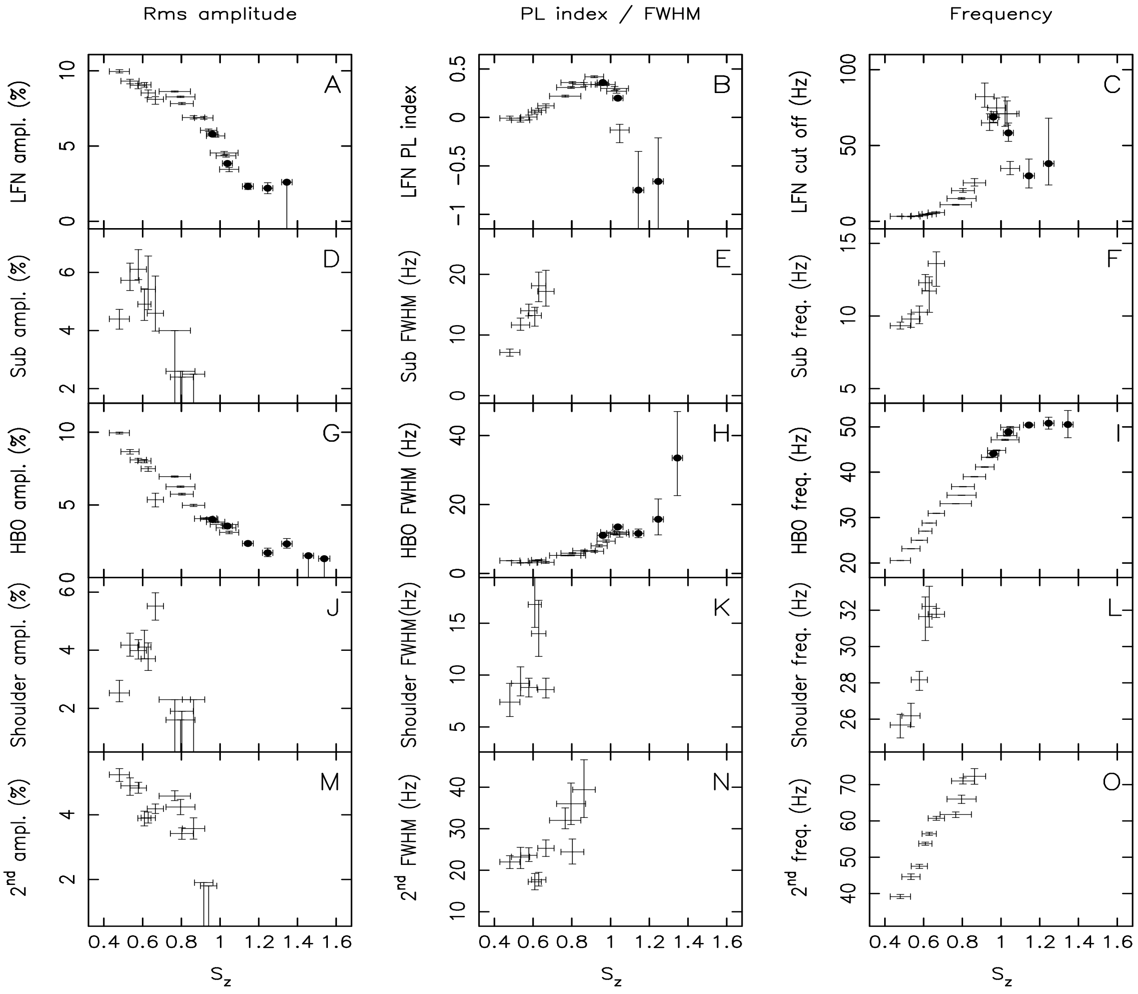

Figure 6.5: (A) Rms amplitude of the low–frequency noise (LFN); (B) power law index of the LFN; (C) cut–off frequency of the LFN; (D) rms amplitude of the noise component at frequencies below the HBO frequency (sub–HBO component); (E) FWHM of the sub–HBO component; (F) frequency of the sub–HBO component; (G) rms amplitude of the HBO; (H) FWHM of the HBO; (I) frequency of the HBO; (J) rms amplitude of the shoulder component used to describe the HBO; (K) FWHM of the shoulder component; (L) frequency of the shoulder component; (M) rms amplitude of the harmonic of the HBO; (N) FWHM of the harmonic; (O) frequency of the harmonic. The points represent data selected according to the HBO selection method and the bullets represent the data selected according to the $\mathrm{S_z}$ *selection method (parameters measured in the 5.0–60 keV band, see text). The two methods overlap starting around* $\mathrm{S_z} \sim$*1.0.*

The LFN fractional rms amplitude depended strongly on photon energy all across the selected frequency range. The rms amplitude increased from 5% at 2–5.0 keV to more than 15% at 13.0–60 keV (S_z=0.48). The power law index, α, of the LFN component was higher at lower photon energies (changing from 0.3–0.5 along the HB at 2–5.0 keV) than at higher photon energies (changing from -0.2–0.2 along the HB at 13.0–60 keV). The cut–off frequency of the LFN component did not change as a function of photon energy.

6.3.2 The HBO component

The fractional rms amplitude of the HBO decreased as a function of S_z (Fig 6.5 G), with values ranging from 10% to 1.7% over the detected range (5.0–60 keV). Upper limits on the HBO component were determined using a fixed FWHM of 15 Hz. The frequency of the HBO increased as a function of S_z but for $S_z > 1.0$ it was consistent with being constant around 50 Hz (Fig 6.5 I).

The ratio of the rms amplitudes of the LFN and the HBO component, of interest in beat frequency models (see Shibazaki & Lamb 1987) decreased from $\sim$1 at an S_z value of 0.48 to $\sim$ 0.6 at S_z values of 0.8–1.0. The ratio increased again to a value of $\sim$0.9 at S_z =1.05 when the source was on the NB.

The HBO rms amplitude depended strongly on photon energy all across the selected frequency range. The rms amplitude increased from 5% at 2–5.0 keV to $\sim$16% at 13.0–60 keV (at S_z=0.48) (see Figure 6.6 [dots] for the HBO energy dependence in the 26–28 Hz range). The increase in fractional rms amplitude of the HBO towards higher photon energies became less as the frequency of the HBO increased. At the highest HBO frequencies the HBO is relatively stronger in the 8.4–13.0 keV band than in the 13.0–60 keV band. The ratio between the fractional rms amplitude as a function of photon energy of the HBO at lower frequencies and the fractional rms amplitude as a function of photon energy of the HBO at higher frequencies is consistent with a straight line with a positive slope. The exact fit parameters depend on the HBO frequencies at which the ratios were taken. This behavior was also present in absolute rms amplitude ($\equiv$ fractional rms amplitude $*\, I_x$, where I_x is the count rate), see Figure 6.7. So, this behavior is caused by actual changes in the QPO spectrum, not by changes in the time–averaged spectrum by which the QPO spectrum is divided to calculate the fractional rms spectrum of the HBO. The FWHM and the frequency of the HBO were the same in each energy band.

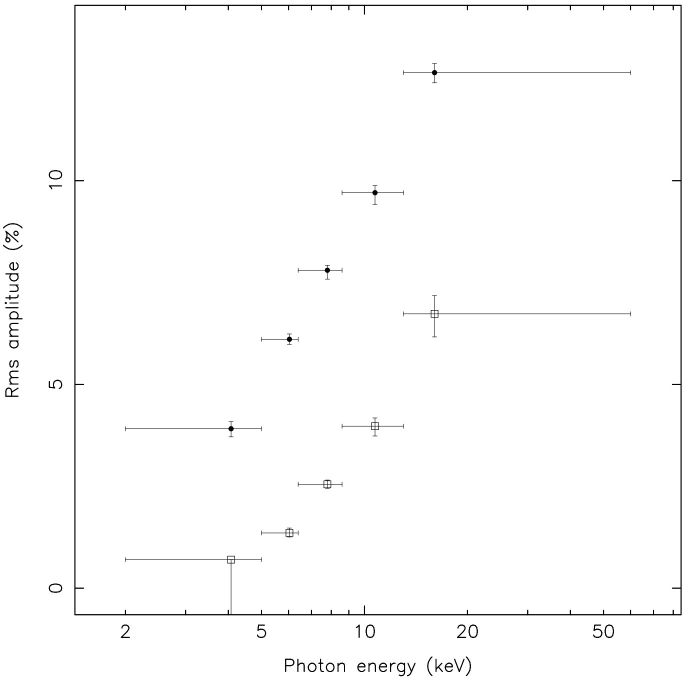

Figure 6.6: The figure shows the typical energy dependence of the rms amplitude of the HBO (bullets) and NBO (squares) as measured in the frequency range 26–28 Hz for the HBO, and as measured in the S_z *1.0–1.9 range for the NBO.*

6.3.3 The second harmonic of the HBO

The rms amplitude of the second harmonic of the HBO decreased as a function of S_z (Fig 6.5 M) from 5.2% to 3.6% (5.0–60 keV). Upper limits on the second harmonic of the HBO were derived using a fixed FWHM of 25 Hz. The frequency of the second harmonic of the HBO was consistent with being twice the HBO frequency when the sub-HBO and the shoulder component were strong enough to be measured (see Fig 6.5 O, and Figure 6.8). When these two extra components could not be determined significantly, due to the limited signal to noise, and we therefore omitted them from the fit function (as explained above), the frequency of the second harmonic of the HBO was clearly less than twice the HBO frequency (see Figure 6.8).

The rms amplitude of the second harmonic of the HBO was also energy dependent. Its rms amplitude increased from less than 4% in the 2–5.0 keV, to more than 9% in the 8.6–13 keV band. The FWHM of the second harmonic varied er-

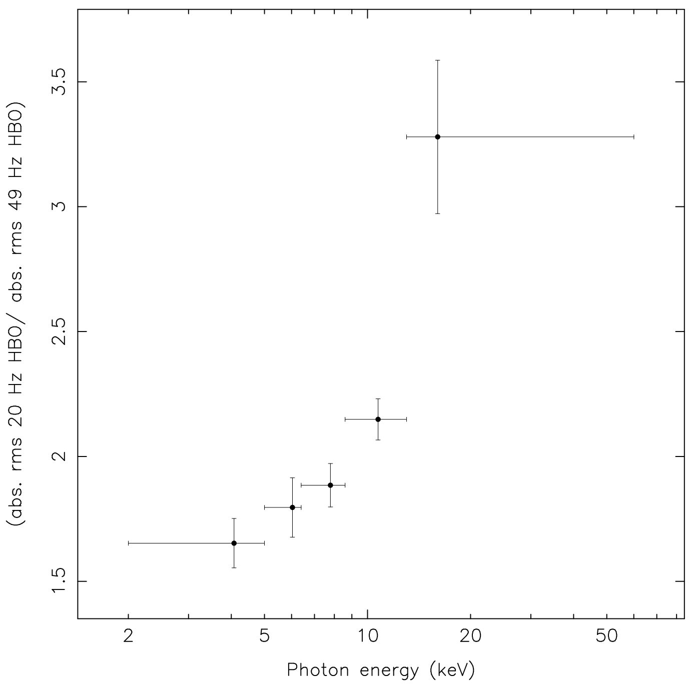

Figure 6.7: The absolute rms amplitude of the HBO at ∼20 Hz divided by the absolute rms amplitude of the HBO at ∼50 Hz as a function of the photon energy.

ratically in the range of 10–50 Hz. This is not necessarily a property of the second harmonic since the HBO shoulder component which was not significant by themselve was omitted from the fit function. This may have influenced the fit to the FWHM of the second harmonic when it was weak. Its frequency was consistent with being the same in each energy band.

6.3.4 The sub-HBO component

The centroid frequency (Fig 6.5 F) and FWHM (Fig 6.5 E) of the Lorentzian at sub–HBO frequencies increased from 9.3±0.3 Hz to 13.6±1.0 Hz and from 7.1±0.6 Hz to 18±3 Hz, respectively, as the source moved up the HB from S_Z = 0.48 to 0.67. The rms amplitude of this component did not show a clear relation with S_Z; its value was consistent with being constant around 5% (Fig 6.5 D). Upper limits on the sub–HBO component were determined using a fixed FWHM of 15 Hz. The frequency of the sub–HBO component is close to half the frequency of the HBO component. The fact that the ratio between the HBO frequency and

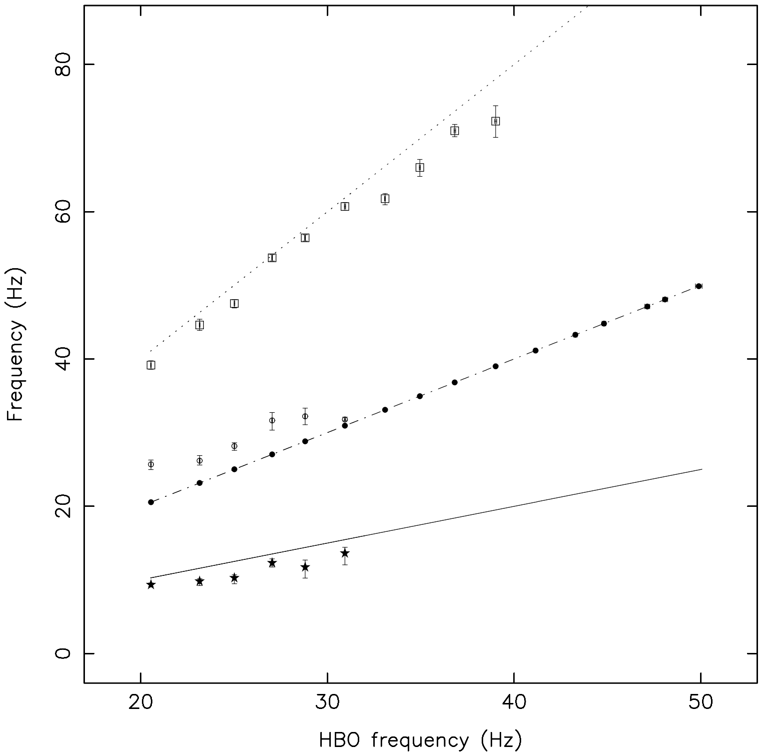

Figure 6.8: The frequencies of the four Lorentzian components used to describe the average 5.0–60 keV power spectra, as a function of the HBO frequency. Shown are from low frequencies to high frequencies; the sub–HBO component (stars), the HBO (bullets), the shoulder component (open circles), and the second harmonic of the HBO (squares). The solid line represents the relation $\nu = 0.5 * \nu_{HBO}$*, the dashed-dotted line represents* $\nu = 1.0 * \nu_{HBO}$*, and the dotted line represents* $\nu = 2.0 * \nu_{HBO}$*. Errors in the HBO frequency are in some cases smaller than the symbols.*

the sub–HBO frequency is not exactly 2 but ~ 2.2 may be accounted for by the complexity of the data and therefore its description.

We detected the sub–HBO component in the three highest energy bands that we defined over an S_z range from 0.48–0.65. Its rms amplitude is higher in the highest energy band (~7% in 13.0–60 keV, and less than 5% in 6.4–8.6 keV) and decreased as a function of S_z, while the FWHM and the frequency increased from 6–12 Hz, and 9–15 Hz, respectively.

6.3.5 The HBO shoulder component

At an S_z value of 0.48 (the left most part of the HB) the frequency of the shoulder component was higher than the frequency of the HBO, and the frequency separation between them was largest (Fig 6.5 L and Figure 6.8). Both the frequency of the shoulder and the HBO increased when the source moved along the HB, but the frequency difference decreased. The FWHM of the shoulder component increased from 7±2 Hz to 17±3 Hz and then decreased again to 8.6±1.0 Hz as the frequency of the HBO peak increased from 25.7±0.7 Hz to 30.9±0.4 Hz (Fig 6.5 K). From an S_z value of 0.61 to 0.67 the frequency was consistent with being constant at a value of 32 Hz. The rms amplitude was consistent with being constant around 4% (5.0–60 keV), over the total range where this component could be detected (Fig 6.5 J), but the data is also consistent with an increase of fractional rms amplitude with increasing HBO frequency. Upper limits on the HBO shoulder component were determined using a fixed FWHM of 7 Hz.

In the various energy bands the HBO shoulder component was detected seven times in total; once in the 2–5.0 keV band, three times in the 6.4–8.6 keV band, and three times in the in the 8.6–13.0 keV band, with rms amplitudes increasing from $\sim$3% in the 2–5.0 keV band to $\sim$6% in the 8.6–13.0 keV band, and a FWHM of $\sim$10 Hz. Upper limits of the order of 3%–4%, and of 5%–7% were derived in the two lowest and three highest energy bands considered, respectively. These are comparable with or higher than the rms amplitudes of this component determined in the 5–60 keV band.

6.3.6 The NBO component

The NBOs were not observed when the source was on the HB, with an upper limit of 0.5% just before the hard vertex (for an S_z value of 0.96). They were detected along the entire NB and they evolved into a broad noise component on the FB. The properties are listed in Table 6.2. The rms amplitude of the NBO gradually increased while the source moved from the upper NB to the middle part of the NB where the rms amplitude is highest. On the lower part of the NB the NBO rms amplitude gradually decreased. Upper limits on the NBO components were determined using a fixed FWHM of 5 Hz.

As the NBO got stronger towards the middle of the NB the profile of the NBO became detectably asymmetric (see Figure 6.9); between S_z=1.25 and 1.54 the NBO was fitted using two Lorentzians. The FWHM of the NBO as a function of the position along the NB was first decreasing from $\sim$10 Hz at S_z=1.038 to

Table 6.2: Properties of the NBO fitted using one or two Lorentzians, as a function of S_z *in the 5.0–60 keV band.*

	NBO			shoulder			Total	
S_z	ν_{NBO} (Hz)	FWHM (Hz)	Rms (%)	$\nu_{shoulder}$ (Hz)	FWHM (Hz)	Rms (%)	$\nu_{weighted}$ (Hz)	Total rms (%)
0.96 ± 0.03	8^a	5^a	< 0.5	–	–	–	–	–
1.04 ± 0.03	6.2 ± 0.4	10 ± 2	1.8 ± 0.2	8^a	5^a	< 1	–	–
1.14 ± 0.03	5.74 ± 0.07	6.3 ± 0.3	3.4 ± 0.1	8^a	5^a	< 2	–	–
1.25 ± 0.03	4.98 ± 0.07	2.2 ± 0.2	2.8 ± 0.3	6.7 ± 0.3	5.0 ± 0.4	3.1 ± 0.3	5.27 ± 0.07	4.2 ± 0.8
1.35 ± 0.03	5.40 ± 0.05	2.2 ± 0.2	4.1 ± 0.3	7.5 ± 0.7	5.4 ± 0.7	2.6 ± 0.4	5.74 ± 0.05	4.9 ± 1.0
1.46 ± 0.03	5.65 ± 0.05	2.5 ± 0.2	4.0 ± 0.2	8.4 ± 1.1	8.5 ± 1.7	2.5 ± 0.4	5.87 ± 0.05	4.7 ± 0.9
1.54 ± 0.03	5.67 ± 0.12	2.9 ± 0.5	3.3 ± 0.5	$7.5^{+1.4}_{-0.8}$	9^{+5}_{-2}	2.8 ± 0.6	5.83 ± 0.18	4.3 ± 1.6
1.65 ± 0.03	5.9 ± 0.2	5.3 ± 0.7	3.2 ± 0.1	8^a	5^a	< 2.3	–	–
1.75 ± 0.03	6.1 ± 0.3	5.2 ± 0.9	2.4 ± 0.2	–	–	–	–	–
1.85 ± 0.04	7.1 ± 0.8	6.7 ± 1.6	2.1 ± 0.2	–	–	–	–	–
1.95 ± 0.04	6.3 ± 0.9	5 ± 3	1.7 ± 0.3	–	–	–	–	–
2.05 ± 0.03	5.6 ± 1.4	12 ± 4	2.6 ± 0.4	–	–	–	–	–
2.15 ± 0.03	4^{+3}_{-10}	22^{+15}_{-8}	$3.2^{+1.6}_{-0.5}$	–	–	–	–	–

[a] Parameter fixed at this value

around 2.5 Hz on the middle part of the NB (S_z values from 1.25–1.54), and then increased again to ~ 5 Hz on the lowest part of the NB.

Due to the fact that the NBO profiles had to be fitted using two Lorentzians in part of the data, the behavior of the NBO frequency as a function of S_z is also not determined unambiguously. Therefore, we weighted the frequencies of these two Lorentzians according to one over the square of the FWHM. The FWHM weighted average of the two centroid frequencies of the two Lorentzians used to describe the NBO was consistent with a small increase as a function of S_z from 5.27 ± 0.07 Hz at S_z=1.25 to 5.83 ± 0.18 Hz at S_z=1.54.

We combined all power spectra with an S_z between 1.0 and 1.9 in order to investigate the energy dependence of the NBO. The rms amplitude of the NBO increased as of function of photon energy (see Figure 6.6 [squares]).

6.3.7 KHz QPOs

Using the HBO frequency selection method in all data combined, the frequency of the kHz QPO peaks increased from 197^{+26}_{-70} Hz to 565^{+9}_{-14} Hz and from 535^{+85}_{-48} Hz to 840 ± 21 Hz for the lower and upper peak, respectively, while the frequency of the HBO increased from 20.55 ± 0.02 Hz to 48.15 ± 0.08 Hz. Using the S_z selection method on the three data sets we defined in Section 6.2 (Figure 6.1),

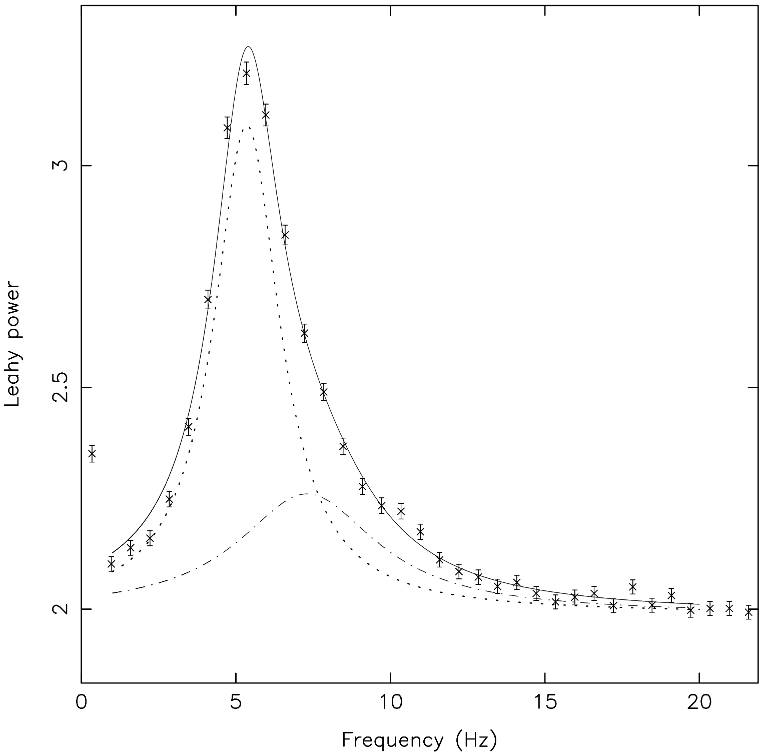

Figure 6.9: Typical Leahy normalized power spectrum on the NB showing the NBO in the energy band 5.0–60 keV (in the S_z *1.2–1.5 range). The asymmetry of the profile is clearly visible; the drawn line represents the best fit model, using two Lorentzian peaks. The dotted line and the dash-dotted line represent the two Lorentzians.*

we found that the relation between the kHz QPO and the HBO is consistent with being the same in all three data sets (Figure 6.10 upper panel). The same relation was found when we combined all data and selected the power spectra according to the HBO frequency.

Upper limits on the kHz QPOs were determined with the FWHM fixed at 150 Hz. When only one of the two kHz QPO peaks was detected the upper limit on the other peak was determined by fixing the frequency at the frequency of the detected peak plus or minus the mean difference frequency between the two peaks, depending on whether the lower or the upper peak was detected. The properties of the kHz QPOs as determined in all data combined when selected according to the HBO frequency are listed in Table 6.3.

The kHz QPO peak separation was consistent with being constant at 339±8

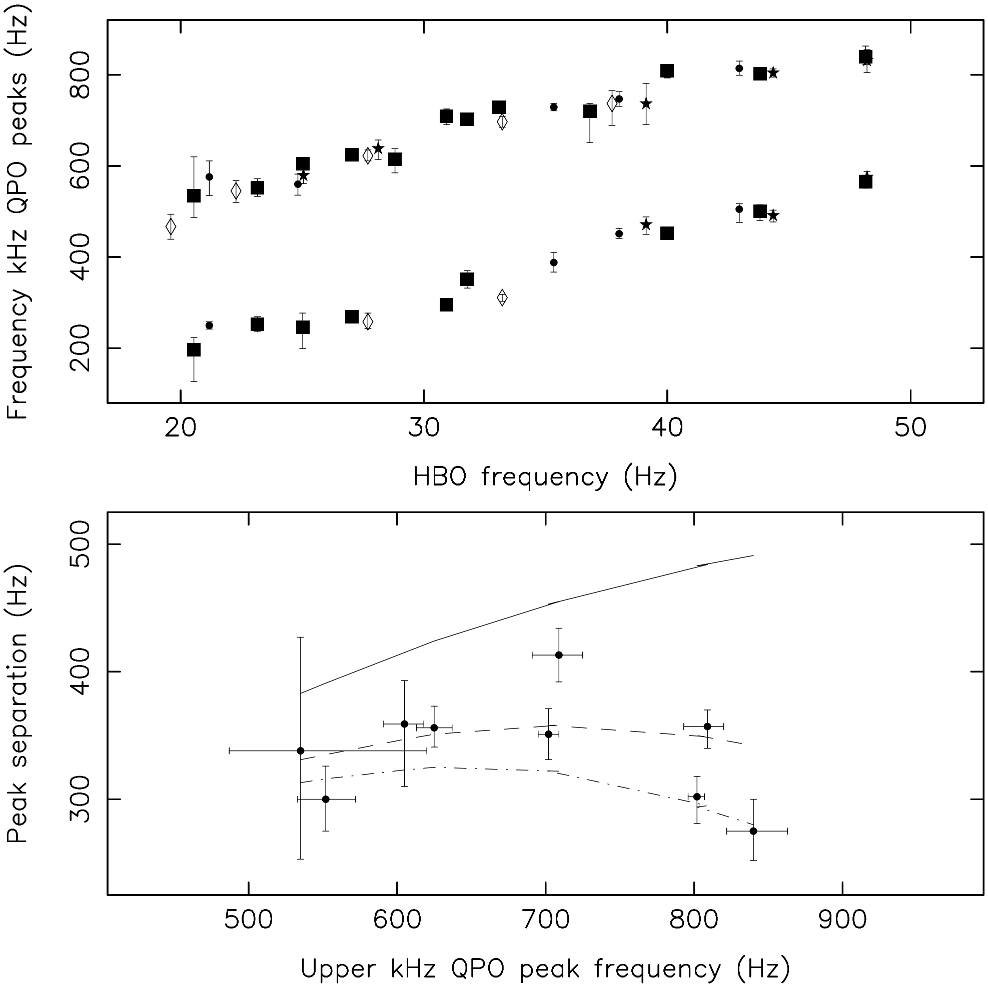

Figure 6.10: Upper panel: Relation between the lower and upper kHz QPO peak frequencies and the HBO frequency, as measured using all the data selected according to their HBO frequency in the 5–60 keV energy band (filled large squares), and using data from observations 1, and 9–18 combined (bullets; see Jonker et al. 1998), data from observations 2–8 combined (stars), and data from observations 19–25 combined (diamonds) selected according to the S_z *selection method. The error bars on the HBO frequency are small compared to the size of the data points, and are therefore omitted. Lower panel: The peak separation vs. upper kHz QPO frequency as measured when selected according to HBO frequency. The solid, dashed, and dash–dotted lines represent the predicted relations between the peak separation and the Keplerian frequency in the Stella & Vietri (1999) model for a neutron star mass of 1.4, 2.0, and 2.2* $M_\odot$*, respectively.*

Table 6.3: Properties of the kHz QPOs as determined in all 5.0–60 keV data combined, selected according to the HBO frequency.

ν_{HBO} (Hz)	Upper kHz ν (Hz)	FWHM upper peak (Hz)	Rms upper peak (%)	Lower kHz ν (Hz)	FWHM lower peak (Hz)	Rms lower peak (%)
20.55 ± 0.02	535^{+85}_{-48}	334^{+103}_{-172}	$4.2^{+0.8}_{-1.2}$	197^{+26}_{-70}	171^{+377}_{-94}	$3.1^{+3.7}_{-0.8}$
23.16 ± 0.02	552 ± 20	176 ± 43	3.3 ± 0.4	252 ± 17	125 ± 58	2.7 ± 0.5
25.02 ± 0.02	605 ± 14	170 ± 34	3.6 ± 0.4	246 ± 40	208^{+151}_{-85}	$2.8^{+1.0}_{-0.5}$
27.04 ± 0.02	625 ± 12	156 ± 36	3.3 ± 0.3	269 ± 11	63 ± 25	2.0 ± 0.3
28.81 ± 0.03	614 ± 27	229^{+118}_{-80}	3.1 ± 0.6	275^a	150^a	< 1.4
30.94 ± 0.04	709 ± 17	189 ± 50	3.4 ± 0.4	296 ± 12	100 ± 38	2.5 ± 0.4
31.8 ± 0.3	702 ± 7	83 ± 18	2.7 ± 0.2	351 ± 19	152^{+92}_{-52}	2.4 ± 0.5
33.09 ± 0.02	729 ± 13	119 ± 31	2.7 ± 0.3	390^a	150^a	< 2.4
36.82 ± 0.05	720^{+17}_{-69}	209^{+389}_{-71}	$3.5^{+2.7}_{-0.5}$	382^a	150^a	< 2.4
40.00 ± 0.06	809 ± 14	86 ± 49	$1.9^{+0.2}_{-0.4}$	452 ± 7	35 ± 27	1.2 ± 0.3
43.81 ± 0.07	802 ± 6	62^{+30}_{-18}	1.8 ± 0.3	500 ± 18	73 ± 31	1.3 ± 0.2
48.15 ± 0.08	840 ± 21	109 ± 61	1.2 ± 0.3	565 ± 12	69^{+46}_{-29}	1.1 ± 0.2

[a] Parameter fixed at this value

Hz over the observed kHz QPO range (Figure 6.10 lower panel), but a decrease towards higher upper peak frequencies similar to that found in Sco X–1 (van der Klis et al. 1997), 4U 1608–52 (Méndez et al. 1998), 4U 1735–44 (Ford et al. 1998b), 4U 1702–429 (Markwardt et al. 1999), and 4U 1728–34 (Méndez & van der Klis 1999) cannot be excluded. The FWHM of neither the lower nor the higher frequency kHz QPO peak showed a clear relation with frequency. The rms amplitude of the lower and upper kHz QPO peak decreased from 3.1% to 1.1%, and from 4.2% to 1.2%, respectively when the HBO frequency increased from 20.55 to 48.15 Hz.

6.4 Discussion

In the present work we combined all *RXTE* data presently available for the Z source GX 340+0 using our new selection method based on the frequency of the HBO peak. This allowed us to distinguish two new components in the low–frequency part of the power spectrum.

These two extra components were strongest when the source was at the lowest count rates on the HB (see Figure 6.1), between $S_Z = 0.48$–0.73, i.e., at the lowest inferred $\dot{M}$. The frequency of one of these components, the sub–HBO component, is close to half the frequency of the HBO component. The frequency ratio was consistent with being constant when the frequency of the sub–HBO changed from

9 to 14 Hz. A similar feature at sub–HBO frequencies has been reported by van der Klis et al. (1997) in Sco X–1. Since the frequency of this component is close to twice the predicted Lense–Thirring (LT) precession frequency for rapidly rotating neutron stars (Stella & Vietri 1998), we shall discuss the properties of this component within this framework.

The other component we discovered, the HBO shoulder component, was used to describe the strong excess in power in the HBO profile towards higher frequencies. If this shoulder component is related to the HBO and not to a completely different mechanism which by chance results in frequencies close to the frequency of the HBO, it can be used to constrain the formation models of the HBO peak. We demonstrated that both the HBO and the NBO have a similar asymmetric profile. In the NBO this was previously noted by Priedhorsky et al. (1986) in Sco X–1. We shall consider the hypothesis that the formation of this shoulder is a common feature of the two different QPO phenomena, even if the two peaks themselves perhaps occur due to completely different physical reasons.

Our results on the kHz QPOs based on more extensive data sets at three different epochs and using the new HBO selection method are consistent with those of Jonker et al. (1998). We discuss the properties of the kHz QPOs within the framework of precessing Keplerian flows (Stella & Vietri 1999), the sonic point model (Miller et al. 1998), and the transition layer model described by Osherovich & Titarchuk (1999), and Titarchuk et al. (1999).

6.4.1 Comparison with other observations

In various LMXBs, QPOs have been found whose profiles are clearly not symmetric. Belloni et al. (1997) showed that for the black hole candidate (BHC) GS 1124–68 the QPO profiles are asymmetric, with a high frequency shoulder. Dieters et al. (1998) reported that the 2.67 Hz QPO of the BHC 4U 1630–47 was also asymmetric with a high frequency shoulder. In the Z source Sco X–1 the NBO profile was also found to be asymmetric (Priedhorsky et al. 1986). It is clear that asymmetric shapes of the QPO profiles are frequently observed in LMXBs and are not restricted to either the black hole candidates or the neutron star systems.

In the BHCs GS 1124–68 (Belloni et al. 1997) and XTE J1550–564 (Homan et al. 2001) several QPOs were discovered which seem to be harmonically related in the same way as we report for GX 340+0, i.e. the third harmonic is not detected, while the first, the second and the fourth harmonic are. If this implies that these QPOs are the same, models involving the magnetic field of the neutron star for their origin could be ruled out. The time lag properties of the harmonic components of the QPOs in XTE J1550–564 are complex and quite distinctive (Wijnands et al. 1999a). In GX 340+0 no time lags of the harmonic components could be measured, but the time lags measured in the HBO in the similar Z source GX 5–1 (Vaughan et al. 1994) are quite different.

In order to study in more detail the relationship found by Wijnands & van der Klis (1999a) between the QPOs and the noise break frequency in the power spectrum of LMXBs, we fitted the LFN component using a broken power law. To determine the value for the break frequency we fixed the parameters of all other components to the values found when using a cut-off power law to describe the LFN. Wijnands & van der Klis (1999a) reported that the Z sources did not fall on the relation between the break and QPO frequency established by atoll sources and black hole candidates. They suggested that the Z source LFN is not similar to the atoll HFN but the noise component found in Sco X–1 at sub-HBO frequencies is. By using the centroid frequency of that peaked noise component as the break frequency instead of the LFN break frequency, the HBO frequencies did fall on the reported relation. On the other hand, we find that using the sub-HBO frequency instead of the HBO frequency together with the LFN break frequency, the Z source GX 340+0 also falls exactly on the relation. Therefore, the suggestion made by Wijnands & van der Klis (1999a) that the strong band–limited noise in atoll and Z sources have a different origin is only one of the two possible solutions to the observed discrepancy. Our proposed alternative solution is that the Z and atoll noise components are the same, but that it is the sub-HBO in Z sources which corresponds to the QPO in atoll sources. An argument in favour of the noise components in Z and atoll sources being the same is that the cut-off frequency of the LFN component increased as a function of S_Z, in a similar fashion as the frequency associated with the atoll high frequency noise (van der Klis 1995; Ford & van der Klis 1998; van Straaten et al. 2000).

Following Psaltis et al. (1999a) we plotted the sub–HBO frequency against the frequency of the lower–frequency kHz QPO. The sub–HBO does not fall on the relation found by Psaltis et al. (1999a) between the frequency of the HBO and the lower–frequency kHz QPO frequency. Instead the data points fall between the two branches defined by the HBO–like QPO frequencies vs. the lower kHz QPO frequency at high frequencies (see Psaltis et al. 1999a).

6.4.2 HBO – kHz QPO relations

Lense-Thirring precession frequency

Stella & Vietri (1998) recently considered the possibility that the HBO is formed due to the LT precession of the nodal points of sligthly tilted orbits in the inner accretion disk, but as they already mentioned the Z sources GX 5–1 and GX 17+2 did not seem to fit in this scheme. For reasonable values of I/M, the neutron star moment of inertia divided by its mass, the observed frequencies were larger by a factor of $\sim$2 than the predicted ones. Jonker et al. (1998) showed that for GX 340+0 the predicted frequency is too small by a factor of 3, if one assumes that the higher frequency peak of the kHz QPOs reflects the Keplerian frequency of matter in orbit around the neutron star, and that the mean peak separation reflects the neutron star spin frequency. Using the same assumptions Psaltis et al. (1999b) also concluded that a simple LT precession frequency model is unable to explain the formation of HBOs in Z sources.

Detailed calculations of Morsink & Stella (1999) even worsen the situation, since their calculations lower the predicted LT frequencies. They find that the LT precession frequencies are approximately a factor of two too low to explain the noise components at frequencies $\sim$20–35 Hz observed in atoll sources (4U 1735–44, Wijnands et al. 1998c; 4U 1728–34, Strohmayer et al. 1996; Ford & van der Klis 1998). Stella & Vietri (1998) already put forward the suggestion that a modulation can be produced at twice the LT precession frequency if the modulation is produced by the two points where the inclined orbit intersects the disk plane (although they initially used this for explaining the discrepancy of a factor of two between the predicted and the observed LT precession frequencies for the Z sources).

The sub–HBO peaked noise component we discovered could be harmonically related to the HBO component. If the sub–HBO is the second harmonic of the fundamental LT precession frequency, as needed to explain the frequencies in the framework of the LT precession model where the neutron star spin frequency is approximately equal to the frequency of the kHz QPO peak separation, the HBO must be the fourth and the harmonic of the HBO must be the eighth harmonic component, whereas the sixth and uneven harmonics must be much weaker. This poses strong (geometrical) constraints on the LT precession process. On the other hand, if the HBO frequency is twice the LT precession frequency, which implies a neutron star spin frequency of $\sim$900 Hz (see Morsink & Stella 1999), the frequency of the sub–HBO component is the LT precession frequency, and the frequency of the second harmonic of the HBO is four times the LT precession frequency. In that case only even harmonics and the LT precession frequency are observed.

Magnetospheric beat frequency and radial-flow models

In this section, we discuss our findings concerning the QPOs and the LFN component in terms of the magnetic beat frequency model where the QPOs are described by harmonic series (e.g. Shibazaki & Lamb 1987).

If the sub–HBO frequency is proven not to be harmonically related to the HBO, the sub–HBO peak might be explained as an effect of fluctuations entering the magnetospheric boundary layer periodically. Such an effect will be strongest at low HBO frequencies since its power density will be proportional to the power density of the LFN (Shibazaki & Lamb 1987). If it is the fundamental frequency and the HBO its first overtone then the magnetospheric beat frequency model proposed to explain the HBO formation (Alpar & Shaham 1985; Lamb et al. 1985) is not strongly constrained.

Within the beat frequency model the high frequency shoulder of the HBO peak can be explained as a sign of radial drift of the blobs as they spiral in after crossing the magnetospheric boundary layer. Shibazaki & Lamb (1987) describe another mechanism which may produce a high frequency shoulder. Interference between the LFN and the QPO caused by a non uniform phase distribution of the blobs will also cause the QPO to become asymmetric. This effect will be strongest when the LFN and the QPO components overlap, as observed. Finally, an asymmetric initial distribution of frequencies of the blobs when entering the magnetospheric boundary layer may also form an asymmetric HBO peak.

The changes in the power law index of the LFN as a function of photon energy can be explained by varying the width or the steepness of the lifetime distribution of the blobs entering the magnetic boundary layer (Shibazaki & Lamb 1987). The decrease in increase of both the fractional and absolute rms amplitude of the HBO as a function of energy towards higher frequencies (Figure 6.7) also constrains the detailed physical interactions occurring in the boundary layer.

Fortner et al. (1989) proposed that the NBO is caused by oscillations in the electron scattering optical depth at the critical Eddington mass accretion rate. How a high frequency shoulder can be produced within this model is not clear. Both the HBO and the NBO shoulder components were detected when the rms amplitude of the HBO and the NBO was highest. In case of the NBO, this may be a result of the higher signal to noise. Since the rms amplitude of the NBO shoulder component is consistent with being $\sim$2/3 of the NBO rms amplitude (see Table 6.2), combining more observations should increase the range over which this shoulder component is detected, if this ratio is constant along S_Z. In case of the HBO the two components seem to merge. While the fractional rms amplitude of the HBO shoulder component increased that of the HBO decreased. When the fractional rms amplitudes were comparable, the HBO was fitted with one Lorentzian. The rms amplitude of both shoulder components increased in a similar way as the rms amplitudes of the NBO and the HBO with photon energy. So, the formation of these shoulder components seems a common feature of both QPO forming mechanisms.

Radial oscillations in a viscous layer

In Sco X–1, Titarchuk et al. (1999) interpreted the extra noise component in the power spectra (van der Klis et al. 1997) as due to radial oscillations in a viscous boundary layer (Titarchuk & Osherovich 1999). If the noise component in Sco X–1 is the sub–HBO component in GX 340+0, the model of Titarchuk & Osherovich (1999) can be applied to the frequencies and dependencies we found for the sub–HBO component in GX 340+0. Fitting our data to the relation between the frequency of the extra noise component and the Keplerian frequency, using the parameters and parametrization given by Titarchuk et al. (1999), we obtained a value of $C_N = 15$ for GX 340+0. This value is much larger than the value obtained for Sco X–1 (9.76). According to Titarchuk & Osherovich (1999) a higher C_N value implies a higher viscosity for the same Reynold's number.

6.4.3 KHz QPOs and their peak separation

Recently, Stella & Vietri (1999) have put forward a model in which the formation of the lower kHz QPO is due to the relativistic periastron precession (apsidal motion) of matter in (near) Keplerian orbits. The frequency of the upper kHz QPO peaks is the Keplerian frequency of this material. The peak separation is then equal to the radial frequency of matter in a nearly circular Keplerian orbit, and is predicted to decrease as the Keplerian frequency increases and approaches the predicted frequency at the marginally stable circular orbit. This model can explain the decrease in peak separation as observed in various sources (see Section 6.3.7).

Beat frequency models stating that the upper kHz QPO peak is formed by Keplerian motion at a preferred radius in the disk (e.g. the sonic point radius, Miller et al. 1998), whereas the lower kHz QPO peak formed at the frequency of the beat between the neutron star spin frequency and this Keplerian frequency, cannot in their original form explain the decrease in peak separation in these two sources. A relatively small extension of the model (Lamb & Miller 2001) can, however, produce the observed decrease in peak separation.

Osherovich & Titarchuk (1999) developed a model in which the kHz QPOs arise due to radial oscillations of blobs of accreting material at the magnetospheric boundary. The lower kHz QPO frequency is in their model identified with the Keplerian frequency. Besides this QPO two eigenmodes are identified whose frequencies coincide with the upper kHz QPO peak frequency and the frequency of the HBO component in the power spectra of Sco X–1 (Titarchuk & Osherovich 1999). Interpreting our findings within this framework did not result in stringent constraints on the model.

We found that the peak separation is consistent with being constant (Figure 6.10 A and B), but neither a decrease towards higher $\dot{M}$ as in Sco X–1, 4U 1608–52, 4U 1735–44, 4U 1702–429, and 4U 1728–34 nor a decrease towards lower $\dot{M}$, as predicted by Stella & Vietri (1999) can be ruled out. If the model of Stella & Vietri turns out to be the right one the mass of the neutron star most likely is in the range of 1.8 to 2.2 $M_{\odot}$ (see Figure 6.10 B). This is in agreement with the mass of Cyg X–2 derived by Orosz & Kuulkers (1999), and with the masses of the neutron stars derived when interpreting the highest observed kHz QPO frequencies as due to motion at or near the marginally stable orbit (Kaaret et al. 1997; Zhang et al. 1997).

Acknowledgments This work was supported in part by the Netherlands Organization for Scientific Research (NWO) grant 614-51-002. This research has made use of data obtained through the High Energy Astrophysics Science Archive Research Center Online Service, provided by the NASA/Goddard Space Flight Center. This work was supported by NWO Spinoza grant 08-0 to E.P.J.van den Heuvel. MM is a fellow of the Consejo Nacional de Investigaciones Científicas y Técnicas de la República Argentina. Support for this work was provided by the NASA through the Chandra Postdoctoral Fellowship grant number PF9-10010 awarded by the Chandra X-ray Center, which is operated by the Smitsonian Astrophysical Observatory for NASA under contract NAS8-39073.

CHAPTER 6

Bibliography

Alpar, M. A. & Shaham, J. 1985, Nature, 316, 239
Belloni, T., van der Klis, M., Lewin, W. H. G., et al. 1997, A&A, 322, 857
Bevington, P. R. & Robinson, D. K. 1992, Data reduction and error analysis for the physical sciences (New York: McGraw-Hill, —c1992, 2nd ed.)
Boirin, L., Barret, D., Olive, J. F., Bloser, P. F., & Grindlay, J. E. 2000, A&A, 361, 121
Bradt, H. V., Rothschild, R. E., & Swank, J. H. 1993, A&AS, 97, 355
Chakrabarty, D. & Morgan, E. H. 1998, Nature, 394, 346
Di Salvo, T., Méndez, M., van der Klis, M., Ford, E., & Robba, N. R. 2001, ApJ, 546, 1107
Dieters, S., Belloni, T., Kuulkers, E., Harmon, A., & Sood, R. 1998, IAU Circ., 6823, 1+
Dieters, S. W. & van der Klis, M. 2000, MNRAS, 311, 201
Ford, E. C. & van der Klis, M. 1998, ApJ, 506, L39
Ford, E. C., van der Klis, M., & Kaaret, P. 1998a, ApJ, 498, L41
Ford, E. C., van der Klis, M., van Paradijs, J., et al. 1998b, ApJ, 508, L155
Fortner, B., Lamb, F. K., & Miller, G. S. 1989, Nature, 342, 775
Hasinger, G. & van der Klis, M. 1989, A&A, 225, 79
Homan, J., van der Klis, M., Wijnands, R., Vaughan, B., & Kuulkers, E. 1998, ApJ, 499, L41
Homan, J., Wijnands, R., van der Klis, M., et al. 2001, ApJS, 132, 377
Jahoda, K., Swank, J. H., Giles, A. B., et al. 1996, Proc. SPIE, 2808, 59
Jonker, P. G., Wijnands, R., van der Klis, M., et al. 1998, ApJ, 499, L191
Kaaret, P., Ford, E. C., & Chen, K. 1997, ApJ, 480, L27
Kuulkers, E. & van der Klis, M. 1996, A&A, 314, 567
Kuulkers, E., Wijnands, R., & van der Klis, M. 1999, MNRAS, 308, 485
Lamb, F. K. & Miller, M. C. 2001, ApJ, 554, 1210
Lamb, F. K., Shibazaki, N., Alpar, M. A., & Shaham, J. 1985, Nature, 317, 681
Markwardt, C. B., Strohmayer, T. E., & Swank, J. H. 1999, ApJ, 512, 125
Méndez, M. & van der Klis, M. 1999, ApJ, 517, L51
Méndez, M., van der Klis, M., Wijnands, R., et al. 1998, ApJ, 505, L23
Miller, M. C., Lamb, F. K., & Psaltis, D. 1998, ApJ, 508, 791
Morsink, S. M. & Stella, L. 1999, ApJ, 513, 827
Oosterbroek, T., van der Klis, M., Kuulkers, E., van Paradijs, J., & Lewin, W. H. G. 1995, A&A, 297, 141
Orosz, J. A. & Kuulkers, E. 1999, MNRAS, 305, 132
Osherovich, V. & Titarchuk, L. 1999, ApJ, 522, L113
Penninx, W., Lewin, W. H. G., Tan, J., et al. 1991, MNRAS, 249, 113
Priedhorsky, W., Hasinger, G., Lewin, W. H. G., et al. 1986, ApJ, 306, L91
Psaltis, D., Belloni, T., & van der Klis, M. 1999a, ApJ, 520, 262
Psaltis, D., Wijnands, R., Homan, J., et al. 1999b, ApJ, 520, 763
Revnivtsev, M., Borozdin, K., & Emelyanov, A. 1999, A&A, 344, L25
Shibazaki, N. & Lamb, F. K. 1987, ApJ, 318, 767
Shirey, R. E., Bradt, H. V., & Levine, A. M. 1999, ApJ, 517, 472
Stella, L. & Vietri, M. 1998, ApJ, 492, L59
—. 1999, Phys. Rev. Lett
Strohmayer, T. E., Zhang, W., Swank, J. H., et al. 1996, ApJ, 469, L9

Titarchuk, L. & Osherovich, V. 1999, ApJ, 518, L95
Titarchuk, L., Osherovich, V., & Kuznetsov, S. 1999, ApJ, 525, L129
van der Klis, M. 1994a, A&A, 283, 469
—. 1994b, ApJS, 92, 511
—. 1995, in X-ray binaries (Cambridge Astrophysics Series, Cambridge, MA: Cambridge Univ. Press, —c1995, edited by Lewin, Walter H.G.; Van Paradijs, Jan; Van den Heuvel, Edward P.J.), p. 252
van der Klis, M. 1998, in NATO ASIC Proc. 515: The Many Faces of Neutron Stars., 337
—. 2000, ARA&A, 38, 717
van der Klis, M., Swank, J. H., Zhang, W., et al. 1996, ApJ, 469, 1
van der Klis, M., Wijnands, R. A. D., Horne, K., & Chen, W. 1997, ApJ, 481, L97
van Paradijs, J., Hasinger, G., Lewin, W. H. G., et al. 1988, MNRAS, 231, 379
van Straaten, S., Ford, E. C., van der Klis, M., Méndez, M., & Kaaret, P. 2000, ApJ, 540, 1049
Vaughan, B., van der Klis, M., Lewin, W. H. G., et al. 1994, ApJ, 421, 738
Wijnands, R., Homan, J., & van der Klis, M. 1999a, ApJ, 526, 33
Wijnands, R., Homan, J., van der Klis, M., et al. 1998a, ApJ, 493, L87
—. 1997a, ApJ, 490, L157
Wijnands, R., Méndez, M., van der Klis, M., et al. 1998b, ApJ, 504, L35
Wijnands, R. & van der Klis, M. 1998, Nature, 394, 344
—. 1999a, ApJ, 514, 939
—. 1999b, ApJ, 522, 965
Wijnands, R., van der Klis, M., Méndez, M., et al. 1998c, ApJ, 495, L39
Wijnands, R., van der Klis, M., & Rijkhorst, E. 1999b, ApJ, 512, L39
Wijnands, R. A. D., van der Klis, M., Kuulkers, E., Asai, K., & Hasinger, G. 1997b, A&A, 323, 399
Zhang, W. 1995, XTE/PCA Internal Memo
Zhang, W., Strohmayer, T. E., & Swank, J. H. 1997, ApJ, 482, L167
—. 1998, ApJ, 500, L167

Chapter 7

Low and high frequency variability as a function of spectral properties in the bright X–ray binary GX 5–1

Peter G. Jonker, Michiel van der Klis, Jeroen Homan, Mariano Méndez, Walter Lewin, Rudy Wijnands, William Zhang

Submitted to Monthly Notices of the Royal Astronomical Society

Abstract

We report on a detailed analysis of data obtained over nearly four years with the *Rossi X–ray Timing Explorer* of the Z source GX 5–1. From a spectral analysis using a hardness–intensity diagram it was found that the source traced out the typical Z–shaped pattern. The study of the power spectral properties showed that when the source moved on the Horizontal Branch towards the Normal Branch the fractional rms amplitudes and timescales of all variability decreased, while their FWHMs increased. The frequency separation of the two kHz QPO peaks decreased from 344 ± 12 to 232 ± 13 while the frequency of the lower and upper kHz QPO increased from 172 ± 10 Hz to 608 ± 6 Hz and 516 ± 10 Hz to 840 ± 12 Hz, respectively. At low frequencies, besides the horizontal branch oscillation (HBO) and its second harmonic, two additional broad Lorentzian components were needed to obtain acceptable fits. These broad Lorentzians have Q–values of $\sim$1–2 and have frequencies 0.5 and 1.5 times the HBO frequency. When interpreted as being related to the HBO, they seem to favor disk models for the HBO

over the magnetic beat–frequency model. The frequency of the Normal Branch Oscillations changed slightly and non–monotonically while on the Normal Branch between ∼6 Hz at both ends and 5.25±0.05 Hz near the middle of the branch. It evolved into a flat–topped noise component on the Flaring Branch. We compared the timing properties of the some of the Z sources. We also compare the timing properties and color–color diagrams (CDs) of GX 5–1 with those of the back hole candidate XTE J1550–564 and the atoll source 4U 1608–52. The CDs are strikingly similar when a color scheme is used that is commonly employed in black hole studies. However, this is a degeneracy as the CDs turn out to be more complicated when colors common in neutron star studies are employed. Apart from some remarkable similarities between the CD of XTE J1550–564 and that of 4U 1608–52, several differences can be seen between these CDs and that of GX 5–1. Conclusions on spectral states or properties based solely on the use of CDs using the "black hole scheme" should be regarded with caution.

7.1 Introduction

Low–mass X–ray binaries (LMXBs) are systems where the compact object, either a neutron star or a black hole, accretes matter from a companion with a mass of less than 1 $M_\odot$. The neutron–star LMXB systems are subdivided on the basis of the pattern they trace out in an X–ray color–color or hardness–intensity diagram (CD or HID, respectively) in atoll and Z sources (Hasinger & van der Klis 1989). The X–ray flux measurements combined with the knowledge of the distance have shown that Z sources have a high luminosity (∼L_{Edd}) and accrete at a rate close to the Eddington accretion rate, whereas atoll sources have typical luminosities and inferred accretion rates 5–100 times lower (e.g. see the compilation of source luminosities by Ford et al. 2000). The three branches of the Z traced out in a CD or HID by Z sources are called (from top to bottom); Horizontal Branch, Normal Branch, and Flaring Branch.

Studies of the X–ray variability of Z sources revealed two types of quasi–periodic oscillations (QPOs) with frequencies less than 100 Hz (Horizontal Branch oscillations; HBO and Normal Branch oscillations; NBO), twin kHz QPO peaks, and three types of rapid flickering ("noise"), the very low–frequency noise (VLFN), the low–frequency noise (LFN), and the high–frequency noise (HFN) (see van der Klis 1995, 2000, for reviews). The properties of noise features and the HBOs, such as the central frequency and the fractional rms amplitude, are strongly correlated with the position of a source along the Horizontal Branch. These correlations, together with the observed increase in the ultra–violet flux in the Z source Sco X–1 (Vrtilek et al. 1991) when the source moves from the Horizontal Branch via the Normal Branch to the Flaring Branch lend support to the idea that the mass accretion rate increases from the Horizontal Branch via the Normal Branch to the Flaring Branch (see van der Klis 1995). However, recent observations (Wijnands et al. 1996; Di Salvo et al. 2000; Homan et al. 2001a), together with problems noted before (most notably secular motion of the Z track; Kuulkers et al. 1994) show that the situation may be more complex (e.g. van der Klis 2001).

KHz QPOs have now been seen in just over twenty LMXBs, including all Z sources (van der Klis 1998, 2000). Potentially they can provide a key to measure the basic properties of neutron stars (spin rates and perhaps magnetic field strengths, radii and masses) and thereby constrain the equation of state of ultra–dense matter, and to verify untested general relativistic effects by tracing space-time just above the neutron star surface (e.g. Kluzniak 1993; Miller et al. 1998; Kaaret et al. 1997; Zhang et al. 1997, 1998; Stella & Vietri 1998, 1999; Psaltis & Norman 2001). The discovery of kHz QPOs in GX 5–1 was reported by Wijnands et al. (1998). The HBOs were discovered by van der Klis et al. (1985), and the NBOs in GX 5–1 by Lewin et al. (1992). The source was also detected at radio (Braes et al. 1972) and infrared wavelengths (Jonker et al. 2000a).

In this paper we present an analysis of all *RXTE* observations of GX 5–1 obtained before 2001. We show for the first time the kHz QPO separation frequency is not constant in GX 5–1. We show that besides the two harmonically related low–frequency QPOs found previously on the Horizontal Branch, two additional harmonically related broad Lorentzian components are needed to obtain a good fit. We discuss the power spectra and color–color diagrams of the black hole candidate XTE J1550–564, the Z source GX 5–1, and the atoll source 4U 1608–52, and conclude that there are some remarkable similarities and differences which have not been appreciated in the past due to differences in analysis conventions between in particular neutron stars and black hole candidates.

7.2 Observations and analysis

GX 5–1 was observed 76 times in the period spanning July 27 1996 to March 3 2000 with the proportional counter array (PCA: Jahoda et al. 1996) on board the *Rossi X–ray Timing Explorer (RXTE)* satellite (Bradt et al. 1993). A log of the observations is presented in Table 7.1. The total observing time was $\sim$564 ksec. During $\sim$40% of the time only a subset of the 5 detectors was active. Two short

Table 7.1: Log of the observations of GX 5–1 used in this analysis.

Obs. No.	Observation ID	Date & Start time (UTC)	Amount of good data (ksec)	Obs. No.	Observation ID	Date & Start time (UTC)	Amount of good data (ksec)
1	10257-05-01-00	21-07-1996 23:42	∼ 0.14	39	30042-01-18-00	21-11-1998 22:35	∼ 12.0
2	10257-05-02-00	24-10-1996 20:02	Omitted	40	30042-01-19-00	22-11-1998 06:35	∼ 6.8
3	10061-02-01-00	02-11-1996 08:34	∼ 14.5	41	30042-01-20-00	22-11-1998 09:47	∼ 3.5
4	10063-01-01-00	03-11-1996 20:10	Omitted	42	40018-02-01-05	01-03-2000 14:26	∼ 1.0
5	10063-02-01-00	03-11-1996 20:30	∼ 10	43	40018-02-01-00	01-03-2000 23:29	∼ 26.0
6	10061-02-02-00	06-11-1996 21:19	∼ 14.8	44	40018-02-01-10	02-03-2000 04:29	∼ 2.3
7	10061-02-03-00	16-11-1996 00:55	∼ 15.4	45	40018-02-01-02	02-03-2000 06:16	∼ 5.5
8	20055-01-01-00	15-02-1997 08:32	∼ 4.8	46	40018-02-01-03	02-03-2000 12:14	∼ 2.6
9	20055-01-02-00	12-04-1997 19:00	∼ 4.8	47	40018-02-01-06	02-03-2000 14:05	∼ 1.9
10	20055-01-03-00	29-05-1997 19:18	∼ 5.3	48	40018-02-01-01	02-03-2000 15:28	∼ 2.7
11	20053-02-01-00	30-05-1997 09:28	∼ 17.6	49	40018-02-01-04	02-03-2000 17:11	∼ 14.6
12	20053-02-01-04	06-06-1997 00:28	∼ 5.2	50	40018-02-02-00	03-03-2000 00:00	∼ 7.6
13	20053-02-02-00	25-07-1997 05:19	∼ 9.2	51	40018-02-02-02	03-03-2000 07:24	∼ 13.9
14	20053-02-01-02	25-07-1997 11:43	∼ 13.1	52	40018-02-02-10	03-03-2000 13:48	∼ 2.7
15	20053-02-01-03	25-07-1997 18:23	∼ 5.2	53	40018-02-02-03	03-03-2000 23:23	∼ 26.0
16	20053-02-01-01	25-07-1997 21:41	∼ 8.3	54	40018-02-02-04	04-03-2000 05:56	∼ 17.0
17	20055-01-04-00	28-07-1997 18:21	∼ 4.8	55	40018-02-02-05	04-03-2000 13:51	∼ 2.3
18	20055-01-05-00	21-09-1997 12:29	∼ 4.6	56	40018-02-02-12	04-03-2000 15:37	∼ 1.6
19	30042-01-01-00	22-08-1998 10:36	∼ 11.3	57	40018-02-02-21	05-03-2000 00:57	∼ 23.1
20	30042-01-02-00	14-09-1998 00:25	∼ 2.8	58	40018-02-02-14	05-03-2000 04:14	∼ 2.7
21	30042-01-03-00	25-09-1998 03:28	∼ 9.6	59	40018-02-02-01	05-03-2000 06:07	∼ 2.4
22	30042-01-04-00	08-10-1998 08:18	∼ 4.6	60	40018-02-02-20	05-03-2000 12:02	∼ 2.4
23	30042-01-02-01	09-10-1998 03:30	∼ 5.7	61	40018-02-02-06	05-03-2000 13:43	∼ 2.3
24	30042-01-05-00	14-10-1998 00:17	∼ 10.5	62	40018-02-02-08	05-03-2000 15:19	∼ 2.4
25	30042-01-06-00	26-10-1998 04:58	∼ 9.7	63	40018-02-02-13	05-03-2000 16:58	∼ 14.8
26	30042-01-07-00	30-10-1998 05:23	∼ 5.9	64	40018-02-02-07	06-03-2000 00:57	∼ 1.9
27	30042-01-08-01	02-11-1998 06:34	∼ 3.0	65	40018-02-02-17	06-03-2000 02:33	∼ 3.5
28	30042-01-08-00	03-11-1998 03:18	∼ 11.9	66	40018-02-02-22	06-03-2000 04:09	∼ 3.4
29	30042-01-09-00	04-11-1998 05:01	∼ 6.1	67	40018-02-02-15	06-03-2000 05:45	∼ 3.5
30	30042-01-10-00	08-11-1998 06:36	∼ 2.7	68	40018-02-02-11	06-03-2000 07:17	∼ 3.7
31	30042-01-11-01	08-11-1998 10:01	∼ 1.3	69	40018-02-02-23	06-03-2000 09:07	∼ 2.7
32	30042-01-11-00	09-11-1998 06:38	∼ 8.6	70	40018-02-01-07	06-03-2000 10:30	∼ 1.9
33	30042-01-12-00	10-11-1998 00:07	∼ 10.3	71	40018-02-02-16	06-03-2000 13:40	∼ 2.2
34	30042-01-13-00	10-11-1998 06:40	∼ 11.2	72	40018-02-01-08	06-03-2000 15:16	∼ 2.2
35	30042-01-14-00	11-11-1998 03:16	∼ 10.4	73	40018-02-02-09	06-03-2000 16:52	∼ 14.9
36	30042-01-15-00	20-11-1998 16:10	∼ 5.4	74	40018-02-02-18	07-03-2000 00:53	∼ 7.2
37	30042-01-16-00	21-11-1998 00:10	∼ 23.4	75	40018-02-02-24	07-03-2000 04:04	∼ 3.6
38	30042-01-17-00	21-11-1998 11:47	∼ 13.9	76	40018-02-02-19	07-03-2000 05:38	∼ 11.1

observations (2 and 4) were omitted from our analysis due to data overflows. Data were always obtained in a mode providing 16 s time–resolution and a high spectral resolution (129 channels covering the effective 2–60 keV range; the Standard 2 mode). In addition, a variety of high time–resolution modes was used in the various observing campaigns; for all observations data with a time resolution of at least 2^{-11} s were obtained in the energy band spanning 2–60 keV.

From the Standard 2 data we computed HIDs. We only used data obtained with the two detectors (proportional counter units 0 and 2) that were always operational since each detector has a slightly different energy response. The hardness, or hard color, and intensity are defined as the logarithm of the 10.2–17.5 / 6.5–10.2 keV count rate ratio and as the count rate in the 2.5–17.5 keV band of a 16 s average, respectively (RXTE energy channels 25–44 / 14–24 and 3–44, respectively). The high voltage setting of the PCA detectors was changed on March

22 1999 (i.e., the gain changed). Combined with the finite energy resolution this forced us to use somewhat different energy boundaries in our computation of the HID for data obtained after March 22 1999 (i.e., 10.1–17.6 keV / 6.6–10.1 keV for the hard color and 2.6–17.6 keV for the intensity for observations 42–76. We used RXTE energy channels 20–36 / 11–19 and 2–36, respectively). Besides the gain change the energy response of the detectors changed slowly with time. These various changes have been partially corrected for using the Crab pulsar as a reference, under the assumption that the spectrum of the Crab pulsar does not vary. This correction is only perfect if the spectral shape of GX 5–1 is equal to that of the Crab (the steps involved in this correction were outlined in Di Salvo et al. 2001 and Jonker et al. 2001). So, a small systematic error is introduced both by the correction for the drift in detector response and the slightly different energy boundaries which we used as a result of the gain change. Together with the secular variation of the source (see e.g. Kuulkers et al. 1996) this led us to compute 5 separate HIDs combining observations 1–7, 8–18, 19–26, 27–41, 42–76 (see Figure 7.1 *left panel*; Table 7.1).

In Figure 7.1 (*right panel*) the 5 HIDs are overplotted. The source was found on the Horizontal Branch, Normal Branch, and Flaring Branch in four of the five HIDs; for the HID of observations 42–76 the source was not found on the Horizontal Branch. The Z tracks were parameterized by fitting a spline through manually selected points along the track in each of the 5 HIDs separately. The position of the source along the track is characterized by a parameter called S_z representing curve length along the track (see Hasinger et al. 1990; Hertz et al. 1992). The S_z values are determined using the logarithm of the colors and count rate (Wijnands et al. 1997b) and normalized by assigning the hard vertex (the Horizontal Branch–Normal Branch junction) the value ‘1’ and setting the soft vertex (the Normal Branch–Flaring Branch junction) to ‘2’. We applied this parameterization to the HID obtained from each of the subsets. The track traced out by the source during observations 42–76 only covers part of the Z. In order to calculate the S_z values along this track we assumed that the hard vertex in that data set was at the same position relative to the soft vertex as in the HID of observations 27–41.

Using the high time–resolution data we calculated power–density spectra (2–60 keV) of data stretches of 16 s, up to a Nyquist frequency of 2048 Hz, using a Fast Fourier Transformation algorithm. The power spectra were normalized to fractional rms amplitude squared per Hz, added, and averaged according to their position along the Z track (the selection method will be described in detail below). Due to the relatively low amplitude of the variability in the high frequency part of the power spectrum, simultaneous fits of the entire frequency range would not

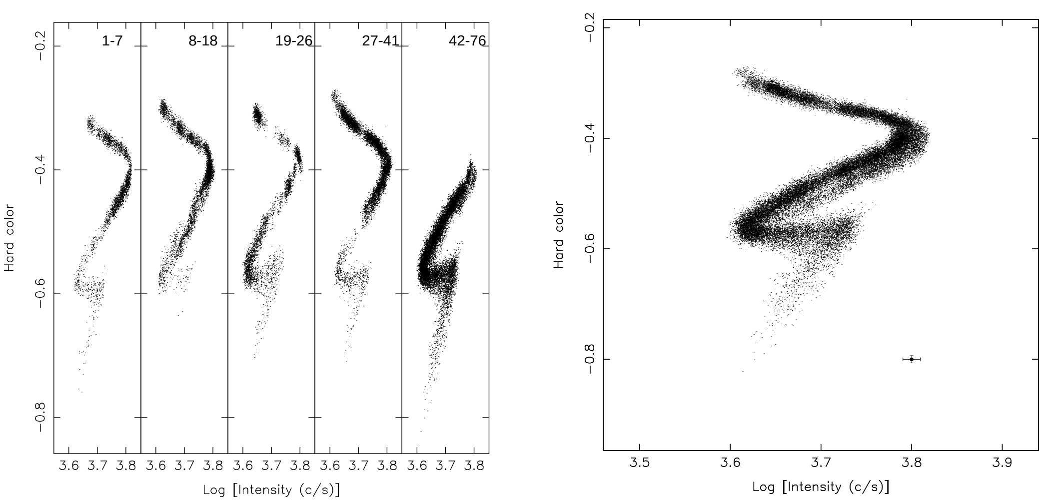

Figure 7.1: Left panel: Hardness–intensity diagrams for observations 1–7, 8–18, 19–26, 27–41, 42–76. Right panel: Hardness–intensity diagram of all observations combined. The hard color is the logarithm of the 10.2–17.5/6.5–10.2 keV count rate ratio for observations 1–41 and that of the 10.1–17.6 / 6.6–10.1 keV count rate ratio for observations 42–76. The intensity is the 2.5-17.5 keV (observations 1–41), and the 2.6–17.6 keV (observations 42–76) count rate. The data were background–subtracted and corrected for changes in the energy response of the PCA detectors (see text), but no deadtime corrections were applied (the deadtime correction is <4%). Typical error bars (not including systematic errors) are shown at the bottom right of the figure in the right panel.

constrain the properties of the high frequency part. Therefore, we fitted the low (1/16–128 Hz) and high (~128–2048 Hz) frequency part of the power spectra separately. The low–frequency part of the average power spectra was fit with a function consisting of an exponentially cut–off power law to describe the noise at low frequencies (LFN) and at most five Lorentzians to fit the QPOs. The component arising in the power spectrum due to the Poisson counting noise was subtracted. For values of $S_Z > 1.0$ a power law was added to the fit function to fit the very low–frequency noise (VLFN). The function used to describe the high–frequency part of the average power spectrum was built up out of two Lorentzians describing the kHz QPOs. Contrary to when we fit the low–frequency part, the continuum due to Poisson noise was not subtracted prior to fitting, therefore we included a constant to account for this Poisson noise. Sometimes also a power law component was added to account for the slope of the underlying continuum, caused by the high frequency tail of one of the low–frequency components. The high frequency tail did not systematically influence our fit–parameters.

From previous studies of GX 5–1 and other Z sources it is known that the frequency of the QPOs on the Horizontal Branch (the HBOs and the kHz QPOs) increases with S_z (Wijnands et al. 1998; Dieters & van der Klis 2000; Jonker et al. 2000b; Homan et al. 2001a). For all but the HID of observations 42–76 (when the source was not found on the Horizontal Branch or the upper part of the Normal Branch and therefore no HBOs were present in the power spectra; see Figure 7.1 *left panel*) we studied the relation between S_z and HBO frequency. These relations, plotted in Figure 7.2, have two notable properties. First, the relation found for observations 27–41 is clearly offset from the other relations. This is an effect of secular motion of the source during the gap in between the observations 27–35 and 36–41. During the first 9 observations (27–35) the source was found on the Horizontal Branch, whilst, after a 9 day gap, during observations 36–41 the source traced a part of the Horizontal Branch close to the Normal Branch, the Normal Branch, and the Flaring Branch. We checked the vertices of the 5 HIDs to search for additional evidence of secular motion but in view of the uncertainties involved in their manual selection, we conclude that the vertices of the 5 HIDs were not significantly different. The second notable property involves the jump in HBO frequency near $S_z \sim 1$ (see also plots in Wijnands et al. 1998). To investigate the nature of the jump further we plotted the hard color vs. the frequency of the HBO. A discontinuity in the rate of change in frequency as a function of hard color was also observed in the hard color vs. frequency plot at a frequency of ~50 Hz. Therefore, the jump in frequency when plotted vs. S_z is not an artefact of the S_z parameterization. We investigated whether a similar jump was present in the frequencies of the kHz QPOs, but we lacked the signal–to–noise to conclude on this.

In order to combine all power spectra with similar HBO frequencies, we shifted all S_z–HBO frequency relations to one "parent" relation. To this end, we fitted a polynome to the relation between S_z and HBO frequency for each of the HIDs separately. We included only measurements for $S_z < 1.0$ in the fit. The order of the polynome was determined such that the reduced χ^2 of the fit was ~1. The parent relation for $S_z < 1.0$ is the best linear fit to the S_z–HBO frequency relation for all the HIDs combined ($\nu_{HBO} = 9.9 + 36.8 \times S_{z,parent}$; the drawn line in Figure 7.2). The shifting procedure works as follows: given the S_z value ($S_{z,\mathrm{initial}}$) obtained from the HID corresponding to the observation the power spectrum is calculated from, the HBO will have a certain predicted frequency which follows from the S_z–HBO frequency relation found for that HID. That predicted HBO frequency corresponds, given the S_z–HBO frequency parent relation, to a $S_{z,\mathrm{parent}}$.

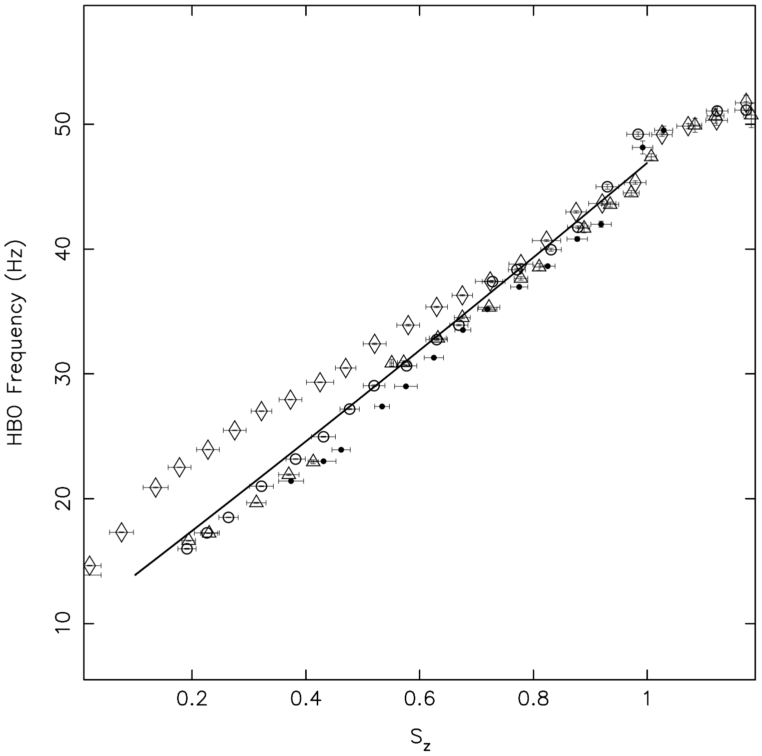

Figure 7.2: The S_z–HBO frequency relation measured for four different HIDs. The S_z–HBO frequency relation found for the HID of the observations 27–41 (diamonds) is clearly offset with respect to the relations found for the other HIDs (dots represent observations 1–7, open circles observations 8–18, and triangles observations 19–26). The drawn line is the parent relation to which all the relations are scaled (see text). Error bars are shown for each measurement; the error on the HBO frequency is in most cases smaller than the size of the symbols.

This $S_{z,\mathrm{parent}}$ is then assigned to the power spectrum instead of $S_{z,\mathrm{initial}}$ (the change of S_z corresponds to a horizontal shift in Figure 7.2). This shifting procedure was done for each 16 s power spectrum separately. Finally, all power spectra were selected according to their $S_{z,\mathrm{parent}}$ values for $S_z < 1.0$; the selection bin width was 0.1. For $S_z > 1.0$ the unshifted values obtained from each separate HID were used in the selection, since both the secular motion and the effects of the changes in the response move the Z track in a direction nearly perpendicular to the Normal Branch. Here the selected bin width was 0.05. The selected power spectra were averaged and fitted with the function described above.

The errors on the fit parameters were determined using $\Delta\chi^2 = 1.0$ (1σ, single parameter). The error on S_z is the standard deviation of the distribution of S_z values in one selection bin. In cases where components were not significantly detected, 95% confidence upper limits were determined using $\Delta\chi^2 = 2.71$. The full–width at half maximum (FWHM) of the Lorentzians was fixed at 10 Hz in case an upper limit was determined to the sub–HBO, its third harmonic or the second harmonic of the HBO, and at 30 Hz in case of the first harmonic (which is the fundamental) of the HBO. The frequency of the component for which an upper limit was determined was not fixed but restricted to a range of values around that expected on the basis of the observed trends. Upper limits to the presence of kHz QPOs were determined using a FWHM of 75 Hz.

7.3 Results

7.3.1 Spectral states

The source was found on the Horizontal Branch, Normal Branch and Flaring Branch. Note the clear "Dipping Flaring Branch" trailing the Flaring Branch (see Figure 7.1, see also Kuulkers et al. 1994). GX 5–1 was found to reside most often on the Normal Branch during the time of our observations (see Figure 7.3, *upper panel*). The average velocity along the Z track (defined as the average of $V_z(i) = \frac{S_z(i+1)-S_z(i-1)}{T(i+1)-T(i-1)}$; Wijnands et al. 1997b; Figure 7.3, *lower panel*) was approximately constant for $0.1 < S_z < 1$ but gradually increased for $S_z > 1$, i.e., in anti–correlation with the time the source spent in each part of the Z diagram, although the product of the two is not exactly constant. Note that the average velocity along the Z track also increased towards the lowest S_z values.

7.3.2 Low–frequency power spectra

We found two new components in the averaged power spectrum of GX 5–1. One of these components was located at frequencies consistent with half the frequency of the HBO, the so–called sub–HBO. This component was reported before in the Z sources Sco X–1, GX 340+0, and GX 17+2 with RXTE (Wijnands & van der Klis 1999; Jonker et al. 2000b; Homan et al. 2001a). The second new component has a frequency which is consistent with three times the frequency of the sub–HBO (or 1.5 times the frequency of the HBO; see Figure 7.4). Fitting the average

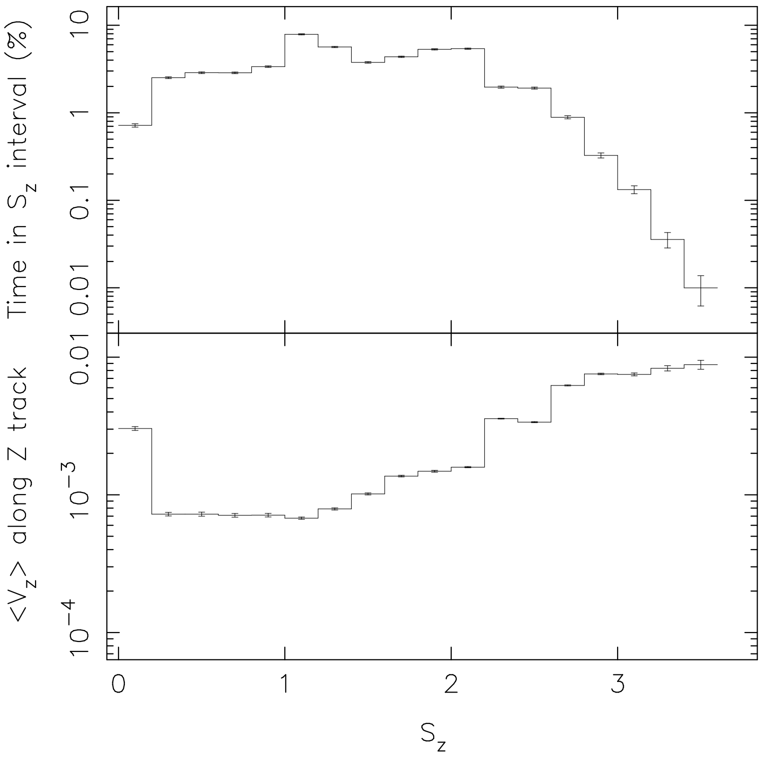

Figure 7.3: Upper panel: Percentage of the total observing time spent in each S_z interval as a function of the S_z value. During our observations the source spent most of the time on the Normal Branch (S_z values between 1 and 2). Lower panel: The average velocity (see text) of the source along the Z track. The average velocity was approximately constant for $S_z < 1$ (except towards the lowest S_z values where it increased) but steadily increased for $S_z > 1$.

low–frequency (1/16–256 Hz) power spectrum of $S_z = 0.60 \pm 0.03$ with a function consisting of a cut–off power law (LFN), and three Lorentzians (sub–HBO, HBO, and 2nd harmonic of the HBO) a χ^2 of 383 for 209 degrees of freedom was obtained. Adding a fourth Lorentzian component at frequencies ~3 times the frequency of the sub–HBO gave a χ^2 of 314 for 206 degrees of freedom. An F–test (Bevington & Robinson 1992) to the χ^2 of the fits with and without the fourth Lorentzian revealed that the probability that the reduction in χ^2 could be achieved by a random process is 6.5×10^{-8}, i.e., the significance of the addition of the fourth Lorentzian component is $\sim 6\sigma$. For the other power spectra where this component was found a similar value was obtained. Although this component is too broad to qualify formally as a QPO (since the Q–value is less than 2; see Table 7.2 and Figure 7.4, *right panel*), for now we refer to this component as the third harmonic to the sub–HBO component (see Figure 7.4). This classification is rendered strong support by the fact that the Q–values of both the sub–HBO and its third harmonic are consistent with being the same (Figure 7.4; *right panel*).

Besides the two new components, the HBO, its second harmonic and the LFN were also detected (see Table 7.2, 7.3). A typical fit ($S_z = 0.60 \pm 0.03$) showing the contributions of the individual components is presented in Figure 7.5. In four of the S_z selections the HBO was fit with two Lorentzian peaks in order to obtain a good fit (see Table 7.2). This is either related to the fact that the HBO moves in frequency within the selection, or the HBO profile itself is asymmetric. Whenever two Lorentzian peaks were used to describe the HBO we obtained the rms and FWHM weighted mean of the two peaks; we used the weighted mean parameters in Figure 7.4 and in Table 7.2. We weighted the frequencies according to one over the square of the FWHM and proportionally to the square of the amplitude. The FWHMs were weighted proportionally to the square of the amplitude. The frequency offsets between the two peaks were ignored in the weighing since one of the two Lorentzian peaks contained several times more power than the other. The powers of the two Lorentzians were added. We would like to remark that the jump in HBO frequency vs. S_z for each HID (Figure 7.2) has disappeared due to the shifting to $S_{z,parent}$.

The fractional rms amplitude (integrated between frequencies ranging from 0–∞) of all the low–frequency Lorentzian components (excluding the NBO) decreased as a function of S_z (see Figure 7.6 upper panels; Table 7.2). For $S_z = 1.0 - 1.5$ the frequency and the fractional rms amplitude of the HBO was consistent with being constant at $\sim$50 Hz and $\sim$2%, respectively. For $S_z > 1.5$ the HBO was not detected with an upper limit of 1.2%. The FWHM of the Lorentzian components increased as a function of S_z (see Figure 7.6 lower panels; Table 7.2).

The fractional rms amplitude of the LFN (0.1–100 Hz) decreased from 7.4% ±0.3% to 3.38%±0.02% as S_z increased from 0.12±0.03 to 1.01±0.02 (Table 7.3). The LFN component could not be measured for $S_z > 1$. The LFN power law index increased from 0.07±0.05 to 0.41±0.01 while the cut–off frequency increased from 2.9±0.5 Hz to $\sim$60 Hz. For $S_z > 1$ we added a power law to the fit function to represent the power at frequencies below 1 Hz; the very low–frequency noise (VLFN). The VLFN fractional rms amplitude (0.001–1 Hz) increased from less than 1% at the hard vertex to more than 20% at $S_z > 3.0$. This increase was gradual for $S_z < 2.0$ but steep for $S_z > 2.0$ (see Figure 7.7, Table 7.3). The VLFN power law index gradually increased to 1.5 and remained constant for $S_z < 2.0$,

Table 7.2: Best fit parameters of the Lorentzian components of the low frequency power spectra (2–60 keV) as a function of S_z.

S$_z$ value^c	Sub frac. rms amp. %	FWHM sub (Hz)	Freq. sub (Hz)	HBO frac. rms amp. %	FWHM HBO (Hz)	Freq. HBO (Hz)	2^{nd}_{HBO} frac. rms amp. %	FWHM 2^{nd}_{HBO} (Hz)	Freq. 2^{nd}_{HBO} (Hz)	3^{rd}_{sub} frac. rms amp. %	FWHM 3^{rd} (Hz)	Freq. 3^{rd} (Hz)
0.12±0.03	$2.5^{+1.7}_{-0.8}$	7±3	7±1	7.8±0.5^b	3.0±0.2^b	14.33±0.05^b	1.9±0.6	6 ±2	27.9±0.3	5.0±0.3	32±4	22±3
0.21±0.03	3.0±0.2	6.7±0.4	7.9±0.2	7.7±0.2^b	3.5±0.1^b	17.02±0.08^b	1.7±0.1	9 ±1	34.4±0.2	4.3±0.1	27±1	27±1
0.31±0.03	2.7±0.2	6.9±0.5	9.4±0.2	7.24±0.03	4.9±0.1	21.53±0.01	1.7±0.3	9 ±2	43.2±0.3	3.4±0.1	27±1	35±1
0.40±0.03	2.5±0.2	8.9±0.7	10.9±0.2	6.38±0.07^b	4.6±0.1^b	23.78±0.05^b	2.1±0.2	15±2	48.8±0.3	3.5±0.2	36±2	33±2
0.50±0.03	2.1±0.2	10±1	12.7±0.3	5.9±0.2 ^{b}	5.5±0.2^b	27.98±0.06^b	1.9±0.2	13±2	55.7±0.2	2.8±0.2	41±2	41±3
0.60±0.03	1.6±0.2	10±1	15.0±0.4	5.45±0.04	6.8±0.1	31.90±0.02	1.6±0.2	13±2	64.2±0.3	2.6±0.1	41±3	51±3
0.70±0.03	2.1±0.2	17±2	17.3±0.6	4.66±0.03	7.6±0.1	35.77±0.03	1.5±0.3	15±3	71.7±0.5	2.2±0.3	35^{+3}_{-10}	58±2
0.80±0.03	1.3±0.3	15±3	21.0±0.6	4.02±0.03	9.1±0.1	38.81±0.03	1.1±0.2	13±4	77.2±0.6	2.2±0.1	45±3	64±2
0.90±0.03	<0.6	10^a	....	3.19±0.02	11.5±0.2	42.61±0.05	0.8±0.1	13±4	79.9±0.9	<0.9	10^a	....
1.01±0.03	<0.5	10^a	....	2.81±0.02	15.5±0.3	47.14±0.08	<0.4	10^a	....	<0.7	10^a	....
1.07±0.02	....	....	....	2.37±0.02	16.4±0.4	50.0±0.1	....	....	....	....	....	....
1.12±0.02	....	....	....	2.18±0.03	20.4±0.8	50.2±0.2	....	....	....	....	....	....
1.18±0.02	....	....	....	1.95±0.04	23±1	50.5±0.3	....	....	....	....	....	....
1.22±0.02	....	....	....	1.69±0.07	29±3	51.3±0.5	....	....	....	....	....	....
1.27±0.02	....	....	....	1.66±0.09	34±4	51±1	....	....	....	....	....	....
1.33±0.02	....	....	....	1.7±0.1	51±9	52±2	....	....	....	....	....	....
1.38±0.02	....	....	....	1.7±0.2	72±15	48±5	....	....	....	....	....	....
1.42±0.02	....	....	....	1.7±0.2	77±15	44±5	....	....	....	....	....	....
1.47±0.02	....	....	....	1.4±0.2	38±11	49±3	....	....	....	....	....	....

[a] Parameter fixed at this value [b] Parameter is the weighted average of two Lorentzians (see text) [c] The error on S$_z$ is the standard deviation of the distribution of S$_z$ values in the selection bin

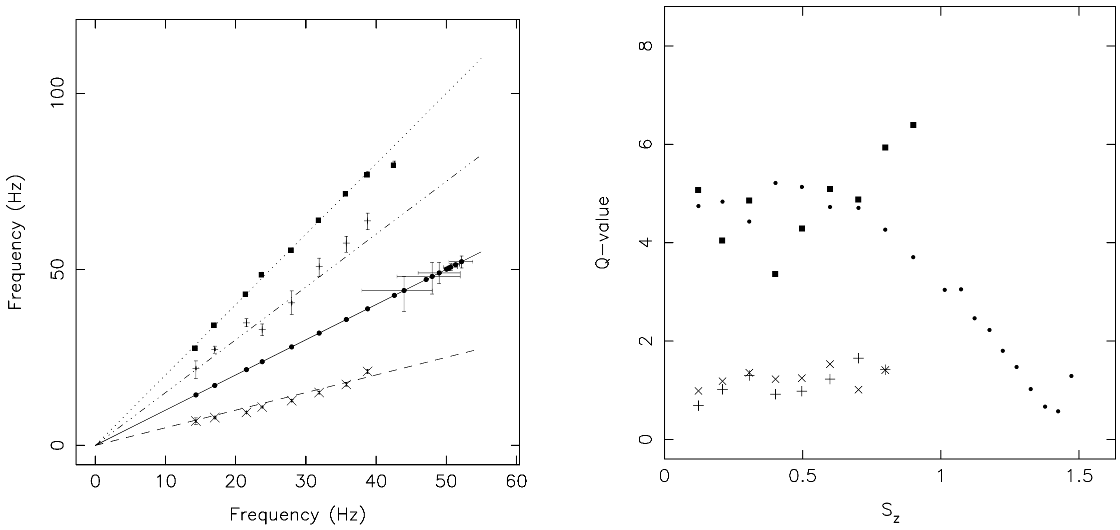

Figure 7.4: Left panel: The frequencies of the four Lorentzian components used to fit the average power spectra for $S_z < 1.5$, plotted against the frequency of the HBO. The lines represent 0.5 (dashed line overlaying the crosses), 1.0 (drawn line overlaying the filled circles), 1.5 (dashed–dotted line overlaying the plus symbols), and 2.0 (dotted line overlaying the squares) times the HBO frequency. Error bars are plotted but in several cases they are smaller than the size of the symbols. Right panel: The Q–values of the 4 harmonics. The HBO and its second harmonic have Q–values near 5 over the range where they are detected simultaneously, thereafter the HBO coherence drops steadily. The Q–values of the sub–HBO and its third harmonic are around 1, with only a slight increase between $S_z \sim 0.1$ and $S_z \sim 0.8$. Error bars are omited for clarity but they are a few times larger than the size of the symbols. The same symbols as in the left panel have been used.

for $S_z > 2.0$ the power law index was consistent with 2.

The frequency of the NBO decreased from 6.1±0.3 Hz at $S_z = 1.07 \pm 0.02$ to 5.25±0.05 Hz at $S_z = 1.33 \pm 0.02$ before it increased again to 6.1±0.1 Hz at $S_z = 1.82 \pm 0.03$. For $S_z > 1.9$ its frequency could not be determined with high accuracy since the FWHM increased to 8 Hz. The fractional rms amplitude of the NBO varied between $1.69\%^{+0.05}_{-0.09}\%$ and 2.38%±0.03% for $S_z = 1.07 \pm 0.02$ and $S_z = 1.52 \pm 0.02$, respectively but it decreased to ∼1.14%±0.05% at $S_z = 1.95 \pm 0.05$. The somewhat erratic behavior in the fractional rms amplitude of the NBO between $S_z = 1.3 - 1.5$ can be explained by the fact that the HBO was very broad and had power in the same frequency range as the NBO. The fractional

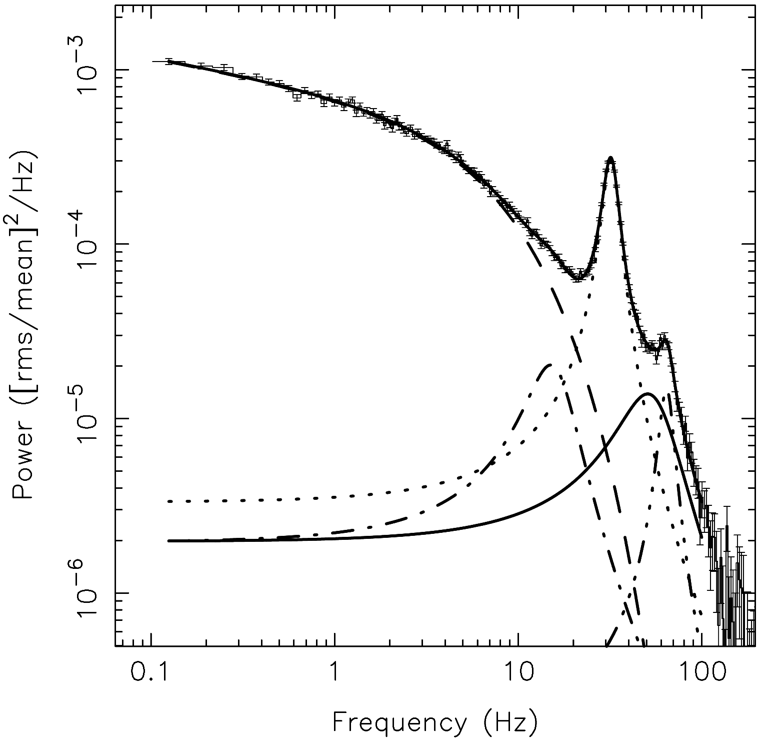

Figure 7.5: Average 2–60 keV power density spectrum for $S_z = 0.60 \pm 0.03$. *The best fit and the individual components used in this fit are indicated; the dashed line represents the LFN, the dotted line the HBO, the dash–dot line the sub–HBO, the solid line its third harmonic, and the dash–three dots line the second hamonic of the HBO. The component arising in the power spectrum due to Poisson noise was subtracted.*

rms amplitude is anti–correlated with the frequency and FWHM of the NBO (see Figure 7.8). At $S_z < 1.0$ stringent upper limits on the presence of the NBO were derived.

At $S_z > 2.0$ the NBO was not detected but instead a cut–off power law was fitted to represent the power at frequencies comparable to the NBO frequencies. This cut–off power law was peaked (power law index of -0.9 ± 0.2) near the soft vertex, with power law index -0.9 ± 0.2 and evolved into a flat–topped noise component at $S_z = 2.15 \pm 0.05$ with a typical power law index of 0.3. The cut–off frequency increased from 4.3±0.6 Hz to 25^{+8}_{-5} Hz. The fractional rms amplitude (0.001-100 Hz) increased from 1.68%±0.07% at $S_z = 2.05 \pm 0.05$ to 2.07%±0.05% at $S_z = 2.15 \pm 0.05$. For $S_z > 2.15$ the fractional rms amplitude was consistent with 1.6%. The noise component became undetectable at an S_z value

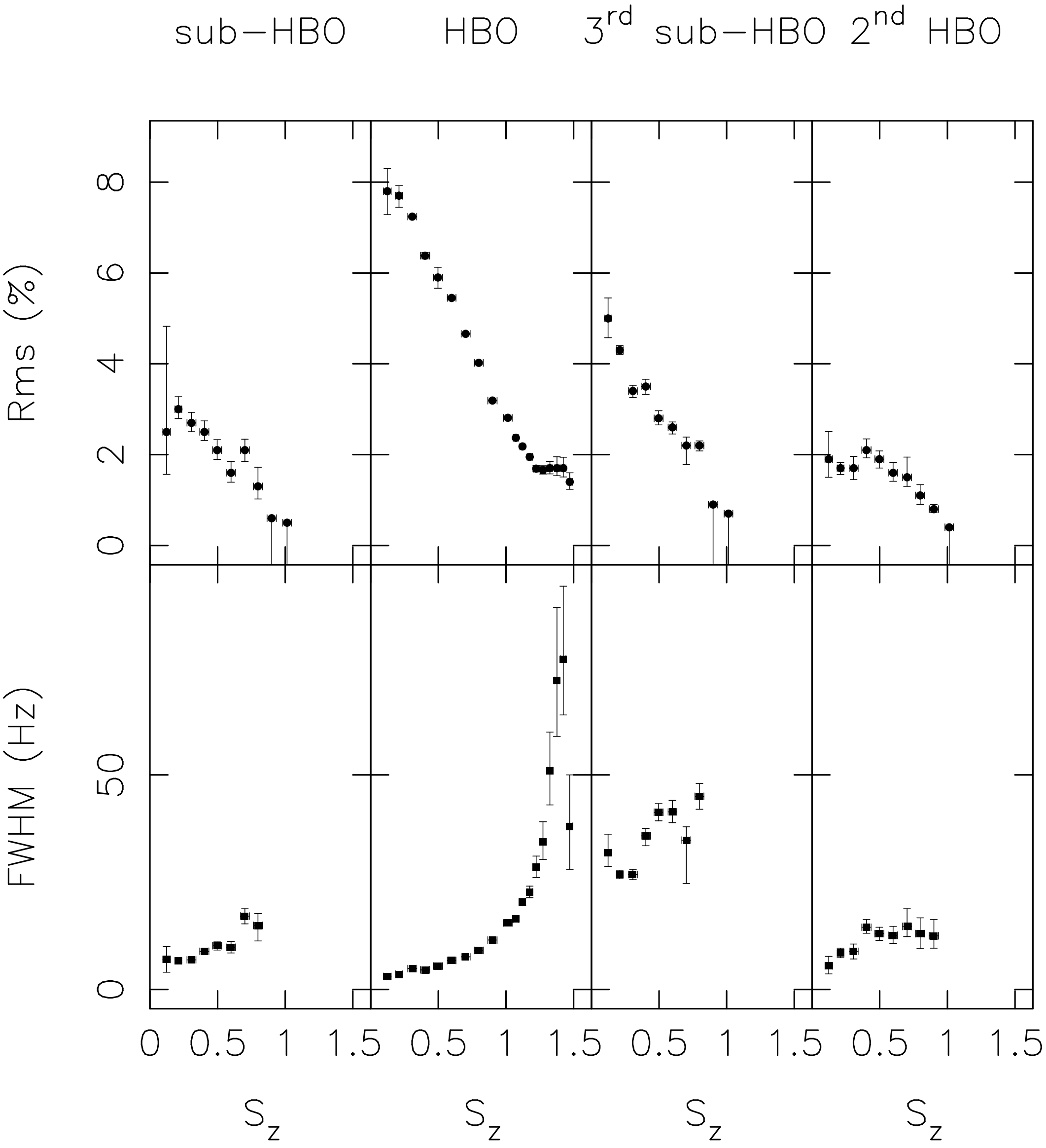

Figure 7.6: The fractional rms amplitude (2–60 keV; top panel) and the FWHM (bottom panel) of the sub–HBO, the HBO, the third harmonic of the sub–HBO, and the second harmonic of the HBO as a function of S_z. Error bars are plotted but may be smaller than the size of the symbols. Upper limits on the fractional rms amplitude of components are plotted using symbols without a positive error bar. The negative error bar extends to below zero.

Table 7.3: Best fit parameters of the cut–off power law, the power law, and the NBO component of the low frequency power spectra (2–60 keV) as a function of S_z.

S_z value^c	LFN frac. rms amp. %	Power law index	Cut–off freq. (Hz)	VLFN frac. rms amp. %	Power law index	NBO frac. rms amp. %	FWHM NBO (Hz)	Freq. NBO (Hz)
0.12±0.03	7.4±0.3	7e-2±5e-2	2.9±0.5	....	....	....	....	....
0.21±0.03	7.57±0.06	2e-2±1e-2	2.97±0.1	....	....	....	....	....
0.31±0.03	7.29±0.06	1e-2±2e-2	3.43±0.1	....	....	....	....	....
0.40±0.03	7.06±0.06	7e-2±1e-2	4.32±0.2	....	....	....	....	....
0.50±0.03	6.83±0.05	0.11±1e-2	5.4±0.2	....	....	....	....	....
0.60±0.03	6.48±0.05	0.20±1e-2	7.4±0.3	....	....	....	....	....
0.70±0.03	5.42±0.07	0.26±1e-2	8.7±0.5	....	....	....	....	....
0.80±0.03	4.81±0.09	0.37±1e-2	15±1	....	....	....	....	....
0.90±0.03	4.65±0.02	0.48±1e-2	68±2	< 0.4	1^a	<0.4	10^a	....
1.01±0.03	3.38±0.02	0.41±1e-2	59±2	< 0.5	1^a	<0.7	10^a	....
1.07±0.02	< 0.5	0.4^a	....	0.92±0.07	1.0±0.1	$1.69^{+0.05}_{-0.09}$	14.4±0.9	6.1±0.3
1.12±0.02	< 0.5	0.4^a	....	1.0±0.1	1.1±0.1	1.80±0.04	9.1±0.4	6.03±0.09
1.18±0.02	....	....	....	1.0±0.2	1.3±0.1	2.04±0.02	7.0±0.2	5.97±0.05
1.22±0.02	....	....	....	1.3±0.3	1.4±0.1	2.14±0.02	5.7±0.1	5.79±0.04
1.27±0.02	....	....	....	3.1±0.1	1.9^a	2.35±0.02	4.8±0.1	5.67±0.03
1.33±0.02	....	....	....	$1.7^{+0.6}_{-0.4}$	1.6±0.2	1.9±0.1	2.7±0.2	5.25±0.05
1.38±0.02	....	....	....	1.4±0.3	1.4±0.1	2.0±0.2	2.3±0.2	5.33±0.06
1.42±0.02	....	....	....	1.8±0.4	1.5±0.1	2.23±0.08	2.6±0.1	5.43±0.04
1.47±0.02	....	....	....	2.6±0.1	1.6^a	2.1±0.1	2.3±0.2	5.48±0.04
1.52±0.02	....	....	....	2.2±0.5	1.5±0.1	2.38±0.03	3.3±0.1	5.75±0.04
1.58±0.02	....	....	....	2.2±0.1	1.5^a	2.17±0.03	3.7±0.2	5.92±0.05
1.63±0.03	....	....	....	2.1±0.1	1.5^a	2.00±0.03	4.0±0.2	6.01±0.05
1.68±0.02	....	....	....	1.9±0.3	1.3±0.1	1.84±0.04	4.2±0.2	6.07±0.06
1.73±0.03	....	....	....	2.5±0.4	1.5±0.1	1.61±0.04	4.3±0.3	6.09±0.08
1.82±0.03	....	....	....	3.0±0.2	1.5±0.1	1.30±0.03	6.2±0.5	6.2±0.1
1.95±0.05	....	....	....	2.8±0.2	1.5±0.1	1.14±0.05	8.1±0.8	5.8±0.2
2.05±0.05	....	....	....	1.6±0.1	1.1±0.1	1.68±0.07^b	-0.9±0.2^b	4.3±0.6^b
2.15±0.05	....	....	....	4.2±0.2	1.8^a	2.07±0.05^b	0.3±0.1^b	18±3^b
2.36±0.08	....	....	....	11±2	2.0±0.1	1.64±0.05^b	0.4±0.1^b	25±5^b
2.64±0.06	....	....	....	17±2	1.9±0.1	1.54±0.07^b	0.2±0.1^b	25^{+8}_{-5} ^{b}
2.90±0.08	....	....	....	18±2	1.8±0.1	<1.2	0.3^a	....
3.13±0.15	....	....	....	22±3	1.9±0.1	....	....	....

^{a} Parameter fixed at this value ^{b} Fitted with a cut–off power law, FWHM stands for power law index, frequency stands for cut–off frequency ^{c} The error on S_z is the standard deviation of the distribution of S_z values in the selection bin

of 2.64±0.06 with an upper limit of 1.2%, where the vertex between the Flaring Branch and the "Dipping Flaring Branch" is at $S_z \sim 2.5$. The fit parameters of the cut–off power law are marked with a '*b*' in Table 7.3.

7.3.3 KHz QPOs

The lower and upper kHz QPO were detected at frequencies ranging from 156±23 Hz to 627^{+25}_{-13} Hz and from 478±15 Hz to 866±23 Hz, respectively (dots and crosses, respectively *top panel*, Figure 7.9 A). The peak separation ($\Delta\nu$) was not constant; the fit of a constant to the peak separation (325±10 Hz) vs. S_z resulted in a χ^2_{red} of 7 for 10 degrees of freedom; an unacceptable fit. We tried various other functions (e.g. see Figure 7.9 *bottom panel* and Table 7.5). From an F–test

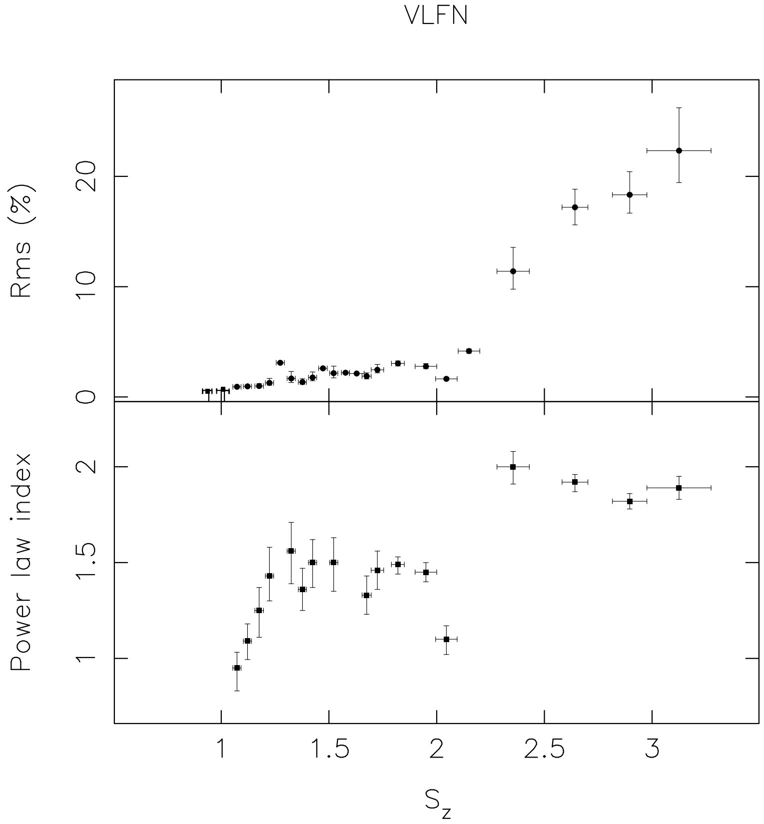

Figure 7.7: The fractional rms amplitude (2–60 keV; top panel) and power law index (bottom panel) of the VLFN as a function of S_z. Error bars are plotted but may be smaller than the size of the symbols.

it was clear that the use of a broken function or a parabola significantly reduced the χ^2 ($\sim 3.5\sigma$, $\sim 3\sigma$, respectively) with respect to a constant, indicating that $\Delta\nu$ is decreasing towards higher S_z at a rate that is not constant but increases. The data indicate a decrease in FWHM of the lower kHz QPO towards larger S_z, but the scatter is large. The FWHM of the upper kHz QPO varies between 100 Hz and 247 Hz; it increases from $\sim$ 100 Hz at $S_z \sim 0.1$ to $\sim$250 Hz at $S_z \sim 0.35$ to decrease gradually to $\sim$100 Hz again at $S_z \sim 1$ (see crosses Figure 7.9 B *top panel*). The fractional rms amplitude of the lower kHz QPO decreased gradually from 3.6%±0.4% to 0.5%±0.1%, that of the upper kHz QPO first increased slightly from 2.0%±0.4% to 2.6%±0.1% to decrease gradually to 0.9%± 0.1% (see dots and crosses respectively, Figure 7.9 C *top panel*). The S_z changed from

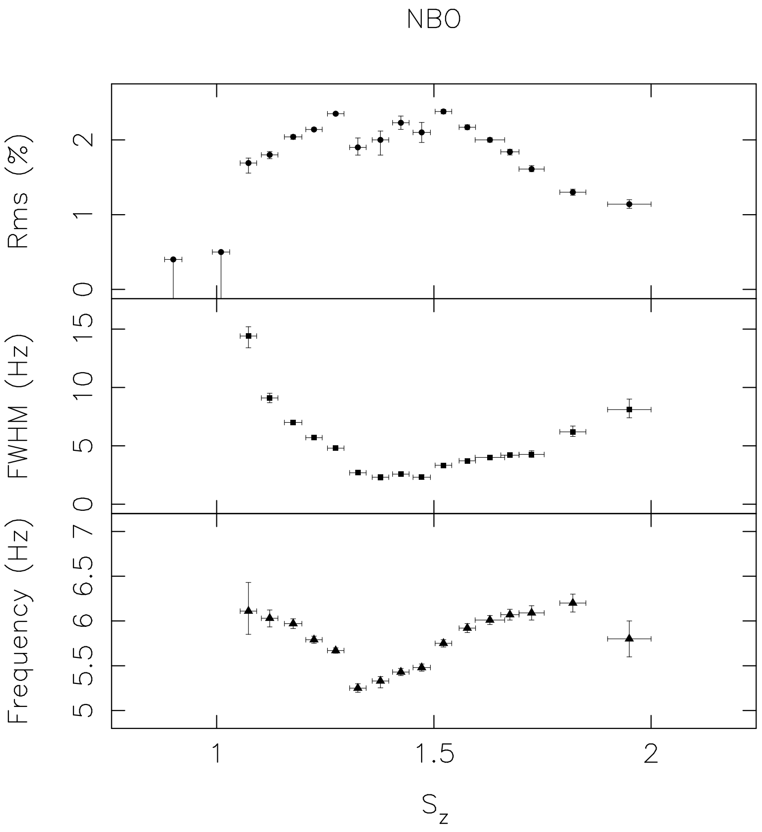

Figure 7.8: The fractional rms amplitude (2–60 keV; top panel), FWHM (middle panel), and frequency (bottom panel) of the NBO as a function of S_z. Error bars are plotted but may be smaller than the size of the symbols. Upper limits on the fractional rms amplitude of the NBO are plotted using symbols without a positive error bar. The negative error bar extends to below zero.

$\sim 0.1 - 1.1$ over the plotted interval. All fit results are given in Table 7.4.

Motivated by the results of Homan et al. (2001a) on GX 17+2 we plotted the frequency of the kHz QPOs and their separation frequency as a function of ν_{HBO} (Figure 7.10). Near $\nu_{HBO} \sim 45$ Hz the peak separation starts to decrease most likely due to an increase in the rate at which the frequency of the lower kHz QPO increases with ν_{HBO}. This ν_{HBO} is consistent with the jump at $\nu_{HBO} \sim 44 - \sim 47$ Hz in a ν_{HBO} vs. S_z plot (see Section 7.2).

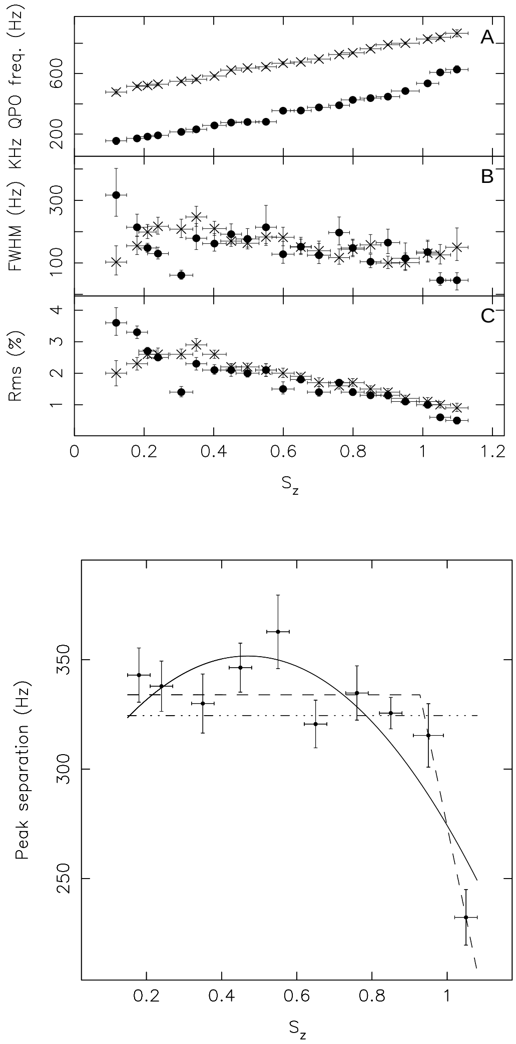

Figure 7.9: The kHz QPO properties as a function of S_z. The measurements presented in the top panel are dependent points since data have been used from partially overlapping bins. (Top panel A: The frequencies of the lower (dots) and upper kHz QPO (crosses), the same symbols for the lower and upper kHz QPO are used throughout the figure. Top panel B: The FWHM of the kHz QPO pair. Top panel C: The fractional rms amplitude (2–60 keV) of the kHz QPO pair. Bottom panel: The peak separation as a function of S_z. The dashed–dotted line represents the best fit constant, the drawn line represents the fit to the data of a parabola, and the dashed line represent a fit using two straight lines joined at the break with slope fixed to zero below the break at $S_z \sim 0.93$ (for the fit parameters see Table 7.5). Error bars are plotted, but the errors in the top panel can be smaller than the size of the symbols.

Table 7.4: Best fit parameters (2–60 keV) of the lower (ν_{low}) and upper (ν_{up}) kHz QPO as a function of the source position along the Z track. Note that overlapping selections in S_z have been used.

S_z value[a]	Fractional rms ampli. ν_{low}	FWHM lower kHz QPO (Hz)	Frequency lower kHz QPO (Hz)	Fractional rms ampli. ν_{up}	FWHM upper kHz QPO (Hz)	Frequency upper kHz QPO (Hz)
0.12±0.03	3.6±0.4	317±77	156±23	2.0±0.4	103±47	478±15
0.18±0.03	3.3±0.2	214±36	172±10	2.3±0.2	155±29	515±9
0.21±0.03	2.7±0.1	148±15	183±3	2.6±0.1	199±23	521±8
0.24±0.03	2.5±0.1	130±19	192±4	2.6±0.2	217±27	530±10
0.31±0.03	1.4±0.2	61 ±15	215±4	2.6±0.2	208±30	549±10
0.35±0.03	2.3±0.2	179±42	232±7	2.9±0.2	247±32	562±11
0.40±0.03	2.1±0.2	162±28	258±7	2.6±0.1	210±23	584±8
0.45±0.03	2.1±0.2	192±32	277±9	2.2±0.1	170±18	623±7
0.50±0.03	2.0±0.1	177±29	280±8	2.2±0.1	163±19	637±7
0.55±0.03	2.1±0.2	241±62	282±12	2.1±0.2	183±29	645±10
0.60±0.03	1.5±0.2	128±35	355±10	2.0±0.2	182±30	668±11
0.65±0.03	1.8±0.1	152±28	356±8	1.9±0.1	151±23	677±8
0.70±0.03	1.4±0.2	125±32	377±10	1.7±0.1	139±27	696±8
0.76±0.03	1.7±0.1	197±45	391±19	1.6±0.1	117±25	726±6
0.80±0.03	1.4±0.1	148±26	426±11	1.7±0.1	144±27	737±7
0.85±0.03	1.3±0.1	104±22	438±7	1.5±0.1	158±30	764±10
0.90±0.03	1.3±0.1	165±39	448±12	1.4±0.1	100±20	790±6
0.95±0.04	1.1±0.1	115±43	485±12	1.2±0.1	101±28	801±8
1.01±0.03	1.0±0.1	135±34	535±20	1.1±0.1	131±33	828±11
1.05±0.03	0.6±0.1	45 ±20	608±6	1.0±0.1	126±31	840±12
1.10±0.03	0.5±0.1	45 ±27	627^{+25}_{-13}	0.9±0.1	150^{+62}_{-42}	866±23
1.18±0.02	<0.7	75[b]	....	<0.9	75[b]	....
1.22±0.02	<0.8	75[b]	....	<0.8	75[b]	....

[a] The error on S_z is the standard deviation of the distribution of S_z values in the selection bin [b] Parameter fixed at this value

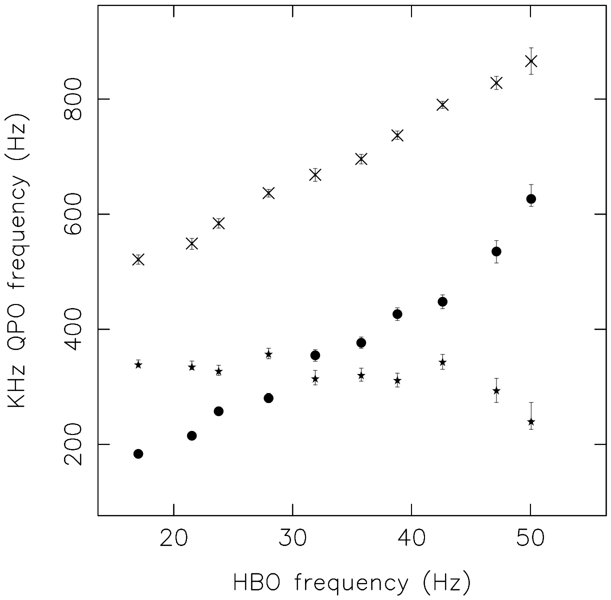

Figure 7.10: The kHz QPO properties as a function of the HBO frequency. The dots represent the lower kHz QPO and the crosses the upper kHz QPO. The frequency of the peak separation is indicated with stars. The rate of increase in lower kHz QPO frequency and therefore also in the peak separation frequency changes near $\nu_{HBO} \sim 45$ *Hz.*

Table 7.5: Fit parameters of different functions describing the peak separation as a function of S_z*. The broken functions are two straight lines concatenated at the break. The last row contains the* χ^2 *and the degrees of freedom (d.o.f.) of the fit. Note that unlike in the top panel of Fig 7.9 only independent measurements have been used in the lower panel.*

	Constant	Linear	Parabola	Broken	Broken
Zeropoint	325±10 Hz	369±21 Hz	291 ± 29 Hz	334±4 Hz	348±9 Hz
Slope	....	−70 ± 30	259 ± 109	0^a	-24±15
Quadratic / break	....	....	−275 ± 90	$S_z = 0.93 \pm 0.06$	$S_z = 0.94 \pm 0.05$
Slope after Break	....	....	....	-832±483	-832±439
χ^2/d.o.f.	66.8 /9	39.9/8	15.0 / 7	7.8 / 7	5.5 / 6

[a] Parameter fixed at this value

7.4 Discussion

A detailed analysis of all *RXTE* observations obtained to date of GX 5–1 was presented. The main result of our high–frequency variability study is that the kHz QPO peak separation is not constant in GX 5–1. The low–frequency power spectra for $S_z < 1.0$ are complex and can be best described by 4 harmonically related Lorentzians, in addition to the low–frequency noise (LFN). Two of these Lorentzians were not known previously in GX 5–1. At $S_z > 1.9$ a new component was found in the power spectra. Below we discuss these findings and compare the timing properties and color–color diagrams of GX 5–1, the black hole candidate XTE J1550–564, and the atoll source 4U 1608–52.

7.4.1 KHz QPOs

We showed that the kHz QPO peak separation is not constant. The data is consistent with a constant peak separation followed by a steep decrease for $S_z \sim 1.0$, or a parabolic relation between the peak separation and S_z. A decrease in peak separation was previously found in Sco X–1 (van der Klis et al. 1997), 4U 1608–52 (Méndez et al. 1998), 4U 1728–34 (Méndez & van der Klis 1999), 4U 1735–44 (Ford et al. 1998), 4U 1702–43 (Markwardt et al. 1999), and GX 17+2 (Homan et al. 2001a). We found that in GX 5–1 the rate of increase in frequency of the lower kHz QPO changes near $\nu_{HBO} \sim 45$Hz, causing the peak separation to decrease.

The frequencies of the kHz QPOs of GX 5–1 are low in comparison with the other kHz QPO Z sources (the lowest frequencies of the lower and upper kHz QPO we found are 156 ± 23 Hz, and 478 ± 15 Hz, respectively). The lowest upper kHz QPO frequency found so far in an atoll source (449±20 Hz for 4U 0614+09; van Straaten et al. 2000) is at the low–frequency limit (~500 Hz for the upper kHz QPO; Miller et al. 1998) imposed by the sonic point beat frequency model. The cause of the lower bound on the Keplerian frequency in the sonic point beat frequency model is that the radiation drag of the luminosity produced near the surface of the neutron star can only remove the required amount of the specific angular momentum of the gas to make it fall to the neutron star when the gas is close to the neutron star (Miller et al. 1998). Unlike 4U 0614+09, in the case of GX 5–1 QPOs with still lower frequency did not occur because the source was not found at lower S_z values and not because the QPO disappeared. Therefore, observations of kHz QPOs in GX 5–1 at even lower S_z values will provide a strong test of the sonic point beat frequency model.

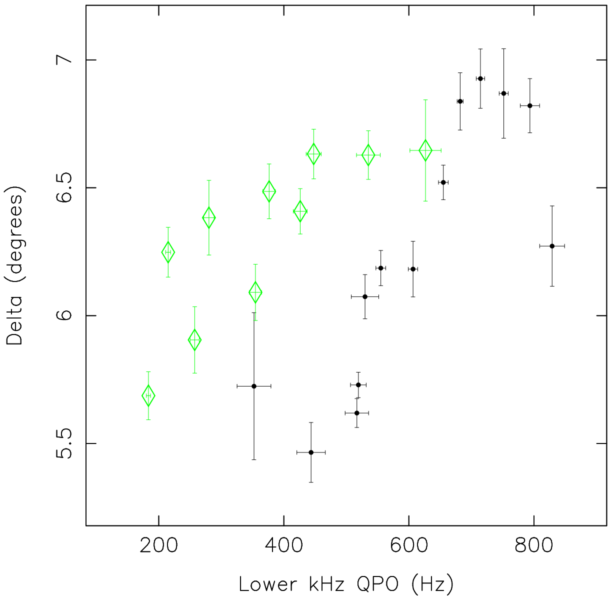

Figure 7.11: The angle δ (defined by Osherovich & Titarchuk 1999) for GX 5–1 (grey diamonds) and GX 17+2 (black dots) as a function of the lower kHz QPO frequency.

In the so–called two–oscillator model (Titarchuk et al. 1998) the angle δ is defined ($\delta = arcsin[(\nu_{upper}^2 - \nu_{lower}^2)^{-0.5}(\nu_{HBO}\nu_{upper}/\nu_{lower})]$, where ν_{lower} is the frequency of the lower kHz QPO, ν_{upper} is the frequency of the upper kHz QPO, and ν_{HBO} is the frequency of the HBO; δ is the angle between the magnetosphere equator and the disk plane in the model Osherovich & Titarchuk 1999). The current version of the theory predicts δ to be constant. However, the measurements of Homan et al. (2001a) for GX 17+2 and the our measurements for GX 5–1 show that δ vs. the frequency of the lower kHz QPO changes is not constant (see Figure 7.11). A fit of a constant gives $\delta = 6.1 \pm 0.2$ and a χ^2 of 377 for 9 d.o.f. for GX 17+2 and $\delta = 6.3 \pm 0.1$ and a χ^2 of 95.2 for 9 d.o.f. for GX 5–1.

7.4.2 Comparison with other Z sources

We have detected a sub–HBO component similar to the component in the Z–sources Sco X–1 (Wijnands & van der Klis 1999), GX 340+0 (Jonker et al. 2000b), and GX 17+2 (Homan et al. 2001a). Furthermore, we found a fourth Lorentzian component whose frequency was consistent with 1.5 times the frequency of the HBO. If we interpret the sub–HBO as the fundamental frequency, then the HBO would be the second harmonic, the newly found peak at 1.5 times the HBO frequency the third harmonic, and the second harmonic of the HBO the fourth harmonic. In such a scheme the odd harmonics should either be formed less coherently than the even harmonics, or an additional broadening mechanism has to be invoked which broadens the odd harmonics more than the even harmonics (see Figure 7.4; *right panel*). This harmonic structure could be explained in a scenario where the HBO is caused by a warped accretion disk with a two–fold symmetry. The warp itself is stable to deviations from its two–fold symmetry, i.e., variations in the warp take place on a timescale long compared to the timescale of variations in the difference between the two sides of the warp, leading to broader odd harmonics. This connects to the models proposed by Stella & Vietri (1998) and Psaltis & Norman (2001). In the magnetic beat–frequency model for the HBO (Alpar & Shaham 1985; Lamb et al. 1985) the sub–HBO should reflect differences between the two magnetic poles. Differences in the magnetic field configuration are not likely to vary in time rapidly, so the extra broadening of the sub–HBO with respect to the HBO is unexplained. This necessitates the introduction of an additional broadening mechanism working on the odd harmonics only after their formation.

Prior to the detection of the sub–HBO and its third harmonic, the frequency of the second harmonic of the HBO was not measured to be exactly twice the HBO frequency (Wijnands et al. 1998); with the introduction of the third harmonic of the sub–HBO in the fit function this discrepancy has disappeared (see Figure 7.4; *left panel*). Power density spectra calculated from data obtained with the EXOSAT and Ginga satellites (Kuulkers et al. 1994; Lewin et al. 1992) were fit using only the even harmonics (the HBO and its 2^{nd} harmonic) and an additional high frequency noise (HFN) component. Now, using the larger collecting area of RXTE we find that the HFN in GX 5–1 is better described by two Lorentzian components which have centroid frequencies of 0.5 and 1.5 times that of the HBO.

The same function we used for our analysis of GX 5–1 was used in the analysis of the similar Z source GX 340+0 (Jonker et al. 2000b). There no third harmonic of the sub–HBO was found. Instead we found excess power (a shoulder) close to the HBO peak, which when fit with a Lorentzian was at a frequency entirely inconsistent with 1.5 times that of the HBO. Reanalysis of those data with the insights gained by our work on GX 5–1 did not alter this conclusion. In GX 340+0 both the HBO and the NBO peak became asymmetric when they were strongest. Similar behavior was found in GX 5–1, where for $S_z < 0.5$ four of the five HBO measurements were done using two Lorentzians with centroid frequencies up to 2 Hz apart with similar FWHMs but different strengths, indicating that the HBO was asymmetric. However, unlike in our analysis of GX 340+0 where the data were selected according to HBO frequency, in the case of GX 5–1 this asymmetry could be an artifact of the selection method as explained in Section 7.3.2. An attempt to fit the average power spectra of GX 17+2 (Homan et al. 2001a) with the same fit function as that of GX 5–1 did not lead to the detection of a third harmonic to the sub–HBO. The asymmetry of the HBO found in GX 340+0 and the third harmonic of the sub–HBO found in GX 5–1 could be two different components, one of which is detected in each source because of the special circumstances affecting detections in each case: the larger amplitude of the HBO in GX 340+0 than in GX 5–1 allows to detect a strong asymmetric (shoulder) component, whereas the higher signal–to–noise in GX 5–1 than in GX 340+0 (due to the fact that GX 5–1 is several times brighter than GX 340+0) leads to the detection of the broad third harmonic. New observations with higher signal–to–noise ratios can reveal whether both components are present in both sources or whether they represent power provided by one single component.

The low–frequency power spectra of the three Z sources discussed above (GX 17+2, GX 340+0, GX 5–1) are quantitatively different. In Sco X–1 and GX 17+2 a QPO is found when the source is on the Flaring Branch (the FBO; Hasinger et al. 1989; Penninx et al. 1990). Such a QPO is absent in GX 340+0, GX 5–1, GX 349+2, and Cyg X–2. The new component we found in the power spectrum of GX 5–1 with frequencies similar to those of the FBO when the source is on the Flaring Branch is much broader than the FBO in Sco X–1 and GX 17+2. The second harmonic of the HBO is relatively strong in GX 17+2 while for GX 5–1 and GX 340+0 only weak harmonics have been detected (see Hasinger & van der Klis 1989; van der Klis 1989). Furthermore, the fractional rms amplitude of the HBO is highest in GX 340+0, and lowest for GX 17+2. The HBO frequency in GX 17+2 was found to decrease on the Normal Branch (Wijnands et al. 1997a; Homan et al. 2001a), whereas in GX 340+0 and GX 5–1 the frequency is consistent with being constant (Jonker et al. 2000b). Besides the Lorentzians also the LFN properties are different; it is always peaked in GX 17+2 whereas this is never the case in GX 5–1 and GX 340+0 (see Hasinger & van der Klis 1989; van der Klis 1989; Homan et al. 2001a; Jonker et al. 2000b). The dependence of the HBO, lower and upper kHz QPO Q–values on S_z is shown in Figure 7.12. The HBO Q–value decreases gradually for $S_z > 0.5$, while that of the kHz QPOs increases. This is opposite to what was found for GX 17+2 (Homan et al. 2001a), where the Q–value of the HBO and that of the kHz QPOs increased as a function of S_z.

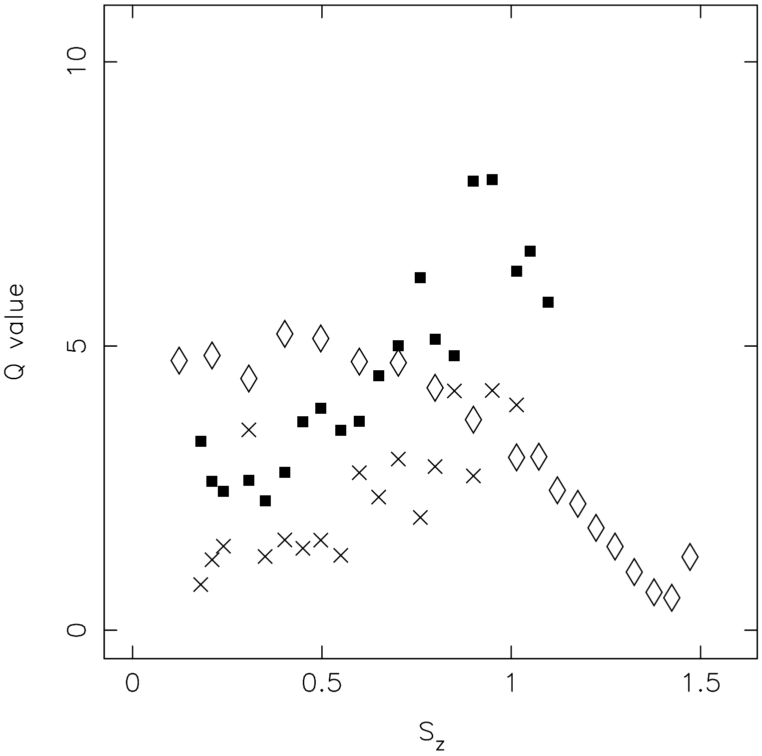

Figure 7.12: The Q–values of the HBO (diamonds), the lower (crosses), and the upper kHz QPO (filled squares) as a function of S_z. The Q–values of both kHz QPOs increase with increasing S_z, while that of the HBO decreases for $S_z > 0.5$. Error bars have been omitted for clarity. The errors of the diamonds (HBO) are ~ 1.5 times the size of the symbols. The errors of the crosses and squares (lower and upper kHz QPO, respectively) are of the order of the amplitude of the scatter in measurements close together in S_z.

7.4.3 Comparing GX 5−1 with XTE J1550−564 and 4U 1608−52

In the power spectra of black hole candidates low–frequency QPOs with harmonics are occasionally found in the low, intermediate and very high state (e.g. GS 1124–68, Belloni et al. 1997b; GX 339–4, Méndez & van der Klis 1997; XTE J1550–564, Sobczak et al. 2000; Homan et al. 2001b). Occasionally, these black hole candidate QPOs have asymmetric profiles. We found a similar harmonic structure of QPOs in the Z source GX 5–1. The Q–values of the harmonics for XTE J1550–564 are similar to those found for GX 5–1: low Q–values for the odd harmonics and high Q–values for the even harmonics (Homan et al. 2001b). However, we checked the energy dependence of the QPOs in GX 5–1 and there are no indications of changes in the Q–values with energy as were found in XTE J1550–564 (Homan et al. 2001b). In general the energy dependence and time lag behavior of the QPOs in GX 5–1 (Vaughan et al. 1999) is different from what was found in XTE J1550–564 (Wijnands et al. 1999). On the Flaring Branch, similar to the High State in black hole candidates, the fractional rms amplitude of the variability is low, and QPOs are weak or absent (in GX 17+2 and Sco X–1, just as in XTE J1550–564 a QPO with a centroid frequency of $\sim$18 Hz is found, but whether they are related is unclear). The similarities between the Horizontal Branch variability and that of the Intermediate/Low State have been pointed out before (van der Klis 1994a; van der Klis 1994b; Wijnands & van der Klis 1999). Furthermore, the trend of a decrease in variability timescale as the source approaches the Flaring Branch/High State is the same in black hole candidates as in GX 5–1 and 4U 1608–52 (cf. Homan et al. 2001b; Méndez et al. 1998).

To further investigate the similarities between a black hole candidate (XTE J1550–564), a Z source (GX 5–1), and an atoll source (4U 1608–52) we created color–color diagrams (CDs) for the three sources in two ways. First, we used the color definitions commonly used for atoll and Z sources (soft and hard color were defined as the logarithm of the 3.6–6.2 / 2.5–3.6 keV and 9.8–16.0 / 6.2–9.8 keV count rate ratio, respectively). These CDs are shown in the *left panels* of Figure 7.13, 7.14, and 7.15. Second, we created CDs in a similar way as van Teeseling & Verbunt (1994), an approach often used for black hole candidates (Belloni et al. 1997a; Homan et al. 2001b; although see also Miyamoto et al. 1991). We defined the hard and soft color as the 9.7–16.0/ 2–6.4 keV and 6.4–9.7/ 2–6.4 keV count rate ratio for observations 1–41, respectively and that of the 9.7–15.8 / 2–6.6 keV and 6.6–9.7 / 2–6.6 keV count rate ratio for observations 42–76, respectively (Figure 7.13, *right panel*). In case of the *right panels* for Figure 7.14 and 7.15 the hard and soft color were defined as the 16.0–19.4 / 2.2–6.2 keV, and 6.5–15.7 / 2.2–6.2 keV count rate ratio, respectively. Note that in the *right panels* the soft color is plotted vs. the hard color, as the convention, introduced by (Ostriker 1977) to plot hard color vs. soft color was abandoned in some of the recent black hole work. In the *right panels* the points have been connected by a line. Lines bridging different parts of the diagrams do not reflect sudden jumps or changes in source state, but are due to gaps introduced by observational windowing.

A similar structure as for XTE J1550–564 was found in the CD of GX 5–1 (Figure 7.13, 7.14 *right panel*). The Flaring Branch is now vertical and located at the left side of the figure, similar to the High State in XTE J1550–564. The Normal Branch connects to the Flaring Branch and points towards the upper right corner of the diagram (both the hard color and the soft color increase as the source moves up the Normal Branch). The Horizontal Branch is a continuation of the Normal Branch, with only a slight bend at the Normal Branch–Horizontal Branch junction. (It is interesting to note that there is also no vertex present in GX 17+2 at the Horizontal– Normal Branch junction at energies above 14.8 keV, Figure 3C of Homan et al. 2001a). The ’Dipping’ Flaring Branch is parallel to the Normal Branch but directed towards the lower left corner. The ’Dipping’ Flaring Branch has been found in the Z sources Cyg X–2, GX 5–1 and GX 340+0 (Kuulkers et al. 1996; Kuulkers et al. 1994; Jonker et al. 2000b). The CD of the atoll source 4U 1608–52 again shows a similar structure as found for XTE J1550–564 (Figure 7.14, 7.15 *right panels*). The island state is found in the top right corner of the *right panel* of Figure 7.15, whereas the lower banana branch connects to the upper banana branch in the lower left corner. The upper banana branch seems similar to the black hole candidate High State and the Z source Flaring Branch.

The CD of the black hole candidate XTE J1550–564, plotted using colors typically applied for neutron star sources is reminiscent of that of an atoll source, although more structure is observed (Figure 7.14 *left panel*). The source was first found in the upper right part of the CD as the outburst started. The path traced by the source as the outburst progressed is indicated with arrows. For a complete description of the outburst of XTE J1550–564 we refer to Cui et al. (1999), Sobczak et al. (2000), and Homan et al. (2001b).

The similarities between the color–color diagrams of the Z source GX 5–1, the atoll source 4U 1608–52, and the black hole candidate XTE J1550–564 strengthen the idea that some of the spectral properties of LMXBs originate in the accretion disk and do not depend on the presence of a solid surface. However, our analysis also indicates that differences between spectral properties of the neutron star Z and atoll sources and the black hole candidates do exist (e.g., the *left panel* of Figure 7.13, 7.14, and 7.15) but may not clearly show up in representations of the CD commonly used for black–hole candidates.

So, although the CDs of a Z or atoll source and that of a black hole candidate appear similar in shape when plotted using colors typical for black hole studies, their appearance is both dissimilar and more complicated when plotted using colors typical for neutron star studies. Whether the complications can be ascribed to the unique nature of the sources considered can only be checked by comparing more sources but the conclusion that dissimilar CDs can appear more similar than they really are in the “black hole” representation can already be drawn. Conclusions regarding the spectral state or properties of the source based on the colors commonly used in black hole candidates should be regarded with caution since an other choice of colors may lead to a qualitatively different CD.

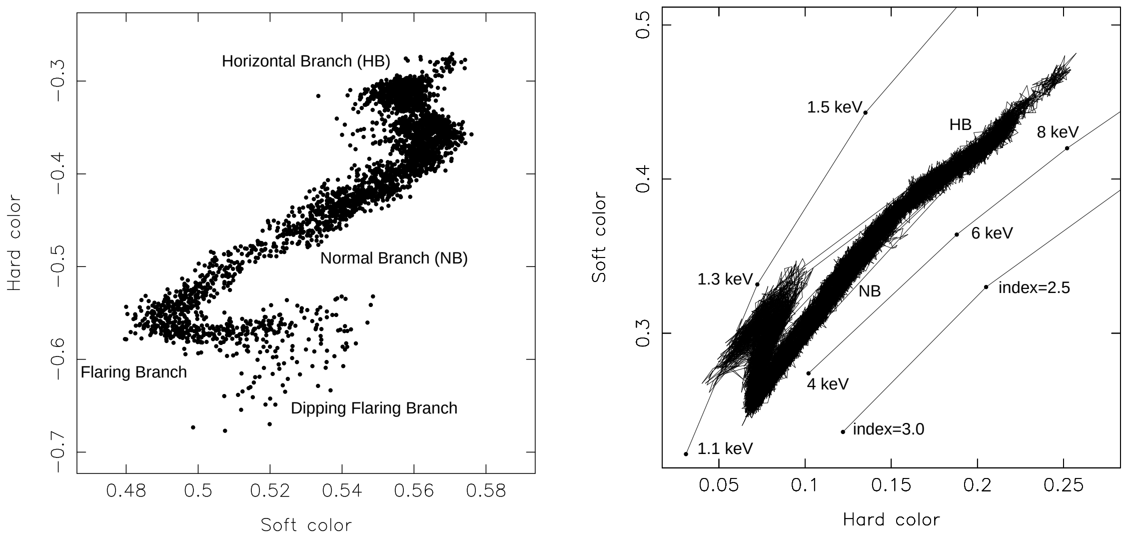

Figure 7.13: Left panel: Color–color diagram of observations 19–41 where the soft and hard color were defined as the logarithm of the 3.6–6.2 / 2.5–3.6 keV and 9.8–16.0 / 6.2–9.8 keV count rate ratio, respectively. Each dot is a 64 s average. Right panel: Color–color diagram of the 6.4–9.7 / 2–6.4 keV (or 6.6–9.7 / 2–6.6 keV for observations 42–76; soft color) count rate ratio vs. the 9.8–16.0 / 2–6.4 keV (or 9.7–15.8 / 2–6.6 keV for observations 42–76; hard color). Each 512 s average is connected to the next by a line. The lines in the right panel indicate what RXTE would have seen if the source spectrum had consisted of only a blackbody (top), a thermal bremsstrahlung (middle), or a powerlaw (bottom line) spectrum. Error bars were omitted for clarity. The data were background subtracted but no deadtime corrections were applied (the deadtime fraction was less than 4%).

Acknowledgments This work was supported in part by the Netherlands Organization for Scientific Research (NWO). This research has made use of data obtained through the High Energy Astrophysics Science Archive Research Center Online Service, provided by the NASA/Goddard Space Flight Center. This work was supported by NWO Spinoza grant 08-0 to E.P.J.van den Heuvel. P.G.J. would like to thank Rob Fender, Kieran O'Brien, and Marc Klein Wolt for various discussions. RW was supported by NASA through Chandra Postdoctoral Fellowship grant under PF9–10010 awarded by CXC, which is operated by SAO for NASA under contract NAS8–39073.

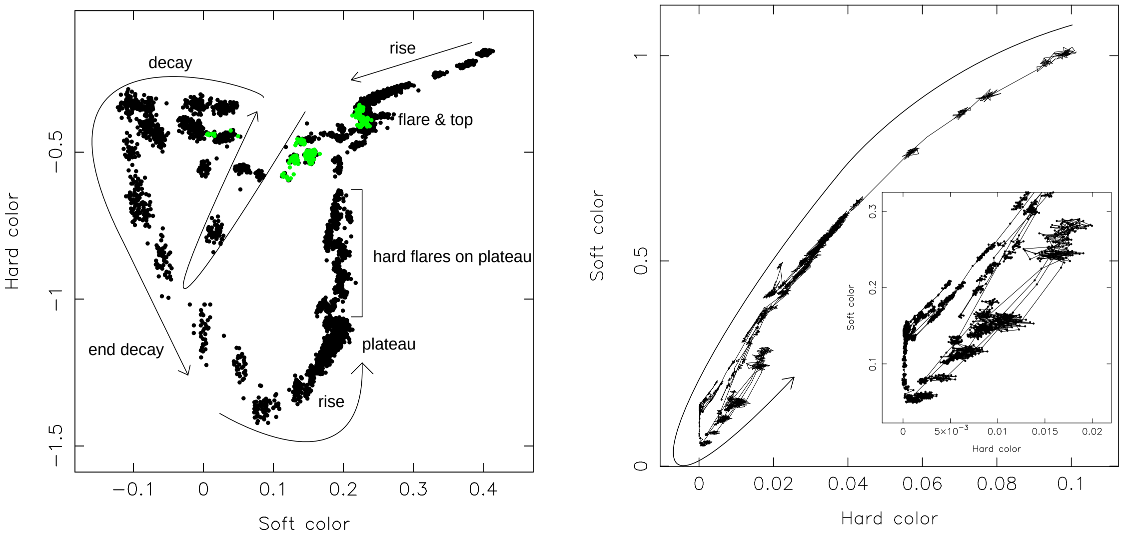

Figure 7.14: Left panel: Color–color diagram of XTE J1550–564. We used all data obtained with the RXTE satellite of XTE J1550–564 during the interval MJD 51065–51259 (gain epoch 3); soft and hard colors were defined as in Figure 7.13 (left panel). Each dot is a 64 s average. The path the source traces as the outburst progresses is indicated. The grey dots are the last days of observations just before the gain change. Right panel: Color–color diagram of the same data as in the left panel. Note that the soft color is plotted vs. hard color. The hard and soft color were defined as the 16.0–19.4 / 2.2–6.2 keV, and 6.5–15.7 / 2.2–6.2 keV count rate ratio, respectively. The data were background subtracted but no deadtime corrections were applied. Each 64 s average is connected to the next by a line. A zoom–in of the lower left corner is visible to the right. Error bars of the data points were omitted for clarity. The arrow indicates the source changes as the outburst progressed.

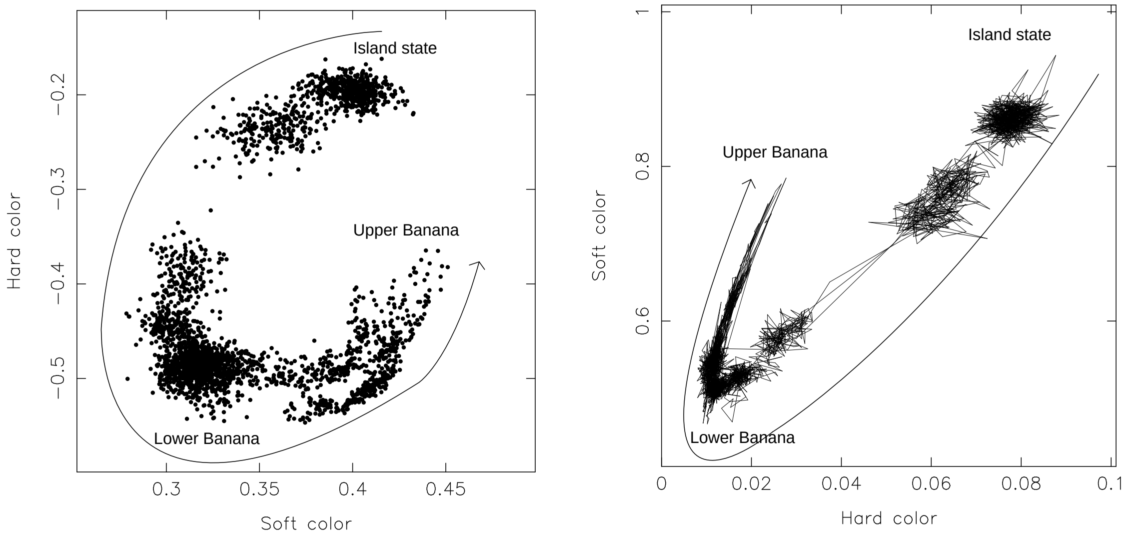

Figure 7.15: Left panel: Color–color diagram of 4U 1608–52. We used the same data as was used by Méndez et al. 1998. Soft and hard colors where defined as in Figure 7.13 (left panel). Each dot is a 64 s average. Right panel: Color–color diagram of the same data as in the left panel. Note that the soft color is plotted vs. hard color. The hard and soft color were defined as the 16.0–19.4 / 2.2–6.2 keV, and 6.5–15.7 / 2.2–6.2 keV count rate ratio, respectively. The data were background subtracted but no deadtime corrections were applied (the deadtime was less than 1%). Each 64 s average is connected to the next by a line. Error bars of the data points were omitted for clarity. The arrow indicates the direction of increase in inferred mass accrettion rate.

CHAPTER 7

Bibliography

Alpar, M. A. & Shaham, J. 1985, Nature, 316, 239

Belloni, T., Méndez, M., King, A. R., van der Klis, M., & van Paradijs, J. 1997a, ApJ, 488, L109

Belloni, T., van der Klis, M., Lewin, W. H. G., et al. 1997b, A&A, 322, 857

Bevington, P. R. & Robinson, D. K. 1992, Data reduction and error analysis for the physical sciences (New York: McGraw-Hill, —c1992, 2nd ed.)

Bradt, H. V., Rothschild, R. E., & Swank, J. H. 1993, A&AS, 97, 355

Braes, L., Miley, G., & Schoenmakers, A. 1972, Nature

Cui, W., Zhang, S. N., Chen, W., & Morgan, E. H. 1999, ApJ, 512, L43

Di Salvo, T., Méndez, M., van der Klis, M., Ford, E., & Robba, N. R. 2001, ApJ, 546, 1107

Di Salvo, T., Stella, L., Robba, N. R., et al. 2000, ApJ, 544, L119

Dieters, S. W. & van der Klis, M. 2000, MNRAS, 311, 201

Ford, E. C., van der Klis, M., Méndez, M., et al. 2000, ApJ, 537, 368

Ford, E. C., van der Klis, M., van Paradijs, J., et al. 1998, ApJ, 508, L155

Hasinger, G., Priedhorsky, W. C., & Middleditch, J. 1989, ApJ, 337, 843

Hasinger, G. & van der Klis, M. 1989, A&A, 225, 79

Hasinger, G., van der Klis, M., Ebisawa, K., Dotani, T., & Mitsuda, K. 1990, A&A, 235, 131

Hertz, P., Vaughan, B., Wood, K. S., et al. 1992, ApJ, 396, 201

Homan, J., van der Klis, M., Jonker, P. G., et al. 2001a, ApJ

Homan, J., Wijnands, R., van der Klis, M., et al. 2001b, ApJS, 132, 377

Jahoda, K., Swank, J. H., Giles, A. B., et al. 1996, Proc. SPIE, 2808, 59

Jonker, P. G., Fender, R. P., Hambly, N. C., & van der Klis, M. 2000a, MNRAS, 315, L57

Jonker, P. G., van der Klis, M., Homan, J., et al. 2001, ApJ

Jonker, P. G., van der Klis, M., Wijnands, R., et al. 2000b, ApJ, 537, 374

Kaaret, P., Ford, E. C., & Chen, K. 1997, ApJ, 480, L27

Kluzniak, W. 1993, A&AS, 97, 265

Kuulkers, E., van der Klis, M., Oosterbroek, T., et al. 1994, A&A, 289, 795

Kuulkers, E., van der Klis, M., & Vaughan, B. A. 1996, A&A, 311, 197

Lamb, F. K., Shibazaki, N., Alpar, M. A., & Shaham, J. 1985, Nature, 317, 681

Lewin, W. H. G., Lubin, L. M., Tan, J., et al. 1992, MNRAS, 256, 545

Markwardt, C. B., Strohmayer, T. E., & Swank, J. H. 1999, ApJ, 512, 125

Méndez, M. & van der Klis, M. 1997, ApJ, 479, 926

Méndez, M. & van der Klis, M. 1999, ApJ, 517, L51

Méndez, M., van der Klis, M., & van Paradijs, J. 1998, ApJ, 506, L117

Méndez, M., van der Klis, M., Wijnands, R., et al. 1998, ApJ, 505, L23

Miller, M. C., Lamb, F. K., & Psaltis, D. 1998, ApJ, 508, 791

Miyamoto, S., Kimura, K., Kitamoto, S., Dotani, T., & Ebisawa, K. 1991, ApJ, 383, 784

Osherovich, V. & Titarchuk, L. 1999, ApJ, 523, L73

Ostriker, J. P. 1977, in Annals of the New York academy of sciences; Eighth Texas symposium on relativistic astrophysics, Vol. 302, 229–243

Penninx, W., Lewin, W. H. G., Mitsuda, K., et al. 1990, MNRAS, 243, 114

Psaltis, D. & Norman, C. 2001, ApJ, submitted

Sobczak, G. J., McClintock, J. E., Remillard, R. A., et al. 2000, ApJ, 544, 993

Stella, L. & Vietri, M. 1998, ApJ, 492, L59

—. 1999, Phys. Rev. Lett
Titarchuk, L., Lapidus, I., & Muslimov, A. 1998, ApJ, 499, 315+
van der Klis, M. 1989, ARA&A, 27, 517
—. 1994a, A&A, 283, 469
—. 1994b, ApJS, 92, 511
van der Klis, M. 1995, in Proceedings of the NATO Advanced Study Institute on the Lives of the Neutron Stars, held in Kemer, Turkey, August 29-September 12, 1993. Editors, M.A. Alpar, U. Kiziloglu, and J. van Paradijs; Publisher, Kluwer Academic, Dordrecht, The Netherlands, Boston, Massachusetts, p. 301
van der Klis, M. 1998, in NATO ASIC Proc. 515: The Many Faces of Neutron Stars., 337
—. 2000, ARA&A, 38, 717
van der Klis, M., Jansen, F., van Paradijs, J., et al. 1985, Nature, 316, 225
van der Klis, M., Wijnands, R. A. D., Horne, K., & Chen, W. 1997, ApJ, 481, L97
van Straaten, S., Ford, E. C., van der Klis, M., Méndez, M., & Kaaret, P. 2000, ApJ, 540, 1049
van Teeseling, A. & Verbunt, F. 1994, A&A, 292, 519
Vaughan, B. A., van der Klis, M., Lewin, W. H. G., et al. 1999, A&A, 343, 197
Vrtilek, S. D., Penninx, W., Raymond, J. C., et al. 1991, ApJ, 376, 278
Wijnands, R., Homan, J., & van der Klis, M. 1999, ApJ, 526, 33
Wijnands, R., Homan, J., van der Klis, M., et al. 1997a, ApJ, 490, L157
Wijnands, R., Méndez, M., van der Klis, M., et al. 1998, ApJ, 504, L35
Wijnands, R. & van der Klis, M. 1999, ApJ, 514, 939
Wijnands, R. A. D., van der Klis, M., Kuulkers, E., Asai, K., & Hasinger, G. 1997b, A&A, 323, 399
Wijnands, R. A. D., van der Klis, M., Psaltis, D., et al. 1996, ApJ, 469, L5
Zhang, W., Smale, A. P., Strohmayer, T. E., & Swank, J. H. 1998, ApJ, 500, L171
Zhang, W., Strohmayer, T. E., & Swank, J. H. 1997, ApJ, 482, L167

Chapter 8

The infrared counterpart of the Z source GX 5–1

P. G. Jonker, R. P. Fender, N.C. Hambly, & M. van der Klis

Monthly Notices of the Royal Astronomical Society, 2000, **315**, Letter 57

Abstract

We have obtained UKIRT infrared observations of the field of the bright Galactic Z source GX 5–1. From an astrometric plate solution tied to Tycho–ACT standards we have obtained accurate positions for the stars in our field which, combined with an accurate radio position, have allowed us to identify the probable infrared counterpart of GX 5–1. Narrow–band photometry marginally suggests excess Brγ emission in the counterpart, supporting its association with an accretion–disc source. No significant variability is observed in a limited number of observations. We compare the H and K magnitudes with those of other Z sources, and briefly discuss possible sources of infrared emission in these systems.

8.1 Introduction

GX 5–1 is the second brightest persistent Galactic X–ray source. The source is well studied in X–rays; it was classified as a Z source on the basis of the pattern it traces in a color-color diagram and its timing properties (Hasinger & van der Klis 1989). Quasi-periodic oscillations with frequencies of 13–50 Hz, 6 Hz, and 200–800 Hz were detected in the X–ray lightcurves (van der Klis et al. 1985a,b; Lewin et al. 1992; Wijnands et al. 1998, respectively). Naylor et al. (1991) identified several candidate infrared counterparts of GX 5–1. Since it is located near the Galactic centre, source confusion and heavy optical obscuration hinder the classification.

GX 5–1 is also a radio source (Braes et al. 1972; Grindlay & Seaquist 1986; Penninx et al. 1988; Berendsen et al. 2000), like all Z sources (Hjellming & Han 1995; Fender & Hendry 2000). The radio emission is likely to arise in a compact jet from the system. The radio counterpart allows for extremely accurate position measurements.

Study of the Z sources has been hampered in most cases by the lack of reliable optical and/or infrared counterparts. For example, Deutsch et al. (1999) showed that the proposed infrared counterpart (Tarenghi & Reina 1972) of another persistently X–ray bright Z source, GX 17+2 was not consistent with the position of its radio counterpart. Furthermore, they detected a faint star close to the proposed counterpart. Callanan et al. (1999) reported variability of about 3.5–4 mag in the K band for the latter, providing additional evidence for its classification as the counterpart.

In this Letter, we present United Kingdom Infrared Telescope (UKIRT) infrared (IR) observations of the X–ray source GX 5–1. We resolve the previously reported counterparts, and show that the radio position is consistent with only one of them.

8.2 Observations, analysis and results

We observed the field of GX 5–1 with UKIRT. Observations were taken in H, K, and in a narrow filter around the Brackett Gamma line (Brγ) in 1999 May and October. A log of the observations can be found in Table 8.1. The observations of 1999, May 23 were obtained using the IRCAM3 camera; the frames consist of 256×256 pixels with a pixel size of 0.286 arc seconds. The observations of 1999, October 8 and 13 were performed using the UFTI camera; the UFTI frames consist

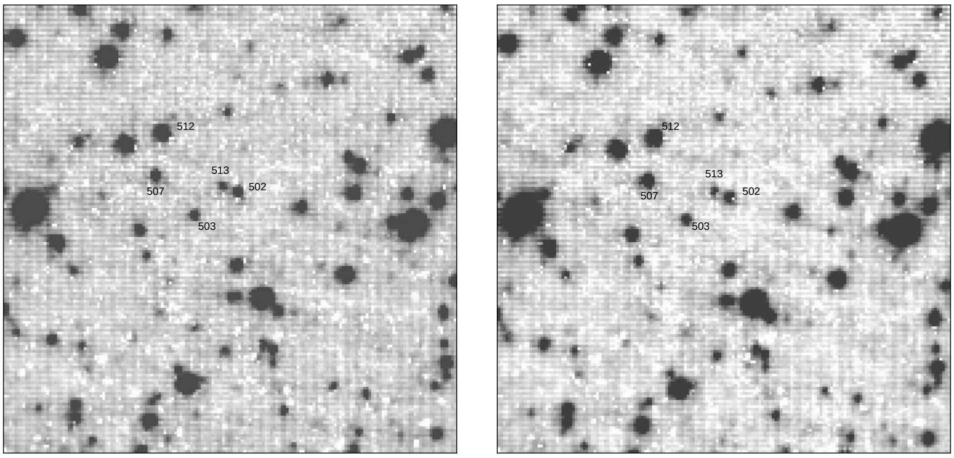

Figure 8.1: Combined images obtained in the K (left) and H (right) bands on May 23, 1999 showing the field of GX 5–1. The labels of the stars are those of Naylor et al. (1991).

Table 8.1: A log of our UKIRT observations of GX 5–1.

Date (1999)	MJD	Filter	No. of exposures
May 23	51321	K, H, Brγ	5, 5, 10
Oct 8	51459	Brγ	9
Oct 13	51464	K	6

of 1024 × 1024 pixels, with a pixel size of 0.0909 arc seconds. The Brγ narrow filter is centred on the wavelength of the Brγ line (2.166 micron; 50% of the light was obtained in the wavelength range 2.151–2.171 μm in case of IRCAM3 observations, and in the range 2.155–2.177 μm in case of UFTI observations). The night was photometric only during the 1999, May 23 observations. The exposure time used in the Brγ filter was 100 seconds, and in the H and K filter band a 10 second exposure was used. On 1999, October 13 an observation time of 100 seconds was used in the K band.

8.2.1 Photometry

All images were dark subtracted. Five (or three in case of the 1999, October 13 observations) dithered IR frames were used to calculate a sky image. This dark subtracted sky image was subtracted from the dark subtracted image after scaling it to the object image level. The resulting images were flatfielded, where the flatfield image was obtained by normalizing the combined five (or three) dithered images. The reduced images were aligned and combined.

In Figure 8.1, we show the observed field in both the K and H filter bands. Clearly visible is that objects 502 and 513, which were blended in the images of Naylor et al. (1991), are resolved into two separate stars. We used three reference stars in the field (503, 507, 512 in the images of Naylor et al. 1991, see Figure 8.1) to obtain differential magnitudes of the counterpart. These stars were calibrated by observing the standard star HD 161903 on 1999, May 23. To obtain the differential magnitudes, we used the point spread fitting (psf) routine to both the reference and object stars using the DoPHOT package (Schechter et al. 1993). The magnitudes derived in this way did not differ significantly from the magnitudes derived using aperture photometry. We corrected the magnitudes for the airmass dependent atmospheric extinction in the H and K band. The magnitudes we derived in the H and K bands are listed in Table 8.2. We seached for variability on timescales of $\lesssim$ 10 minutes and in between the observations, but no significant variability was observed in any of the stars listed in Table 8.2. We determined an upper limit on photometric variability on timescales of $\lesssim$ 10 minutes of 0.6 magnitudes in the H and K band. In Table 8.2 we also list the flux densities obtained in the H and K filter bands, as well as the Brγ–K instrumental magnitude difference. No standard magnitude in the Brγ filter is known for the star HD 161903, therefore we could only calculate instrumental magnitudes in this band.

Accretion disks are known to sometimes produce Brγ emission lines (eg. Bandyopadhyay et al. 1997, 1999). Therefore, if a strong Brγ emission line is present in the accretion disk of GX 5–1 the counterpart could appear brighter in this filter. We compared the instrumental Brγ–K color of the stars 502, 513, and our reference stars (503, 507, and 512); these are also listed in Table 8.2. Star 513 seems to have a smaller instrumental Brγ–K color, although the effect is only marginally detected. We also checked for variability in the Brγ band, but no significant variability was found on timescales of minutes with an upper limit of 0.45 magnitude.

8.2.2 Astrometry

We used the higher resolution UFTI images obtained on 1999, October 8 for our astrometry. To define astrometric solutions for the IR frames we used secondary astrometric standards derived from United Kingdom Schmidt photographic plate material measured using the precision microdensitometer SuperCOSMOS (eg.

Table 8.2: The observed magnitudes, flux densities in the H and K band, and the $H - K$ color on May 23, 1998. Additionally the $Br\gamma - K$ instrumental magnitude color is given.

Stars	H magnitude	Flux density H (mJy)	K magnitude	Flux density K (mJy)	H–K	$Br\gamma$–K
502	13.3 ± 0.1	4.9	12.6 ± 0.1	6.0	0.7	0.74 ± 0.08
503	13.5 ± 0.1	4.1	12.9 ± 0.1	4.5	0.6	0.73 ± 0.09
507	12.42 ± 0.06	11.0	12.42 ± 0.08	7.1	0.0	0.98 ± 0.09
512	11.70 ± 0.03	21.3	11.28 ± 0.04	20.2	0.42	0.79 ± 0.04
513	14.1 ± 0.2	2.3	13.7 ± 0.2	2.2	0.4	0.6 ± 0.1

Hambly et al. 1998). The global astrometric solution for the Schmidt plate was derived using the Tycho–ACT reference catalogue (Urban et al. 1998), and includes correction for non-linear systematic effects caused by the mechanical deformation of the plates during exposure. We used the ”short red”survey plate R5803 (epoch 1979.5, field number 521). These short exposures, taken at low galactic latitudes, are far less crowded than the sky limited survey plates and reach R$\sim$20 (as opposed to R$\sim$ 22 for the deep survey plates). They are ideal for accurate astrometry of secondary standards as faint as R=20 which overlaps with unsaturated objects on the IR frames. The rms residual per ACT star in the global astrometric photographic plate solution was $\sim$ 0.2 arcsec in both coordinates. A solid–body linear plate solution (ie. 4–coefficient) was derived between 7 stars in common between the photographic and IR data, yielding a plate scale of 0.0903 arcsec/pix and rms errors per secondary standard of $\sim$ 0.1 arcsec in either coordinate. We estimate that there will be no systematic zero–point errors in the global IR array astrometric solution larger than $\sim$ 0.25 arcsec.

Since the uncertainty in the radio position is small ($<$40 mas, Berendsen et al. 2000) compared to the estimated uncertainty in the astrometric solution, the overall uncertainty in the radio–infrared alignment was estimated to be 0.25 arcsec. The coordinates of the stars 502 and 513 are listed in Table 8.3. Comparing these positions with the accurate radio position of GX 5–1 given by Berendsen et al. (2000), we conclude that of the detected stars, star 513 is the only plausible counterpart of GX 5–1 (see Figure 8.2).

8.3 Discussion

We have shown that star 513 of Naylor et al. (1991) is most likely the IR counterpart of the low–mass X–ray binary (LMXB) GX 5–1, since its position coincides

Table 8.3: Positions of the stars 502 and 513 obtained from a global astrometric plate solution. The accurate radio position from Berendsen et al. (2000) is also listed. In the last collumn the separation (d) between the radio position and the position of star 502 and 513 is given.

Stars	RA	DEC	σ	d
502	18:01:08.109	-25:04:43.02	0.25”	$\sim$ 1.9”
513	18:01:08.222	-25:04:42.46	0.25”	$\sim$ 0.2”
Radio	18:01:08:233	-25:04:42.044	0.04”	

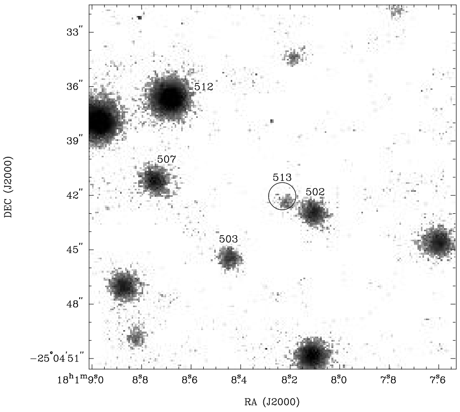

Figure 8.2: Logarithmically scaled section of the combined Brγ images obtained on 1999, October 8. The 3σ error in the astrometric solution is shown as a circle centred on the radio position of GX 5–1. The labels of the stars are those of Naylor et al. (1991).

with the accurate position of the radio counterpart. Furthermore, the Brγ–K instrumental color is smaller for star 513, when compared to the reference stars in the field. This effect, although only marginally detected might be caused by the presence of a Brγ emission line in the spectrum of star 513. The presence of an absorption line could result in a higher Brγ–K color, which might explain the higher value obtained for star 507.

The H and K magnitudes we derived are significantly lower than the H and K magnitudes derived by Naylor et al. (1991), but as they mention in their paper they estimate systematic errors to play a role (although these errors were estimated to be smaller than the discrepancy with our results). Bandyopadhyay et al. (1999) obtained IR spectra of the stars 502 and 503. Since they did not

Table 8.4: K band magnitudes, distance estimates, estimates of N_H*, calculated absolute* M_K*, best estimates of the* P_{orb} *and spectral type of different Z sources and GX 13+1.*

Stars	K band	D (kpc)[1]	N_H ($10^{21} cm^{-2}$)[1]	M_K	P_{orb} (hr)	Companion Type
Sco X–1	11.9 [2]	2.8	2.9	-0.5	18.9[9]	<G5 III[7] ($M_K \geq -1.4$)
GX 17+2	14.5 [3]	7.5	17.3	-1.1	–	–
	18.5			+2.9		
Cyg X–2	13.8 [2]	8.0	2.8	-0.9	236.2[8]	A9 III[8]($M_K \sim -0.7$)
GX 5–1	13.7	9.0	25.4	-2.8	–	–
GX 340+0	17.3 [4]	11.0	50	-1.0	–	–
GX 349+2	∼14 [5]	5.0	8.8	0.0	∼22[5,10] or 14 d[11]	–
GX 13+1	∼12 [6]	7.0	25.4	-3.8	–	K5 III[7]($M_K \sim -3.8$)

1. Christian & Swank (1997), Sco X–1 from Bradshaw et al. (1999); 2. Priv. comm. T. Shabhaz; 3. Callanan et al. (1999), magnitude when flaring; 4. Miller et al. (1993); 5. Wachter & Margon (1996); 6. Charles & Naylor (1992); 7. Bandyopadhyay et al. (1999); 8. Casares et al. (1998); 9. Gottlieb et al. (1975); 10. Barziv et al. (1997); 11. Southwell et al. (1996)

find evidence for emission typical of an accretion disk in these two stars, they suggested that star 513 might be the counterpart of GX 5–1. The counterpart (star 513) did not vary significantly in any of the three filters (H, K, and Brγ) we used. Its reddening uncorrected H–K color index is 0.4. Using the conversion of $N_H = 0.179 A_V 10^{22} cm^{-2}$ (Predehl & Schmitt 1995) and the estimate of N_H for GX 5–1 of $\sim 2.5 \times 10^{22} cm^{-2}$ (Christian & Swank 1997; see Table 8.4) we obtain $A_V \sim 14$. Using the relations found by Rieke & Lebofsky (1985) we obtained an intrinsic $(\mathrm{H}-\mathrm{K})_\circ = -0.5$. This is bluer than stellar (Tokunaga 2000), which may indicate an overestimate of the extinction. Limiting the intrinsic emission in the near–infrared to be no steeper than the Rayleigh–Jeans tail of a black–body implies $A_V \lesssim 12$.

In Table 8.4 we compare the K–band absolute magnitudes of the six Z sources plus the 'hybrid Z/atoll' source GX 13+1, based on the estimated distance and N_H to each source. There is a rather large range, from as bright as -3.8 for GX 13+1 to possibly as faint as $+2.9$ for GX 17+2 if the observed K magnitude in quiescence is as faint as ~ 18.5 (Callanan et al. 1999). Uncertainties in distance estimates and reddening are likely to be significant at a level of about ±1 magnitude, and so cannot account for the broad range. Several different components may contribute significantly to the emission in the near–infrared; as a guide to their significance (see below) we have also listed binary orbital periods and, where available, the spectral types of the mass donors in Table 8.4. Thermal emission will be produced both by the stellar companion and the accretion disc (for a discussion of their relative contributions see also Bandyopadhyay et al. 1997, 1999). We may expect the accretion-disc contribution to depend on the size of the disc (van Paradijs & McClintock 1994), which in turn should be a function of the orbital period of the system. We note that for the three systems with some attempt at spectral classification of the mass donor there is a good agreement between the absolute K band magnitudes derived and those expected for the companion spectral class. This implies that GX 5–1 should contain a relatively bright mass donor. Luminosity class III was found for the companion star in Sco X–1 and Cyg X–2 (see Table 8.4, and references therein). Following the conjecture made by Hasinger & van der Klis (1989) that all Z sources have evolved companions, we assume also luminosity class III for GX 5–1. The companion star in GX 5–1 is then most likely of spectral type K.

There may also be an additional contribution from infrared synchrotron emission, as found in the black hole system GRS 1915+105 (Fender & Pooley 1998 and references therein). If at all, this should only occur when the source is radio–bright. The Z sources are brightest at radio wavelengths when they are observed on the Horizontal Branch (HB) in the X-ray color–color diagram (Penninx et al. 1988; Hjellming & Han 1995). Radio flaring in Z sources typically has amplitudes of a few mJy (Hjellming & Han 1995 and references therein); if the synchrotron emission has a flat spectrum to the near–infrared we might observe a (reddened) contribution of $\gtrsim 1$ mJy at times. For GX 5–1 this could cause up to 1 magnitude variability. If star 513 is not the counterpart of GX 5–1, the counterpart must have been $\gtrsim 2.5$ magnitudes fainter in the K band at the time of our observations. Future spectroscopic observations and/or the detection of variability should confirm star 513 as the counterpart.

To conclude, we have most likely identified the IR counterpart of the bright Z–type X–ray source GX 5–1 based upon positional coincidence with the radio counterpart, an identification which is supported by marginal evidence for excess Brγ emission. We have discussed the possible origins of IR emission in this system and in the other Z sources (and GX 13+1), and suggest that GX 5–1 may contain a KIII mass donor.

Acknowledgments The UKIRT is operated by the Joint Astronomy Centre on behalf of the U.K. Particle Physics and Astronomy Research Council. The data reported here were obtained as part of the UKIRT Service Programme. We would like to thank Sandy Leggett for the May 23 observations and helpful comments in reducing the observations, John Davies for the October observations, Paul Vreeswijk for help with the reduction of the images, Tim Naylor for providing us with electronic versions of the images presented in Naylor et al. (1991) facilitating comparisons, and the referee, Phil Charles for his comments which improved the paper.

Bibliography

Bandyopadhyay, R., Shahbaz, T., Charles, P. A., van Kerkwijk, M. H., & Naylor, T. 1997, MNRAS, 285, 718

Bandyopadhyay, R. M., Shahbaz, T., Charles, P. A., & Naylor, T. 1999, MNRAS, 306, 417

Barziv, O., Kuulkers, E., Méndez, M., et al. 1997, A&A, 325, 1035

Berendsen, S. G. H., Fender, R., Kuulkers, E., Heise, J., & van der Klis, M. 2000, MNRAS, 318, 599

Bradshaw, C. F., Fomalont, E. B., & Geldzahler, B. J. 1999, ApJ, 512, L121

Braes, L., Miley, G., & Schoenmakers, A. 1972, Nature

Callanan, P. J., Filippenko, A. V., & Garcia, M. R. 1999, IAU Circ., 7219, 3+

Casares, J., Charles, P. A., & Kuulkers, E. 1998, ApJ, 493, L39

Charles, P. A. & Naylor, T. 1992, MNRAS, 255, 6P

Christian, D. J. & Swank, J. H. 1997, ApJS, 109, 177+

Deutsch, E. W., Margon, B., Anderson, S. F., Wachter, S., & Goss, W. M. 1999, ApJ, 524, 406

Fender, R. P. & Hendry, M. A. 2000, MNRAS, 317, 1

Fender, R. P. & Pooley, G. G. 1998, MNRAS, 300, 573

Gottlieb, E. W., Wright, E. L., & Liller, W. 1975, ApJ, 195, L33

Grindlay, J. E. & Seaquist, E. R. 1986, ApJ, 310, 172

Hambly, N. C., Miller, L., MacGillivray, H. T., Herd, J. T., & Cormack, W. A. 1998, MNRAS, 298, 897

Hasinger, G. & van der Klis, M. 1989, A&A, 225, 79

Hjellming, R. & Han, X. 1995, , eds Lewin, van Paradijs, van den Heuvel (ISBN 052141684, Cambridge Univ. Press, 1995.)

Lewin, W. H. G., Lubin, L. M., Tan, J., et al. 1992, MNRAS, 256, 545

Miller, B. W., Margon, B., & Burton, M. G. 1993, AJ, 106, 28

Naylor, T., Charles, P. A., & Longmore, A. J. 1991, MNRAS, 252, 203

Penninx, W., Lewin, W. H. G., Zijlstra, A. A., Mitsuda, K., & van Paradijs, J. 1988, Nature, 336, 146

Predehl, P. & Schmitt, J. H. M. M. 1995, A&A, 293, 889

Rieke, G. H. & Lebofsky, M. J. 1985, ApJ, 288, 618

Schechter, P. L., Mateo, M., & Saha, A. 1993, PASP, 105, 1342

Southwell, K. A., Casares, J., & Charles, P. A. 1996, in ASSL Vol. 208: IAU Colloq. 158: Cataclysmic Variables and Related Objects, 365+

Tarenghi, M. & Reina, C. 1972, Nature Physical Science, 240, 53

Tokunaga, A. 2000, Astrophysical Quantities (Allen's astrophysical quantities, 4th ed. Publisher: New York: AIP Press; Springer, 2000. Editedy by Arthur N. Cox. ISBN: 0387987460)

Urban, S. E., Corbin, T. E., & Wycoff, G. L. 1998, AJ, 115, 2161

van der Klis, M., Jansen, F., van Paradijs, J., et al. 1985a, IAU Circ., 4043, 1+

—. 1985b, Nature, 316, 225

van Paradijs, J. & McClintock, J. E. 1994, A&A, 290, 133

Wachter, S. & Margon, B. 1996, AJ, 112, 2684+

Wijnands, R., Méndez, M., van der Klis, M., et al. 1998, ApJ, 504, L35

Chapter 9

Discovery of a kHz QPO in 2S 0918–549

Peter G. Jonker, Michiel van der Klis, Jeroen Homan, Mariano Méndez, Jan van Paradijs, Tomaso Belloni, Chryssa Kouveliotou, Walter Lewin, & Eric C. Ford

The Astrophysical Journal, 2001, **553**, 335

Abstract

We report the discovery of a kilohertz quasi–periodic oscillation (kHz QPO) in the low–mass X–ray binary (LMXB) 2S 0918–549. The kHz QPO has a frequency of 1156±9 Hz, a FWHM of 70±20 Hz, and a fractional rms amplitude of 18%±2%. We also detected for the first time a type I X–ray burst in this source. The compact object must therefore be a neutron star. Finally, we were able to classify the source as an atoll source exhibiting the full complement of spectral/timing states of this class (island and banana). From the peak burst flux an upper limit on the persistent luminosity can be derived of 0.5% of the Eddington luminosity, making 2S 0918–549 one of the least luminous LMXBs showing a kHz QPO. We compare the fractional rms amplitudes of the upper kHz QPO across the ensemble of LMXBs. We find a strong anticorrelation with luminosity. In LMXBs with luminosities $\sim$100 times lower than those of Z–sources, the fractional rms amplitude is a factor $\sim$10 larger.

9.1 Introduction

Observations with the *Rossi X–ray Timing Explorer* (RXTE) satellite have revealed the presence of several quasi–periodic phenomena in the Fourier power spectra of low–mass X–ray binaries (LMXBs). They occur on timescales similar to the dynamical timescale near a neutron star, i.e. at frequencies around 1000 Hz. Kilohertz quasi–periodic oscillations (kHz QPOs) have been discovered in more than 20 sources (van der Klis et al. 1996; Strohmayer et al. 1996b; see for the most recent review van der Klis 2000). In several LMXBs nearly coherent oscillations were discovered during type I X-ray bursts (Strohmayer et al. 1996b; for a review see Swank 2001); these burst oscillations presumably occur at frequencies close to the neutron star spin frequency (Strohmayer et al. 1996b). Recently, another high frequency quasi-periodic phenomenon was discovered in the power spectra of three LMXBs (Jonker et al. 2000).

The kHz QPOs are nearly always found in pairs, although in a few sources so far only one kHz QPO has been found (Zhang et al. 1998; Marshall & Markwardt 1999; Homan & van der Klis 2000). Their frequencies vary over several hundred Hz on timescales of hours to days; in the best studied sources, it is found that the frequency separation of the twin kHz QPOs, $\nu_2 - \nu_1$, decreases monotonically by 50–100 Hz over the observed frequency range as the frequency of the kHz QPO increases (see e.g. van der Klis et al. 1997; Méndez et al. 1998b; Méndez et al. 1998; Méndez & van der Klis 1999); observations of the kHz QPO frequencies in the other sources are consistent with this trend (Jonker et al. 1998; Psaltis et al. 1998).

Various models exist for these QPOs. Immediately after their discovery a beat frequency model was proposed (Strohmayer et al. 1996b), of which the sonic–point model is the most current (Miller et al. 1998; revised by Lamb & Miller 2001). Later, Stella & Vietri (1999) proposed the relativistic precession model (but see Marković & Lamb 2001) and Osherovich & Titarchuk (1999) introduced the two–oscillator model. In the latter model the QPO at ν_1 (the lower kHz QPO) occurs at the Keplerian frequency of material orbiting the neutron star, whereas in the other two models the QPO at ν_2 (the upper kHz QPO) is the one that is Keplerian. Recently, Psaltis & Norman (2001) proposed the transition layer model in which the twin kHz QPO peaks arise due to disk oscillations at frequencies close to those predicted by the relativistic precession model.

In this Letter, we report the discovery of a kHz QPO and a type I X–ray burst in 2S 0918–549. The source turns out to be one of the least luminous kHz QPO sources, however, the fractional rms amplitude of the QPO is quite high. We

Table 9.1: Log of the observations of 2S 0918–549 used in this analysis. The count rates in column 5 are the average, background subtracted, 2–60 keV count rates obtained as if 5 PCUs were always operational.

	Observation ID	Date & Start time (UTC)	Amount of data (ksec)	Average count rate cnts/sec (2–60 keV)
1	20071-11-01-02	02-05-1997 23:57	∼4.2	∼36
2	20071-11-01-03	03-05-1997 02:15	∼2.1	∼36
3	20071-11-01-04	03-05-1997 06:42	∼1.8	∼45
4	20071-11-01-05	03-05-1997 08:26	∼1.4	∼50
5	20071-11-01-06	04-05-1997 08:27	∼1.5	∼53
6	20071-11-01-00	04-05-1997 22:41	∼11.3	∼47
7	20071-11-01-01	05-05-1997 22:16	∼6.0	∼48
8	20071-11-01-07	09-05-1997 10:10	∼2.4	∼54
9	20064-06-01-00	15-08-1997 01:38	∼4.8	∼84
10	20064-06-02-00	21-09-1997 22:51	∼5.0	∼68
11	50060-01-01-00	12-05-2000 12:24	∼30.0	∼135
12	50060-01-01-01	14-05-2000 19:43	∼2.1	∼187
13	50060-01-01-02	15-05-2000 04:59	∼2.4	∼208

study the dependence of the fractional rms amplitudes of the upper kHz QPO on source luminosity across the ensemble of LMXBs and show that they are strongly anticorrelated.

9.2 Observations and analysis

We have used observations obtained with the proportional counter array (PCA; Jahoda et al. 1996) onboard the *RXTE* satellite (Bradt et al. 1993). A log of the observations and the average source count rates at the time of the observation can be found in Table 9.1. In total ∼75 ksec of data were used in our analysis. Data were obtained in four different modes. The Standard 1 and 2 modes, which are always operational, respectively provide data with a time resolution of 0.125 seconds in just one energy bin and 16 seconds in 129 energy bins covering the effective PCA 2 to 60 keV range. Additionally, data were obtained using the mode providing the highest time resolution ($\sim 1\mu s$), combined with the full energy resolution *RXTE* can provide (256 energy bins covering the 2 to 60 keV; the GoodXenon mode). This mode saturates on count rates higher than ∼8000 counts per second.

In order to follow spectral variations we created color–color diagrams (CDs) by plotting a soft color vs. a hard color. The soft color was defined as the ratio between the count rates in the 3.5–6.4 keV and 2–3.5 keV energy band; the hard color was defined as that between the 9.7–16.0 keV and 6.4–9.7 keV energy band. The data were background subtracted but no dead–time corrections were applied (the dead–time is less than ∼2%). The colors of the 1997 observations were corrected for PCA gain changes, using Crab observations obtained in May 1997, and May 2000. Assuming the Crab is constant, observed color changes of the Crab between the observations of May 1997 and May 2000 should reflect changes of the instrument's spectral response. The observed changes in Crab were ∼6% in the soft color and ∼1% in the hard color. The colors were converted to those which would have been detected by the PCA on May 2000 (cf. Di Salvo et al. 2001). Residual color errors due to the differences between the spectra of Crab and 2S 0918–549 are less than the statistical errors.

We calculated Fast Fourier Transforms with a Nyquist frequency of 4096 Hz of data segments of 16 seconds (2–60 keV). The power density spectra were averaged and fitted with a function consisting of Lorentzians (to represent peaks arising in the power spectrum due to QPOs), a constant to account for the power due to Poisson counting statistics, and an exponentially cutoff power law to represent the noise component apparent at low frequencies. Errors on the fit parameters were calculated using $\Delta\chi^2 = 1.0$ (1σ single parameter). The 95% confidence upper limits were determined using $\Delta\chi^2 = 2.71$.

9.3 Results

The color–color diagram of 2S 0918–549 (see Figure 9.1; left) resembles that of an atoll source. The squares represent the average of 256 s of data from observations 1–10, the filled circles are 128 s averages from observation 11, and the open circles are 128 s averages from observations 12 and 13. Together with the timing properties (described below) it is clear that the squares represent the Island state and the open and filled circles the banana branch of an atoll source.

The average power spectrum of observations 1–10 combined (see Figure 9.1, right, top) shows a strong band limited noise component, which could be described using an exponentially cutoff power law with a fractional rms amplitude of 26%±1% (integrated over 0.1–100 Hz, 2–60 keV), a power law index of 0.47±0.05, and a cutoff frequeny of 21±6 Hz. We derived a 95% confidence upper limit on the presence of a kHz QPO with a full-width at half maximum (FWHM) 100 Hz in the range of 300–1200 Hz of ∼30% (rms).

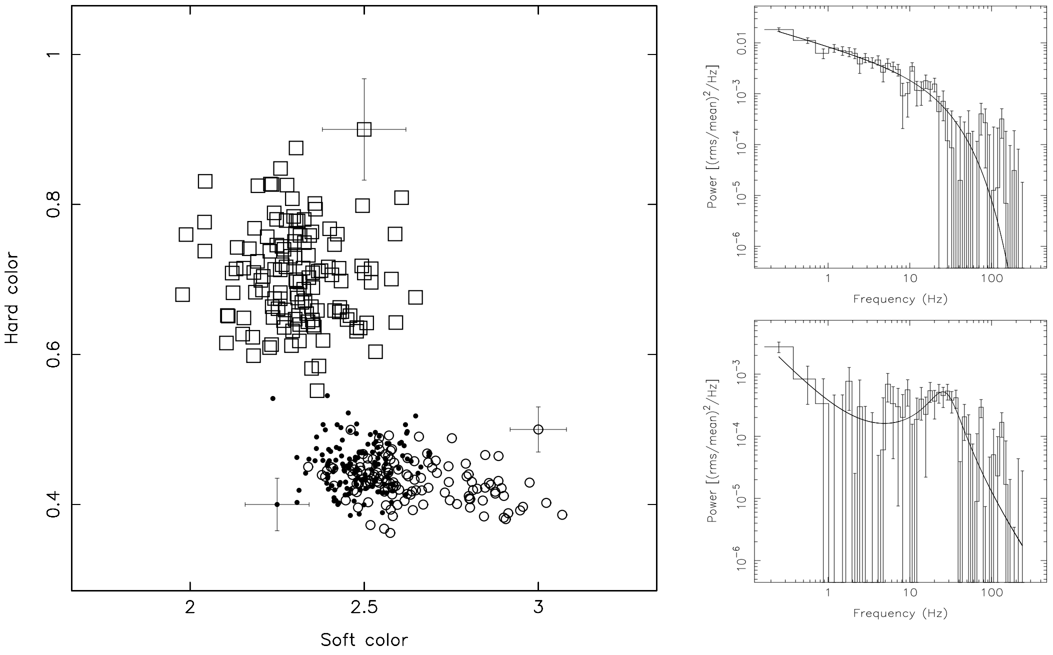

Figure 9.1: Left: Color–color diagram of 2S 0918–549. The data were background subtracted, the colors of the 1997 observations were converted to the May 2000 observations using the Crab as a reference (see text), and the burst was removed. No dead–time corrections have been applied (the dead–time is ~2%). The squares and circles are 256 s and 128 s averages, respectively. Typical error bars are shown for each category. The pattern resembles the Island state (squares) and the banana branch (open and filled circles) of atoll sources (see Hasinger & van der Klis 1989). The data in which the kHz QPO was present are represented by filled circles. Right, top: Rms normalized, Poisson noise subtracted average power spectrum of the observations 1–10 (squares). Strong band limited noise is present, establishing the identification of the Island state. The solid line is the best fit to the data with a cut–off powerlaw. Right, bottom: Rms normalized, Poisson noise subtracted average power spectrum of the observations 11–13 (circles). Banana state power law noise and a peaked noise component are present. The solid line is the best fit to the data with a powerlaw and a Lorentzian component.

We discovered a kHz QPO at 1156±9 Hz, with a FWHM of 68±23 Hz, and a fractional rms amplitude of 18%±2% (2–60 keV) in the average power spectrum of observation 11 (see Figure 9.2). In addition, the average power spectrum of observation 11 (Figure 9.1, right, bottom) shows a peaked noise component at a frequency of 25±2 Hz, with a fractional rms amplitude of 17%±2%, and a FWHM of 22±6 Hz. To investigate the peak noise component and the kHz QPO further, we also calculated power spectra using data in the 4.0–18.0 keV energy band. The values measured in the 4.0–18.0 keV energy band are the same within the errors, although the significance of the detection of the kHz QPO is somewhat higher (6.1σ compared to 5.7 σ in the 2–60 keV band). We subdivided the 4.0–18.0 keV power spectra of observation 11 in two parts. The frequency of the kHz QPO increased from 1126±9 Hz in the first part of observation 11 to 1218±20 Hz at the end. The source moved further up the banana branch, from an average hard and soft color of 0.452±0.003 and 2.49±0.01 to 0.431±0.003 and 2.64±0.01, respectively. The background subtracted count rate in the 4.0–18.0 keV energy band, the FWHM, and the fractional rms amplitude are consistent with being the same in the two parts. The properties of the peaked noise component were consistent with being the same in the two selections.

No power spectral components were detected in the average power spectrum of observations 12 and 13 combined. We derived an upper limit on the presence of a 100 Hz wide kHz QPO of ~13% rms in the range between 300–1200 Hz in both the 2–60 keV and the 4.0–18.0 keV energy band, and an upper limit of 5%–6% on the presence of a power law component at frequencies in the range of 0.1 to 100 Hz in both the 2–60 keV and the 4.0–18.0 keV energy band, with a power law index of 1.0.

During observation 11 a type I X–ray burst occurred (see Figure 9.3). This is the first detection of a burst in 2S 0918–549, and establishes the compact object as a neutron star. As apparent in Figure 9.3 the burst profile was complex, with a smooth exponential decay with an e-folding time of 8.95±0.05 s beginning ~ 10 seconds after the initial rise. Due to the very high count rates of more than 20000 counts per second (3 detector count rate) the GoodXenon mode saturated. The total count rate displayed in Figure 9.3 is for the 0.125 s Standard 1 data which were not affected by this saturation. During the part of the decay where the count rate was less than 8000 counts per second spectral analysis shows cooling of the blackbody spectral component. Using the 16 s Standard 2 mode we derive a flux for the 16 s bin containing the burst peak of 3.5×10^{-8} erg cm^{-2} s^{-1} (2-20 keV). Since the mean count rate in this 16 s time bin is a factor of ≥ 2.5 lower than the peak count rate as measured using the 1/8 s bin of the Standard 1 observations, we

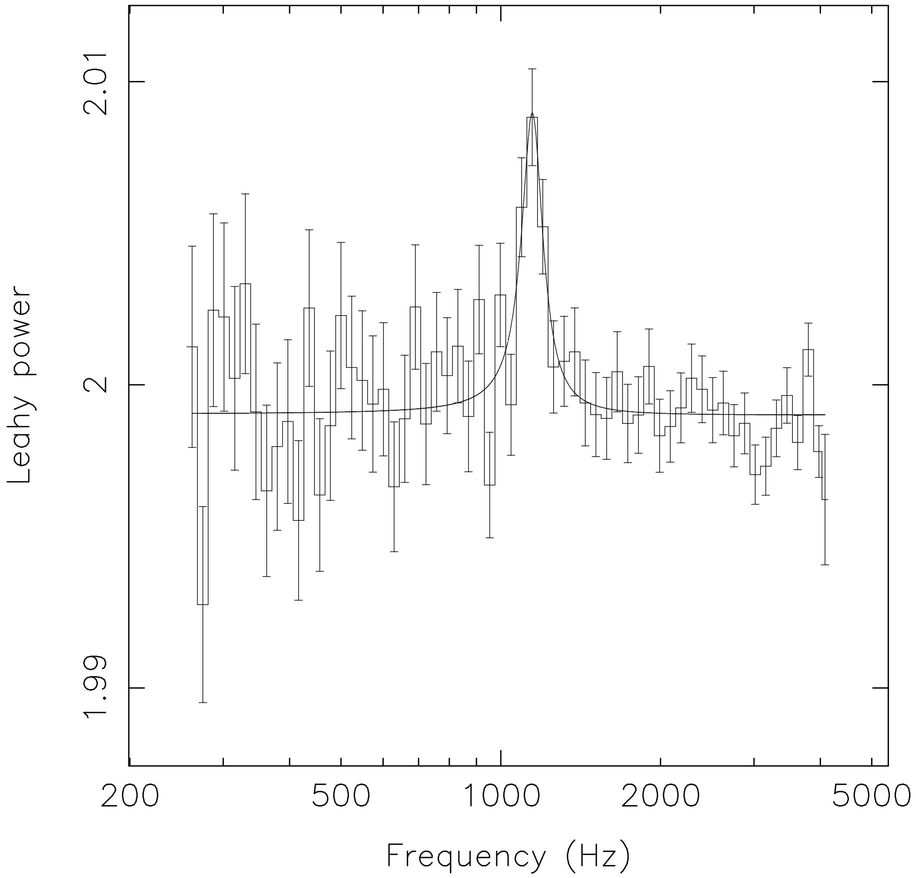

*Figure 9.2: Average 4.0–18.0 keV power density spectrum of observation 11, normalized after Leahy et al. (1983), showing the kHz QPO at 1156±9 Hz (*6.1σ *single trial). The solid line represents the best fit to the data.*

use this factor to improve our estimation of the peak burst flux. We did not correct for the deadtime effects which become important at the count rates at the peak of the burst (~25%), this provides a lower limit on the peak flux. The pre–burst flux is less than 4.2×10^{-10} erg cm^{-2} s^{-1} (2-20 keV). So, the persistent emission of the source when it is on the lower banana branch is less than 0.5 percent of the Eddington luminosity. Assuming the peak burst flux to be isotropic and at or below the Eddington limit of 2.5×10^{38} erg s^{-1} we derive an upper limit to the distance of 4.9 kpc.

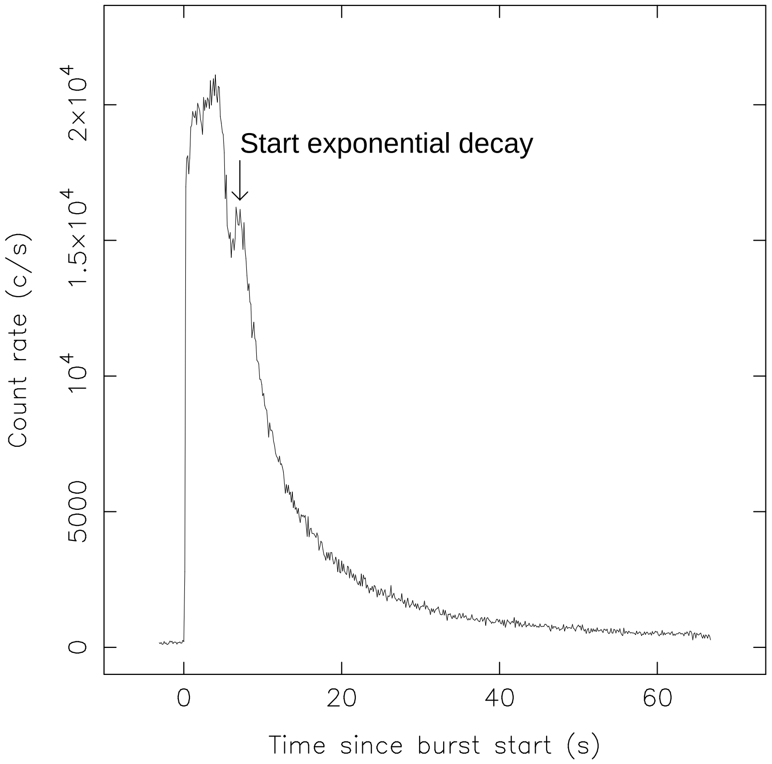

Figure 9.3: Lightcurve showing the profile of the type I X-ray burst occurring during observation 11. The X-axis denotes the time since the start of the burst. Note the complex burst profile and the large increase in count rate during the burst compared with the persistent emission. The count rate is that of the three detectors that were operational only.

9.4 Discussion

We discovered a kHz QPO at a frequency of ∼1156 Hz with a fractional rms amplitude of nearly 20% (2–60 keV) in the X–ray emission of the LMXB 2S 0918–549. For the first time in this source a type I X–ray burst was detected, establishing the nature of the compact object in 2S 0918–549 as a neutron star. We derived an upper limit to the persistent luminosity when the source is on the lower banana branch of 0.005 L_{Edd} making 2S 0918–549 one of the least luminous LMXBs in which a kHz QPO has been observed. The spectral and timing properties indicate that this source is a low–luminous atoll source, displaying the full complement of spectral and timing states (island state and a full banana branch). Similar to other kHz QPO sources, e.g. Méndez et al. (1999), the kHz QPO was only observed when the source was on the lower part of the banana branch. Its frequency changed from 1126±8 Hz to 1218±20 Hz, when the source moved further on the banana branch, similar to other atoll sources (e.g. Méndez et al. 1999). Its frequency is similar to the frequency of the *upper* kHz QPO in other atoll sources in a similar lower–banana state (e.g. Di Salvo et al. 2001, Méndez et al. 1999). The frequency of the lower kHz QPO is usually lower in that part of the CD. Furthermore, when both QPOs of the twin kHz QPOs are detected simultaneously the frequency of the lower kHz QPO has never been found at frequencies larger than $\sim$900 Hz in any LMXB (see van der Klis 2000). Therefore, we conclude that this kHz QPO is most likely the upper peak of the kHz QPO pair which is detected in most other LMXBs.

After 4U 0614+109, 2S 0918–549 is another example of a very low luminous LMXB whose kHz QPOs are strong, whereas in the most luminous LMBXs, the Z–sources, the kHz QPOs tend to be weak (see also the review of van der Klis 2000). To further investigate this, we compared the fractional rms amplitudes of the kHz QPO in 2S 0918–549 with those of the upper kHz QPO in other LMXBs. In order to account for the fact that in a given source the fractional rms amplitude of the kHz QPO changes as its frequency changes we measured the fractional rms amplitude at both the lowest and highest frequency at which the upper kHz QPO is found. From extensive studies for several sources it is clear that the fractional rms amplitude of the upper kHz QPO decreases monotonically as the frequency of the upper peak increases (e.g. Wijnands et al. 1997; Jonker et al. 1998; Wijnands et al. 1998; Méndez et al. 2001). This ensures that the method we used will yield a good indication of the range in fractional rms amplitude spanned in each source. The sample we studied here contains only those sources for which a significant detection of the upper kHz QPO in the 5–60 keV energy range was possible (4U 0614+09; Ford et al. 1996 4U 1915–05, Boirin et al. 2000; 4U 1728–34, Strohmayer et al. 1996a; 4U 1608–52, Méndez et al. 1998a; 4U 1702–42, Markwardt et al. 1999; 4U 1636–53, Zhang et al. 1996; 4U 1820–30, Smale et al. 1996; XTE J2123–058, Homan et al. 1999; KS 1731–260, Wijnands & van der Klis 1997), or in case of the Z-sources, the 5-60 keV fractional rms amplitude that was reported in the literature (Cyg X–2, Wijnands et al. 1998; GX 17+2, Wijnands et al. 1997; GX 340+0, Jonker et al. 1998). Sco X–1 was not included since the fractional rms amplitude of the QPOs can not be calculated accurately at present due to the severe dead-time effects present in this source. We calculated the 5–60 keV fractional rms amplitude in order to avoid as much as possible systematic effects on the derived fractional rms amplitudes of the peaks due to the different

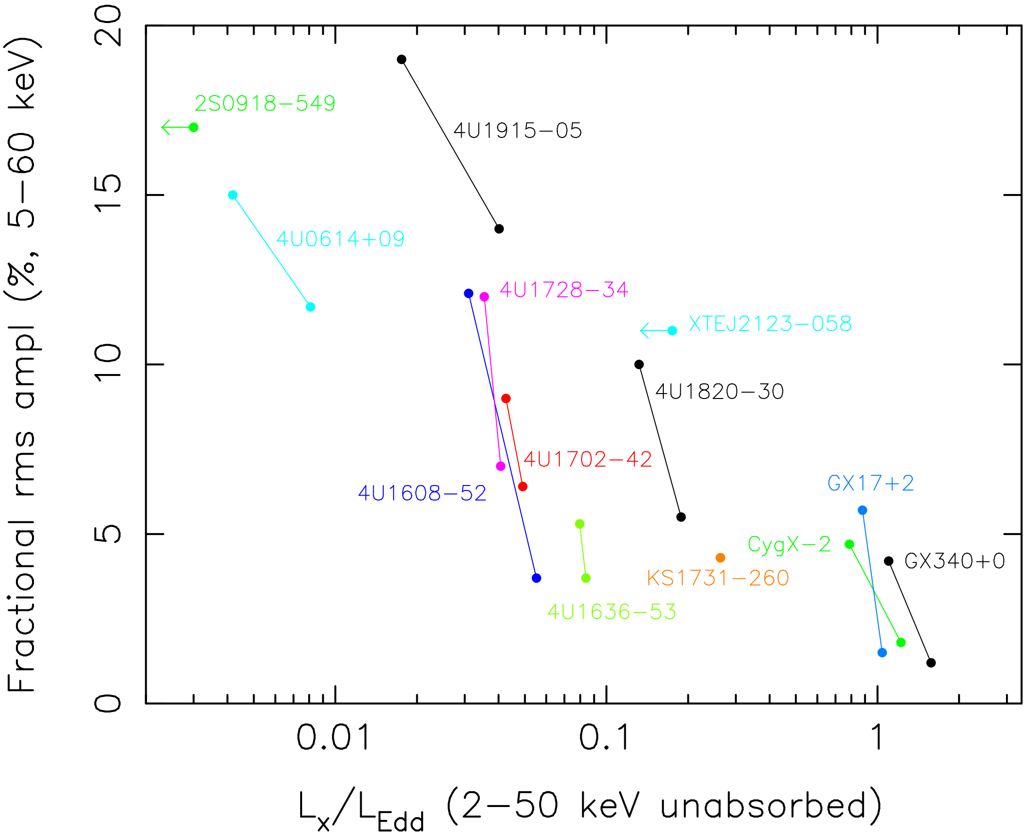

Figure 9.4: Luminosity versus fractional rms amplitude (5–60 keV) of the upper kHz QPO in various LMXBs. Apparent is the decrease in fractional rms amplitude as the source luminosity increases, both within one source and between sources.

N_H values towards the various sources.

The range in fractional rms amplitude of the upper kHz QPO in each source is plotted in Figure 9.4 as a function of the simultaneously measured luminosity (for the distances and the method used to calculate these luminosities see Ford et al. 2000 and references therein; the distance to 4U 1915–05 was taken from Smale et al. 1988). It is apparent that the upper kHz QPOs detected in low–luminosity sources have relatively large fractional rms amplitudes, when compared with the fractional rms amplitude of the kHz QPO in the bright LMXBs (e.g. the Z-sources). The frequencies of the end–points for each source are given in Table 9.2.

van Paradijs & van der Klis (1994) found that the hardness, defined as the ratio

Table 9.2: The lowest and highest frequency of the upper kHz QPO for each source used to create Figure 4.

Source name	Lowest frequency upper kHz (Hz)	Highest frequency upper kHz (Hz)
2S 0918–549	1156±9	1156±9
4U 0614+09	421±13	1161±5
4U 1915–05	542±14	1013±8
4U 1608–52	883±4	1091±8
4U 1728–34	552±7	1139±13
4U 1702–42	1000±9	1059±11
4U 1636–53	1152±4	1213±11
4U 1820–30	675±4	1050±4
XTE J2123–058	1129±8	1129±8
KS 1731–260	1176±3	1176±3
Cyg X–2	731±19	1007±15
GX 17+2	645±9	1086±8
GX 340+0	535±70	840±20

of counts between the 40–80 keV band and the 13–25 keV band, is in neutron star LMXBs correlated with the X–ray luminosity. This suggests that the X–ray flux variability of the source at the kHz QPO frequency is correlated with the hardness in that band (see also Ford et al. 1997). Within a source a similar correlation between the fractional rms amplitude of the upper kHz QPO and the hardness of the energy spectrum has been found; the harder the source the higher the fractional rms amplitude of the upper kHz QPO (e.g. 4U 0614+091, Ford et al. 1997, van Straaten et al. 2000; 4U 1608–52, Méndez & van der Klis 1999; Aql X–1, Reig et al. 2000; 4U 1728–34, Di Salvo et al. 2001; Cyg X–2, Wijnands et al. 1998; GX 17+2, Wijnands et al. 1997; GX 340+0, Jonker et al. 1998).

A two–component accretion flow (radially and through a disk, Ghosh & Lamb 1979) has been considered to explain that the frequency of the kHz QPO does not depend on source luminosity (Ford et al. 2000). The observed anticorrelation between the fractional rms amplitude of the upper kHz QPO and the source luminosity cannot solely be explained by an increase of an unmodulated part of the accretion flow towards higher source luminosity, since the increase in luminosity is too large compared with the decrease in fractional rms amplitude. Therefore, this cannot explain the findings of Ford et al. (2000). The same conclusion was drawn by Méndez et al. (2001) on other grounds. It is important to consider the anticorrelation presented in this work and the absence of a correlation reported by Ford et al. (2000) in mechanisms producing kHz QPOs.

Acknowledgments This work was supported in part by the Netherlands Organization for Scientific Research (NWO) grant 614-51-002. This research has made use of data obtained through the High Energy Astrophysics Science Archive Research Center Online Service, provided by the NASA/Goddard Space Flight Center. This work was supported by NWO Spinoza grant 08-0 to E.P.J.van den Heuvel. WHGL gratefully acknowledges support by NASA.

Bibliography

Boirin, L., Barret, D., Olive, J. F., Bloser, P. F., & Grindlay, J. E. 2000, A&A, 361, 121
Bradt, H. V., Rothschild, R. E., & Swank, J. H. 1993, A&AS, 97, 355
Di Salvo, T., Méndez, M., van der Klis, M., Ford, E., & Robba, N. R. 2001, ApJ, 546, 1107
Ford, E., Kaaret, P., Tavani, M., et al. 1997, ApJ, 475, L123
—. 1996, IAU Circ., 6426, 2+
Ford, E. C., van der Klis, M., Méndez, M., et al. 2000, ApJ, 537, 368
Ghosh, P. & Lamb, F. K. 1979, ApJ, 234, 296
Hasinger, G. & van der Klis, M. 1989, A&A, 225, 79
Homan, J., Méndez, M., Wijnands, R., van der Klis, M., & van Paradijs, J. 1999, ApJ, 513, L119
Homan, J. & van der Klis, M. 2000, ApJ, 539, 847
Jahoda, K., Swank, J. H., Giles, A. B., et al. 1996, Proc. SPIE, 2808, 59
Jonker, P. G., Méndez, M., & van der Klis, M. 2000, ApJ, 540, L29
Jonker, P. G., Wijnands, R., van der Klis, M., et al. 1998, ApJ, 499, L191
Lamb, F. K. & Miller, M. C. 2001, ApJ, 554, 1210
Leahy, D. A., Darbro, W., Elsner, R. F., et al. 1983, ApJ, 266, 160
Marković , D. & Lamb, F. K. 2001, MNRAS
Markwardt, C. B., Strohmayer, T. E., & Swank, J. H. 1999, ApJ, 512, 125
Marshall, F. E. & Markwardt, C. B. 1999, IAU Circ., 7103
Méndez, M. & van der Klis, M. 1999, ApJ, 517, L51
Méndez, M., van der Klis, M., & Ford, E. 2001, ApJ
Méndez, M., van der Klis, M., Ford, E. C., Wijnands, R., & van Paradijs, J. 1999, ApJ, 511, L49
Méndez, M., van der Klis, M., & van Paradijs, J. 1998, ApJ, 506, L117
Méndez, M., van der Klis, M., van Paradijs, J., et al. 1998a, ApJ, 494, L65
Méndez, M., van der Klis, M., Wijnands, R., et al. 1998b, ApJ, 505, L23
Miller, M. C., Lamb, F. K., & Psaltis, D. 1998, ApJ, 508, 791
Osherovich, V. & Titarchuk, L. 1999, ApJ, 522, L113
Psaltis, D., Méndez, M., Wijnands, R., et al. 1998, ApJ, 501, L95
Psaltis, D. & Norman, C. 2001, ApJ, submitted
Reig, P., Méndez, M., van der Klis, M., & Ford, E. C. 2000, ApJ, 530, 916
Smale, A. P., Mason, K. O., White, N. E., & Gottwald, M. 1988, MNRAS, 232, 647
Smale, A. P., Zhang, W., & White, N. E. 1996, IAU Circ., 6507, 1+
Stella, L. & Vietri, M. 1999, Phys. Rev. Lett
Strohmayer, T., Zhang, W., & Swank, J. 1996a, IAU Circ., 6320, 1+
Strohmayer, T. E., Zhang, W., Swank, J. H., et al. 1996b, ApJ, 469, L9
Swank, J. H. 2001, in IAU Symposium 195, ed. P. C. H. Martens, S. Tsuruta, and M. A. Weber, (San Francisco: ASP)
van der Klis, M. 2000, ARA&A, 38, 717
van der Klis, M., Swank, J. H., Zhang, W., et al. 1996, ApJ, 469, 1
van der Klis, M., Wijnands, R. A. D., Horne, K., & Chen, W. 1997, ApJ, 481, L97
van Paradijs, J. & van der Klis, M. 1994, A&A, 281, L17
van Straaten, S., Ford, E. C., van der Klis, M., Méndez, M., & Kaaret, P. 2000, ApJ, 540, 1049
Wijnands, R., Homan, J., van der Klis, M., et al. 1998, ApJ, 493, L87
—. 1997, ApJ, 490, L157

Wijnands, R. A. D. & van der Klis, M. 1997, ApJ, 482, L65
Zhang, W., Jahoda, K., Kelley, R. L., et al. 1998, ApJ, 495, L9
Zhang, W., Lapidus, I., White, N. E., & Titarchuk, L. 1996, ApJ, 473, L135

Chapter 10

Discovery of a new, third kHz QPO in 4U 1608–52, 4U 1728–34, and 4U 1636–53. Sidebands to the lower kHz QPO?

Peter G. Jonker, Mariano Méndez, Michiel van der Klis

Astrophysical Journal Letters, 2000, **540**, L29

Abstract

We report the discovery of a third kilohertz quasi–periodic oscillation (kHz QPO) in the power spectra of the low–mass X–ray binaries 4U 1608–52 (6.3σ), 4U 1728–34 (6.0σ), and 4U 1636–53 (3.7σ) which is present simultaneously with the previously known kHz QPO pair. The new kHz QPO is found at a frequency that is 52.8±0.9 Hz, 64±2 Hz, 58.4±1.9 Hz higher than the frequency of the lower kHz QPO in 4U 1608–52, 4U 1728–34, and 4U 1636–53, respectively. The difference between the frequency of the new kHz QPO and the lower kHz QPO increased in 4U 1608–52 from 49.6±1.4 Hz to 53.9±0.5 Hz when the frequency of the lower kHz QPO increased from 672 Hz to 806 Hz. Simultaneously the difference between the frequency of the new kHz QPO and the upper kHz QPO increased by $\sim$60 Hz, suggesting that the new kHz QPO is unrelated to the upper kHz QPO. In 4U 1636–53 a fourth, weaker, kHz QPO is simultaneously detected (3σ) at the same frequency separation below the lower kHz QPO, suggesting the new kHz QPOs are sidebands to the lower kHz QPO. We discuss the nature of this new kHz QPO and its implications on the models for the kHz QPOs.

10.1 Introduction

In the last four years observations with the *Rossi X–ray Timing Explorer* (RXTE) satellite have revealed the presence of several quasi–periodic phenomena at frequencies higher than 100 Hz in the Fourier power spectra of low–mass X–ray binaries (LMXBs). First, the kilohertz quasi–periodic oscillations (kHz QPOs) were discovered (van der Klis et al. 1996b,a; Strohmayer et al. 1996a,b; for the most recent review see van der Klis 2000). Somewhat later, nearly coherent oscillations were discovered during type I X–ray bursts in several of these LMXBs; these burst oscillations presumably occur at frequencies close to the neutron star spin frequency (Strohmayer et al. 1996b; for a review see Swank 2001)

The kHz QPOs are nearly always found in pairs. Although their frequencies can vary over several hundred Hz, the frequency separation between the twin kHz QPOs, $\nu_2 - \nu_1$, remains approximately constant, close to the inferred spin frequency of the neutron star (but see e.g. van der Klis et al. 1997; Méndez et al. 1998; Méndez et al. 1998; Méndez & van der Klis 1999). Various models exist for the origin of these QPOs. Immediately after their discovery a beat frequency model was proposed (Strohmayer et al. 1996b), of which the sonic–point model is the most elaborate example (Miller et al. 1998). Later, Stella & Vietri (1999) proposed the relativistic precession model (see also Psaltis & Norman 2001; Marković & Lamb 2001) and Osherovich & Titarchuk (1999b) introduced the two–oscillator model. In the latter model the QPO at ν_1 (the lower kHz QPO) occurs at the Keplerian frequency of material orbiting the neutron star, whereas in the other two models the QPO at ν_2 (the upper kHz QPO) is the one that is Keplerian.

The possibility that sidebands to the two main kHz peaks could occur was mentioned by several authors (Miller et al. 1998; Psaltis & Norman 2001), but no sidebands, nor in fact any other kHz QPOs beyond the initial pair were detected up to now (see e.g., Méndez & van der Klis 2000). In the LMXBs 4U 1608–52, 4U 1728–34, and 4U 1636–53 the kHz QPOs have been extensively studied on previous occasions (4U 1608–52, Berger et al. 1996; Méndez et al. 1998, 1999; Yu et al. 1997; 4U 1728–34, Strohmayer et al. 1996a,b; Ford & van der Klis 1998; Méndez & van der Klis 1999; 4U 1636–53, Zhang et al. 1996; Wijnands et al. 1997; Méndez et al. 1998; Kaaret et al. 1999; Méndez 2000).

In this Letter, we describe the discovery of a new, third kHz QPO close to the lower kHz QPO in these three sources, which is probably an upper sideband to the lower kHz QPO. We discuss briefly the possible implications of this discovery in terms of the existing models for the kHz QPOs.

Table 10.1: Log of the observations of 4U 1636–53 used in this analysis. For the observations we used in our analysis of the other sources see main text.

Observation ID	Date & Start time (UTC)
10088-01-01-00	27-04-1996 13:45
10088-01-02-00	29-04-1996 17:37
10088-01-03-00	30-04-1996 16:03
10088-01-07-01	09-11-1996 20:53
10088-01-08-03	31-12-1996 18:23
10088-01-06-01	06-01-1997 05:58
10088-01-06-07	06-01-1997 08:32
30053-02-01-000	24-02-1998 23:26
30053-02-01-001	25-02-1998 05:55
30053-02-02-02	19-08-1998 08:15
30053-02-02-01	19-08-1998 13:03
30053-02-01-01	20-08-1998 01:50
30053-02-01-02	20-08-1998 03:26

10.2 Observations and analysis

We have used observations obtained with the proportional counter array (PCA; Jahoda et al. 1996) onboard the RXTE satellite (Bradt et al. 1993). The observations of 4U 1608–52 used here are the same as those described by Méndez et al. (1999); the observations of 4U 1728–34 are those used by Strohmayer et al. (1996a,b); Ford & van der Klis (1998); Méndez & van der Klis (1999). The observations of 4U 1636–53 used in this paper are listed in Table 10.1.

We used data with a time resolution of at least 122μs to calculate power spectra of data segments of 64 s up to a Nyquist frequency of 4096 Hz in two different energy bands, from 2.0–8.7 keV and from 8.7–60 keV if available, and in one band combining the total effective PCA energy range (2.0–60 keV). Observation 10094-01-01-00 of 4U 1608–52 only covered the 2.0–13.2 keV band and we excluded it in the calculation of the fractional rms amplitudes of QPOs. We selected only those power spectra in which a narrow (full–width at half maximum, FWHM, less than $\sim$10 Hz) lower kHz QPO was observed. This resulted in $\sim$67, $\sim$92, and $\sim$80 ksec of data in the 2.0–60 keV range which corresponds to $\sim$18%, $\sim$12%, and

$\sim$15% of the total amount of analyzed data for 4U 1608–52, 4U 1728–34, and 4U 1636–53, respectively.

We traced the lower kHz QPO using a dynamical power spectrum (e.g. see plate 1 in Berger et al. 1996) displaying consecutive power spectra to visualize the time evolution of the QPO frequency. For each source separately, we fitted this QPO peak in each power spectrum in the range 100 Hz above and 100 Hz below the traced QPO frequency (so to exclude the upper kHz QPO) with a constant plus a Lorentzian. For each source separately, we used the shift-and-add method described by Méndez et al. (1998) to shift each lower kHz QPO peak to the same frequency and average the aligned power spectra. We then fitted each average power spectrum (one per source) with a constant plus Lorentzians to represent the QPOs. Errors on the fit parameters were calculated using $\Delta\chi^2 = 1.0$ (1σ single parameter). The 95% confidence upper limits were determined using $\Delta\chi^2 = 2.71$.

10.3 Results

Figure 10.1 shows the resulting power spectra for 4U 1608–52, 4U 1728–34, and 4U 1636–53 after applying the abovementioned procedure. We discovered a new kHz QPO in these three sources at a frequency that is, respectively, 52.8±0.9 Hz, 64±2 Hz, and 58.4±1.9 Hz higher than that of the lower kHz QPO, at a significance level of 6.3σ, 6.0σ, and 3.7σ (single trial), respectively (Table 10.2). This new kHz QPO is detected at the same time as the twin kHz QPOs that were already known in these sources.

In 4U 1636–53 we detected a fourth kHz QPO, at the same frequency separation below the lower kHz QPO (Figure 10.1, Table 10.2). This new kHz QPO was detected in a single trial, at a 3σ significance level. The presence of two, symmetrically located, peaks on either side of the lower kHz QPO suggests the new kHz QPOs are sidebands to the main peak and from now on we will refer to these new kHz QPOs as such. No significant lower sidebands could be detected in the other two sources.

We applied an F–test to the χ^2 of the fits with and without the upper sideband in order to test its significance. We derived values for the significance of the upper sideband similar to those calculated from the errors in the fit parameters which we quoted above. Conservatively estimating the number of trials involved in obtaining our results at $\sim$400 (the number of frequencies where we searched for a QPO, $\sim$4000, divided by the FWHM of the QPO $\sim$10 Hz) still results in a $> 5\sigma$ detection in case of 4U 1608–52.

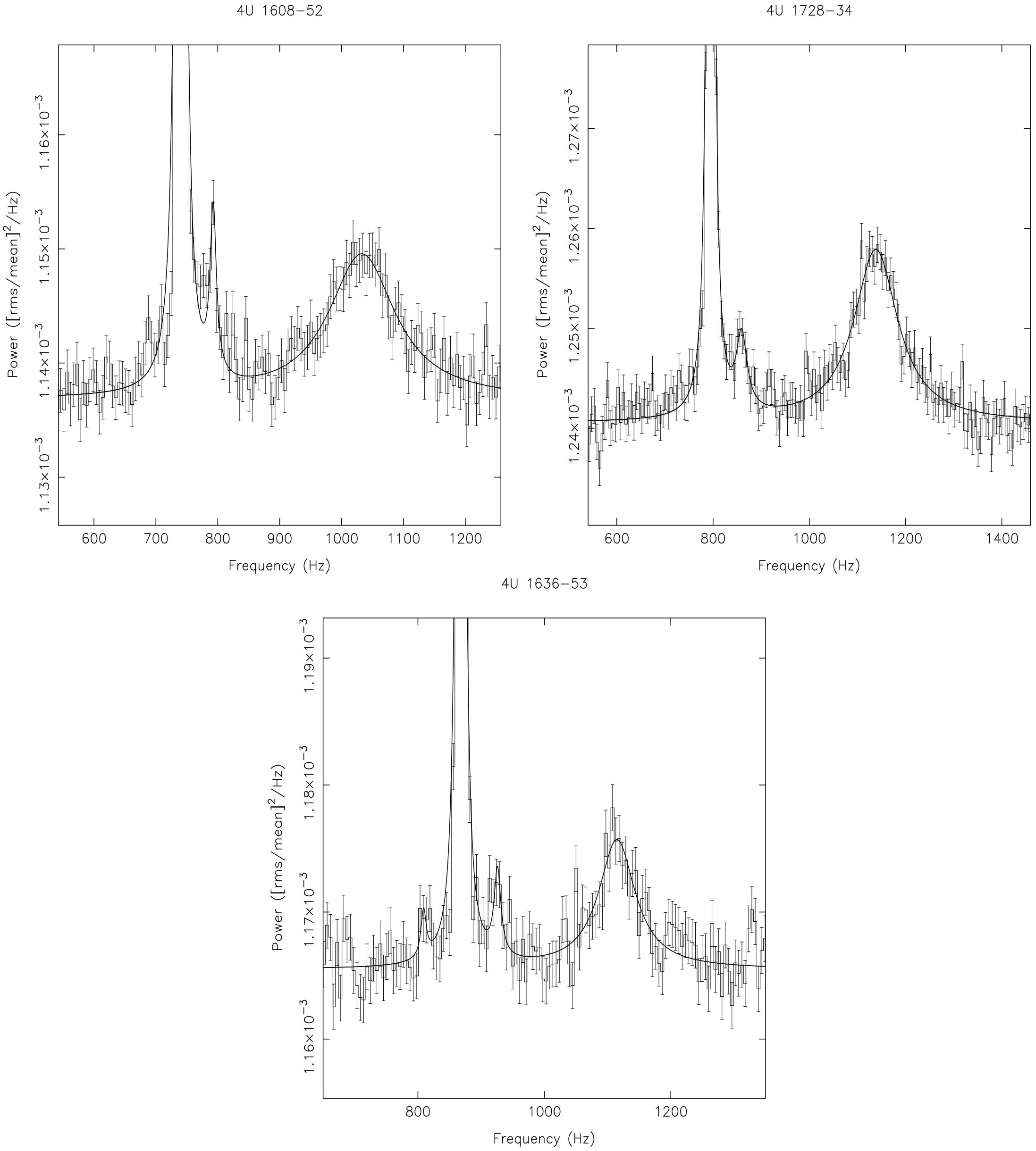

Figure 10.1: Power density spectra of the three sources showing the lower and upper kHz QPO and to the high frequency side of the lower kHz QPO the new QPO. The power is rms normalized after Belloni & Hasinger (1990). Note that due to the applied shift–and–add method, only the frequency difference with respect to the frequency to which the power spectra were shifted is meaningful (see also Table 10.2).

Table 10.2: The properties (2.0–60 keV) of the lower (ν_1), upper (ν_2) kHz QPO peaks, and of the new kHz QPO (ν_{SB}) for 4U 1608–52, 4U 1728–34, and 4U 1636–53.

	4U 1608–52			4U 1728–34			4U 1636–53		
Parameter	∼67 ksec[d]	∼33 ksec[e]	∼34 ksec[e]	∼92 ksec[d]	∼42 ksec[e]	∼50 ksec[e]	∼80 ksec[d]	∼40 ksec[e]	∼39 ksec[e]
rms_1 (%)	8.47±0.02	8.66±0.03	8.89±0.02	6.71±0.02	6.56±0.04	6.99±0.03	6.66±0.02	7.30±0.02	5.98±0.03
FWHM_1 (Hz)	4.85±0.03	5.45±0.06	4.38±0.04	7.5±0.1	9.1±0.1	6.6±0.1	4.75±0.04	4.28±0.04	5.8±0.1
ν_1 (Hz)[a]	740	672	806	795	733	847	867.5	843	893
rms_2 (%)	5.1±0.2	6.2±0.2	4.0±0.2	5.5±0.1	6.1±0.1	4.9±0.3	3.3±0.2	3.7±0.2	3.1±0.2
FWHM_2 (Hz)	131±10	105±8	130±18	111±6	95±5	141±20	70±7	99±15	51±9
$\Delta\nu$ (Hz)[b]	293±3	308±3	253±6	343±2	350±2	324±5	247±3	260±5	242±3
rms_{SB} (%)	1.77±0.14	2.0±0.2	1.3±0.1	1.79±0.15	2.1±0.2	1.4±0.2	1.18±0.17	1.1±0.2	1.5±0.2
FWHM_{SB} (Hz)	12±3	15±4	5±2	27±7	38±10	15±6	13±6	10±3	27±10
Δ_{SB} (Hz)[c]	52.8±0.9	49.6±1.4	53.9±0.5	64±2	65±4	65±2	58.4±1.9	56.6±2.7	62.4±5.1
rms_{SB2} (%)[f]	<0.9	<1.2	<1.1	<1.3	<1.5	<0.9	0.8±0.2	1.0±0.1	<1.0

[a] Average frequency for the lower kHz QPO before shifting. [b] Frequency separation, $\Delta\nu = \nu_2 - \nu_1$, between the upper and lower kHz QPO. [c] Frequency separation, $\Delta_{SB} = \nu_{SB} - \nu_1$, between the upper sideband and the lower kHz QPO. [d] Measurements for all available data [e] Data were divided according to the frequency of the lower kHz QPO. [f] 95% confidence upper limits to the amplitude of the lower sideband were calculated by fixing the other parameters at the values obtained for the upper sideband.

For each source we divided the data into two parts based on the frequency of the lower kHz QPO in the power spectra. In each of these parts we shifted the lower kHz QPO peak to the same frequency as before and fitted the average power spectrum. In 4U 1636–53 and 4U 1728–34 the separation between the upper sideband and the main peak, Δ_{SB}, is consistent with being the same in the two parts, whereas in 4U 1608–52 Δ_{SB} increases significantly (2.9σ, Table 10.2). In 4U 1608–52, the frequency of the upper sideband increases by $\sim$139 Hz as the frequency of the lower kHz QPO increases by $\sim$134 Hz. The fact that the distance of the sideband remains approximately constant (to within $\sim$4.5 Hz) as both peaks move over $\sim$135 Hz is an additional argument supporting the interpretation of the new kHz QPO as a sideband to the lower kHz QPO. Simultaneously, the frequency distance of the sideband to the upper kHz QPO changes by nearly 60 Hz; this and the fact that the sideband is much narrower than the upper kHz QPO, strongly argues in favor of the sideband being un–related to the upper kHz QPO.

To correct for the relative motion of the sideband with respect to the main peak, which artificially broadened it in our previous analysis, we calculated the frequencies to which each power spectrum should be shifted in order to align the sideband, assuming a linear relation between the frequencies of the sideband and the main peak. Applying this new shift to the data of 4U 1608–52 we indeed obtained a narrower sideband (9.7±2.2 Hz), although the effect is marginal. Aligning the power spectra on a hypothetical lower sideband did not result in a significant detection in 4U 1608–52. The upper sideband is also significantly detected in 4U 1608–52 when only a fraction of the data is selected and no shift-and-add is applied, although at a smaller significance level.

Applying the same shifts to the power spectra calculated for the two energy bands, we measured the dependence of the fractional rms amplitude on photon energy of the detected QPOs. Only for 4U 1608–52 we were able to significantly detect the sideband in both energy bands. The increase in fractional rms amplitude with energy in 4U 1608–52 is different for the lower and upper kHz QPO (see Méndez et al. 1998b). Although the fractional rms amplitude of the sideband increased from 1.7%±0.2% to 2.6%±0.3% as a function of photon energy (2.0–8.7–20 kev) in 4U 1608–52, the uncertainties on the measurements of the fractional rms amplitudes of the sideband did not enable us to distinguish between the two different trends observed for the kHz QPO pair. The FWHM of the lower kHz QPO, that of the upper kHz QPO, and that of the sideband nor the sideband separation nor the peak separation between the upper and lower kHz QPO changed significantly with respect to the values obtained in the total energy band.

We also investigated the lower frequency part of the power spectra for the presence of a QPO at a frequency equal to the difference between the sideband and the lower kHz QPO. We detected a low frequency QPO (LFQPO) at 40.9±0.7 Hz with a FWHM of 19±2 Hz and a fractional rms amplitude of 2.8±0.1% in 4U 1608–52 (see also Psaltis et al. 1999). In 4U 1728–34, a LFQPO at 41.5±0.2 Hz, with a FWHM of 19.9±0.8 Hz and a fractional rms amplitude of 5.3±0.1% was present (see also Ford & van der Klis 1998; Di Salvo et al. 2001). In 4U 1636–53 no LFQPO was found, but a broad noise component was detected which could be described with an exponentially cutoff power law with a cut off frequency of 70±18 Hz, a power law index of 0.0±0.1, and a fractional rms amplitude of 2.8±0.1%.

10.4 Discussion

We have discovered a new kHz QPO at frequencies close to the frequency of the lower kHz QPO in the three LMXBs 4U 1608–52, 4U 1728–34, and 4U 1636–53. This new kHz QPO moves in frequency with the lower kHz QPO and maintains a distance to it which is nearly (but not exactly) constant; its distance to the upper kHz QPO varies much more. In 4U 1636–53 an additional QPO was found symmetrically located at the lower frequency side of the lower kHz QPO peak (3σ). These facts suggest that the new kHz QPOs are sidebands to the lower kHz QPO.

If these QPOs are sidebands due to an amplitude modulation of the lower kHz QPO, there must be an additional mechanism reducing the amplitude of the lower sideband or enhancing the upper sideband, since in 4U 1608–52 and 4U 1728–34 the presence of a symmetric lower sideband can be excluded. If the lower kHz QPO is a beaming oscillation, a single-sideband (rotational) beat frequency scenario could apply (e.g. Alpar & Shaham 1985). However, this would lead to a lower rather than an upper sideband, opposite to what is observed, unless the modulating part of the disk is counter rotating. When both rotational modulation and amplitude modulation of the formation of the lower kHz QPO produce sidebands, but of opposite phase, destructive interference could in principle cause the amplitude of the lower frequency sideband to be suppressed. Kommers et al. (1998) observed sidebands to the pulses of the pulsar 4U 1626–67 at much lower frequencies (~0.1Hz). There the lower sideband was stronger than the upper one and they proposed a model using both amplitude modulation and rotational modulation of the pulsar beam.

The frequency separation between the sideband and the main peak (~50–60 Hz), hereafter ‘sideband separation’ is reminiscent of typical frequencies of horizontal branch oscillations (HBOs) in Z sources and low frequency QPOs (LFQ-

POs) in atoll sources. However, the frequency of the LFQPO ($\sim$41 Hz) apparent in two of the three sources is inconsistent with the observed sideband separation. Furthermore, the increase in sideband separation with increasing lower kHz QPO frequency we observed in 4U 1608–52 is less than the increase in HBO frequency with lower kHz QPO frequency usually seen (Psaltis et al. 1999). So, the sidebands appear to be unrelated to the LFQPO in these atoll sources. Mechanisms that might explain these QPOs, such as the magnetospheric beat frequency model (Alpar & Shaham 1985; Lamb et al. 1985) or the Lense-Thirring precession model (Stella & Vietri 1998) could be used in explaining the LFQPO and the sideband, however one model can not explain both simultaneously unless the LFQPO and the sideband reflect frequencies at different radii in the disk.

None of the kHz QPO models in the literature (e.g. the sonic point model, Miller et al. 1998; Lamb & Miller 2001, the relativistic precession model, Stella & Vietri 1998, and the two–oscillator model, Osherovich & Titarchuk 1999a) in their present form predict the presence of an upper sideband to the lower kHz QPO with a sideband separation different from the LFQPO frequency.

One of the effects possibly occurring in the sonic point beat frequency model (Miller et al. 1998; Lamb & Miller 2001) could perhaps explain the formation of the upper sideband we discovered. The density enhancements along the spiral flow responsible for the generation of the lower kHz QPO rotate around the neutron star $\sim$5–10 times before reaching the surface (Miller et al. 1998; Lamb & Miller 2001). Therefore, the orbital frequency of the enhancements is higher than the orbital frequency at the sonic point, the beat frequency will end up at slightly higher frequencies than the frequency of the lower kHz QPO. Since the sideband has a FWHM of $\sim$10 Hz corresponding to at least $\sim$100 cycles at a Keplerian frequency of 1000 Hz, the beat frequency will end up at frequencies 50–100 Hz higher. The orbital frequency of the enhancements and the change in the sideband separation as a function of the frequency of the lower kHz QPO, as observed in 4U 1608–52, will depend on the details of the physical processes at work close to the neutron star.

Acknowledgments This work was supported in part by the Netherlands Organization for Scientific Research (NWO) grant 614-51-002. This research has made use of data obtained through the High Energy Astrophysics Science Archive Research Center Online Service, provided by the NASA/Goddard Space Flight Center. This work was supported by NWO Spinoza grant 08-0 to E.P.J.van den Heuvel. MM is a fellow of the Consejo Nacional de Investigaciones Científicas y Técnicas de la República Argentina. PGJ would like to thank Jeroen Homan for stimulating discussions and Rob Fender for comments on an earlier version of this work. We would like to thank the anonymous referee for his/her comments which improved the paper.

Bibliography

Alpar, M. A. & Shaham, J. 1985, Nature, 316, 239
Belloni, T. & Hasinger, G. 1990, A&A, 227, L33
Berger, M., van der Klis, M., van Paradijs, J., et al. 1996, ApJ, 469, L13
Bradt, H. V., Rothschild, R. E., & Swank, J. H. 1993, A&AS, 97, 355
Di Salvo, T., Méndez, M., van der Klis, M., Ford, E., & Robba, N. R. 2001, ApJ, 546, 1107
Ford, E. C. & van der Klis, M. 1998, ApJ, 506, L39
Jahoda, K., Swank, J. H., Giles, A. B., et al. 1996, Proc. SPIE, 2808, 59
Kaaret, P., Piraino, S., Ford, E. C., & Santangelo, A. 1999, ApJ, 514, L31
Kommers, J. M., Chakrabarty, D., & Lewin, W. H. G. 1998, ApJ, 497, L33
Lamb, F. K. & Miller, M. C. 2001, ApJ, 554, 1210
Lamb, F. K., Shibazaki, N., Alpar, M. A., & Shaham, J. 1985, Nature, 317, 681
Marković , D. & Lamb, F. K. 2001, MNRAS
Méndez, M. 2000, in Rossi2000: Astrophysics with the Rossi X-ray Timing Explorer. March 22-24, 2000 at NASA's Goddard Space Flight Center, Greenbelt, MD USA, p.E59, E59–+
Méndez, M. & van der Klis, M. 1999, ApJ, 517, L51
—. 2000, MNRAS, 318, 938
Méndez, M., van der Klis, M., Ford, E. C., Wijnands, R., & van Paradijs, J. 1999, ApJ, 511, L49
Méndez, M., van der Klis, M., & van Paradijs, J. 1998, ApJ, 506, L117
Méndez, M., van der Klis, M., Wijnands, R., et al. 1998, ApJ, 505, L23
Miller, M. C., Lamb, F. K., & Psaltis, D. 1998, ApJ, 508, 791
Osherovich, V. & Titarchuk, L. 1999a, ApJ, 523, L73
—. 1999b, ApJ, 522, L113
Psaltis, D., Belloni, T., & van der Klis, M. 1999, ApJ, 520, 262
Psaltis, D. & Norman, C. 2001, ApJ, submitted
Stella, L. & Vietri, M. 1998, ApJ, 492, L59
—. 1999, Phys. Rev. Lett
Strohmayer, T., Zhang, W., & Swank, J. 1996a, IAU Circ., 6320, 1+
Strohmayer, T. E., Zhang, W., Swank, J. H., et al. 1996b, ApJ, 469, L9
Swank, J. H. 2001, in IAU Symposium 195, ed. P. C. H. Martens, S. Tsuruta, and M. A. Weber, (San Francisco: ASP)
van der Klis, M. 2000, ARA&A, 38, 717
van der Klis, M., Swank, J. H., Zhang, W., et al. 1996a, ApJ, 469, 1
van der Klis, M., Wijnands, R., Kuulkers, E., et al. 1996b, IAU Circ., 6511, 2+
van der Klis, M., Wijnands, R. A. D., Horne, K., & Chen, W. 1997, ApJ, 481, L97
Wijnands, R. A. D., van der Klis, M., van Paradijs, J., et al. 1997, ApJ, 479, L141
Yu, W., Zhang, S. N., Harmon, B. A., et al. 1997, ApJ, 490, L153
Zhang, W., Lapidus, I., White, N. E., & Titarchuk, L. 1996, ApJ, 473, L135

Chapter 11

Discovery of an X–ray pulsar in the low–mass X-ray binary 2A 1822−371

Peter G. Jonker, Michiel van der Klis

The Astrophysical Journal Letters, 2001, **553**, L43

Abstract

We report the discovery of 0.59 s X–ray pulsations from the low–mass X–ray binary, 5.57 hr dipping and eclipsing ADC source 2A 1822–371. Pulse arrival time analysis indicates a circular orbit with e <0.03 (95% confidence) and an asin$i$ for the neutron star of 1.006(5) lightseconds, implying a mass function of $(2.03 \pm 0.03) \times 10^{-2} M_{\odot}$. The barycentric pulse period was 0.59325(2) s in 1996.270 and 0.59308615(5) s in 1998.205, indicating an average spin up with $\dot{P}/P = (-1.52 \pm 0.02) \times 10^{-4}$yr^{-1}. For a magnetic field strength of $\sim$1–5$\times10^{12}$ G as derived from the X–ray spectrum the implied intrinsic X–ray luminosity is $\sim$2–4$\times10^{37}$erg s^{-1}. The pulse amplitude is low, but increases steeply as a function of energy from a sinusoidal amplitude of 0.25% in 2–5.4 keV to $\sim$3% above 20 keV. We discuss the constraints on the masses of the companion star and the fact that several aspects of the energy spectrum are in qualitative accordance with that of a strongly magnetised neutron star.

11.1 Introduction

The lightcurve of the low–mass X–ray binary (LMXB) 2A 1822–371 shows clear signs of orbital modulation in both the X–ray and optical bands (White et al. 1981; Seitzer et al. 1979; Mason et al. 1980), with a period of 5.57 hours. White et al. (1981) showed that the X–rays are emitted from an extended source, a so called Accretion Disk Corona (ADC) which is periodically partially eclipsed by the companion star (at orbital phase 0.0) as well as partially obscured by structure in the accretion disk whose height above the orbital plane varies but is greatest at phase 0.8 and least at phase 0.2 (White et al. 1981). The implied inclination is $i > 70^\circ$ (Mason et al. 1980). The short orbital period makes 2A 1822–371 a compact LMXB. If powered by a Roche lobe filling main–sequence star the companion mass is $0.62 M_\odot$, however, the companion spectrum is inconsistent with that of a normal K–star (Harlaftis et al. 1997).

The orbital period has been measured from eclipse timing to gradually increase (Hellier et al. 1990); the best ephemeris to date was provided by Parmar et al. (2001). The observed X–ray spectrum is complex and various models have been used to describe the data. With a power law index of ~ 1 (Parmar et al. 2001) the continuum is harder than that of typical LMXBs which have power law indices of 1.5–2.5. There is also evidence for a strong soft component in the 1-10 keV range (Heinz & Nowak 2001; Parmar et al. 2001). An upper limit on the presence of pulsations in the 1–30 keV band of 1% was derived by Hellier et al. (1992).

Soon after the discovery of accreting X–ray pulsars (Giacconi et al. 1971) it was realized that these are strongly magnetized ($B > 10^{12}$ G) neutron stars accreting matter from an accretion disk (Pringle & Rees 1972; Lamb et al. 1973) or a stellar wind (Davidson & Ostriker 1973). Whereas accretion–powered pulsars are common in massive X–ray binaries, they are rare in LMXBs, a fact that has been explained in terms of neutron star magnetic field decay (presumably accretion–induced) in the generally much longer–lived low–mass systems (Bhattacharya & Srinivasan 1995). The lower field would allow the disk to extend to close to the neutron star and spin it up to millisecond periods. This is in accordance with binary evolutionary models predicting that LMXBs are the progenitors of binary millisecond radio pulsars (Radhakrishnan & Srinivasan 1982; Alpar et al. 1982; see for a detailed description Bhattacharya 1995). This scenario was confirmed by the discovery of the first accreting millisecond pulsar, in the LMXB SAX J1808.4–3658 (Wijnands & van der Klis 1998). In this Letter, we report the discovery of pulsations in the LMXB 2A 1822–371, and describe our measurements of both the orbital Doppler shifts and the spin–up of the pulsar. We briefly discuss the constraints on the masses of the two binary components and also the energy spectrum of the pulsar.

11.2 Observations and analysis

We used 16 observations obtained on 1996 Sept. 26 and 27 (observations 1–5), 1998 June 28 and 29 (observations 6–11), and July 24 and 25 (observations 12–16) with the proportional counter array (PCA; Jahoda et al. 1996) onboard the *Rossi X–ray Timing Explorer* (RXTE) satellite (Bradt et al. 1993). The total amount of good data was ∼73 ksec. All observations yielded data with a time resolution of at least 2^{-13} s, in 64 energy bands covering the effective 2.0–60 keV energy range of RXTE.

As part of a systematic search for pulsars in LMXBs (Jonker et al. in prep.), a power spectrum of Solar System barycentered data was created using an FFT technique. The Nyquist frequency was 64 Hz. A weak 0.59 s pulsed signal was discovered first in the 2.0–60 keV power spectrum. Investigation of the pulsed signal in various energy bands and different sub–sets of the data showed that the signal–to–noise ratio was highest in the 9.4–22.7 keV band of observations 12–16. Therefore, we initially used this energy band and subset of the data for our analyses.

We measured the Solar System barycentric pulse period in 19 data segments of observations 12–16 each with a length of ∼1500 s (half a typical RXTE contiguous data segment) using an epoch folding technique. The period of the pulsar showed clear evidence of the 5.57 hour orbital modulation due to orbital Doppler shifts with an amplitude corresponding to an $a\sin i$ of about 1 light second. Correcting for the orbital delays using the previously known orbital ephemeris (Parmar et al. 2001) and our best measure of $a\sin i$ obtained from the pulse period analysis, we epoch–folded each 1500 s segment in observations 12–16, and measured the phase of each folded profile by fitting it with a sinusoid. The residual phases were then fitted with a model using a constant pulse period and a circular orbit. This satisfactorily described the observed dependencies on both time and orbital phase. The best–fit orbital and pulse parameters are given in Table 11.1. The measured pulse arrival times and the best–fit orbital delay curve are displayed in Figure 11.1.

Assuming our measured $a\sin i$ and the orbital ephemeris of Parmar et al. (2001) we found for observations 1–5 a pulse period of 0.59325(5) s. This is significantly longer than that during observations 12–16 (see Table 11.1), a conclusion that is insensitive to the details of the orbital corrections. From this difference we derived a pulse period derivative of $\dot{P} = (-2.85 \pm 0.04) \times 10^{-12}\,\mathrm{s\,s^{-1}}$. Due to the weakness of the signal and the limited amounts of data we were not able to phase–connect the data within observations 1–5 or 6–11, nor could we maintain the pulse count

Table 11.1: Orbital parameters of 2A 1822–371. The number in brackets indicates the 1σ uncertainty in the last digit.

Barycentric pulse period (s) at 1998.205, P_{1998}	0.59308615(5)
Projected semimajor axis (light sec.), asin$i$	1.006(5)
Orbital period (s), P_{orb}	20054.240(6)[a]
Epoch of superior conjunction (HJD), T	2450993.27968(2)
Eccentricity, e (95% confidence)	$< 3.1 \times 10^{-2}$
Mass function, $f_x(M_\odot)$	$(2.03 \pm 0.03) \times 10^{-2}$
Barycentric pulse period (s) at 1996.270, P_{1996}	0.59325(2)
Pulse period derivative (s/s), $\dot{P}$	$(-2.85 \pm 0.04) \times 10^{-12}$

[a] From orbital ephemeris of Parmar et al. (2001)

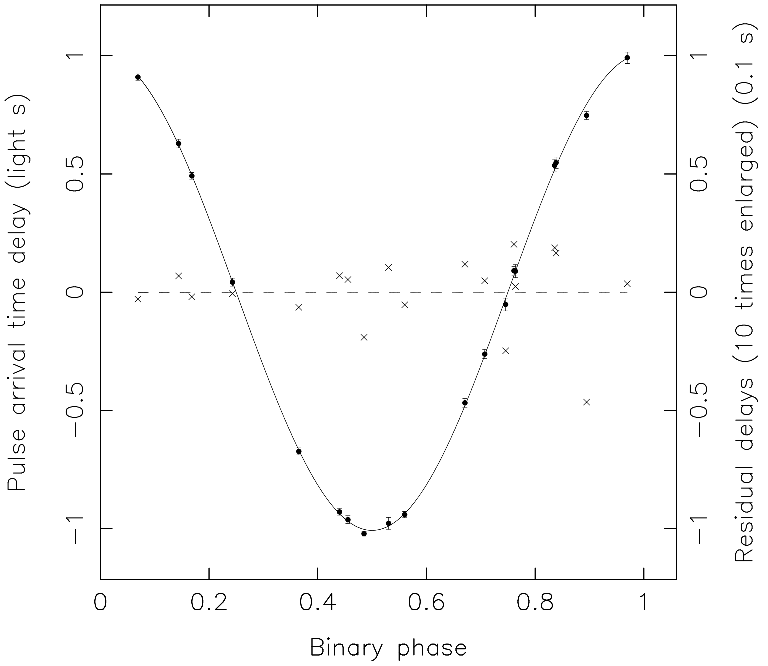

Figure 11.1: The arrival time delay in light seconds of the pulses due to the orbital motion of the neutron star as a function of binary phase. Phase zero is superior conjunction. Each dot represents ∼1500 s of data obtained in observations 12–16. The sinusoid is the best fit to the dots. The residuals of the fit (crosses) are shown at a 10 times expanded scale. Error bars are shown for the dots; for clarity they are omitted for the residuals.

between the epochs of observations 1–5, 6–11, or 12–16.

Using the parameters in Table 11.1 we folded 30 ksec of data of observations 12–16 in the energy bands 2.0–5.4–9.4–13.8–22.7–60 keV to measure the pulse shape and the pulse amplitude as a function of energy. The pulse profiles are consistent with being the same in each energy band and did not change significantly as a function of binary phase. The best pulse profile was obtained combining the energy bands 9.4–13.8 keV and 13.8–22.7 keV (see Figure 11.2). We fitted a single sinusoid to the profile in each energy band to measure the amplitude. The pulse amplitude depends strongly on energy, increasing from 0.25%±0.06% in the 2.0–5.4 keV band to 2.8%±0.5% in the 22.7–60 keV band (Figure 11.3). The pulse amplitude was lower in observations 1–5 than in observations 6–11 and 12–16 ($\sim$1.2% versus $\sim$1.7% and $\sim$2.1% in the 13.8–22.7 keV band, respectively). Although a single sinusoid is not a perfect representation of the pulse profile this will not significantly affect the derived pulse phase differences or pulse amplitude spectrum, as the profile is constant within the errors.

11.3 Discussion

Using data obtained with the RXTE satellite we have discovered 0.59 s X–ray pulsations from the low–mass X–ray binary (LMXB) 2A 1822–371 with $\dot{P}/P = -1.5\times10^{-4}\mathrm{yr}^{-1}$. This is the sixth LMXB to show pulsations (Table 11.2) and the fourth whose orbital pulse delay curve was measured. Contrary to SAX J1808.4–3658, 2A 1822–371 is optically bright and has a well–constrained inclination (because it is eclipsing), which might allow for a future full binary solution. Before our measurements, the nature of the compact object in 2A 1822–371 was somewhat uncertain. Heinz & Nowak (2001) showed that it could either be a white dwarf, a neutron star or a low–mass black hole. Our detection of pulsations, together with spin period changes on a timescale of $\sim10^4$ years establishes that the compact object is a neutron star. We derive a mass function for the companion star of $(2.03\pm0.03)\times10^{-2}M_{\odot}$. This, combined with the knowledge of the inclination constrains the masses of the two components to a small area in a plot of companion star mass versus neutron star mass (the shaded region in Figure 11.4). If the companion is a main sequence Roche–lobe filling star subject to the usual lower main sequence mass–radius relation (Kippenhahn & Wiegert 1990) its mass is $0.62M_{\odot}$ (the horizontal line in Figure 11.4). This would imply a quite massive neutron star. Spectroscopic observations provide a lower limit to the semi–amplitude of the radial velocity of the companion star (Harlaftis et al. 1997). From that lower

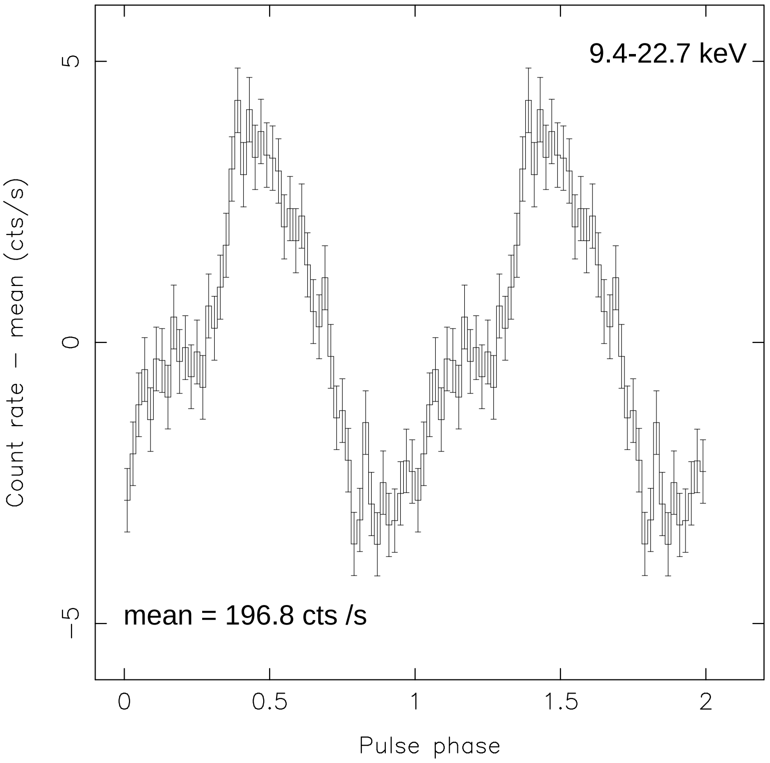

Figure 11.2: The measured pulse profile obtained from epoch folding the 9.4–22.7 keV data of observations 12–16. The mean count rate (indicated) was subtracted. For clarity two periods are plotted. The profile is clearly non–sinusoidal. Phase zero is at HJD 2451019.4011752. The bin size is ∼0.01 s. One sigma error bars are shown.

limit we constrain the mass of the neutron star to be more than $0.6^{+1.0}_{-0.3}M_\odot$ (the vertical line in Figure 11.4 at 0.3 $M_\odot$ represents the 67% confidence limit). Furthermore, they showed that the inner face of the companion star is 10 000–15 000 K hotter than its back face. This is probably due to effects of X–ray heating, which could render the companion significantly undermassive for its size. For a 1.4 $M_\odot$ neutron star the companion has a mass of 0.4–0.45 $M_\odot$ (see Figure 11.4).

An estimate of the strength of the magnetic field depends among other things on the source luminosity. The luminosity of 2A 1822–371 was estimated (Mason & Cordova 1982) to be $\mathrm{L_X} \sim 1.1\times\ 10^{35}\mathrm{erg\,s^{-1}}\ (\mathrm{d/1kpc})^2$. For a distance of 2.5 kpc (Mason & Cordova 1982) this would lead to $\sim 10^{36}$erg/s. However, since all observed X–rays are thought to have been scattered by an ADC (see Section 1), the true source luminosity may be as high as $\sim 10^{38}$erg/s (White &

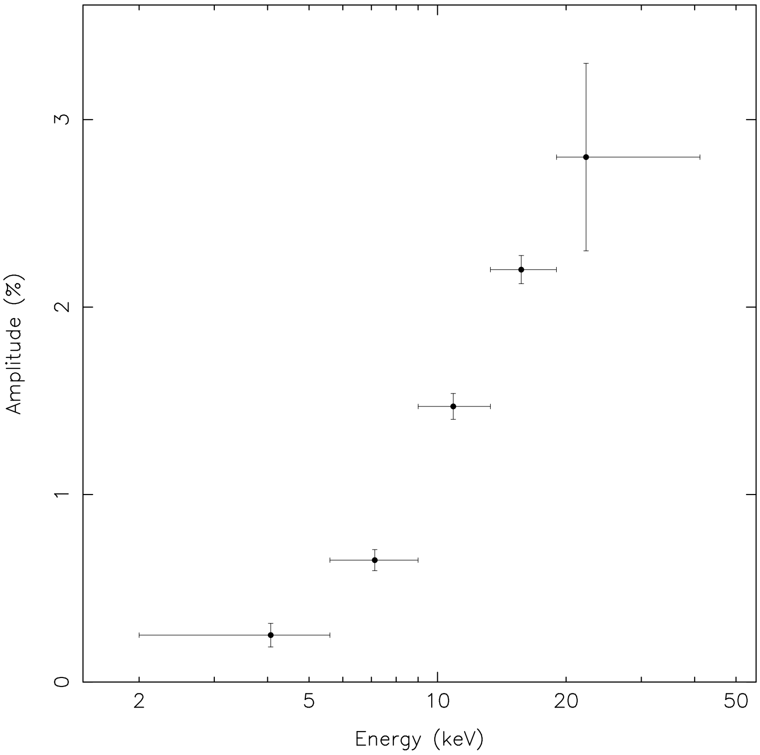

Figure 11.3: Pulse amplitude as a function of energy. The horizontal bars denote the width of the energy bands, while the vertical bars denote 1σ uncertainties. The x–coordinate of the dots is the weighted mean photon energy in each band. The pulse amplitude increases steeply with energy.

Holt 1982). Such a high luminosity would be consistent with the observed binary orbital period change (Heinz & Nowak 2001). From the luminosity and the spin–up rate the magnetic field can be determined (cf. Ghosh & Lamb 1979); for $\mathrm{L_X} \sim 10^{38}\mathrm{erg\,s^{-1}}$ we derive a magnetic field strength, B, of $\sim 8\times10^{10}$ G, whereas for $\mathrm{L_X} \sim 10^{36}\mathrm{erg\,s^{-1}}$ B $\sim 8\times10^{16}$ G, which implies that the luminosity is probably not that low. If we assume that the neutron star is spinning at its equilibrium period, then for $\mathrm{L_X} \sim 10^{36}\mathrm{erg\,s^{-1}}$ we find B$\sim 5\times10^{10}$ G and for $\mathrm{L_X} \sim 10^{38}\mathrm{erg\,s^{-1}}$ B$\sim 5\times10^{11}$ G. In all this we assumed $M_{ns} = 1.4M_{\odot}$, $I = 10^{45}$ g cm^2, and $R = 10^6$ cm for the mass, moment of inertia, and radius of the neutron star.

The X–ray spectrum of 2A 1822–371 was studied by various authors (White et al. 1981; Hellier & Mason 1989; Hellier et al. 1992; Heinz & Nowak 2001; Parmar et al. 2001; Iaria 2001), using data obtained with different satellites (*Einstein*,

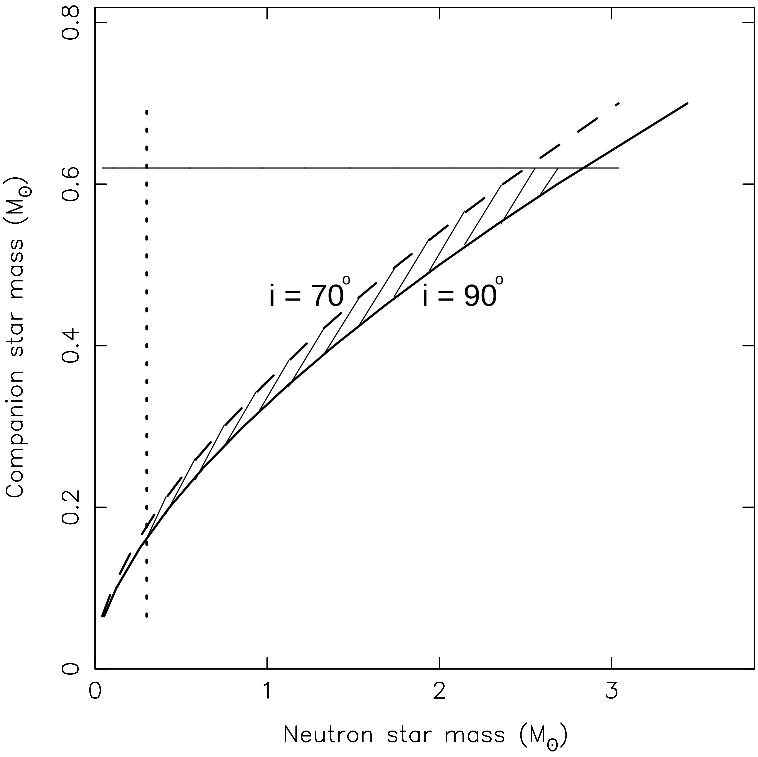

Figure 11.4: Companion star mass as a function of neutron star mass. The system is located between the two curves representing $i = 70°$ and $i = 90°$. The region to the left of the dotted line is excluded (67% confidence) due to the lower limit on the radial velocity of the companion star (Harlaftis et al. 1997). The horizontal line is the mass of the companion assuming it is a Roche–lobe filling main sequence star. The allowed region (shaded) assumes that the companion could be undermassive, not more massive than this.

EXOSAT, Ginga, ASCA, RXTE, and *BeppoSax*). Parmar et al. (2001) discussed several unusual features of the spectrum of 2A 1822–371 and although Compton scattering in the ADC probably also affected the spectrum (White & Holt 1982), in principle some of these features could be explained by the presence of a $\sim 10^{12}$ G pulsar instead of 10^8–10^9 G neutron star. With a power law index of $\sim$1 the continuum spectrum is much harder than that of LMXBs of similar luminosity (Parmar et al. 2001). This is, however, a common power law index for X–ray pulsars (White et al. 1983). The observed cut–off at $\sim$17 keV (Parmar et al. 2001) could also be explained by the presence of the pulsar. The cut–off energy of pulsars is thought to be approximately half the cyclotron energy (Makishima & Mihara 1992; see White et al. 1995 for a overview). The strength of the B–field which can thus be derived from the cut–off, assuming a redshift at the neutron star surface of 0.3, is $\sim 4 \times 10^{12}$ G. The relation between the electron temperature and the energy of the cyclotron resonance (Makishima et al. 1999), leads for a kT_e of ~4–10 keV (Parmar et al. 2001; Iaria 2001, although fit with a slightly different continuum function than Makishima et al. 1999) to magnetic field estimates of ~ 1–5×10^{12} G, again assuming a redshift at the neutron star surface of 0.3. These estimates of the magnetic field are consistent with the estimates derived from the spin–up above. The intrinsic source luminosity would be ~ 2–$4 \times 10^{37} \mathrm{erg\,s^{-1}}$ given the $\dot{P}/P$ we measured.

The neutron star was found to spin up on a timescale of ~6500 years; $\dot{\nu}$ is $(8.1 \pm 0.1) \times 10^{-12} \mathrm{Hz\,s^{-1}}$. Comparing this $\dot{\nu}$ with that in the other LMXB X–ray pulsars (Table 11.2) we note that the spin–up rate measured over ~666 days is large for an LMXB X–ray pulsar, but that of the transient system GRO J1744–28 is even larger (Finger et al. 1996). Recent observational evidence summarized by Bildsten et al. (1997) reveals alternating episodes of spin–up and spin–down in disk–fed neutron stars. If the $\dot{\nu}$ we measured of 2A 1822–371 between 1996.270 and 1998.205 would be the average of multiple spin–up and spin–down episodes, then the maximum spin–up rate would be even higher. However, episodes of steady spin–up or spin–down lasting nearly a decade have been observed in GX 1+4 and 4U 1626–67 (Chakrabarty et al. 1997a; Chakrabarty et al. 1997b).

The increase in pulse amplitude with photon energy is steeper than has been found for other low–mass X–ray pulsars (4U 1626–67, Rappaport et al. 1977; Her X–1, White et al. 1983; SAX J1808.4–3658, Wijnands & van der Klis 1998). Furthermore, the pulse amplitude is low compared with other LMXB X–ray pulsars. Previous studies revealed that in 2A 1822–371 scattering is important (White et al. 1981; Hellier & Mason 1989; Hellier et al. 1992; Parmar et al. 2001; Heinz & Nowak 2001). Multiple scatterings of the pulsed emission in an ADC of $0.3R_\odot$ (White et al. 1981) would have washed out the pulse due to light travel time delays. Therefore, at least a portion of the ADC should not be very optically thick. Compton scattering in such an ADC could explain the observed pulse amplitude spectrum.

Table 11.2: Comparing the X–ray pulsars in LMXBs.

Source	P_{Pulse} (s)	$\dot{\nu}$ (Hz/s)	P_{orb} (days)	asin$i$	References
SAX J1808.4–3658	0.00249	$< 7 \times 10^{-13}$	0.0839	0.062809(1)	1,2
GRO J1744–28	0.467	1.2×10^{-11}	11.8	2.6324(1)	3,4
2A 1822–371	0.5931	8.1×10^{-12}	0.232	1.006(5)	5
Her X–1	1.24	5×10^{-13}	1.70	13.1853(2)	4,6
4U 1626–67	7.66	8×10^{-13}	0.0289	....	4,7
GX 1+4	120	6×10^{-12}	~304	....	4,8,9,10

[1]Wijnands & van der Klis 1998 [2]Chakrabarty & Morgan 1998 [3]Finger et al. 1996 [4]Bildsten et al. 1997 [5]this paper [6]Tananbaum et al. 1972 [7]Rappaport et al. 1977 [8]Lewin et al. 1971 [9]Chakrabarty et al. 1997a [1]0Pereira et al. 1999

Acknowledgments This work was supported in part by the Netherlands Organization for Scientific Research (NWO) grant 614-51-002. This research has made use of data obtained through the High Energy Astrophysics Science Archive Research Center Online Service, provided by the NASA/Goddard Space Flight Center. This work was supported by NWO Spinoza grant 08-0 to E.P.J.van den Heuvel. PGJ would like to thank Rob Fender and Jeroen Homan for carefully reading an earlier version of the manuscript, Tiziana Di Salvo for discussions on the X–ray spectrum, and Kieran O'Brien for poiting out an error in a figure in an earlier version.

Bibliography

Alpar, M. A., Cheng, A. F., Ruderman, M. A., & Shaham, J. 1982, Nature, 300, 728

Bhattacharya, D. 1995, Millisecond pulsars, eds Lewin, van Paradijs, van den Heuvel (ISBN 052141684, Cambridge Univ. Press, 1995.)

Bhattacharya, D. & Srinivasan, G. 1995, The magnetic fields of neutron stars and their evolution, eds Lewin, van Paradijs, van den Heuvel (ISBN 052141684, Cambridge Univ. Press, 1995.)

Bildsten, L., Chakrabarty, D., Chiu, J., et al. 1997, ApJS, 113, 367+

Bradt, H. V., Rothschild, R. E., & Swank, J. H. 1993, A&AS, 97, 355

Chakrabarty, D., Bildsten, L., Finger, M. H., et al. 1997a, ApJ, 481, L101

Chakrabarty, D., Bildsten, L., Grunsfeld, J. M., et al. 1997b, ApJ, 474, 414+

Chakrabarty, D. & Morgan, E. H. 1998, Nature, 394, 346

Davidson, K. & Ostriker, J. P. 1973, ApJ, 179, 585

Finger, M. H., Koh, D. T., Nelson, R. W., et al. 1996, Nature, 381, 291

Ghosh, P. & Lamb, F. K. 1979, ApJ, 234, 296

Giacconi, R., Gursky, H., Kellogg, E., Schreier, E., & Tananbaum, H. 1971, ApJ, 167, L67

Harlaftis, E. T., Charles, P. A., & Horne, K. 1997, MNRAS, 285, 673

Heinz, S. & Nowak, M. A. 2001, MNRAS, 320, 249

Hellier, C. & Mason, K. O. 1989, MNRAS, 239, 715

Hellier, C., Mason, K. O., Smale, A. P., & Kilkenny, D. 1990, MNRAS, 244, 39P

Hellier, C., Mason, K. O., & Williams, O. R. 1992, MNRAS, 258, 457

Iaria, R., D. T. B. L. . R. N. R. 2001, ApJ

Jahoda, K., Swank, J. H., Giles, A. B., et al. 1996, Proc. SPIE, 2808, 59

Kippenhahn, R. & Wiegert, A. 1990, Stellar structure and evolution

Lamb, F. K., Pethick, C. J., & Pines, D. 1973, ApJ, 184, 271

Lewin, W. H. G., Ricker, G. R., & McClintock, J. E. 1971, ApJ, 169, L17

Makishima, K. & Mihara, T. 1992, Frontiers in X–ray astronomy (Proc. of the 28th Yamada Conference

Makishima, K., Mihara, T., Nagase, F., & Tanaka, Y. 1999, ApJ, 525, 978

Mason, K. O. & Cordova, F. A. 1982, ApJ, 262, 253

Mason, K. O., Seitzer, P., Tuohy, I. R., et al. 1980, ApJ, 242, L109

Parmar, A. N., Oosterbroek, T., Del Sordo, S., et al. 2001, A&A

Pereira, M. G., Braga, J., & Jablonski, F. 1999, ApJ, 526, L105

Pringle, J. E. & Rees, M. J. 1972, A&A, 21, 1+

Radhakrishnan, V. & Srinivasan, G. 1982, Curr. Sci, 51, 1096

Rappaport, S., Markert, T., Li, F. K., et al. 1977, ApJ, 217, L29

Seitzer, P., Tuohy, I. R., Mason, K. O., et al. 1979, IAU Circ., 3406, 1+

Tananbaum, H., Gursky, H., Kellogg, E. M., et al. 1972, ApJ, 174, L143

White, N., Nagase, F., & Parmar, A. N. 1995, The properties of X-ray binaries (Cambridge Astrophysics Series, Cambridge, MA: Cambridge Univ. Press, —c1995, edited by Lewin, Walter H.G.; Van Paradijs, Jan; Van den Heuvel, Edward P.J.), p. 1

White, N. E., Becker, R. H., Boldt, E. A., et al. 1981, ApJ, 247, 994

White, N. E. & Holt, S. S. 1982, ApJ, 257, 318

White, N. E., Swank, J. H., & Holt, S. S. 1983, ApJ, 270, 711

Wijnands, R. & van der Klis, M. 1998, Nature, 394, 344

Onderzoek naar lage massa röntgendubbelsterren met röntgen tijd–variaties

Lage massa röntgendubbelsterren

Dit proefschrift gaat over tijd–variaties in de röntgenstraling van zogenaamde lage massa röntgendubbelsterren. Deze röntgendubbelsterren bestaan uit een ster met een 'lage' massa van minder dan ~ 1 zonsmassa en een compact object (zie bijvoorbeeld Figuur 12.1). Het compacte object is gevormd tijdens een supernova–explosie. Zo'n explosie vindt plaats als een zware ster door zijn brandstofvoorraad heen is. De brandstof, veelal waterstof of helium, is nodig om via kernfusiereacties energie op te wekken. Deze energie levert de druk die nodig is om de zwaartekracht te weerstaan. Als die druk wegvalt, implodeert de kern van de ster tot een neutronenster of een zwart gat terwijl de energie die vrijkomt bij dit ineenstorten van de kern onder meer wordt gebruikt om de buitenste lagen weg te blazen. Dit proefschrift bevat resultaten van onderzoek naar lage massa röntgendubbelsterren waarbij het compacte object een neutronenster is. De materie van de neutronenster bestaat bijna uitsluitend uit neutronen. Deze neutronen zitten dicht op elkaar gepakt en kunnen zo de druk uitgeoefend door de zwaartekracht weerstaan.

In een röntgendubbelster stroomt materie van de 'gewone' ster naar het compacte object, in de dubbelsterren in dit proefschrift dus van de lage massa ster naar de neutronenster. Dit kan verscheidene oorzaken hebben. Wanneer de brandstof in de kern van de lage massa begeleider op raakt wordt de straal van de ster groter, aan de buitenste lagen worden dan meer getrokken door de neutronenster dan door de lage massa ster. Hierdoor gaat materie overstromen naar de begeleider. Een andere manier waarop materieoverdracht op gang kan komen hangt samen met de evolutie van het dubbelstersysteem als geheel. Als de twee sterren in hun baan om

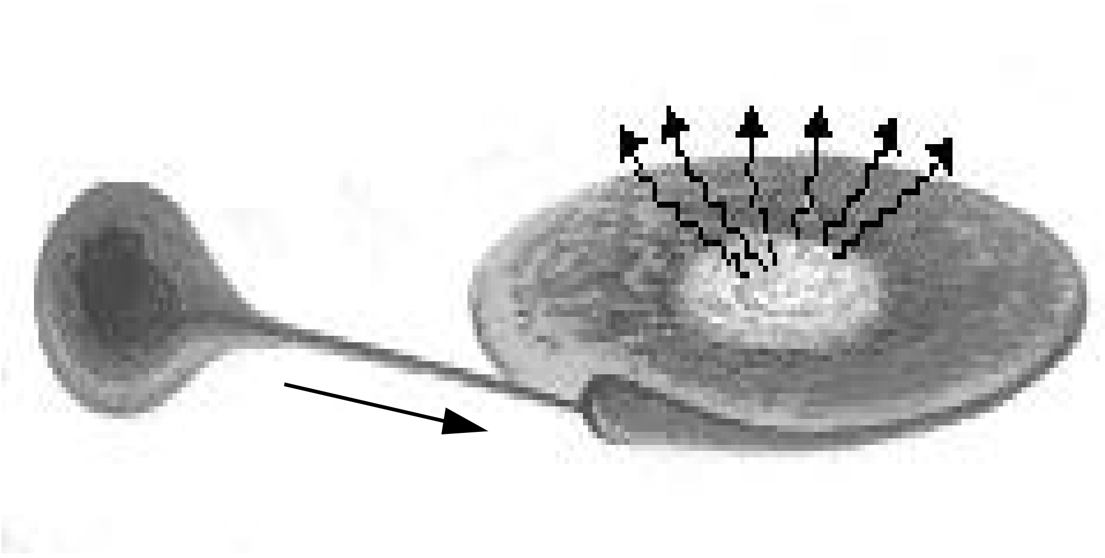

Figuur 12.1: Dit is een voorbeeld van hoe een lage massa röntgendubbelster er uit zou kunnen zien (met dank aan NASA). Materie stroomt van de ster (linksonder), via een schijf naar het compacte object. De begeleidende ster en de schijf draaien in dit geval tegen de wijzers van de klok in.

elkaar dichterbij elkaar komen (bijvoorbeeld doordat baanenergie via gravitatie–straling weggevoerd wordt) worden de buitenlagen van de lage massa ster naar de neutronenster getrokken. Uit deze twee voorbeelden blijkt wel dat er een bepaalde minimale verhouding bestaat tussen de afstand tussen de twee sterren en de straal van de begeleider, waarvoor nog net geen materie gaat overstromen. Wordt deze verhouding kleiner dan gaat er wel materie overstromen.

Als materie van de begeleider onder invloed van het zwaartekrachtveld van de neutronenster komt valt het niet direct op de neutronenster maar gaat het er een baan omheen beschrijven. Er vormt zich een zogenaamde accretieschijf waarin de materie langzaam naar binnen spiraliseert. Gedurende de val naar de neutronenster komt veel potentiele energie vrij. Deze wordt via wrijvingsprocessen omgezet in warmte die wordt uitgestraald. Het grootste deel van de energie komt vrij vlakbij en op het oppervlak van de neutronenster. Daar heeft de materie dan ook een temperatuur van ongeveer 10 miljoen K, waardoor röntgenstraling wordt uitgezonden.

Waarom zijn deze systemen interessant?

Eén van de belangrijkste doelen van het onderzoek naar dit soort systemen is het achterhalen van de samenhang tussen druk, dichtheid en temperatuur van de materie waar een neutronenster uit bestaat (de toestandsvergelijking). De materietoestand van de neutronenster kan in aardse laboratoria niet worden gemaakt. De maximale massa die een neutronenster kan hebben kan berekend worden uit de toestandsvergelijking en is een belangrijke parameter in het onderzoek. Een andere belangrijke tak van onderzoek richt zich op het achterhalen van de eigenschappen van de ruimte–tijd vlak bij een neutronenster. Een Newtoniaanse beschrijving van het zwaartekrachtveld voldoet hier niet. Relativistische effecten zijn hier groot en daardoor beter toegankelijk voor metingen. Tevens treden sommige van de relativistische effecten alleen op in sterke zwaartekrachtvelden zoals die bijvoorbeeld vlakbij de neutronenster te vinden zijn. Eén van deze effecten is het bestaan van ‘een binnenste stabiele cirkelbaan’ rond de neutronenster. Deeltjes die binnen de straal van de binnenste stabiele cirkelbaan komen vallen binnen korte tijd naar het oppervlak van de neutronenster. Dit is een puur relativistisch effect dat in de Newton mechanica niet voorkomt. Aangezien de röntgenstraling afkomstig is van de binnenste delen van de accretieschijf en van het neutronensteroppervlak is te verwachten dat de invloed van relativistische effecten zichtbaar zal zijn via deze röntgenstraling.

Echter, er zijn vele neutronensterren, sommige met en sommige zonder een accretieschijf, waarvan gebleken is dat ze een sterk magneetveld hebben (10^8–10^{12} Gauss; de sterkte van het aardmagneetveld is ongeveer 1 Gauss). Zo’n sterk magneetveld beïnvloedt de materiestromen in het binnenste deel van de schijf sterk. In systemen met een magneetveld van 10^{11}–10^{12} Gauss domineert het magneetveld de accretiestromen tot op een afstand van wel duizend km van de neutronenster. Door het magneetveld, dat in hoofdzaak dezelfde structuur heeft als dat van een staafmagneet met een noord– en een zuidpool, wordt materie uit de accretieschijf naar de magnetische polen geleid (zie Figuur 12.2). Als de materie op die polen neerstort komt er veel energie vrij. Doordat de neutronenster roteert verandert de hoeveelheid röntgenstraling die wij van de magneetpolen zien periodiek; dit zijn zogenaamde pulsaties. Zo’n periodiek signaal van de neutronenster kan als baken gebruikt worden. Via dit baken kan de baanbeweging van de neutronenster worden afgeleid. Als ook de baanbeweging van de lichte begeleidende ster bekend is kan de massa van de neutronenster nauwkeurig bepaald worden. Dus ook via de invloed van het magneetveld op de materiestroom wordt veel informatie verkregen over de eigenschappen van de neutronenster.

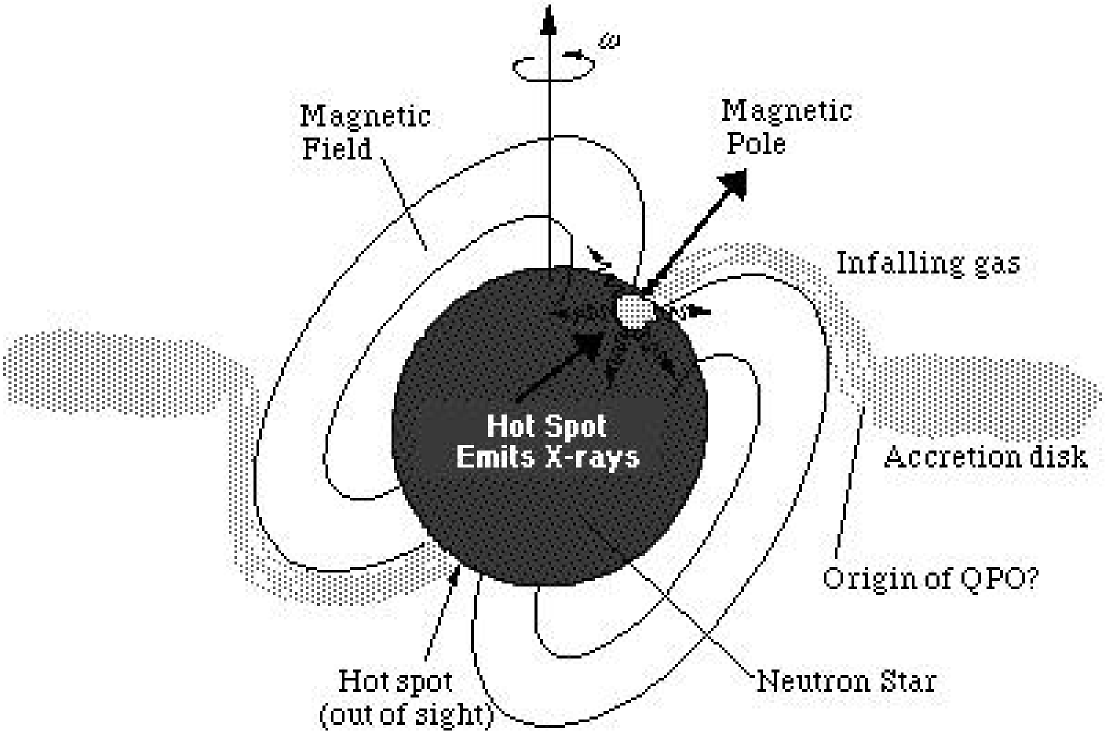

Figuur 12.2: Dit is een schematische weergave van een röntgenpulsar (met dank aan NASA). Zichtbaar zijn o.a. de magnetische veldlijnen waarlangs de materie uit de accretieschijf naar de magnetische polen wordt geleid. De draai–as van de neutronenster en de plaats waar quasi–periodieke oscillaties (QPOs, zie verder in de tekst) mogelijk vandaan komen zijn ook aangegeven.

Tenslotte worden röntgendubbelsterren ook bestudeerd vanwege hun rol in ster–evolutie. Door de toestroom van materie en verval van het magneetveld tijdens de lage massa röntgendubbelster fase gaat de neutronenster sneller roteren. De neutronenster wordt opgezweept zoals een tol door klappen van een zweep. De materie die op de neutronenster stort komt net als de zweep met hoge snelheid aan. Nadat de materieoverdracht stopt wordt de neutronenster zichtbaar als milliseconde radiopulsar. In 1998 is de eerste accreterende milliseconde röntgenpulsar ontdekt, geheten SAX J1808.4–3658. Dit is een sterke aanwijzing dat het geschetste scenario juist is.

Hoe worden deze systemen onderzocht?

Om de fysische omstandigheden waaronder de röntgenstraling ontstaat te achterhalen worden de verdeling van de hoeveelheid licht over het golflengtegebied (de spectrale energieverdeling) en de variaties in de hoeveelheid licht als functie van de tijd onderzocht. De gegevens waarvan gebruik is gemaakt zijn verkregen via een satelliet van NASA, in het Engels *Rossi X–ray Timing Explorer* geheten en afgekort naar het engelse acronym met RXTE.

De röntgen tijd–variaties kunnen op verschillende manieren worden onderzocht. Eén daarvan, het als functie van de tijd uitzetten van de hoeveelheid geregistreerde lichtdeeltjes levert al veel informatie op (zie Figuur 12.3). Zo vallen snelle kortdurende afnames in de hoeveelheid röntgenstraling op, zogenaamde dips, terwijl ook de sterke, kortdurende flits direct in het oog springt. Deze flitsen worden veroorzaakt door explosief verlopende kernfusiereacties van voornamelijk waterstof en/of helium op het oppervlak van de neutronenster. Wanneer van een lage massa röntgendubbelster zulke röntgenflitsen (of de hierboven beschreven pulsaties) worden waargenomen is het duidelijk dat het compacte object een neutronenster moet zijn en geen zwart gat. Echter, vooral snelle en zwakke tijdsvariaties zijn niet goed te onderzoeken in een lichtkromme. Een lichtkromme kan via een zogenaamde Fourier transformatie worden omgerekend naar een variatiespectrum. In een variatiespectrum wordt de mate van variatie in de röntgenstraling uitgezet als functie van de frequentie waarop de straling varieert (zie Figuur 12.4). Het is gebleken dat veel van de variaties quasi–periodiek zijn, dat wil zeggen dat er steeds gedurende korte tijd enige cycli van een periodieke variatie te zien zijn, maar op langere termijn is toch geen vaste periode aan te wijzen. In een variatiespectrum levert dit een brede piek op. Door de eigenschappen van die quasi–periodieke oscillatie pieken (QPOs) te meten, zoals sterkte, breedte, frequentie en variaties hierin kunnen de oscillaties systematisch worden onderzocht.

In dit proefschrift spelen de relaties tussen en de frequenties van drie QPOs een belangrijke rol. Het betreft de QPO waarvan de frequentie varieert tussen de $\sim$10–50 Hz en twee QPO pieken met frequenties varierend van 200–1200 Hz, zogenaamde kHz QPOs (zie Figuur 12.5). Deze kHz QPOs laten zeer snelle variaties zien die duiden op beweging vlakbij de neutronenster. Naar verwachting zal de vorming van deze pieken te maken hebben met, of in elk geval beïnvloed zijn door, de extreme omstandigheden vlakbij de neutronenster.

Het is gebleken dat de variatie–eigenschappen van de lage massa röntgenbronnen systematisch veranderen in de tijd. Uit het gelijktijdig onderzoeken van de spectrale energieverdeling en de snelle tijdsvariaties van het röntgenstraling bleek

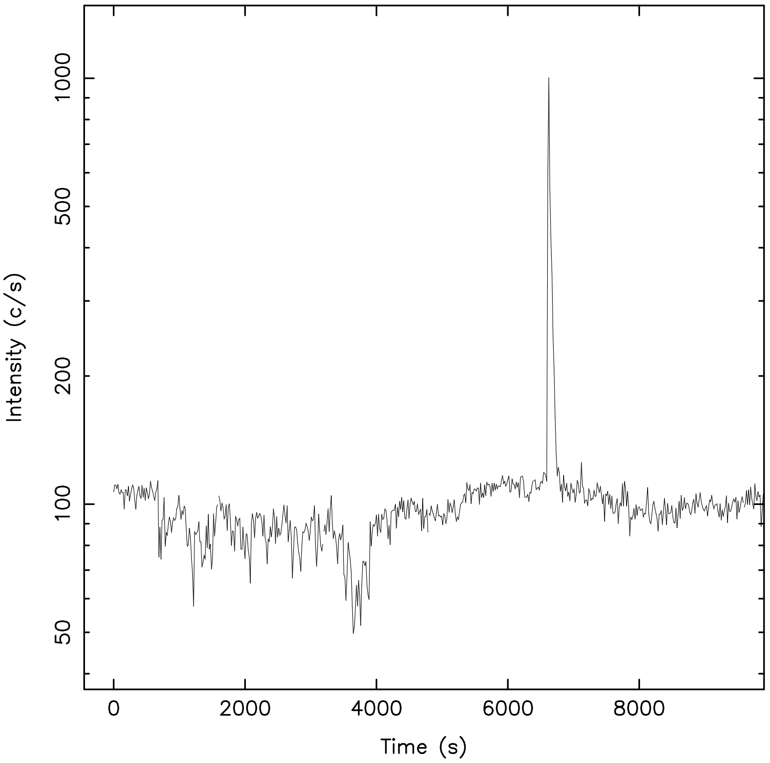

Figuur 12.3: Lichtkromme van de bron 4U 1323–62. Zichtbaar zijn de onregelmatige variaties tussen tijden 1000–4000 s en de korte sterke röntgenflits.

dat deze gecorreleerd zijn. Kleine veranderingen in de spectrale energieverdeling kunnen worden onderzocht door kleur–kleur diagrammen te maken. Hiertoe wordt de spectrale energieverdeling verdeeld in typisch drie of vier banden. De verhouding tussen de röntgenhelderheid in twee van deze banden wordt ‘kleur’ genoemd. Een kleur–kleur diagram van een zogenaamde Z–bron is gegeven in Figuur 12.6. De eigenschappen van de quasi–periodieke componenten in een variatie spectrum van zo’n Z–bron hangen sterk af van de positie van de bron langs de Z.

Wat zijn de resultaten?

In de hoofdstukken 3 en 4 wordt de ontdekking van een quasi–periodieke oscillatie (QPO) met een frequentie van ongeveer 1 Hz beschreven. Deze QPO heeft

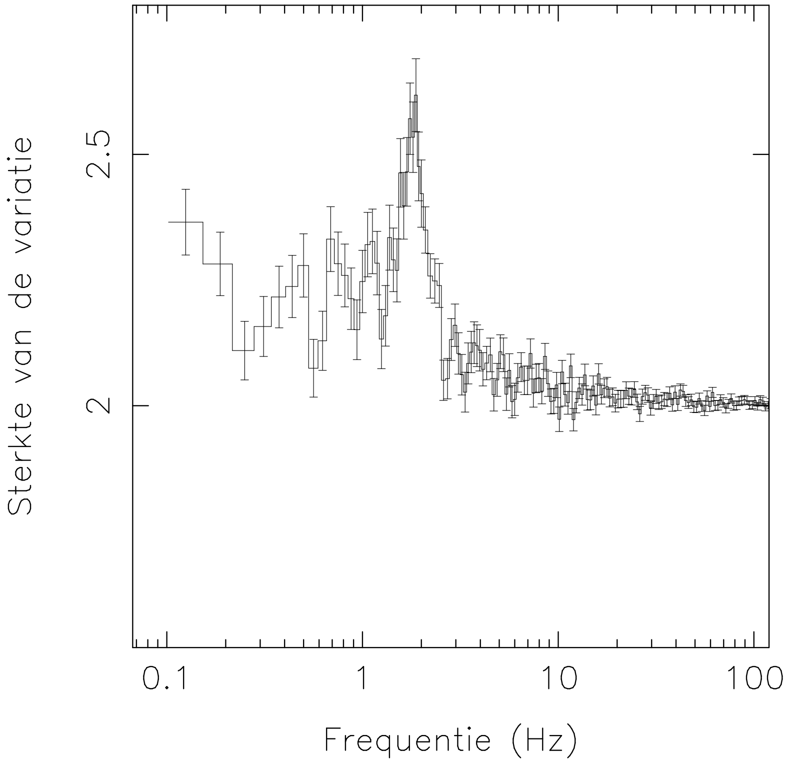

Figuur 12.4: Variatiespectrum van de bron 4U 1323–62. Duidelijk zichtbaar is de quasi–periodieke oscillatie op een frequentie van ∼2 Hz. Deze variatie is in de lichtkromme van deze data niet te onderscheiden.

bijzondere eigenschappen waaruit veel over zijn vormingsmechanisme kan worden afgeleid. Zo is duidelijk dat deze QPO moet ontstaan doordat de centrale röntgenbron quasi–periodiek wordt afgedekt. Zo'n QPO is alleen in bronnen gevonden waarvan bekend is dat de hoek waaronder wij ze bekijken erg groot is: onze gezichtslijn naar de neutronenster loopt dus vlak langs het oppervlak van de schijf. Door gebruikt te maken van de unieke eigenschappen van deze QPO kunnen we afleiden dat de geometrie van de accretieschijf en/of de centrale bron verandert (Hoofdstuk 4).

Een groot gedeelte van dit proefschrift (de Hoofdstukken 5, 6 en 7) behandelt onderzoek aan de variatie–eigenschappen van twee Z bronnen. In beide bronnen is een nieuwe QPO waargenomen. Deze nieuwe QPO en twee eerder gevonden QPOs hebben een frequentieverhouding van nagenoeg 2 en 4. Dit is een aanwijzing dat ze veroorzaakt worden door hetzelfde fenomeen, waarbij de variatie

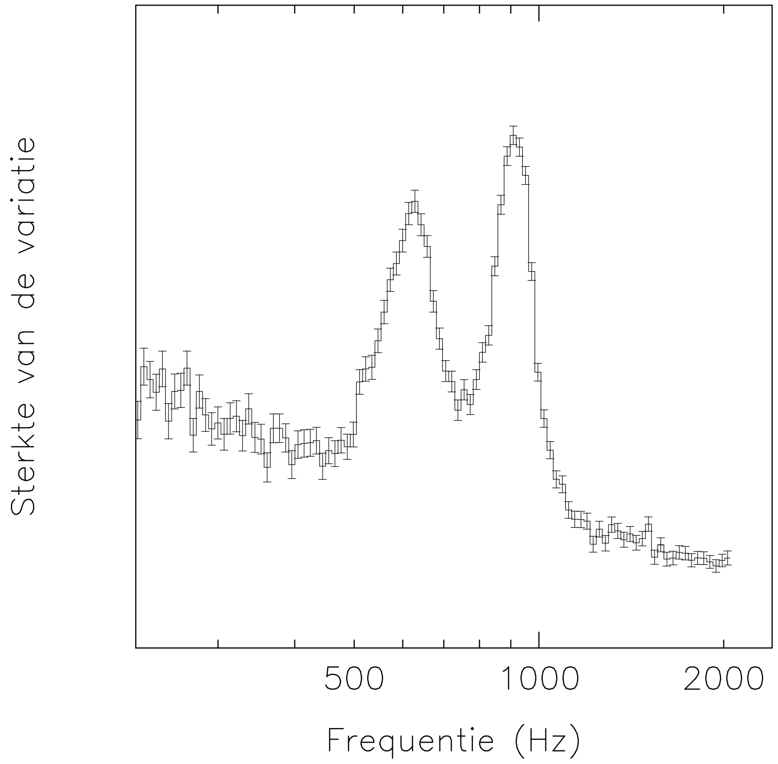

Figuur 12.5: Variatiespectrum van de helderste persistente röntgenbron aan de hemel, Sco X–1. Duidelijk zichtbaar zijn de quasi–periodieke oscillaties met frequenties van $\sim$*600 en* $\sim$*950 Hz.*

die veroorzaakt wordt door dit onbekende fenomeen niet sinusvormig is. Op dit moment is er een heftig debat gaande over wat het fenomeen is dat de variaties veroorzaakt. Een van de modellen, het ‘twee–oscillatoren model’ kan onze bevindingen niet verklaren en is dus onjuist. Er is voorgesteld dat precessie van de deeltjesbanen vlakbij de neutronenster de modulatie veroorzaakt. Deze precessie wordt gedomineerd door een relativistisch effect genaamd ‘frame dragging’, in het Nederlands ‘het slepen van ruimte–tijd’. De mate van precessie hangt onder andere af van de draaisnelheid en de verhouding van de straal en de massa van de neutronenster. Volgens een andere theorie wordt de variatie in de hoeveelheid röntgenstraling veroorzaakt door invloed van het magneetveld van de neutronenster op de materiestromen. Het pleit over welke van de laatste twee modellen juist is is nog niet beslecht, maar onze waarnemingen hebben aangetoond dat de frequenties en de breedtes van de pieken makkelijker te verklaren zijn door precessie

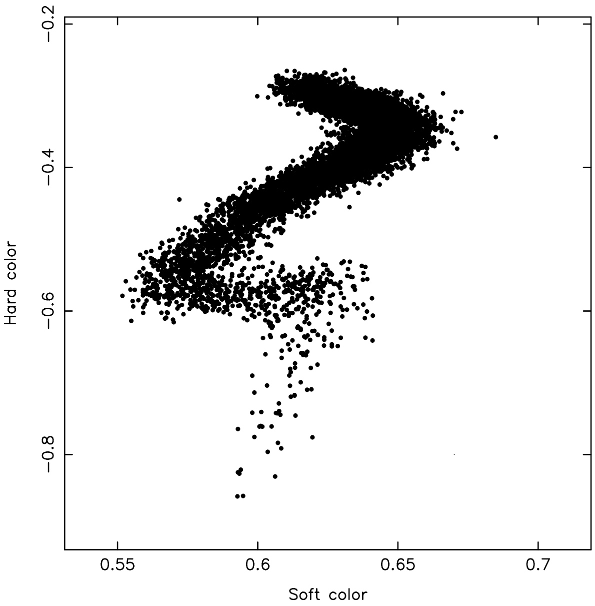

Figuur 12.6: Een kleur–kleur diagram van de Z–bron GX 340+0.

van de deeltjesbanen.

De ontdekking van een quasi–periodieke oscillatie met een frequentie van ongeveer 1150 Hz (een zogenaamde kHz QPO) in de zwakke bron 2S 0918–53 was de aanleiding de sterktes van dit soort kHz QPOs van verschillende bronnen met elkaar te vergelijken. Het blijkt dat in heldere bronnen dit soort variaties slechts een kleine fractie zijn van de totale intensiteit van de röntgenstraling (typisch een paar procent), terwijl tot wel 20% van de röntgenstraling gemoduleerd wordt door de kHz QPO bij zwakke bronnen. De reden hiervoor is nog niet helemaal duidelijk, maar een goede mogelijkheid is dat in de heldere bronnen een deel van de materie van alle kanten naar de neutronenster toe stroomt. Deze materiestroom zou dan niet gemoduleerd zijn door de kHz QPO maar wel röntgenlicht uitzenden, terwijl de stroom die via de accretieschijf het neutronensteroppervalk bereikt wel gemoduleerd is.

De bovengenoemde kHz QPOs komen voort uit de snelle deeltjesbanen $\sim$15–20 km boven het neutronensteroppervlak. Of de kHz QPO pieken een rechtstreeks gevolg zijn van de sterke zwaartekrachtvelden of van een samenspel van het magneetveld en het zwaartekrachtveld is nog niet duidelijk. Wat wel duidelijk is is dat relativistische effecten op de beweging van deeltjes in dit gebied niet te verwaarlozen zijn. Om de theoretische modellen te testen zijn extra gegevens nodig.

Alle theorieën voorspellen bijvoorbeeld dat er nog meer (zwakkere) QPOs zouden moeten zijn bij hoge (kHz) frequenties dan de twee bekende. Wij hebben inderdaad een derde kHz QPO piek ontdekt, nadat er al vijf jaar naar gezocht was. De ontdekking wordt beschreven in Hoofdstuk 10. Hoewel dat weer betwist wordt door andere theoreten, is er nu nog maar één model wat deze extra piek kan verklaren. Volgens dit model zijn de frequenties van de kHz QPO pieken resonantiesfrequenties die onder invloed van relativistische effecten in een accretieschijf worden opgewekt.

In Hoofdstuk 11 wordt de ontdekking van een röntgenpulsar beschreven. Dit is een van de zes lage massa röntgendubbelstersystemen waarvan we zeker weten dat het magneetveld een zeer sterke invloed heeft op de materiestromen vlak bij de neutronenster, maar pas de vierde waarvan we via de variaties in de aankomsttijden van de röntgenpulsaties de baan van de neutronenster kunnen meten. Het blijkt dat de rotatie snelheid van de neutronenster nog betrekkelijk laag is, hoewel we ook hebben ontdekt dat de neutronenster steeds sneller gaat draaien. Het speciale aan dit systeem is dat we de hoek waaronder wij het systeem bekijken relatief goed weten en dat de begeleidende ster veel licht geeft en dus met een gewone telescoop goed te bestuderen is. Dit alles samen maakt dat we zeer waarschijnlijk voor het eerst in een lage massa röntgendubbelster de massa van de neutronenster kunnen gaan bepalen. Deze zomer worden waarnemingen gedaan met de Very Large Telescoop die ons in staat moeten stellen dit te doen.

Publication list

Published in refereed journals: first author

- Jonker, P.G., van der Klis, M. 2001, ApJ, 553, L43 *Discovery of an X–ray pulsar in the low–mass X–ray binary 2A 1822–371*
- Jonker, P.G., van der Klis, M, Homan, J., Méndez, M., van Paradijs, J., Belloni, T., Kouveliotou, C., Lewin, W.H.G., Ford, E.C. 2001, ApJ, 553, 335 *Discovery of a kilohertz Quasi–periodic oscillation in 2S 0918–549*
- Jonker, P.G., Méndez, M., van der Klis, M. 2000, ApJ, 540, L29 *Discovery of a new, third kilohertz quasi–periodic oscillation in 4U 1608–52, 4U 1728–34, and 4U 1636–53: Sidebands to the lower kilohertz quasi-periodic oscillation?*
- Jonker, P.G., Fender, R.P., Hambly, N.C., van der Klis, M., 2000, MNRAS, 315, L57 *The infrared counterpart of the Z source GX 5–1*
- Jonker, P.G., van der Klis, M., Wijnands, R., Homan, J., van Paradijs, J., Méndez, M., Ford, E.C., Kuulkers, E., Lamb, F.K., 2000, ApJ, 537, 374 *The power spectral properties of the Z source GX 340+0*
- Jonker, P.G., van der Klis, M., Homan, J., Wijnands, R., van Paradijs, J., Méndez, M., Kuulkers, E., Ford, E.C., 2000, ApJ, 531, 453 *Discovery of a* ~ 1 *Hz quasi-periodic oscillation in the low-mass X-ray binary 4U 1746–37*
- Jonker, P.G., van der Klis, M., Wijnands, R., 1999, ApJ, 511, L41 *A persistent* ~ 1 *Hz quasi-periodic oscillation in the dipping low-mass X-ray binary 4U 1323–62*
- Jonker, P.G., Wijnands, R., van der Klis, M., Psaltis, D., Kuulkers, E., Lamb, F.K., 1998, ApJ, 499, L191 *Discovery of kilohertz quasi-periodic oscillations in the Z source GX 340+0*

Published in refereed journals: co–author

- Brocksopp, C., Jonker, P.G., Fender, R.,P., Groot, P.J., van der Klis, M., Tingay, S.J. 2001, MNRAS, 323, 517 *The 1997 hard state outburst of the X–ray transient GS 1354–64/ BW Cir*

- Boyd, P.T., Smale, A., Homan, J., Jonker, P.G., van der Klis, M., Kuulkers, E. 2000, ApJ, 542, L127 *Canonical Timing and spectral behavior of LMC X–3 in the low/hard state*

- Ford, E.C., van der Klis, M., Méndez, M., Wijnands, R., Homan, J., Jonker, P.G., van Paradijs, J. 2000, ApJ, 537, 368 *Simultaneous measurements of X-ray luminosity and kilohertz quasi-periodic oscillations in low-mass X-ray binaries*

- Psaltis, D., Wijnands, R., Homan, J., Jonker, P.G., van der Klis, M., Miller, M.C., Lamb, F.K., Kuulkers, E., van Paradijs, J., Lewin, W.H.G., 1999, ApJ, 520, 763 *On the magnetospheric beat-frequency and Lense-Thirring interpretations of the horizontal branch oscillation in the Z sources*

- Homan, J., Jonker, P.G., Wijnands, R., van der Klis, M., van Paradijs, J., 1999, ApJ, 516, L91*A variable 0.58–2.44 Hz quasi-periodic oscillation in the eclipsing and dipping low-mass X-ray binary EXO 0748–676*

- Psaltis, D., Méndez, M., Wijnands, R., Homan, J., Jonker, P.G., van der Klis, M., Lamb, F.K., Kuulkers, E., van Paradijs, J., Lewin, W.H.G., 1998, ApJ, 501, 95 *The beat-frequency interpretation of kilohertz quasi-periodic oscillations in neutron star low-mass X-ray binaries*

IAU Circulars

- Homan, J., Jonker, P.G., van der Klis, M., & Kuulkers, E. 2000, IAU Circ. 7425

Submitted to refereed journal

- Jonker, P.G., van der Klis, M., Homan, J., Méndez, M., Lewin, W., Wijnands, R., Zhang, W. submitted MNRAS *Low and high frequency variability as a function of spectral properties in the bright X–ray binary GX 5–1*
- Jouteux, S., Stappers, B., Ramachandran, R., Jonker, P.G., van der Klis, M., submitted *Analysis of Fourier Techniques for searching for pulsars in close binary systems.*
- Yu, W., van der Klis, M., Jonker, P.G., ApJ, 2001, in press *Dependence of the kHz QPO properties on the Normal Branch Oscillation phase in Scorpius X–1*

Dankwoord

Michiel, ik ben jou zeer veel dank verschuldigd voor de samenwerking en de vrijheid in de afgelopen 4 jaar. Volgens mij ben je een erg goede manager, je voelt ook goed aan wanneer je mensen niet of slechts sporadisch hoeft aan te sporen. Ik heb erg veel van je geleerd en ik ben je zeer erkentelijk voor je geduldig uitleggen als ik soms door de stress vergat na te denken.

Op het instituut, met Rob als kamergenoot de eerste twee jaar en daarna met Martin, was de sfeer erg prettig. Ik denk dat de vaste kern, Martin, daar erg belangrijk voor is. Jeroen, dank voor het vele samenwerken, samen eten en samen praten. Rudy, dank voor het in- en samenwerken (de DS is nooit af maar rijdt wel).

Mijn vrienden, met name Theunis, Jan, André, Marcus, en Martin, dank ik voor de prettige tijd samen buiten theoffice uren. Ook het Orcahuis en dan bedoel ik natuurlijk haar bewoners, wil ik danken voor de plezierige woonsfeer tijdens de eerste twee jaar van mijn promotie en de jaren daarvoor; hierbij wil ik mijn goede vriendin Natalie en de vaste Orcahuis–kern Derk en Jan–Karel in het bijzonder noemen. Verder dank voor de hulp bij de DS sleutel acties (met name Derk), kolonist–blaat–avonden (Bas, Camiel, Mark), het fietsen (Bas, Jan–'op 10 meter in het wiel'–Karel) en de samen–eet–avonden.

Mijn ouders wil ik danken voor alle hulp, het praten, en het vertrouwen; dit boekje is ook voor jullie. Leander dank voor het maken van de kaft en voor je inzicht tijdens onze ontwerp/brainstorm fase. Janine en Xavier; dank dat ik altijd als ik het wilde mocht bijkomen bij jullie.

Tenslotte een paragraaf voor mijn lief; Monique. Het moet vermoeiend zijn geweest om elke keer, hetzij op weg naar huis, hetzij net thuis aangekomen mijn relaas aan te horen over wat ik gedaan en of ontdekt had. Ik ben heel blij jou als vriendin en steun te hebben. Gelukkig hebben wij nog een heel leven samen.